



**UNIVERSITÀ DEGLI STUDI DELL'AQUILA**  
**DIPARTIMENTO DI INGEGNERIA INDUSTRIALE E DELL'INFORMAZIONE E DI**  
**ECONOMIA**

Dottorato di Ricerca in Ingegneria industriale e dell'informazione e di economia  
Curriculum Ingegneria Meccanica, energetica e gestionale  
XXXIII ciclo

**Direct Injection of liquid and gaseous fuels into Internal Combustion Engines**

SSD ING-IND/08

Dottorando  
Ing. Francesco Duronio

Coordinatore del corso  
Prof. Giuseppe Ferri

Tutor  
Prof. Angelo De Vita

A.A. 2019/2020



*“... Così preziosa come il vino  
Così gratis come la tristezza  
Con la tua nuvola di dubbi e di bellezza. ”*

Fabrizio De André, 1981.



## *Abstract*

The adoption of direct injection systems in internal combustion engines seems to be a proficient way to reduce tailpipe pollutant emissions, fuel consumption and enhance vehicles performances. Indeed, in the last decades the ever-increasing concerns about the environmental pollution and the green-house effect demonstrate the absolute necessity to achieve, among the many human activities, a sustainable mobility too. In this scenario many solutions have been developed to enhance the environmental performance of the vehicles. The hybrid or fully electric vehicles alone are not the solution of this issue, at least in the short period. Consequently, the author decides to investigate internal combustion engines and, in particular, injection processes performed directly in combustion chamber. Direct injection, established practice in compression ignition engines, is challenging to be implemented in spark ignition engines due to the intrinsic nature of the latter but allow meeting the latest rules about pollutant emissions. Latest advancement in the field of fluid dynamic simulations and of experimental non-invasive optical techniques allow to deeply analyze injection processes and effectively adopt them in commercial vehicle. Therefore, in this work the concept of direct injection was intensively studied and declined for liquid and gaseous fuels. At the first category belong Gasoline Direct Injection (GDI) engines which are a promising technology that is giving a new life to gasoline engines. Thermal efficiency enhancement and engine downsizing are the key improvement achievable. Special attention will be paid to flash boiling sprays in GDI engines that is a topic of great scientific interest in the last years and a phenomenon capable to improve GDI technology. Among the gaseous fuel Compressed Natural Gas (CNG) was chosen in this study. CNG compared with gasoline has higher-octane number, higher hydrogen to carbon ratio, and lower energy-specific CO<sub>2</sub> emissions. Furthermore, it can be produced in renewable ways and is more widespread and cheaper than conventional liquid fossil fuels. In this regard, the direct injection of CNG engines can be considered a promising technology for highly efficient and low-emission future engines. The jets produced by a single hole and a multi hole device were studied detailing the characteristics of under-expanded structures present in supersonic gaseous jets. A proper Computational Fluid Dynamic (CFD) method, featuring high order scheme discretization, was developed and tested. The results of the simulations have been validated by means of the experimental data collected.



## *Ringraziamenti*

Al mio tutor, Prof. Angelo De Vita, per le molteplici opportunità fornite che hanno reso possibile lo svolgimento del mio percorso dottorale.

Ai ricercatori del "Laboratorio Spray" dell'Istituto Motori del CNR di Napoli, Dott. Luigi Allocca, Ing. Alessandro Montanaro e Dott. Giovanni Meccariello per la preziosa collaborazione.

Ai Prof.ri, Andrea Di Mascio, Michele Anatone, Carlo Villante e Luca Di Angelo per la disponibilità sempre dimostrata.

Infine un ringraziamento va anche al collega Ing. Stefano Ranieri.



# Contents

<b>Abstract</b>	<b>v</b>
<b>Ringraziamenti</b>	<b>vii</b>
<b>1 Introduction</b>	<b>1</b>
1.1 License To Kill . . . . .	1
1.2 Man, Energy and Environment . . . . .	2
1.3 Energy and Mobility . . . . .	6
1.4 From Growth to Degrowth . . . . .	7
1.5 "Energie et Equitè" (Elogio alla bicicletta) . . . . .	11
1.6 Atmospheric Pollution and Mobility . . . . .	12
1.7 The Future of Internal Combustion Engine . . . . .	15
1.8 Internal Combustion Engine: New Frontiers of Research and Development . . . . .	20
1.9 Aims and outline of the thesis . . . . .	23
<b>2 Fuel Supply Systems</b>	<b>25</b>
2.1 Engine Fuel Supply Requirements . . . . .	25
2.2 Carburettor . . . . .	26
2.3 Indirect and direct injection . . . . .	28
2.4 The scientific approach for spray's characterization . . . . .	30
2.5 Outline of interest areas . . . . .	31
<b>3 Optical measurement techniques for spray characterization</b>	<b>33</b>
3.1 Historical background of optical techniques . . . . .	33
3.2 Schlieren imaging . . . . .	35
3.2.1 The razor-blade . . . . .	42
3.3 Mie Scattering imaging . . . . .	45
<b>4 CFD Techniques for Spray Characterization</b>	<b>47</b>
4.1 Governing Equation of a Mono-Phase Fluid Flow . . . . .	47
4.2 Turbulence Modelling . . . . .	49
4.2.1 Physics of Turbulence . . . . .	49
4.2.2 Turbulence Numerical Simulation . . . . .	50
DNS Simulation . . . . .	51
Reynolds averaged Navier Stokes (RANS) Modelling . . . . .	51
Large eddy simulation (LES) Modelling . . . . .	54
4.3 The Finite Volume Method . . . . .	55
4.3.1 Convection Term Discretization . . . . .	56
4.3.2 Diffusion Term Discretization . . . . .	57

4.3.3	Temporal Discretization . . . . .	58
4.3.4	Solution Of The Algebraic Equations . . . . .	59
4.4	Liquid Spray CFD Simulation . . . . .	60
<b>5</b>	<b>Gasoline Direct Injection Engines - Latest Technologies and Trends</b>	<b>65</b>
5.1	Overview of the Chapter Topics . . . . .	65
5.2	Spray Breakup Process . . . . .	67
5.3	GDI Spray Measurement Techniques . . . . .	72
5.4	Mathematical Modelling of Liquid Spray . . . . .	75
	Wave Breakup Model . . . . .	76
	Blob injection model . . . . .	78
	LISA model . . . . .	79
	Rayleigh-Taylor model . . . . .	80
	Reitz-Diwakar model . . . . .	81
	Taylor-analogy model . . . . .	81
5.4.1	Influence of spray's thermodynamic parameters . . . . .	85
5.5	Spray-wall interaction . . . . .	87
5.6	Mixture Formation and Combustion . . . . .	95
5.6.1	Effects of Engine Design Parameters on Mixture Formation . . . . .	95
	Injection Pressure . . . . .	95
	Fuel Temperature . . . . .	95
	Injection Strategies . . . . .	96
	Injector and Spark-Plug Positions . . . . .	96
	Spark Advance . . . . .	97
	Piston Shape . . . . .	97
	Valve Position and Orientation . . . . .	97
5.6.2	Other Parameters . . . . .	98
5.7	Combustion Modelling . . . . .	99
5.8	Emissions Studies . . . . .	102
5.8.1	Effects of Injection Parameters and Combustion Strategy . . . . .	104
5.8.2	Effects of Fuel Characteristics . . . . .	104
5.9	Injector Deposits and Fouling . . . . .	106
5.10	New Frontiers . . . . .	109
<b>6</b>	<b>ECN Spray G Experimental-Numerical Characterization</b>	<b>111</b>
6.1	Investigation Methodology . . . . .	111
6.2	Experimental Apparatus . . . . .	112
6.3	Numerical Background . . . . .	115
6.4	Results . . . . .	118
<b>7</b>	<b>Numerical modelling of flash-boiling breakup and spray collapse</b>	<b>125</b>
7.1	Flash Boiling in GDI engines . . . . .	125
7.2	Thermophysical description of flash boiling . . . . .	126
7.3	ECN Spray G: Numerical characterisation of flash-boiling conditions . . . . .	128
7.4	Numerical methodology . . . . .	130
7.5	Case study setup . . . . .	132

7.6	Results and discussion . . . . .	135
7.7	Conclusions . . . . .	147
<b>8</b>	<b>Natural gas as an alternative energy carrier</b>	<b>149</b>
8.1	Compressed natural gas: points of strength and drawbacks . .	149
8.2	Compressed Natural Gas in ICE . . . . .	153
8.2.1	Bi-Fuel Engines . . . . .	153
8.2.2	Dual-Fuel Engines . . . . .	153
8.3	Compressed Natural Gas Direction Injection Engines . . . . .	154
8.4	Physics of High Pressure Gaseous Jets . . . . .	156
8.5	The Under-Expanded Jets in CNG Injection Processes . . . . .	168
<b>9</b>	<b>Gaseous Jet Characterization: Single-Hole Injector Case Study</b>	<b>175</b>
9.1	Investigation Methodology . . . . .	175
9.2	Experimental Activities . . . . .	176
9.3	Image Processing Procedure . . . . .	178
9.4	Numerical Approaches . . . . .	181
9.5	Experimental Results . . . . .	185
9.5.1	Effect of Injection Pressure . . . . .	185
9.5.2	Effect of Pressure in the Vessel . . . . .	186
9.5.3	Effect of the gas Temperature in the chamber . . . . .	187
9.6	Numerical Results . . . . .	193
<b>10</b>	<b>Gaseous Jet Characterization: Multi-Hole Injector Case Study</b>	<b>203</b>
10.1	Multi-Hole Injector and Gaseous Jets . . . . .	203
10.2	Investigation Methodology . . . . .	204
10.3	Experimental Activities . . . . .	208
10.4	Image Processing Procedure . . . . .	209
10.5	Numerical Methodology . . . . .	210
10.5.1	Governing Equations of Compressible Flows . . . . .	210
10.5.2	Discretization and Solution . . . . .	211
10.5.3	Turbulence Modelling . . . . .	211
10.5.4	Code Validation . . . . .	212
10.6	Multi-hole Injector Case Study . . . . .	216
10.7	Experimental Results . . . . .	218
10.7.1	Effect of Injection Pressure . . . . .	218
10.7.2	Effect of back-pressure . . . . .	220
10.8	Numerical Results . . . . .	223
<b>11</b>	<b>Conclusions</b>	<b>233</b>
11.1	Summary . . . . .	233
11.2	Liquid Fuel Injection in GDI Engines . . . . .	233
11.3	Gaseous Injection Processes in Direct Injection Engines . . . . .	235
	<b>Bibliography</b>	<b>239</b>



# List of Figures

1.1	Does man has license to kill the Earth ? . . . . .	2
1.2	Variation in the average temperature of the planet compared to the period 1850-1900 [238]. . . . .	3
1.3	Photo of a fire coral that experienced severe bleaching in the 2016 mass bleaching event [23]. . . . .	4
1.4	Antarctic krill ( <i>Euphausia superba</i> ) . . . . .	4
1.5	The site of a palm oil plantation. On the left is a lush tropical forest, but on the right, trees have been completely cut off. . . . .	5
1.6	A fox roaming in the Chernobyl's ghost town [364]. . . . .	6
1.7	Global greenhouse gas emissions by sector [124]. . . . .	7
1.8	Impact of the transport sector on the emission of pollutants. [108]. . . . .	13
1.9	Mortality rate due to environmental pollution. [113]. . . . .	13
1.10	Many car makers will struggle to hit 95g/km fleet average CO <sub>2</sub> by 2021, warns PA Consulting. . . . .	16
1.11	Driving into 2025:The Future of Electric and ICE Vehicles [98]. . . . .	17
1.12	Production and operation emissions of three German ICE vehicles and its BEVs counterpart. [47]. . . . .	18
1.13	CO <sub>2</sub> emissions during life cycle for GE, DE and BEVs. (a) European Union (EU); (b) Japan; (c) US; (d) China; (e) Australia. [173]. . . . .	19
1.14	Mobility costs as a function of annual driving. [47]. . . . .	19
2.1	Schematic representation of a basic carburettor [93] . . . . .	27
2.2	Systems of fuel injection [1]:a) Single Point Injection, b) Multipoint Injection, c) Direct Injection; 1 – Fuel supply, 2 – Air intake, 3 – Throttle, 4 – Intake manifold, 5 – Fuel injector (or injectors), 6 – Engine . . . . .	28
3.1	Left-to-right: candle plume and original shadowgraph observations [338] . . . . .	33
3.2	Supersonic nozzle flow pattern photographed in Prandtl laboratory [338] . . . . .	34
3.3	Light rays in uniform density medium. . . . .	36
3.4	Light rays in medium with an angle. . . . .	36
3.5	Light rays in heterogeneous medium. . . . .	37
3.6	Diagram of light ray deflection in heterogeneous media [235]. . . . .	37
3.7	Geometric theory of light refraction of a two dimensional schlieren with a gradient of the index of refraction in y-direction [53]. . . . .	39
3.8	Simple schlieren system [161]. . . . .	39

3.9	Schematic configuration of schlieren set-up [161]. . . . .	40
3.10	Typical schlieren apparatus: z-configuration. . . . .	41
3.11	Geometric characteristics of z-type configuration . . . . .	41
3.12	Configuration of double-pass mirror system [187] . . . . .	42
3.13	Schlieren system highlighting different apertures [187] . . . . .	43
3.14	Sketch of the light paths in configuration with knife edge and without knife edge [187] . . . . .	43
3.15	Sketch of schlieren with different index gradient . . . . .	44
3.16	Effect of knife-edge movement on the schlieren image for a horizontal knife-edge cutting off the light beam from below. (a) Knife-edge is very close to the second concave mirror; (b) Knife-edge is correctly placed. (c) Knife-edge is beyond the focal plane of the second concave mirror . . . . .	44
3.17	Scattering cross section [2]. . . . .	45
5.1	Schematic representation of a liquid fuel spray. . . . .	68
5.2	Structure and shape of the free spray. . . . .	69
5.3	Breakup regimes as a function of $Re$ , $Z$ and gas density . . . . .	70
5.4	Secondary breakup regimes as function of $We$ . . . . .	71
5.5	Visible light (a), single frame X-ray radiograph (b), X-ray CT images (c), and subsequent post-processing elaborations of a spiral spray hollow-cone nozzle. . . . .	74
5.6	Schematic representation of surface perturbations in the wave-breakup model [304]. . . . .	76
5.7	Schematic representation of blob injection model [300]. . . . .	78
5.8	DNS simulation of a liquid jet. . . . .	84
5.9	Classification of drop impact mechanisms. . . . .	91
5.10	The heat transfer regimes of a droplet impinging an heated wall. . . . .	92
5.11	Impact regimes and transition conditions for heated walls. . . . .	92
5.12	Experimental and numerical spray data from Montanaro et al.'s investigations. . . . .	93
5.13	Water drop impact on a wetted surface as simulated with SPH method. . . . .	93
5.14	Effects of piston shape on turbulent kinetic energy. . . . .	98
5.15	Operating modes of a GDI engine. . . . .	100
5.16	Injector's micrographs in three different conditions: clean, fouled and cleaned-up. . . . .	107
6.1	Axial Penetration Length Measurement. . . . .	112
6.2	Spray G Injector Geometry [21]. . . . .	113
6.3	Schematic of plume directions with respect of camera line-of-sight [21]. . . . .	113
6.4	Optical setup for quasi-simultaneous Mie scattering and schlieren imaging technique. . . . .	115
6.5	Mass-Flow Rate. . . . .	118
6.6	Comparison between experimental schlieren images (right half circle) and numerical computed iso-octane mass fraction (left half circle) for ECN Standard condition. . . . .	119

6.7	Numerical and experimental penetration for ECN Standard case.	120
6.8	Temporal evolution of the centerline axial velocity at a distance of 15 mm from the nozzles of the injector. Experimental and numerical data were plotted against the injection period.	121
6.9	Iso-octane vapour mass fraction and velocity vectors at $t=800 \mu\text{s}$	121
6.10	Sauter Mean Diameter (SMD) evaluation at a distance of 15 mm from the nozzles of the injector. Experimental and numerical data were plotted against the radial distance from the injector axis.	122
6.11	Iso-octane vapour mass fraction time evolution	123
7.1	Typical pressure vs specific volume curve for a pure substance. Dashed area indicates the metastable superheated liquid region.	127
7.2	Time evolution of bubble–droplet system.	130
7.3	Droplet velocity after breakup updating.	132
7.4	Mass flow-rate profiles corresponding to the three injection pressures.	134
7.5	Numerical and experimental liquid penetration for G_SFB200 case.	135
7.6	Numerical and experimental vapour penetration for G_SFB200 case.	136
7.7	Comparison between experimental schlieren images (right half of each circle) and numerical iso-octane mass fractions (left half of each circle) for G_SFB200 condition.	137
7.8	Numerical and experimental liquid penetration for G2 case.	138
7.9	Numerical and experimental vapour penetration for G2 case.	138
7.10	Comparison between experimental schlieren images (right half of each circle) and numerical results representation (left half of each circle) for G2 condition.	139
7.11	$R_p$ map of the flash-boiling spray at $480 \mu\text{s}$ after SOI for the G2 (top) and G_SFB200 (bottom) conditions.	140
7.12	Representation of the relative pressure drop for G_SFB200 and G2 conditions. The low-pressure zone, in red, causes the spray to collapse.	141
7.13	Sauter mean diameter ( $SMD_{32}$ ) evolution at a distance of 15 mm from the nozzles. Experimental [104] and numerical data were plotted against the time after SOI.	142
7.14	Sauter mean diameter ( $SMD_{32}$ ) and breakup criterion ( $k_b(t)$ ) plotted against axial distance from injector tip.	143
7.15	Droplet film thickness plotted against time since breakup has occurred.	143
7.16	Comparison between the experimental schlieren images (right) and the numerically computed iso-octane mass fraction (left) for three different injection pressures: 200, 150 and 100 bar at $640 \mu\text{s}$ from the SOI.	144
7.17	Numerical and experimental liquid penetration for the three injection pressures 100, 150, and 200 bar, G_SFBxxx cases.	145

7.18	Numerical and experimental vapour penetration for the three injection pressures 10, 15, and 20 MPa, G_SFBxxx cases. . . . .	145
7.19	SMD plotted against axial distance from injector tip for the three injection pressures of 100, 150, and 200 bar. . . . .	146
8.1	Number of natural gas vehicles worldwide by years [154]. . .	150
8.2	CNG price compared to gasoline and diesel. . . . .	151
8.3	Reduction in CO <sub>2</sub> emissions [108]. . . . .	152
8.4	Schematic representation of inwardly and outwardly opening injectors [91]. . . . .	155
8.5	Diagram of high pressure direct injection system (left) and diagram of hot surface assisted compression ignition (right) [396].	156
8.6	Normal shock wave. . . . .	158
8.7	Supersonic flow along a corner of $\theta$ angle [17]. . . . .	160
8.8	Geometric characteristics of an oblique shock [17]. . . . .	160
8.9	De-attached and oblique shock [17]. . . . .	161
8.10	Oblique shock reflection on a wall surface [17]. . . . .	161
8.11	Mach reflection [17]. . . . .	162
8.12	Oblique shock wave reflection from a constant pressure boundary [17]. . . . .	163
8.13	Oblique shock wave reflection from a constant pressure boundary [17]. . . . .	163
8.14	Intersection of two shock waves with different length [17]. . .	164
8.15	Mach intersection of two shock waves [17]. . . . .	164
8.16	Schematic representation of an under-expanded jet flow regions.	166
8.17	Structure of a subsonic jet (left) and Schlieren image (right) [344]	166
8.18	Structure of a moderately under-expanded jet (left) and Schlieren image (right) [344]. . . . .	167
8.19	Structure of a strongly under-expanded jet (left) and Schlieren image (right) [344]. . . . .	167
8.20	PLIF images of a gaseous jet, at different advance times. A) subsonic jet; B) casting moderately under-expanded; C) strongly under-expanded casting. False colors indicate the density distribution in the jet. . . . .	169
8.21	Effects of injection pressure on turbulent mixing . . . . .	170
8.22	Under-expanded jet simulated by [134]. (a), (b) Instantaneous LES prediction of the mass fraction of the passive scalar at $t=15$ and $110 \mu\text{s}$ , respectively; (c), (d) Instantaneous LES prediction of the density gradient at $t=15$ and $110 \mu\text{s}$ , respectively, (e) time-averaged Schlieren image . . . . .	172
8.23	PLIF images of a gaseous jet, at different advance times. A) subsonic jet; B) casting moderately under-expanded; C) strongly under-expanded casting. False colors indicate the density distribution in the jet. . . . .	173
9.1	Definitions of measured parameters. . . . .	176
9.2	Experimental Setup. . . . .	177
9.3	Sketch of the gas injection system. . . . .	178

9.4	Image Processing Procedure. . . . .	180
9.5	Pintle Lift. . . . .	181
9.6	Computational cells over time. . . . .	182
9.7	Sectional view of the computational domain and assignment of initialization regions. . . . .	184
9.8	Detail of injector's upper part with related boundary conditions.	184
9.9	Evolution of the gaseous jet structure at the varying of the in- jection pressure . . . . .	186
9.10	Effect of injection pressure on Mach disk height . . . . .	187
9.11	Axial jet penetration over time for $p_{ch} = 0.1$ MPa. . . . .	188
9.12	Axial jet penetration vs. time at $p_{ch} = 0.4$ MPa. . . . .	189
9.13	Variation of jet cone angle vs. injection pressure at $p_{ch} = 0.4$ MPa.	189
9.14	Evolution of the gaseous jet structure at the varying of the chamber pressure. . . . .	190
9.15	Axial jet penetration vs. time for $p_{inj} = 1.2$ MPa. . . . .	190
9.16	Variation of jet cone angle vs. chamber pressure at $p_{inj} = 1.2$ MPa.	191
9.17	Evolution of the gaseous jet structure at the varying of the tem- perature of the gas in the chamber . . . . .	191
9.18	Axial jet penetration vs. time for $p_{inj} = 0.6$ MPa. . . . .	192
9.19	3D visualization of the simulated jet. . . . .	193
9.20	Experimental and numerical axial jet penetration vs. time for Case 1 ( $p_{inj} = 1.2$ MPa and $p_{ch} = 0.1$ MPa). . . . .	194
9.21	Experimental and numerical axial jet penetration vs. time for Case 2 ( $p_{inj} = 1.2$ MPa and $p_{ch} = 0.4$ MPa). . . . .	195
9.22	Gaseous jet structure's evolution at different time-step for Case 1 ( $p_{inj} = 1.2$ MPa and $p_{ch} = 0.1$ MPa) obtained plotting the den- sity gradient. . . . .	196
9.23	Experimental and Numerical Mach Disk Height vs. time for $p_{inj} = 1.2$ MPa and $p_{ch} = 0.1$ MPa . . . . .	197
9.24	Gaseous jet structure's evolution at different time-step for Case 1 ( $p_{inj} = 1.2$ MPa and $p_{ch} = 0.4$ MPa) obtained plotting the den- sity gradient. . . . .	198
9.25	Nozzle Pressure Definition . . . . .	198
9.26	2D-map of Density Gradient - Mach Disk particular . . . . .	199
9.27	2D-map of Density Gradient - Mach Disk particular . . . . .	199
9.28	Evolution of the gaseous jet structure in term of $y_{CH_4}$ 2D-map - $p_{inj} = 1.2$ MPa and $p_{ch} = 0.1$ MPa . . . . .	200
9.29	Probability distribution of mass fraction $y_{CH_4}$ for Case 1 and Case 2 at $t_{ASOI} = 0.75$ ms. . . . .	201
10.1	Silhouette of the high-pressure injector. . . . .	204
10.2	X-Ray tomography of the injector showing its internal geometry.	205
10.3	X-ray bottom view of the injector showing the nozzle pattern.	206
10.4	Current command signal and nozzle inlet pressure time be- haviour. . . . .	207
10.5	Optical setup for schlieren technique in Z-type configuration.	208
10.6	Image processing procedure. . . . .	209

10.7	Flowchart representing the developed solver structure and summarize the operations performed in each calculation step. . . .	213
10.8	Shock tube validation case: comparison of exact solution with the numerical computed pressure. . . . .	214
10.9	Shock tube validation case: comparison of exact solution with numerical computed density. . . . .	214
10.10	Shock tube validation case: comparison of exact solution with numerical computed temperature. . . . .	215
10.11	Shock tube validation case: comparison of exact solution with numerical computed velocity magnitude. . . . .	215
10.12	The boundary conditions. . . . .	216
10.13	Total pressure boundary condition. . . . .	217
10.14	Particular view of the refinement region of the grid. . . . .	218
10.15	Evolution of the gaseous jet structure at three different injection pressures . . . . .	219
10.16	Axial jet tip penetration vs. time at three different injection pressures and $p_{amb}=0.5$ MPa. . . . .	220
10.17	Jet penetration speed vs. time at three different injection pressures and $p_{amb}=0.5$ MPa. . . . .	221
10.18	Effect of chamber back-pressure on spray evolution at $t_{SOI}=1.0$ ms and $p_{amb}=0.5$ MPa. . . . .	222
10.19	Axial jet penetration vs. time at four different back-pressures and $p_{inj}=5.0$ MPa. . . . .	222
10.20	Experimental and numerical axial jet tip penetration vs. time	223
10.21	Temporal evolution of the spray within the injector's ducts with a multi-plot of Mach number on the left hand side and logarithm of density gradient ( $\log(\nabla\rho)$ ) on the right side of each picture. . . . .	224
10.22	Flow structure - inviscid flow . . . . .	225
10.23	Flow structure - viscous flow . . . . .	227
10.24	Temporal evolution of the spray development region represented by methane concentration ( $Y_{CH_4}$ ) volume rendering. . . . .	228
10.25	Temporal evolution of the spray represented with logarithm of density gradient. . . . .	229
10.26	Zoomed view of the near-nozzle zone where, at the end of the injection; under-expanded structures compares. . . . .	230
10.27	Mach number as function of axial distance from the central nozzle outflow section. . . . .	230
10.28	Probability distribution of fuel mass fraction $Y_{CH_4,i}$ computed at four different time steps. . . . .	231
10.29	Probability distribution of fuel mass fraction $Y_{CH_4,i}$ computed at four different time steps. . . . .	232

# List of Tables

5.1	Spray Physics Summary Table . . . . .	71
5.2	Spray Measurement Techniques Summary Table . . . . .	75
5.3	Mathematical Models Summary Table . . . . .	85
5.4	Spray's Thermo-Dynamic Parameter Influence Summary Table . . . . .	86
5.5	Spray-Wall Interaction Summary Table . . . . .	94
5.6	Mixture Formation Process Summary Table . . . . .	99
5.7	Combustion Modelling Summary Table . . . . .	102
5.8	Emissions Studies Summary Table . . . . .	106
5.9	Injector Deposits and Fouling Summary Table . . . . .	109
5.10	New Frontiers Summary Table . . . . .	110
6.1	Case study therm-dynamic parameters . . . . .	111
6.2	Spray G Injector Characteristics. . . . .	114
6.3	CFD sub-models used. . . . .	116
6.4	Breakup models constants . . . . .	116
6.5	Spray angles used for the numerical simulation . . . . .	116
7.1	Ambient to saturation pressure ratio ranges . . . . .	127
7.2	Main characteristics of the Spray G injector . . . . .	128
7.3	Case study summary . . . . .	133
7.4	Lagrangian framework physical sub-models. . . . .	133
7.5	Geometrical and hydraulic injection parameters. . . . .	133
7.6	Breakup parameters. . . . .	134
7.7	Parameters used for the two Rosin–Rammler distributions. . . . .	141
9.1	Experimental parameters . . . . .	175
9.2	Adapter nozzle geometrical parameters . . . . .	177
9.3	Operating conditions numerically simulated . . . . .	181
10.1	Adopted experimental parameters. . . . .	206
10.2	Adopted experimental parameters. . . . .	206
10.3	Sutherland's law $A_s$ and $T_s$ constants adopted values . . . . .	210
10.4	Validation case initial conditions . . . . .	212
10.5	Case Study Initial Conditions . . . . .	217



# List of Abbreviations

**BEVs** battery electric vehicles.

**CFD** computational fluid dynamics.

**CI** spark ignition engines.

**CNG** compressed natural gas.

**DDM** Discrete Droplet Model.

**DI** direct injection.

**DNS** direct numerical simulation.

**DPF** Diesel Particulate Filter.

**EVs** electric vehicles.

**FV** Finite Volume.

**GDI** gasoline direct injection.

**GHG** green house gases.

**HEVs** hybrid electric vehicles.

**ICE** internal combustion engine.

**ICEVs** internal combustion engine vehicles.

**LCA** life cycle assessment.

**LES** large eddy simulation.

**LNG** liquified natural gas.

**LTC** Low temperature combustion.

**NG** natural gas.

**PFI** port fuel injection.

**PM** particulate matter.

**RANS** Reynolds averaged Navier Stokes.

**SCR** Selective Catalytic Reduction Catalyst.

**SI** spark ignition engines.

**TWC** Three Way Catalysts.

# Chapter 1

## Introduction

### 1.1 License To Kill

*“Man thinks 'cause he rules the earth he can do with it as he please  
And if things don't change soon, he will  
Oh, man has invented his doom  
First step was touching the moon*

*Now, there's a woman on my block  
She just sit there as the night grows still  
She say who gonna take away his license to kill? ”*

— License To Kill, Bob Dylan (Infidels - 1983)

The lyrics of this song, written by Bob Dylan in 1983, now sounds very actual and meaningful. Man acquired like a license to shape the planet where he lives to his pleasure without taking account the effect of such actions. In some ways, as written in the lyrics, we can say that man acquired a “*license to kill*” (Fig. 1.1).

In last century the worldwide ecosystem was undoubtedly modified by the human activities. The dream of “*..touching the moon*” as the man's belief to be able to overcome every physic limit, to dominate the nature and bend its behaviour for a continuous progress of anthropic activities are deeply false. Just fifty years ago, venturing to the moon, for the very first time, we looked back at our own planet and since then we are realizing as anthropic activities are destroying different ecosystems all over the world and putting in danger the same human specie presence on the Earth. Climate change, wildlife populations reduction and the presence of pollutant substances in the air, on the fresh waters and on the earth are effects known to everyone and broadly documented. For the first time in human history, the stability of nature can no longer be taken for granted and what we will do in the next decades will determine the future for all life on Earth.

In the last century, the concept of sustainability is gaining an increasing importance because it identifies the capacity for the biosphere and human civilization to co-exist on the Earth. Sustainability can be declined in different fields such as economy, environment and social life. This means that



FIGURE 1.1: Does man has license to kill the Earth ?

almost all the human activities now must be performed accounting for their environmental impact in order to enable the Earth to continue supporting life. Unfortunately, this purpose has not completely achieved yet because it involves turning upside down our life's habits. However, increasing concern around these problems, is bringing to small but significant changes. This "revolution", I hope, will be accomplished in the coming decades otherwise there won't be life on Earth.

## 1.2 Man, Energy and Environment

Starting point of all human activities are the energy sources, without energy nothing can be done. Our life is completely dependent from energy. We are "energetic slaves". Man uses energy since the beginning of his history on Earth, also to simply heat himself with a fire. Man learnt to transform energy accordingly to his requirements but, in last decades, he is facing two great problems: not all the energy sources are unlimited and the way he is using energy is not sustainable. At the same time, the world population is ever increasing and so the energy requirements too. Today the principal energy resource that fuels our lives are fossil combustibles and their combustion. We are bound to fossil resources in many ways: socially, technologically, economically and politically but, at the same time, we know that we must break this bond, definitely. Indeed it has been proved that if all the fossil resources would be completely exploited the so called greenhouse effect would deeply threats life on Earth.

In order to exploit the chemical energy contained in the fossil fuels we must oxidize them. The combustion of such hydrocarbons produces, among the others, carbon dioxide that is principal gas responsible of climate change and, definitely, land and ocean temperature increase. The graph of Figures

1.2 shows the variation in the average temperature of the planet compared to the period 1850-1900.

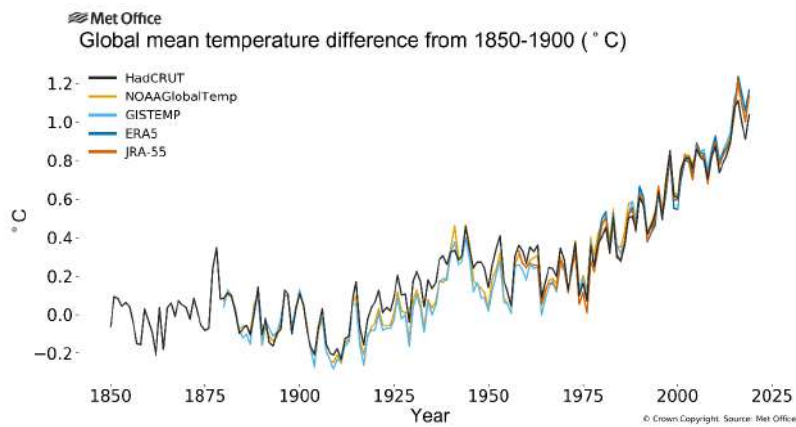


FIGURE 1.2: Variation in the average temperature of the planet compared to the period 1850-1900 [238].

Anthropogenic green house gases (GHG) emissions have increased since the pre-industrial era, driven largely by economic and population growth, and are now higher than ever. This has led to an increase in global surface temperature of approximately one Celsius degree since pre-industrial times. If warming reaches two degrees Celsius, more than seventy percent of Earth's coastlines will see sea-level rise greater than 20 centimetres, resulting in increased coastal flooding, beach erosion, salinization of water supplies and other impacts on humans and ecological systems [394].

Rather than proposing quantitative data or graphs already broadly discussed and everywhere available, there are many examples, unknown at the most, that clarify what man is causing to natural world enhancing green-house effect.

One of the greatest threats of marine ecosystem regards the coral reefs. Coral reef's bleaching is the result of increased sea surface temperature (Fig. 1.3). Bleaching occurs when prolonged increased sea temperatures cause a breakdown in the relationship between the corals and their symbiotic zooxanthellae (algae). The coral subsequently expel the zooxanthellae, lose their colour (bleaching) and become weak. Some corals are able to recover, often with compromised immune systems, but in many cases they die [78]. Reefs provide jobs for people in tourism industries, and they also protect coastal areas from surging seas. But perhaps more importantly, 25% of fish species spend some part of their life cycle in reefs, despite the fact that coral reefs cover less than 1% of the ocean floor.

A new study based on careful analysis of ninth years of scientific catch data from the South Atlantic Ocean shows that the geographic distribution of Antarctic krill has contracted nearly 300 miles southward in concert with ocean warming (Figure 1.4). Krill-free-swimming, shrimp-like crustaceans-play a central role in Antarctica's marine food web, transferring energy and



FIGURE 1.3: Photo of a fire coral that experienced severe bleaching in the 2016 mass bleaching event [23].

carbon from phytoplankton and zooplankton to fish, penguin, seals, and whales. Changes in krill distribution are thus of considerable concern for both oceans life and for commercial fishery interests [22].



FIGURE 1.4: Antarctic krill (*Euphausia superba*)

Across the world, we are losing tropical forest at the rate of nearly fifteen million hectares every year. Land use changes, especially in the form of deforestation, are the second largest anthropogenic source of atmospheric carbon dioxide emissions, after fossil fuel combustion. Jungles store and capture more carbon than any other habitat on land. They cool our planet, provide food and medicines. But forests are, especially, the planet's treasure trove of diversity. We have now replaced up to twenty-seven million hectares of

virgin jungle with a single species of tree. This is oil palm, one of the world's most productive crops. But these mono-cultures support only a fraction of the diversity found in primary rain forests, and it is pushing many animals to extinction.



FIGURE 1.5: The site of a palm oil plantation. On the left is a lush tropical forest, but on the right, trees have been completely cut off.

But our planet, if given the chance, is almost unbelievably resilient. Perhaps the best proof we have of his ability to recover can be seen on the site of one of our greatest disasters. Chernobyl. In 1986, one of the four reactors at the Chernobyl nuclear plant exploded. It turned this utopian vision of the future into a ghost town. Over one-hundred thousand people were immediately evacuated, never to return. The fallout zone was declared uninhabitable for the next twenty-thousand years. Yet despite the radiation, there has been a remarkable recovery. Within only a decade, vegetation began to germinate in the ruined city. And as the forest re-established itself, animals began to appear. Within only 20 years, science has recorded populations of animals similar to that in the wilder parts of Europe. The dramatic recolonization of Chernobyl in the space of only 30 years is proof of natural world extraordinary resilience.

Such deal demonstrates that it is not late to modify our life habits, to attempt stopping climate change achieving a human-ecosystem equilibrium.



FIGURE 1.6: A fox roaming in the Chernobyl's ghost town [364].

### 1.3 Energy and Mobility

Today our capitalistic society is gorged with energy, the amount worldwide produced has to ever increase in order to power the economic growth. In this kind of society the necessity of moving almost everything was born: people, foods and goods are just few examples. Among the others, the transport sector contributes to a large extent to global greenhouse gas emissions. Latest data (Figure 1.7) demonstrate that approximately one third of the energy produced in a year fuels mobility.

So, further than energy consumer, man became "transport consumer" too. We live with the illusion of sparing time using more "horse-powers". The need to gain time, through ever faster vehicles and a desirable optimization of infrastructures, leads man away from the enhancement of his personal-skills, assimilating him more and more to a consumer of time, energy and transport rather than free citizen.

The geography of territories was modified by the needs of the transport industry which, paradoxically, move away what it claims to bring together through energy and infrastructures.

In this society the car, further than a tool for this race in "time sparing", becomes an extension of man and a strong status-symbol. It performs a mere (and useless) aesthetic function, certifying power and privilege.

Franco La Cecla, in the preface of [393], offers a relevant view of the car :

*"Non è un caso che le auto oggi assomiglino sempre di più ad auto di diplomatici o a veicoli da guerra. Presuppongono un paesaggio di paesi bombardati da attraversare con vetri fumè. L'auto è oggi il disprezzo del mondo là fuori, il poterne chiaramente fare a meno".*

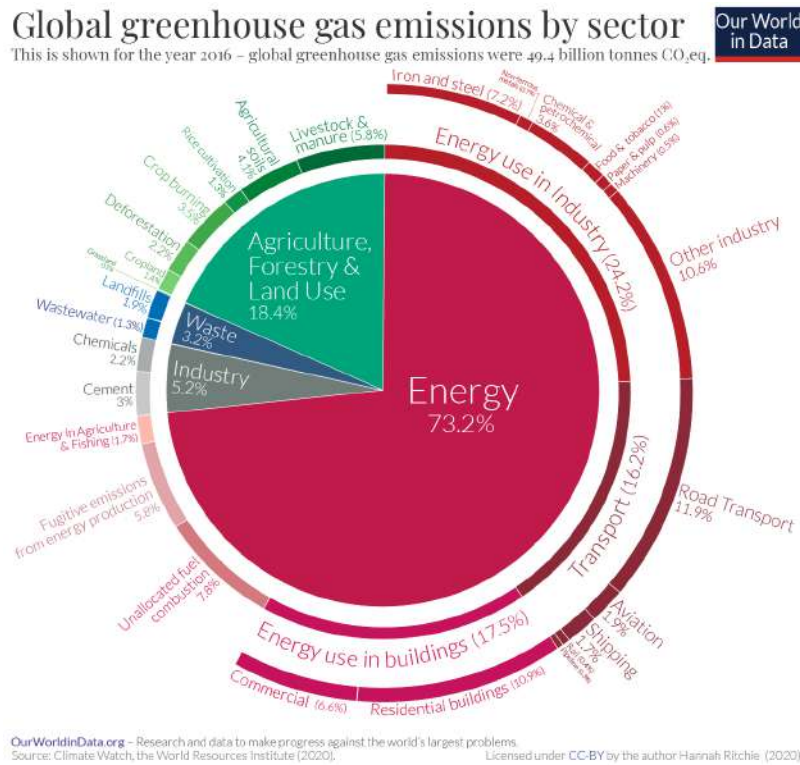


FIGURE 1.7: Global greenhouse gas emissions by sector [124].

The world becomes the movie that runs behind the windows, in background, while our legs and arms are a prosthesis of the machine synonymous of progress and freedom. The car becomes a place where we spend a significant part of our time. Even a place for having sex ! Immersed in this synthetic and mechanical reality we do not realize what is outside, we do not realize the pollution, we do not realize that this kind of mobility is a weapon aimed at everything that is outside it. What to do?

## 1.4 From Growth to Degrowth

We live in an era of stagnation, rapid impoverishment of a vast part of the population, growing inequalities, and socio-ecological disasters - from Katrina, Haiti and Philippines, to Fukushima, the spill in the Gulf of Mexico, or the burial of toxic waste in Campania, to climate change and the continuous disaster of preventable deaths by lack of access to land, water, and food.

There is a failure, even by radical thinkers, to come up with new responses that are not articulated around the twin imperatives of our society: growth and development. If the desire for growth causes economic, social, and environmental crises, then growth cannot be the solution. Fortunately, alternatives are springing up on the ground. They range from new forms of living, producing, and consuming in common to new institutions that can secure the livelihoods of all without growth. One of them can be synthesized in concept of degrowth. Different people arrive at it from different angles. Some,

because they see that there are limits to growth. Others, because they believe we are entering a period of economic stagnation and we should find ways to maintain prosperity without growth. Yet others because they believe that a truly egalitarian society can only be one that liberates itself from capitalism and its insatiable pursuit of expansion, one that learns to collectively limit itself and work without the calculus of self-interested utility. Degrowth defies a single definition. Like freedom or justice, degrowth expresses an aspiration which cannot be pinned down to a simple sentence. Degrowth is a frame, where different lines of thought, imaginaries, or courses of action come together. It is a network of ideas and conversations, strongly rooted in the radical and critical traditions, but open-ended and amenable to multiple connections. Degrowth signifies, first and foremost, a critique of growth. It calls for the decolonization of public debate from the idiom of economism and for the abolishment of economic growth as a social objective. Beyond that, degrowth signifies also a desired direction, one in which societies will use fewer natural resources and will organize and live differently than today. Sharing, simplicity, conviviality, care and the commons are primary significations of what this society might look like. Usually, degrowth is associated with the idea that smaller can be beautiful. Degrowth signifies not only a society with an equitable downscaling of production and consumption, but more importantly, a society with a different structure and serves new functions. In a degrowth society everything will be different: different activities, different forms and uses of energy, different relations, different gender roles, different allocations of time between paid and non-paid work, different relations with the non-human world. Degrowth connects diverse ideas, concepts and proposals having, at the same time some, key-points. The first is the criticism of growth [87]. Next is the criticism of capitalism, a social system that requires and perpetuates growth. Two other strong currents in the degrowth literature are, first, the criticism of Gross Domestic Product (GDP), and second, the criticism of commodification, the process of conversion of social products and socio-ecological services and relations into commodities with a monetary value. However, degrowth is not limited only to criticism. On the constructive side, the degrowth imaginary centres around the reproductive economy of care, and the reclaiming of old and the creation of new commons. Caring in common is embodied in new forms of living and producing, such as eco-communities and cooperatives and can be supported by new government institutions, such as work-sharing or a basic and maximum income, institutions which can liberate time from paid work and make it available for unpaid communal and caring activities. Degrowth is not the same as negative GDP growth. Still, a reduction of GDP, as currently counted, is a likely outcome of actions promoted in the name of degrowth. A green, caring and communal economy is likely to secure the good life, but unlikely to increase gross domestic activity two or three per cent per year. Advocates of degrowth ask how the inevitable and desirable decrease of GDP can become socially sustainable, given that under capitalism, economies tend to either grow or collapse. In the minds of most people, growth is still associated with

an improvement, or well-being. Because of this some progressive intellectuals take issue with the use of the word degrowth. It is inappropriate, they claim, to use a "negative word" to signify desired changes. However, the use of a negation for a positive project aims precisely to decolonise an imaginary dominated by a one-way future consisting only of growth. It is the automatic association of growth with better that the word "degrowth" wants to dismantle. For degrowthers it is the unquestionable desirability of growth in the common sense that needs to be confronted if a discussion for a different future is to open up [196]. Degrowth is a deliberately subversive slogan. Of course some sectors, such as education medical care, or renewable energy, will need to flourish in the future, while others, such as dirty industries or the financial sector shrink.

"Development", even if it were to be cleaned of its heavy historical meaning, or beautified with adjectives such as balanced, local or sustainable, is a problematic keyword. The word suggests an unfolding towards a predetermined end. An embryo "develops" into a mature adult, who then ages and dies. A premise of modern liberal societies, however, is the denial of any ultimate collective end as well as the denial of anything but ascent. Development becomes self-referential: development for the sake of development, the unfolding of a predetermined, not-to-be-questioned arrow of progress with no end in sight. A frequent criticism to the degrowth proposal is that it is applicable only to the overdeveloped economies of the Global North. The poorer countries of the Global South still need to grow to satisfy basic needs. Indeed, degrowth in the North will liberate ecological space for growth in the South. Poverty in the South is the outcome of the exploitation of its natural and human resources at low cost by the North. Degrowth in the North will reduce the demand for, and the prices of, natural resources and industrial goods, making them more accessible to the developing South.

In a degrowth society we would aspire to localise our economies as far and as appropriately as possible. This would assist with reducing carbon-intensive global trade, while also building resilience in the face of an uncertain and turbulent future.

Through forms of direct or participatory democracy we would organise our economies to ensure that everyone's basic needs are met, and then redirect our energies away from economic expansion. This would be a relatively low-energy mode of living that ran primarily on renewable energy systems.

Renewable energy cannot sustain an energy-intensive global society of high-end consumers. A degrowth society embraces the necessity of "energy descent", turning our energy crises into an opportunity for civilizational renewal.

We would tend to reduce our working hours in the formal economy in exchange for more home-production and leisure. We would have less income, but more freedom. Thus, in our simplicity, we would be rich.

Wherever possible, we would grow our own organic food, water our gardens with water tanks, and turn our neighbourhoods into edible landscapes as the Cubans have done in Havana. Community gardens can help achieve sufficiency. We do not need to purchase so many new clothes. Let us mend or

exchange the clothes we have, buy second-hand, or make our own. In a degrowth society, the fashion and marketing industries would quickly wither away. A new aesthetic of sufficiency would develop, where we creatively re-use and refashion the vast existing stock of clothing and materials, and explore less impactful ways of producing new clothes.

We would become radical recyclers and do-it-yourself experts. This would partly be driven by the fact that we would simply be living in an era of relative scarcity, with reduced discretionary income.

But human beings find creative projects fulfilling, and the challenge of building the new world within the shell of the old promises to be immensely meaningful, even if it will also entail times of trial. The apparent scarcity of goods can also be greatly reduced by scaling up the sharing economy, which would also enrich our communities.

One day, we might even live in cob houses that we build ourselves, but over the next few critical decades the fact is that most of us will be living within the poorly designed urban infrastructure that already exists. We are hardly going to knock it all down and start again. Instead, we must "retrofit the suburbs", as leading permaculturalist David Holmgren argues [146]. This would involve doing everything we can to make our homes more energy-efficient, more productive, and probably more densely inhabited.

This is not the eco-future that we are shown in glossy design magazines featuring million-dollar "green homes" that are prohibitively expensive.

Degrowth offers a more humble and more realistic vision of a sustainable future.

A degrowth transition to a steady-state economy could happen in a variety of ways. But the nature of this alternative vision suggests that the changes will need to be driven from the "bottom up", rather than imposed from the "top down".

But it is critical to acknowledge the social and structural constraints that currently make it much more difficult than it needs to be to adopt a lifestyle of sustainable consumption.

Actions at the personal and household levels will never be enough, on their own, to achieve a steady-state economy. We need to create new, post-capitalist structures and systems that promote, rather than inhibit, the simpler way of life. These wider changes will never emerge, however, until we have a culture that demands them. So first and foremost, the revolution that is needed is a revolution in consciousness.

In this context the role of scientific world and, in particular, of the engineering is central. As defined by San Bernardo the engineers are who:

*Sed sunt qui scire volunt ut edificent:  
et charitas est.*

This willingness of the "knowing for creating" must be made available to the humanity for solving this huge problem of nowadays.

## 1.5 "Energie et Equitè" (Elogio alla bicicletta)

The ideal of economic "degrowth" regards all the aspects of our society and, in particular, the mobility sector too. The philosopher Ivan Illich in his work "Energie et equite" [155] develops a praise to the bicycle and its environmental prerogatives. It has a low cost and generates enormous creativity without false expectations in a measured context of energy consumption, between shortage and abundance.

*Man on a bicycle can go three or four times faster than the pedestrian, but uses five times less energy in the process. He carries one gram of his weight over a kilometre of flat road at an expense of only 0.15 calories. The bicycle is the perfect transducer to match man's metabolic energy to the impedance of locomotion. Equipped with this tool, man outstrips the efficiency of not only all machines but all other animals as well.*

...

*Bicycles are not only thermodynamically efficient, they are also cheap. With his much lower salary, the Chinese acquires his durable bicycle in a fraction of the working hours an American devotes to the purchase of his obsolescent car. The cost of public utilities needed to facilitate bicycle traffic versus the price of an infrastructure tailored to high speeds is proportionately even less than the price differential of the vehicles used in the two systems. In the bicycle system, engineered roads are necessary only at certain points of dense traffic, and people who live far from the surfaced path are not thereby automatically isolated as they would be if they depended on cars or trains. The bicycle has extended man's radius without shunting him onto roads he cannot walk. Where he cannot ride his bike, he can usually push it.*

...

*The bicycle also uses little space. Eighteen bikes can be parked in the place of one car, thirty of them can move along in the space devoured by a single car. It takes three lanes of a given size to move 40,000 people across a bridge in one hour by using automated trains, four to move them on buses, twelve to move them in their cars, and only two lanes for them to pedal across on bicycles. Of all these vehicles, only the bicycle really allows people to go from door to door without walking. The cyclist can reach new destinations of his choice without his tool creating new locations from which he is barred.*

*Bicycles let people move with greater speed without taking up significant amounts of scarce space, energy, or time. They can spend fewer hours on each mile and still travel more miles in a year. They can get the benefit of technological breakthroughs without putting undue claims on the schedules, energy, or space of others. They become masters of their own movements without blocking those of their fellows. Their new tool creates only those demands which it can also satisfy. Every increase in motorized speed creates new demands on space and time. The use of*

*the bicycle is self-limiting. It allows people to create a new relationship between their life-space and their life-time, between their territory and the pulse of their being, without destroying their inherited balance. The advantages of modern self-powered traffic are obvious, and ignored. That better traffic runs faster is asserted, but never proved. Before they ask people to pay for it, those who propose acceleration should try to display the evidence for their claim.*

The solution proposed by Illich maybe could be not properly realistic but, offers food for thoughts. Our society have to re-think the concept of mobility and, only after that, how to perform such activity. Ad example our cities are full of cars circulating with almost always no passengers, only the driver [288] and so the spontaneous question is: Is it necessary to move one thousand kilogram of steel to carry just eighty kilos of a person? Can we done it, definitively, in a more sustainable way?

Such example wants to highlight the fact that a sustainable mobility system must arise, first of all, from a new ethic. The technological advancements of the vehicles, alone, cannot be the solution of the mobility problem. At the opposite, the vehicles of nowadays are the result of hundred years of design research and improvements lately aiming to achieving an ever minor environmental impact. In this scenario, the scientific research in the field of vehicle design merged together with this new environmental preservation awareness will be likely the unique trump card for a gradual transition to a new conception of mobility and, in general, a new society.

## 1.6 Atmospheric Pollution and Mobility

Anthropogenic activities and especially the mobility sector, further than being responsible of GHG emissions, produce the so called atmospheric pollution too. According to data reported by the European Environment Agency (EEA), the incidence of the transport sector on the total emissions of the main air pollutants is far from negligible, as evident from Figure 1.8.

The presence of such substances in air produces harmful effects on human health and the environment. These contaminants are usually not present in the normal composition of the air or, at most, with low concentrations. Air pollution poses a serious threat to health and the earth's climate. According to the World Health Organization (WHO), air pollution is responsible for approximately 4.2 million deaths per year due to hearth stroke, respiratory diseases and lung cancer [113].

As shown in Figure 1.9, according to the WHO, in the 2012 approximately 12.6 million people (equal to 22.7% of all deaths) died as a result of living or working in unhealthy environments. Taking into account both death and disability (Disability-adjusted life year), the overall disease rate is 21.8%. Atmospheric pollution has also natural sources such as volcanic eruptions and wildfires but the major contributors are the anthropogenic activities. In this context, the focus will be exclusively on urban pollution, caused by the combustion of fossil fuels in industrial processes and mobility. Unlike GHG,

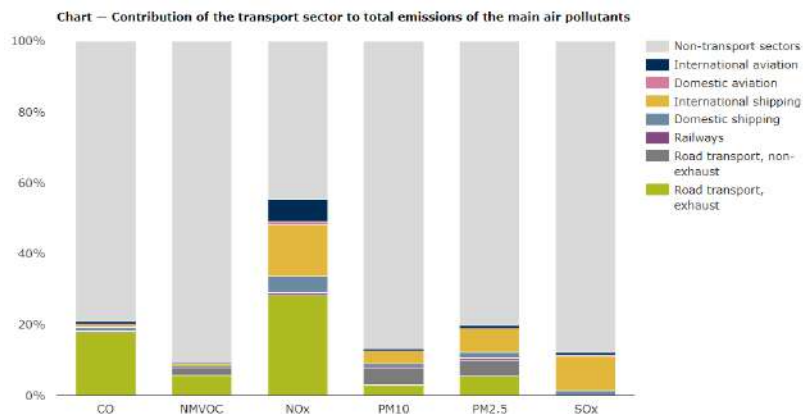


FIGURE 1.8: Impact of the transport sector on the emission of pollutants. [108].

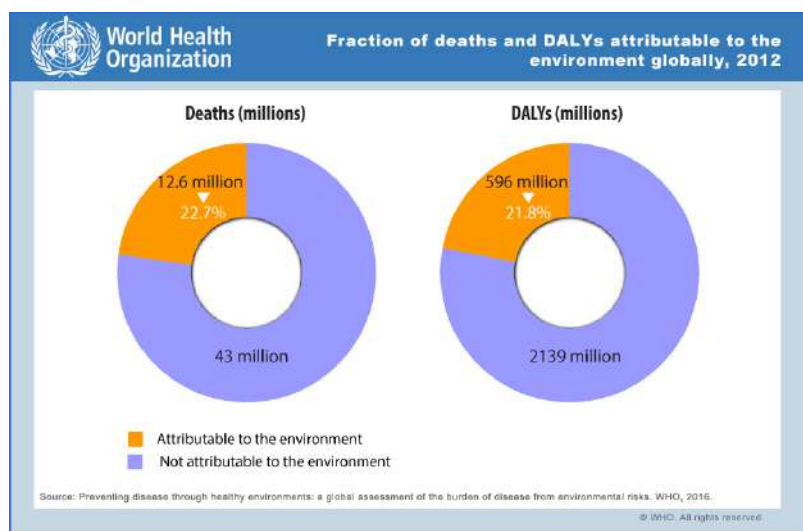


FIGURE 1.9: Mortality rate due to environmental pollution. [113].

which can remain in the atmosphere for tens to thousands of years, these substances disperse in small spaces and very short times. Pollutants can be classified as primary or secondary. Examples of primary pollutants are the carbon monoxide gas emitted from motor vehicle exhausts or sulphur dioxide released from factories. On the opposite secondary pollutants, rather than being directly-emitted, form in the air when primary pollutants react or interact. Ground level ozone is a prominent example of a secondary pollutant.

The main polluting species, the causes of their emission and the effects on both human health and the environment are listed below:

- Sulphur oxides ( $SO_x$ ): the sulphates present in the soil are absorbed as food by plant species and remains trapped in most of the fossil fuel.

Sulphur oxides, products of combustion reactions, can lead to the formation of sulphuric acid which is the main responsible of acid rain. Furthermore, given the high solubility in water, sulphur oxide is easily absorbed by the mucous membranes of the nose, causing respiratory problems for man; it also irritates skin and eyes.

- Nitrogen oxides ( $NO_x$ ): products of combustion processes, especially linked to vehicular transport, thermoelectric power plants and domestic heating. Molecular nitrogen ( $N_2$ ) is naturally present in large quantities in the atmosphere and is practically inert under normal conditions; however, at high temperature, it reacts with oxygen dissociating. Approximately 90-95% of nitrogen oxides resulting from combustion processes are nitrogen monoxides, but similarly to sulphur, other types of nitrogen oxide can also be formed, such as nitrogen dioxide ( $NO_2$ ). Both monoxide and nitrogen dioxide are harmful to humans and can increase the incidence of respiratory diseases and cause changes in lung cells and tissues. From an environmental point of view, nitrogen oxides considerably contribute to the formation of ozone ( $O_3$ ).
- Carbon monoxide ( $CO$ ): it is an odourless and colourless gas which is released as a result of incomplete combustion of all substances containing carbon. It is emitted as a result of fires and volcanic eruptions, but above all as a result of combustion processes of anthropogenic origin, especially those relating to transport sector. Carbon monoxide is a hemotoxin: by binding to the iron ion in the hemoglobin of the blood it forms a complex, called carboxyhemoglobin, which hinders the transport of oxygen in the blood, making it particularly harmful to individuals with heart and lung diseases.
- Ozone ( $O_3$ ): it is a typical secondary pollutant result of photochemical reactions in the troposphere between atmospheric oxygen and other pollutants (nitrogen oxides, hydrocarbons and aldehydes). It is naturally present in the stratosphere, where it plays the essential role of absorbing ultraviolet light, while can cause lung diseases in humans if present in the troposphere. Being a powerful oxidant, it can corrode metals.
- Un-burnt hydrocarbons ( $HC$ ): they are produced by the incomplete combustion of organic material, therefore emitted by vehicles and thermoelectric power plants. Some of the un-burnt hydrocarbons are carcinogenic; while the ones characterized by greater toxicity belong to the family of aromatic hydrocarbons (eg benzene).
- Solid particulate matter ( $PM$ ): consists of all the very small particles, solid or liquid, dispersed in the atmosphere. Particulate matter is classified according to the diameter of the particles:  $PM_{10}$  consists of coarse

particles with a diameter up to 10  $\mu\text{m}$  while PM<sub>2.5</sub>, or fine dust, includes all fine particles with a diameter up to 2.5  $\mu\text{m}$ . Most of the particulate matter has anthropogenic origin: it is emitted directly into the atmosphere as a primary pollutant from industrial plants, vehicle exhaust systems, construction sites and wood combustion processes. It can originate as a secondary pollutant as a result of chemical transformations and condensation of the primary gaseous pollutants. Considered the very small size, particulate matter, is the most dangerous because it can penetrate the filters of the human respiratory apparatus and reach the lungs;

It follows that the concept of sustainability must be declined also in terms of air pollution. All the human activities must be performed taking into account of their impact also in these terms. In last years, thanks to energy policies, the use of renewable sources for energy production and the development of technologies for polluting species abatement, the emission of pollutant substance has been reduced.

## 1.7 The Future of Internal Combustion Engine

The research and development in the field of vehicle design is ruled by the ever stringent tailpipe emission regulations. Worldwide vehicles manufacturer must respect the set of standards on pollutant emissions called, ad example in UE states, Euro (followed by an Arabic number for the light duty vehicles or a Roman number for the heavy duty ones).

To ensure compliance with the imposed values, European legislation involves pollutants measurement on a reference cycle carried out on a roller bench: the car is put into operation on rollers simulating the tire-road contact by means of the roller-rubber contact. Until 2018 the reference cycle was the "New European Driving Cycle" (NEDC) but now, in order to establish a homologation cycle that was more representative of real driving conditions, the NEDC was replaced by the "Worldwide Harmonized Light Vehicles Test Procedure" (WLTP). This new homologation procedure, in addition to being of longer duration, both in terms of distance and test time, also includes road tests, i.e. in real driving conditions ("Real Driving Emission" - RDE). Euro 6d, last regulation today active, among the others, limits CO<sub>2</sub> emissions of new cars to 95 g/km by 2021. Those limits are very stringent; for their achievement the car manufacturers have had, over the years, to adapt the engines and the devices for the abatement of polluting species to the exhaust. An idea of the importance for car manufacturers of respecting such normatives can be understood from words of Kia Europe's Artur Martins: "The fine for 1g over your target is 95 €multiplied by all of your volume. For Kia that's 500,000 cars. So almost a 50€million fine for 1g over the limit!" It follows that the bigger the miss, and the bigger the volume, the more a car maker will have to pay.

Forecast provided by PA Consulting, shown in Figure 1.10, demonstrate that many car makers likely will miss this target.

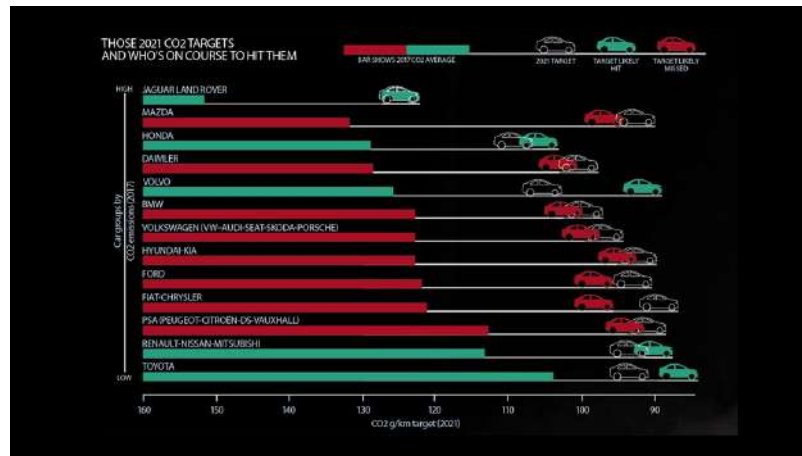


FIGURE 1.10: Many car makers will struggle to hit 95g/km fleet average CO<sub>2</sub> by 2021, warns PA Consulting.

The rise of the SUV, and the fall of the diesel engine are the responsible of such situation. SUVs are taller, less aerodynamic and heavier than conventional cars, so emit more carbon. Concurrently, negative publicity for compression-ignition engines led to a collapse in registrations without taking into account that the high efficiency of such technology limits carbon dioxide emissions.

Nowadays the key technology for transport of people and goods is the internal combustion engine (ICE). Internal combustion engine (ICE) is relatively simple, reliable and has high power-to-weight ratio but, now, facing the already mentioned issues, his prominence cannot taken for granted. Various forms of electric and hybrid vehicles are foreseen being the future of transport sector in order to hit the aforementioned targets.

Electric vehicles (EVs), for definition, are equipped with electric propulsion systems and are classified in three categories: battery electric vehicles (BEVs), hybrid electric vehicles (HEVs), and fuel-cell electric vehicles (FCEVs).

Technical Committee 69 (Electric Road Vehicles) of the International Electrotechnical Commission proposed the definition of hybrid electric vehicles (HEVs) as vehicles in which propulsion energy is available from two or more kinds or types of energy stores, sources or converters and at least one of them can deliver electrical energy.

In the next decade, as forecasted by JP Morgan [98] (Fig. 1.11), internal combustion engine vehicles (ICEVs) will continue to maintain a relevant share of the market but not as today: in 2025 pure-ICE vehicles will have around 70% share, falling to around 40% by 2030.

At the same time, the growth in battery electric vehicles (BEVs) and hybrid electric vehicles (HEVs) is climbing and by 2025, BEVs and HEVs will account for an estimated 30% of all vehicle sales. Comparatively, in 2016 just under 1 million vehicles or 1% of global auto sales came from plug-in electric vehicles (PEVs). By 2030, J.P. Morgan estimates this will rise close to a 18% market share. While this jump is significant, it doesn't compare to the kind of growth expected in hybrid electric vehicles. This sector is forecast to swell

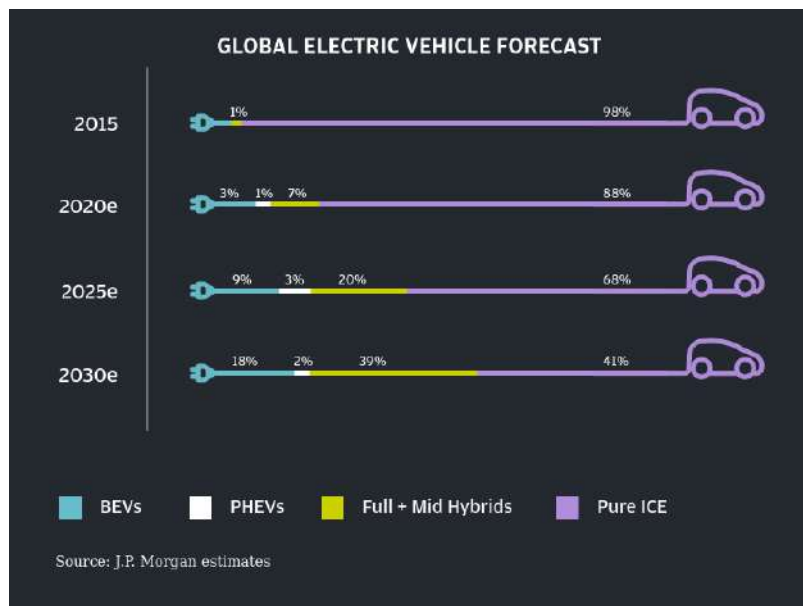


FIGURE 1.11: Driving into 2025: The Future of Electric and ICE Vehicles [98].

from just 3% of global market share to more than 25 million vehicles or 41% of global sales over the same period. Looking at this data it appears clear that ICE will not die but it will have a new life, not uniquely alone as today happens in traditional vehicles, but also within a more complex propulsion system presents in HEVs.

Electric vehicles are regarded as having the potential to lower emissions in the mobility sector and comply with the emissions standards. However, Life Cycle Analysis (LCA) and Well-to-Wheel analysis demonstrated how this statement is not completely true and, furthermore, highlight as high costs might hinder their market development.

From cradle-to-grave emissions of three German ICE vehicles and its BEVs counterpart were compared by [47] and reported in Figure 1.12. The BEVs emissions are strongly dependant on the form of the electricity production, for this reason three scenario were considered bringing to different emission levels:

- Scenario 1-optimistic: assumes a quick switch from fossil to renewable energy sources.
- Scenario 2-pessimistic: predicts a high CO<sub>2</sub> intensity in the German grid.
- Scenario 3: assumes electricity production only from renewable energy sources.

Considering the optimistic scenario 1 of electricity production, BEVs shows an emission reduction of around 35% nowadays (Fig. 1.12). This relative benefit remains roughly constant until year 2030. Accordingly to scenario 2

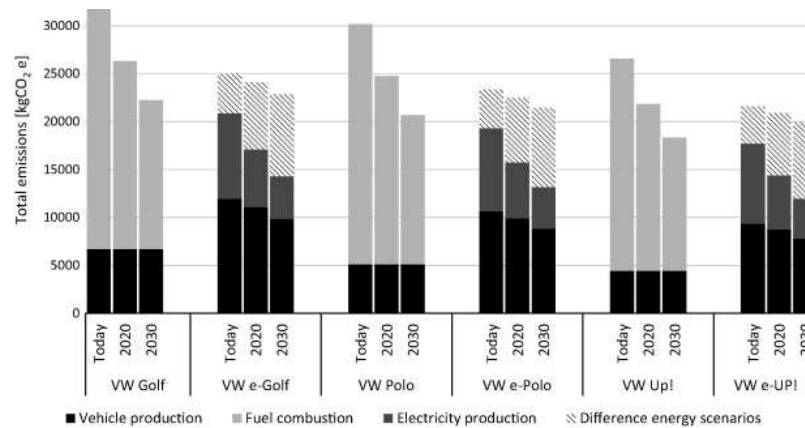


FIGURE 1.12: Production and operation emissions of three German ICE vehicles and its BEVs counterpart. [47].

of electricity production, the yet still existing BEVs advantage of 20% but, in long term view, it turns in an ICE advantage up to 9% (Fig. 1.12). This development is explained by the fact that ICE increase in efficiency, the electric grid decarbonisation however does not take place in scenario 2. A non-surprising clear advantage for BEVs results in consideration of the scenario 3.

The CO<sub>2</sub> emissions of ICEVs, and BEVs are dependent on the regions as well as the CO<sub>2</sub> emissions of battery production [173]. Literature studies suggested that BEVs is not only solution for reducing CO<sub>2</sub> emissions globally, but it is important for car manufacturers to introduce ICEVs as well as BEVs to each region in consideration of electricity mixes. Figure 1.13 reports the calculation results of total life cycle CO<sub>2</sub> emissions for five regions (a - EU, b - Japan, c - US, d - China and e - Australia) and for gasoline ICE (GE), diesel ICE (DE) and BEVss.

The results indicate that the emissions amounts significantly vary by region and an important increment of CO<sub>2</sub> emissions is due to the battery replacement after 160.000 km. Furthermore the different assumption for the different regions bring break-even point sensible variation.

The comparison of Total Cost Ownership (TCO) of electric and reference ICE vehicles demonstrates that ICE today face an advantage of 15–20% [47]. Regarding the annual break-even distance, as shown in Figure 1.14, it is roughly equal to 20000 km [47]. The U.S. Department of Transportation's Federal Highway Administration states the average person drives around 21000 km every year. It follows that customers does not have great economic advantages in choosing electric propulsion vehicles. Such deals demonstrate how, in the near future, electric vehicles cannot be the unique technology for achieving a sustainable mobility. ICE alone, in pure-combustion vehicles, or together with electric unit in hybrid vehicles, will remain present. The research and development cannot be abandoned. Besides, with the ever increasing share market of HEVs, enhancement of ICE propulsion system can be exploited in this kind of vehicles too.

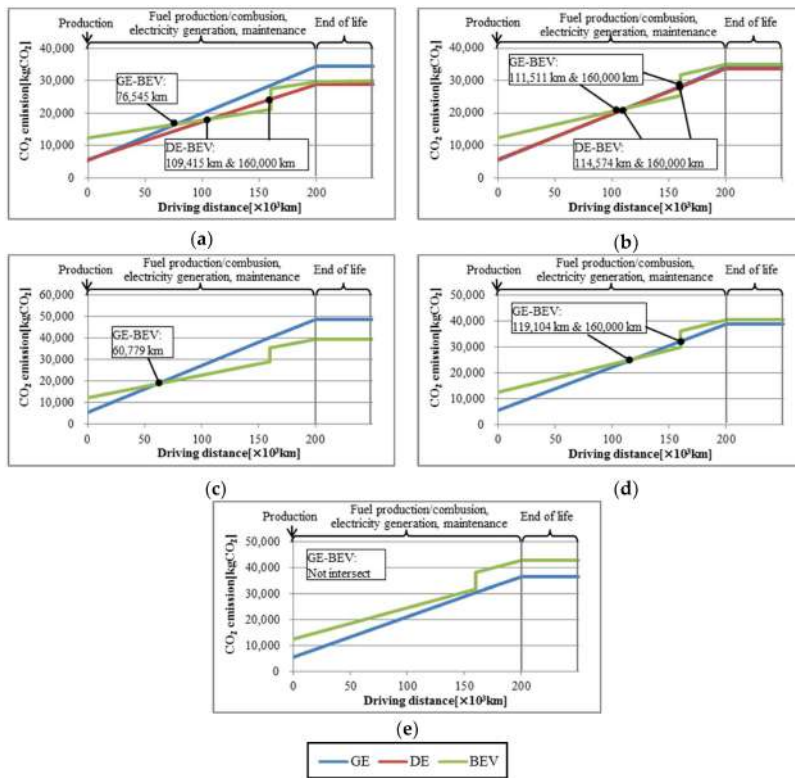


FIGURE 1.13: CO<sub>2</sub> emissions during life cycle for GE, DE and BEVs. (a) European Union (EU); (b) Japan; (c) US; (d) China; (e) Australia. [173].

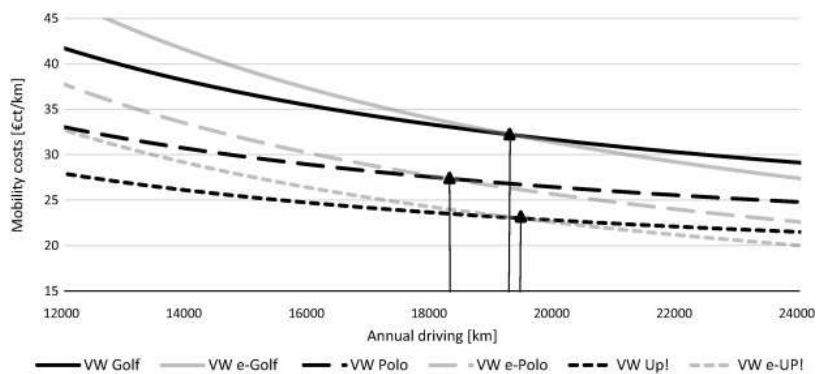


FIGURE 1.14: Mobility costs as a function of annual driving. [47].

## 1.8 Internal Combustion Engine: New Frontiers of Research and Development

In this scenario the research in field of ICEVs design is directed towards the attainable improvement in brake-specific fuel consumption and tailpipe emission reduction, with the final aim of decreasing the environmental impact.

ICE can be classified according to the combustion process triggering into:

- Spark ignition engines (SI): a mixture of air and fuel is ignited by a spark-plug, generating a rather rapid combustion. They are also called Otto engines and usually work with gasoline fuel;
- Spark ignition engines (CI): the combustion is triggered, under certain pressure and temperature conditions, by the self-ignition of the air/fuel mixture. A slower and more gradual combustion process. They are also called Diesel cycle engines because they operate with diesel fuel;

The main pollutants produced in a spark ignition engines are carbon monoxide (CO), unburnt hydrocarbons (HC) and nitrogen oxides (NO<sub>x</sub>).

Carbon monoxide arises as a result of the incomplete oxidation of hydrocarbons and the partial dissociation of the carbon dioxide formed at high temperatures. The principal engine parameter that affects the concentration of CO in the exhaust gases is the air-fuel ratio: it increases with the enrichment of the fuel mixture and decreases for poor mixtures.

The causes that lead to the formation of un-burnt hydrocarbons are various. The flame front does not arrive in crevices and interstices (such as those between the cylinder, piston and piston rings) leaving un-burnt substances. Sometimes the flame front stops before having ignited all the charge or the candle is not even able to ignite the mixture (misfire) which is then discharged together with the burnt gases of the other cycles. The mixture ratio and the ignition advance influence the concentration of HC. It decreases as the air / fuel ratio increases, because the amount of oxygen available to oxidize the fuel increases, but for too low equivalence ratios the HCs increase because there is partial combustion or misfire due to excessively low speed and temperature values. HC emissions are also reduced as the ignition advance decreases: the end of combustion is delayed, continuing during the exhaust stroke, allowing the unburned hydrocarbons to mix with the combustion products and any oxygen present.

Due to the high temperatures (greater than 2000 K), reached in the flame front zone, thermal dissociation of the nitrogen and oxygen molecules into atoms takes place producing nitrogen oxides. Therefore, the concentrations of nitrogen oxides essentially depend on two factors: maximum values of temperature and oxygen content in the feed mixture. The air / fuel ratio is therefore the engine parameter to be observed as it affects the combustion temperature.

The formation of polluting species in compression-ignition engines is mainly due to air/fuel distribution which varies over space and time therefore may

leading to incomplete combustion. Un-burnt hydrocarbons can be generated in the peripheral part of the spray where the amount of fuel is too low to lead to self-ignition and the propagation of the flame front. Therefore, thermal cracking and partial oxidation of the fuel can occur. Other HCs can be generated in the central core of the jet where partial oxidation occurs due to local oxygen deficiency. Contrarily than SI engine, CI engines, works with poor mixture too. The greater availability of oxygen guarantee a good oxidation of the CO reducing concentration at the exhaust which is much lower than that SI engine.

In a CI engine NO<sub>x</sub> formation occurs in the weakly lean areas surrounding the fuel jet, which, due to the presence of oxygen and the high temperatures, burn first and also in the central core of the spray, where temperatures are maximum. Nitrogen oxides represent the main gaseous pollutant of a CI engine.

Last but not least to be mentioned, especially for CI engines, but also for SI engines with direct injection, is the particulate matter (PM). It consists on carbon particles deriving from incomplete combustion and brought into suspension by the exhaust gases. Particulate formation in the combustion chamber is a complex mix of chemical and physical processes (pyrolysis, nucleation, oxidation, piston wetting, carbonisation, particle coagulation and agglomeration). At the outlet section of the exhaust ducts, the PM appears as a set of single carbonaceous cores or as a more complex cluster structure. These fine particles, less than one-tenth the diameter of a human hair, pose a serious threat to human health, as they can penetrate deep into the lungs.

The scientific research in the field of ICE today, more than ever, is aiming to develop solutions, at every level to tear down tailpipe emissions. The simplest idea is to use after-treatment systems, inserted on the exhaust duct, in order to modify the chemical composition of exhaust. Among the others can be mentioned:

- Three Way Catalysts (TWC): the trivalent catalytic converter performs a triple action on the exhaust gases reducing NO<sub>x</sub> to N<sub>2</sub> and oxidizing HC and CO to, respectively CO<sub>2</sub> and H<sub>2</sub>O. In order to operate correctly, the engine must work with a strictly stoichiometric mixture: an excess of free oxygen (lean mixture) makes difficult to reduce nitrogen oxides, while a defect (rich mixture) decreases the probability of oxidation of CO and HC;
- Selective Catalytic Reduction Catalyst (SCR): post-treatment unit for nitrogen oxides reduction typically through a urea solution injected in the exhaust gases flow;
- Diesel Particulate Filter (DPF): it is a component that forces the burnt gases to pass through a porous septum (generally made of ceramic material, so as to withstand high temperatures) which retains particulate matter larger than those of the pores. The DPF must be periodically cleaned, through an operation called "regeneration".

Going backward in the chain of events taking place in a ICEVs it must be mentioned combustion. An higher efficiency can be obtained through innovative combustion engines strategies such as low temperature combustion, lean burn gasoline combustion, and clean diesel combustion that produce very low engine-out emissions of oxides of nitrogen (NO<sub>x</sub>) and particulate matter (PM).

Low temperature combustion (LTC) is a flameless, staged burning of the fuel (gasoline, diesel, or biofuel) in an engine's combustion chamber at temperatures that are lower than what occurs during conventional engine combustion.

In lean burn gasoline combustion, a flame moves through either premixed or non-premixed (i.e., stratified) mixtures of fuel and air. In this process, the engine dilutes the fuel with either more air than is required to burn it (excess intake air) or recirculated exhaust gases.

The burning processes of clean diesel combustion and conventional diesel combustion are quite similar. However, in conventional diesel combustion (also known as diffusion combustion), the rate at which the fuel spray mixes with air inside the cylinder before it reaches the flame determines the rate at which the fuel and air burn in the flame while, in clean diesel combustion, more fuel-air mixing occurs prior to the flame. This enables cleaner combustion that produces less soot as well as retains or improves the high efficiency of diesel engines.

The correct evolution of such advanced combustion methods depends on the mixture formation and, previously, mainly on the fuel supply system. Timing and modalities with the fuel is inserted within the engine are crucial to obtain a correct mixing with air and, finally, to realize an efficient and clean combustion. Since late '90 fuel is provided by the unit injector replacing old carburetors. Consequently the injection process plays a relevant role in the chain of events happening in a ICE and for this reason it will be the common thread of this work.

Physics of the spray formation will be studied both experimentally and numerically paying particular attention on the development of consistent simulation methodologies capable to reproduce the spray evolution in environments thermodynamically similar to the engine ones.

Nowadays, the availability of advanced technological capabilities, lead to a reconsideration the application of in-cylinder direct injection techniques to spark-ignition engines. This technology, alone or in conjunction with the adoption of gaseous alternative fuels, is believed to be able to reach important achievements like:

- performance enhancement
- consumption reduction
- emissions limitation
- engine down-sizing

However, due to short timing for air/fuel mixing and small space available within the combustion chamber scientific deepening of such processes is mandatory in order to hit the previously mentioned targets.

Alongside to these deals, many alternative sustainable fuels have been proposed for their environmental prerogatives: they are renewable, have lower carbon emissions, are particulate free and can be produced also from vegetables or, generally, in sustainable ways. Among the others, it can be mentioned biogas, biodiesel, propane, ammonia, dimethyl ether (DME) vegetable oil, boron, P-series fuel (a unique blend of NG liquids, ethanol and methyltetrahydrofuran), compressed natural gas (CNG) and liquified natural gas (LNG). Considering gaseous nature of many of them, particular attention is been paid on the development of efficient direct-injection techniques in order to achieve correct dosage, air mixing and finally combustion.

## 1.9 Aims and outline of the thesis

The intention of the current work is to perform a comprehensive characterization of the spray injection processes of both liquid and gaseous fuels in direct injection-spark ignition engines. In particular, the primary aim is to formulate and develop computational frameworks based on the current state-of-the-art commercial and open-source Computational Fluid Dynamics (CFD) capabilities, for modelling various physical aspects involved in DI-SI engines. Moreover, the present research aims to shed more light on the physical behaviour and fluid dynamics of various complex phenomena involved within the concept of advanced high pressure DI systems and DI-SI engines.

The main work of the present thesis is organised into chapters 2 to 10. An overview of the contents of each chapter is as follows:

**Chapter 2** reviews the features of injection systems, illustrates the two macro-areas in which current work is subdivided and, finally, explain the approach adopted for studying injection processes.

**Chapter 3** illustrates the experimental techniques used for spray characterization

**Chapter 4** illustrates the numerical methodology adopted for spray characterization.

**Chapter 5** focus the attention on gasoline direct injection (GDI) technology providing a literature review. Finally the case study analysed are listed.

**Chapter 6** investigates the features of the Spray G injection process in standard engine conditions .

**Chapter 7** illustrates the physics of flash-boiling sprays and the numerical methodology developed. The jets issued from the Spray G injector in flash-boiling conditions are investigated with the newly developed approach so relative results reported.

**Chapter 8** focus the attention on the direct injection of CNG. Finally the case study analysed are listed.

**Chapter 9** includes the single-hole DI device case study providing full details of the approach used and the results obtained.

**Chapter 10** illustrates the newly developed density based solver for studying high pressure gaseous injection process and its application on a prototype multi-hole injector.

**Chapter 11** summarizes the main findings and the conclusions of the present thesis.

## Chapter 2

# Fuel Supply Systems

### 2.1 Engine Fuel Supply Requirements

The spark ignition engine uses fuels that are volatile enough to be premixed with air before combustion is initiated between the spark plug electrodes. The task of the fuel supply system is therefore to dose the quantity of fuel suitable to obtain, with the intake air, a mixture of suitable richness over the entire range of use of the engine. The optimum mixture ratio for a spark ignition engine varies, to some extent, according to the operating conditions. In general, it can be said that, with the same speed of rotation and load, it is possible to identify an optimal value of the air-fuel ratio for which the maximum power is obtained (slightly rich mixture), and a different value for having the maximum efficiency (minimum specific consumption). These considerations can be generalized and for any effect that want be optimized (minimum emission, minimum CO, minimum fuel consumption, etc...), an appropriate mixing ratio value can be determined.

Depending on the operating conditions it will therefore be necessary to find a compromise between the different requirements, choosing the value of a which ensures the desired performances. Summarizing the problem, as general indication, we can refer to the following three typical situations:

- Case of an engine whose power supply can be adjusted according to the requirements of good performance and low consumption, while the exhaust gases quality is sufficient by just controlling the power supply and combustion. At low rotational speeds to increase the flame front propagation speed and make the motor operation more stable (better starting torque) a slightly rich blend should be kept. At constant speed, as the load varies, the mixture ratio required is on average lean for intermediate loads (usually used for cruising) and must be enriched approaching to the conditions of full power.
- Case of an engine subject to the stringent regulations regarding exhaust emissions that requires the use of purification methods. The mixture ratio with which the engine must be fuelled is mainly imposed by the emission abatement technique adopted at the exhaust. The most common solution is based on the use of a trivalent catalyst (capable of working with CO, HC and NO, at the same time). The equivalence ratio range, within which this catalyst can perform its action effectively, is

very narrow around the stoichiometric mixture ratio. It follows that in an engine that uses such exhaust after-treatment system, the fuel supply system must guarantee a stoichiometric mixture over a large part of the operating plan.

- Case of an engine in whose combustion chamber there is a non-homogeneous spatial distribution of equivalence ratio: rich mixture in the vicinity of the spark plug with an increasing leaning moving away from it (stratified charge). In this case of stratified charge it is possible, for the same speed, to adjust the indicated mean pressure, (i.e. the load), by varying the quantity of fuel supplied for each cycle (as in the Diesel engine), rather than the mass of the intake mixture. However, in most stratified charge engines, this ability to control the combustion process still cannot be used for all engine operation conditions

The fuel supply systems of an internal combustion engine and, in particular, spark ignition must therefore dose the required quantity of fuel and mix it with the air, in order to satisfy the complex requirements in terms of mixture formation just mentioned. To do this normally they exploit two different physical principles:

- they use the depression created by the air flow drawn in by the engine to recall the quantity of fuel required (carburettor)
- they pressurize the fuel with a special pump and inject it finely pulverized into the mass of the intake air (injection).

The main characteristics of these two fuel systems will be analysed in the rest of the chapter starting for historical reasons from the carburettors.

## 2.2 Carburettor

Carburettors were the first devices for fuel supplying in spark ignition engines due to their simplicity. However, it was the wide-spreading of internal combustion engines as propulsion systems for road transport vehicles that determined their continuous technological development. The increasingly stringent limitations on tailpipe emissions have ended up imposing injection systems for this fundamental category of engines. However, for sake of completeness, the main characteristics of carburettors are reported. Given the multiple requirements of engines, the carburettor became a complex component, consisting of a group of systems that work individually or simultaneously, to ensure the desired mixture ratio in all conditions. There are various design solutions, but the same physical principle is used in the most widely used types. The flow of air drawn in by the engine is used as the main quantity to control the mixture ratio, using the depression produced by it in the restricted section of the passage duct, to recall and dose the fuel. An elementary carburettor of this type therefore consists of the following essential organs (Figure 2.1):

- a *venturi duct*, formed by a converging-diverging nozzle. in whose narrow section the necessary depression is generated for the recall of the fuel. The throat diameter of the nozzle must be such as to create a sufficient vacuum to suck the fuel even when the engine is powered with a small air flow rate, without on the other hand producing an excessive pressure drop at full power;
- a *fuel discharge nozzle* that is, a duct that carries the fuel, previously metered by the flow control jet, into the restricted section of the venturi;
- a *float chamber* in which the fuel level is kept constant, by means of a float which acts on a conical valve to cut off the fuel flow from the tank. The result is thus obtained of keeping the hydrostatic load on the jet constant, subtracting it, for example: from changes in the fuel level in the tank, from the pressure value of the delivery pump, from changes in the carburettor's output, etc.
- a *throttle valve* for regulating the mass of mixture drawn in by the engine. It is located downstream of the main parts of the carburettor just described. By choking the inlet manifold, it varies, and therefore regulates the engine load.

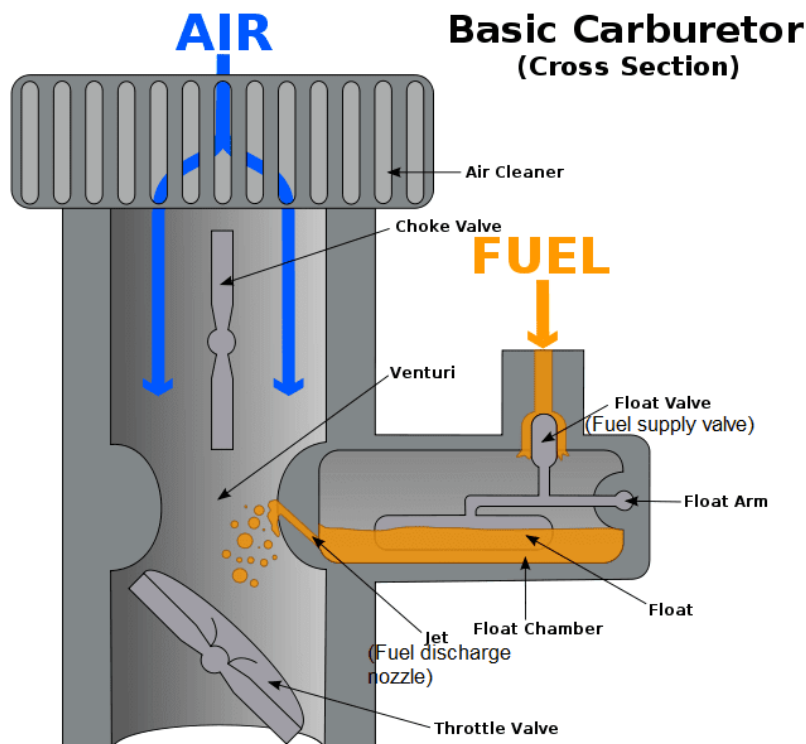


FIGURE 2.1: Schematic representation of a basic carburettor [93]

## 2.3 Indirect and direct injection

Fuel injection is the operation that allows to prepare the air/fuel mixture suitable for the correct operation of SI engine. The injection systems dose the fuel in proportion to the air-flow breathed by the engine exploiting an increase in fuel pressure with respect to the air, generated by the injection pump. During injection, the fuel jet comes out at high speeds from the injector nozzle, forming a spray of fine droplets.

Among the others, injection systems for spark ignition engines can be classified accordingly to the position of the injector in direct injection and indirect injection. Figure 2.2 shows the three main locations where the injector is commonly placed relative to the engine.

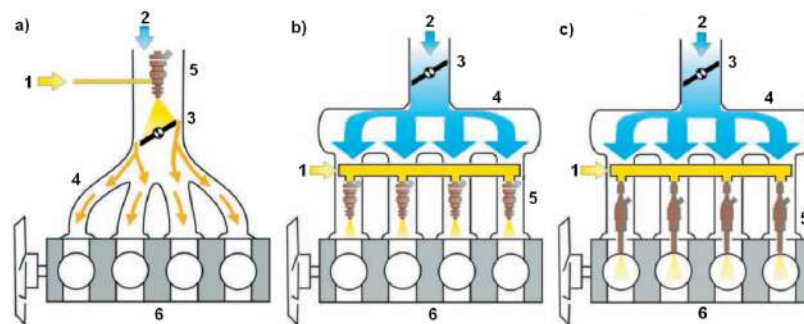


FIGURE 2.2: Systems of fuel injection [1]: a) Single Point Injection, b) Multipoint Injection, c) Direct Injection; 1 – Fuel supply, 2 – Air intake, 3 – Throttle, 4 – Intake manifold, 5 – Fuel injector (or injectors), 6 – Engine

In direct injection systems the injectors are placed on the head of each cylinder, so the fuel is sprayed directly into the individual combustion chambers. In indirect injection, on the other hand, the fuel is injected into the intake air stream before it enters the cylinder. Among the different possible injector positions, the most important are single point and multi point injection. In the first case, even for a multi-cylinder engine, the fuel spray is sprayed into the air by a single injector normally placed upstream of the throttle valve. In the second spray is formed by as many injectors as the cylinders. The injectors are positioned in the intake manifold, in front of the intake valve, thus avoiding any problem of correct distribution of the fuel between the various cylinders, because the spray produced by each injector must travel a short distance before entering its own cylinder.

The indirect injection process does not have to be synchronized with the engine-cycle. Indeed, the fuel injected, mixes with air and can also accumulate near the intake valve, until it opens. The problems of air/fuel mixing are, therefore, much less critical than those typical of direct injection. In fact, thanks to the free-timing, longer times are available and it is possible to exploit the homogenizing action of ducts and valves. Considering the low injection pressures (0.3 - 0.4 MPa) and, that indirect devices are not exposed

to burnt gases, injectors costs are moderate and reliable. The advantages offered by indirect injection can therefore be summarized in:

- good homogenization of the charge due to the mixing process in ducts and valves due to the relatively long times available before starting combustion;
- low injection pressures because the main function of the injector is to dose the correct quantity of fuel rather than produce a spray with stringent pulverization and penetration characteristics;
- limited thermal loads on the injectors because they are not in contact with the burnt gases used and there are not fouling issues due to carbon deposits;
- low system costs thanks to both the low injection pressures required and the possibility of using simple and economical injectors.

On the other hand, indirect injection brings to lower engine efficiency, higher fuel consumption and eventually higher pollutant emissions. For these reasons, lately, a growing interest was achieved by direct injection systems. The direct injection into the cylinder must be strictly timed with respect to the engine cycle. The injection must be anticipated during the intake in order to obtain a homogeneous air/fuel mixture. This gives the maximum time for the fuel spray to mix with the incoming air and vaporize. However, since the time available for the homogenization of the charge is less than that relating to the indirect injection, it is necessary to increase the air turbulence. Higher injection pressure (than the ones used for indirect injection) is required to comply with shorter injection timings. DI allows to obtain an appropriate stratification of the charge with decreasing richness moving away from the candle. This stratification process is obtained by the delay of the injection until just before ignition (starting by the end of the compression stroke). A further advantage of this system is the possibility of using wide crossings between the exhaust and the intake valve with consequent good washing. Furthermore, any risk of fuel condensation on the walls of the ducts and on the intake valve is eliminated although part of the spray can reach the piston and cylinder walls (especially in small bore engines). On the other hand, the injector is more robust and expensive because it has to withstand higher injection pressures and greater mechanical and thermal stresses typical of a combustion chamber.

The advantages of direct injection can therefore be summarized as follows:

- overcomes the limitations of working with a homogeneous charge;
- allows to use innovative forms of combustion such as stratified charge with a decreasing air/fuel ratio going far from the spark plug or controlled self-ignition

- allows to control the engine load in an innovative way (together with the use of: variable valve actuation systems, supercharging, downsizing, etc.), reducing fuel consumption in partial load conditions:
- limits the formation of pollutants by controlling the development of the combustion process and the use of a strong recirculation of burnt gases.

## 2.4 The scientific approach for spray's characterization

The starting point of the spray characterization is an experimental campaign. In the last few years, various experimental procedures have been developed to capture images of the injection process at different thermo-fluid-dynamic operating conditions which should be the most representative of the engine conditions. The combustion chamber is an unfriendly measuring environment: the turbulent gas phase, the flame itself and the particular thermodynamic conditions make it difficult to perform measurements without altering the environment's conditions. Qualitative imaging techniques and quantitative procedures can be exploited in order to have a representation of the spray's morphology.

The parameters that allow to describe the jet morphology differs if gaseous or liquid spray is considered. However, in both cases determining experimentally the actual structure of a spray, i.e. the distribution of the fuel within the jet, is still a rather difficult task. Therefore, it has to be considered only some global parameters: the penetration length, the cone angle, and the tip velocity. This last parameter decreases over time, the penetration of the jet grows continuously as it develops over time, while the cone angle, usually, does not vary significantly. Talking about the liquid spray, as soon as it comes out of the injector's nozzle, it pulverizes into drops and liquid particles. Droplet dimensions are a relevant parameter for evaluating the spray's quality. Sauter mean diameter (SMD), the most used, is defined as:

$$SMD = \frac{\sum_{i=1}^{N_d} d_i^3}{\sum_{i=1}^{N_d} d_i^2} \quad (2.1)$$

where  $N_d$  is the overall number of droplets and  $d_i$  the  $i$ -th droplet's diameter.

The evaluation of air/fuel mixing within gaseous fuel-jets deserves a separate discussion. Experimental techniques featuring tracer substances adoption are unavoidable. Such procedures are quite complex to perform and express all their limitations leaving the field open to numerical approaches.

Computational fluid dynamics simulation allows to reconstruct the spray morphology and, especially, evaluate physical parameters instead difficult to be measured. Experimental data are thus used by researchers to tune and validate computational fluid dynamics (CFD) spray models that become powerful tools to understand such phenomena. Furthermore once validated, the

numerical models, allow to perform quickly parametric investigations sparing time and money needed for setting an experimental campaign.

Numerical models can be divided in two categories depending on the final aim:

- Mono-phase models: adopted for the simulation of gaseous injection processes. They feature an accurate turbulence representation and high-order discretization schemes (both in time and space) capable to represent the strong discontinuities of supersonic flows.
- Bi-phase models: adopted for the simulation of liquid fuel injection processes. They feature an Eulerian-Lagrangian combined approach for simulating, respectively, gas phase and liquid-fuel phase plus, a set of physical sub-models, for describing the two phases interaction and the other phenomena.

Together, the experimental and numerical results, provide a better comprehension of the operating condition's effect on the spray characteristics, allowing us to optimise the injection process and so to obtain low emissions and a more efficient combustion. In the next chapter the principal features of both CFD and experimental techniques are described.

## 2.5 Outline of interest areas

The current work regards the characterization of the spray formed by DI injectors for spark ignition engines (SI) engine. In particular, the analysis will be divided into two main areas of interest:

- GDI Injections: the global volume of gasoline direct injection engines is expected to overtake that of port fuel injection (PFI) engines by 2020 [136, 322]. The GDI systems are broadly recognized as a powerful technology to reduce the worldwide energy supply demand and the environmental pollution. The GDI technology allows to achieve a higher engine efficiency, a cleaner combustion and the engine downsizing. In such configuration the quality of the injection process full-fills a relevant role and strongly affects the chain of events of mixture-formation, combustion and pollutants production. Hence, it becomes unavoidable reaching a comprehensive characterization of fuel jet. Experimental techniques, in conjunction with CFD modelling procedures featuring Discrete Droplet Model (DDM) approach, will be adopted for a comprehensive description of the multi-phase flow of a liquid spray. Spray's formation of GDI injectors will be studied with particular attention on the conditions of high-injection pressure and operating in flash-boiling conditions. Flash boiling is the sudden phase change of a fluid from liquid phase to the vapour one and it occurs operating at high temperature levels of the injected fuel and low back-pressure values. Such configurations are demonstrating many advantages in the applications for GDI engines providing a better fuel atomization, a better mixing

with the air, a consequent more efficient combustion and, finally, reduced tailpipe emissions. An innovative approach will be developed in OpenFOAM environment for properly simulating the flash-boiling phenomenon features.

- **Gaseous Injections:** lately, a great interest is growing for the adoption of gaseous fuels too in direct injection systems. In this work it will be considered CNG because alone or in combination with other fuels, CNG represents an attractive way to reduce exhaust emission (high H/C ratio), can be produced in renewable ways, and is more widespread and cheaper than gasoline or diesel fuels. Unfortunately, it has some drawbacks such as a low energetic density and presents difficult combustion dynamics, requiring a deep studying. Gas direct injection (DI) processes involves the the formation of characteristic sonic structures, shock waves and under-expanded jets in the combustion chamber. An accurate characterization of such phenomena is crucial for a consequent application in DI-CNG engines. Appropriate CFD methodologies will be developed in OpenFOAM environment in order to evaluate correctly the fuel-jet evolution within the combustion chamber. At the same time, improvements on the injectors design are required. For these reason in current work single hole and multi hole injector operating at different injection pressure will be considered in order to investigate the optimal configuration capable to provide the required of spray's quality.

## Chapter 3

# Optical measurement techniques for spray characterization

### 3.1 Historical background of optical techniques

The father of optical studies is Robert Hooke (1635-1703) one of the biggest experimenters in the 17th Century. He was simultaneously involved with telescope, microscopy, glass technologies and optical techniques. He established a new field of study with his famous 'Micrographia' on which there is a discussion of light refraction by density variations in liquid and in atmosphere. With his study he explained the twinkling of stars, convection phenomena in fluids, turbulent mixing, chromatic aberration and stratified flow. For the first time he studied a thermal disturbance looking at schlieren effect as pupils of eye that cut off refracted rays. His study was not recognized as a schlieren technique for three centuries. He replaced upon human pupil of the eye the light-dark boundary of a candle flame with one lens, or concave mirror. When a candle was positioned distant to the lens this illuminated completely the pupil areas. While when a second candle was inserted near the lens it refracted some rays strongly that they fall outside the pupil, revealing the transparent convective plume of the candle because the eye sees a different light intensity. Hooke understood that the convective plume of the candle was visible by way of its shadow on a white paper by the sun. This description is the beginning of a shadowgraph technique (Figure 3.1).

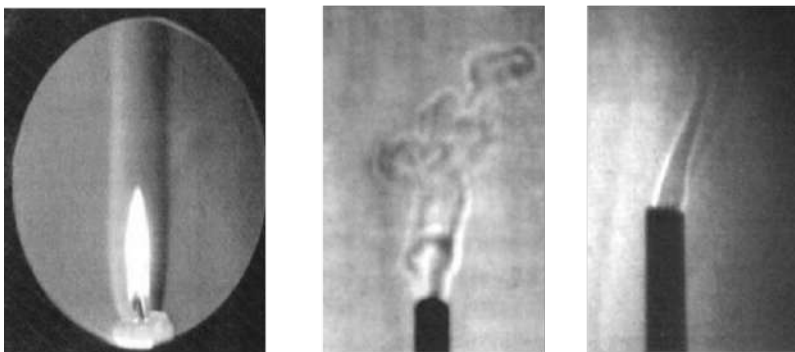


FIGURE 3.1: Left-to-right: candle plume and original shadowgraph observations [338]

Only about a decade after Christiaan Huygens (1629-1695) re-invented a version of a schlieren technique. During the 18th Century only Jean Paul Marat (1743-1793) published a volume of the physics of fire in which he painted the first optical flow image. A warm air is visible, it is less dense than the ambient and refracts light to form a bright fringe around and inner dark zone. Marat had painted the laminar plume in its transition to turbulence. In the 19th century J.B. Leon Foucault (1819-1868) made a important contribution: he used a knife-edge to refine astronomical telescope mirrors and indirectly was vital for schlieren technique today, in this way he has introduced a filter for image. Another fundamental physic of this Century is Ernst Mach (1838-1916) that with these precedent studies measured a wave speed proving that the waves of sparks were supersonic. Mach's schlieren observation confirmed that non-linear waves could travel faster than sound (acoustic speed is 340 m/s). In 1885s Mach recognized that nondimensional parameter  $V/a$ , the Mach number where  $V$  is the wave speed and  $a$  is the speed of sound, governs the behaviour of shock waves. Ludwig Prandtl (1875-1953) and his students at Gottingen University started to study a supersonic gas flow and one student, Theodor Meyer, derived the theory of oblique waves in supersonic flow and Ernst Magin made schlieren observation of them (Figure 3.2).

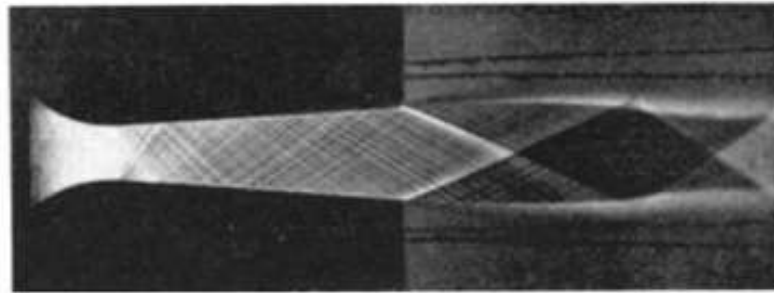


FIGURE 3.2: Supersonic nozzle flow pattern photographed in Prandtl laboratory [338]

In the 20th Century the field of ballistics was employed. Carl Cranz (1858-1945) was an engineer and professor of Ballistics in Berlin and with Hubert Schardin (1902-1965) made a crucial contribution to high-speed photography. They improved a multi-spark camera today known as the Cranz-Schardin camera. This camera enables to capture high-speed imaging of physical phenomena at more than a million frames per second. Therefore, with this camera many important study were carried out as shock-tube flow or ballistic impacts. At the end of World War II Schardin wrote his major publication *Schlieren Methods and Their Applications*. In 1945, he and his research group were required from US and France for their knowledge in ballistic field. Therefor at Saint Louis, in France, Schardin became the first German director of the German-French Research Institute Saint-Louis that is still today a renowned centre for ballistics, shock-tubes and optical flow diagnostic. Rudolf Hermann (1905-1991) and his team designed a large supersonic

wind tunnel in 1939s and the key instrument was a schlieren system: a major application to schlieren and shadowgraph was created. It was a good development for the flow study because without flow visualization wind tunnel was not useful. While the recent history of schlieren and shadowgraph techniques concern new approach for large point of view. Leonard M. Weinstein (1940-), a Nasa scientist, developed new concept of instrumentation applicable in different field of engineering. He turned his attention on lens-and-grid schlieren techniques completing the general optic incomplete design of these system that was started by Schardin and now several tunnel facilities can be used, for example systems for flow visualization cheaper than conventional schlieren optics. More than 70 new schlieren system were based on work of this scientist.

The experimental campaigns performed in this work feature exclusively schlieren and Mie-scattering techniques. In particular gaseous sprays were recorded using the first one while, liquid sprays, were analysed with both techniques. In particular, Mie scattering, capturing mainly the liquid phase, was adopted for distinguish between liquid and vapour. Consequently the physics of such techniques are described in the following.

All the measurement proposed in this work were performed at the "Laboratorio Spray" of the Istituto Motori of CNR - Naples.

## 3.2 Schlieren imaging

Schlieren is a simple, inexpensive and somewhat spectacular optical technique for visualizing density gradients in fluids, it has popularly used for studying shock-waves in air-flows. Schlieren imaging is used for studying turbulent multiphase flows too and it can visualize internal structures of the gas-phase fluid flow, which is invisible without a proper optics setup [187].

Our eyes and ordinary cameras cannot distinguish the phase differences in a light beam but the schlieren method does it. The physical concept of schlieren is the refraction of the light. When light rays interact with matter they can deflect or not: if the light travel through a homogenous media, vacuum or space, the rays have a uniformly phase and a constant value, on the other hand if light passes through heterogeneous media, such as fluids in motion, the rays refract and deflect. Then schlieren technique translates phase differences into amplitudes. The electromagnetic nature of the light allows defining the wave fronts. The wave front is the locus of all points where the waves vibrate together, and they have the same phase. The light rays are always perpendicular to fronts of wave. The wave front form can be spherical or flat. When light rays travel in a heterogeneous media the index of refraction changes, the light changes its velocity and fronts of waves have not the same form. When the light crosses a medium with parallel sides and uniform density (Figure 3.3), the rays go down or speed up, depending of density of the medium, keeping constant their direction and after passing the medium get again their initial velocity [82].

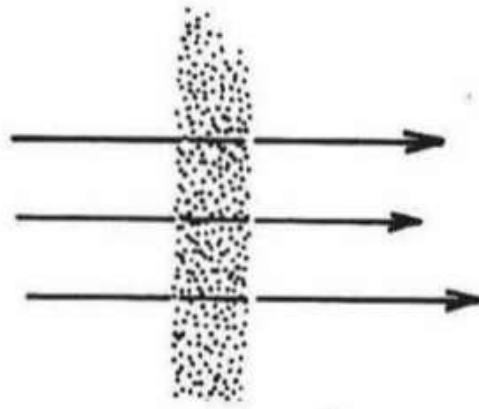


FIGURE 3.3: Light rays in uniform density medium.

When light rays pass through a medium with uniform density, parallel faces but in non-orthogonal configuration (Figure 3.4), their direction is altered entering in the medium but at the exit rays regain their original direction.

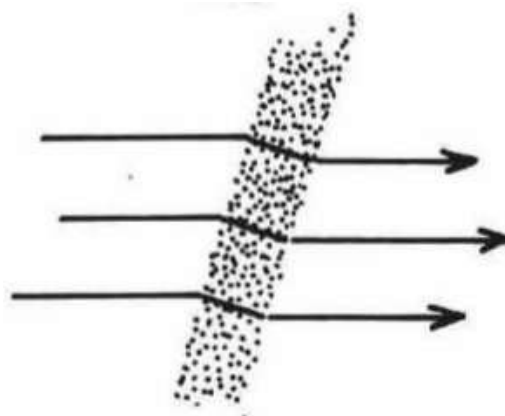


FIGURE 3.4: Light rays in medium with an angle.

The last configuration is showed in Figure 3.5: the medium has both non-parallel faces and heterogeneous density, the direction of the light rays change in medium and when they exit their configuration is not the same as in enter face.

Definitely, light propagates uniformly in homogenous media and so for all test methods a light source is required. An easy example is starlight: if earth's atmosphere was uniform starlight would reach us as parallel light rays but the atmosphere is not uniform. There are, for example, turbulences and thermal convections that change the atmospheric density: starlight bends and it means that a medium is characterized by a refractive index. Refractive index indicates its changing speed because the light slows upon when there is a interaction with media. The refractive index can be computed as:

$$n = \frac{c_0}{c} \quad (3.1)$$

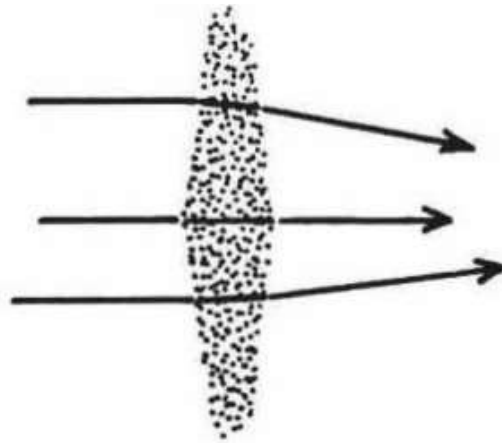


FIGURE 3.5: Light rays in heterogeneous medium.

where  $c$  is the light speed in the medium and  $c_0$  is the universal light speed in vacuum ( $c_0 = 3 \times 10^8$  m/s). For air and gases, there is a relationship between the refractive index and the gas density:

$k$  is the Gladstone-Dale constant that depends on  $\lambda$ , the light wavelength. For standard condition the value of  $k$  is 0,23 cm<sup>3</sup>/g [161]. From this formulation it is possible to understand that changing density of two orders it leads to a 3% change of  $n$ . A diagram of refracting light through a heterogeneous media is showed, in Figure 3.6, to explain a deconstruction of schlieren light refraction: a planar light wave is initially vertical but later, the light wave passes through a schlieren object and it becomes displaced.

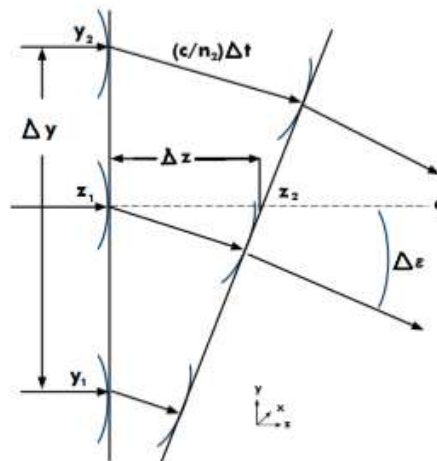


FIGURE 3.6: Diagram of light ray deflection in heterogeneous media [235].

It is necessary to assume a negative vertical refractive index gradient in  $y$  direction:

$$\frac{\partial n}{\partial y} < 0 \quad (3.2)$$

There is no refractive gradient in x or z directions.  $\Delta Z/\Delta t$  is the differential distance of the light covered in differential time,  $\Delta\varepsilon$  is the differential angle of refracted light. From Figure 3.6 expression of differential angle can be written:

$$\Delta\varepsilon = \frac{\frac{c}{n_2} - \frac{c}{n_1}}{\Delta y} \Delta t \quad (3.3)$$

the expression for differential time is:

$$\Delta t = \Delta z \frac{n}{c} \quad (3.4)$$

combining 3.3 and 3.4 by replacing  $c$  from 3.4 in 3.3 it is possible to find:

$$\Delta\varepsilon = \frac{n}{n_1 n_2} \frac{n_1 - n_2}{\Delta y} \Delta z \quad (3.5)$$

considering the limit in zero and simplifying  $\frac{n}{n_1 n_2}$  to  $\frac{1}{n}$  :

$$\frac{\partial\varepsilon}{\partial z} = \frac{1}{n} \frac{\delta n}{\delta y} \quad (3.6)$$

and defining:

$$\partial\varepsilon = \frac{\delta y}{\delta z} \quad (3.7)$$

it is obtained:

$$\frac{\partial^2 y}{\partial z^2} = \frac{1}{n} \frac{\delta n}{\delta y} \quad (3.8)$$

this last expression relates to the curvature of refracted ray to the magnitude of refracted index and therefore integrating 3.6 in the appropriate direction it is possible to find deviation angles (schlieren images):

$$\varepsilon_y = \frac{1}{n} \int \frac{\delta n}{\delta y} \delta z \quad (3.9)$$

It means that the gradient of refractive index causes rays deflection. Figure 3.7 shows light rays bended due to a gradient of refractive index on a two dimensional schlieren system.

The index gradients, that in previous figure is positive, can cover one, two or three dimensions. The angular deflection is larger with high pressure.

The simplest configuration of schlieren technique (Figure 3.8) called *Lens system* [187] includes a point light source, 2 lenses, a knife-edge and a screen.

The light source is used to illuminate uniformly the test area and the image is visualized on a screen or recorded on a camera. The first lens collimates the light into a parallel beam that crosses test section area. The light changes direction when it passes through area with different light refraction index that is due to different gas density or different gas composition. If an object blocks the beam, it will create a shadow that can be recorded photographically. For this purpose, a knife edge is then placed between the test area and

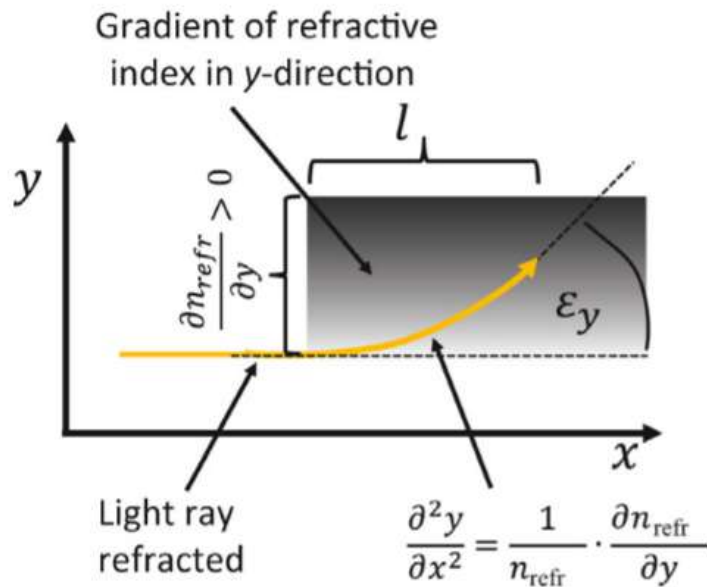


FIGURE 3.7: Geometric theory of light refraction of a two dimensional schlieren with a gradient of the index of refraction in y-direction [53].

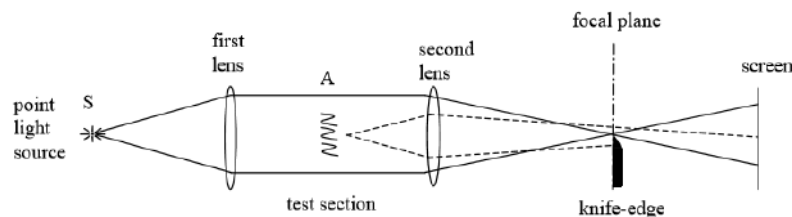


FIGURE 3.8: Simple schlieren system [161].

its image so that it blocks half of the image.

Precisely, in Figure 3.8,  $S$  is a point light source and is collimated by a first lens which focal point coincides with the location of the source. Then the parallel beam passes through a test section area and a second lens refocuses the beam to an image of the point source. From there the beam proceeds to a viewing screen where a real inverted image of the test section is formed [161]. It must be clarified that the second lens images the object  $A$  onto the screen with a magnification of  $-1$  if the distance between lens 2 and the object is two times the focal length. A magnification is with minus sign because as described above it is replaced with its original dimension but upside down [53]. Between a second lens and screen is added a knife-edge that is a razor blade to blocking the image of the source point.  $A$  is a schlieren object analysed, it is positioned in test section area and it bends light rays from their initial path. The second lens focuses the ray from each point in  $A$  to a corresponding point in the screen image [161]. The rays deflected upward brightens a point in the screen, but the rays deflected downward are blocked by knife-edge and the corresponding image on the screen is dark compared to

the bright background. The knife edge serves as a cut-off filter for intensity.

The simplicity of such *Lens system* offers a great advantage as there is no off-axis aberration, which is the biggest challenge in mirror systems. Despite this, the lenses in this type of schlieren system are required to be of very high quality, which leads to high cost and high maintenance level. Also, lenses are restricted in size: their diameters cannot be as large as parabolic mirrors, meaning that these systems cannot be used to observe a large region of interest. Due to its straight layout, the *lens system* is also longer in length (requiring more space for the total arrangement) [187].

The configuration shown in Figure 3.8 comprises lens instead a concave mirrors and it is possible to examine a relation: if  $p$  is the distance between the test area and the second mirror,  $q$  is the distance between the second mirror and the screen,  $f_2$  is the focus of the lens 2, the following relation must be satisfied.

$$\frac{1}{p} + \frac{1}{q} = \frac{1}{f_2} \quad (3.10)$$

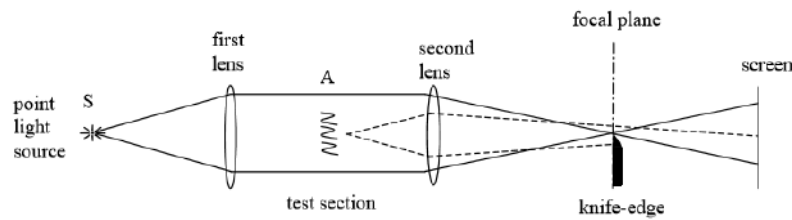


FIGURE 3.9: Schematic configuration of schlieren set-up [161].

Always considering Figure 3.9, a light source that generates a light beam of diameter  $a_s$  is kept at the focus of lens  $L1$ . The dotted line shows the path of the light beam in the presence of disturbance in the test region. The second lens  $L2$ , whose focus is the knife-edge collects the light beam and passes onto a screen. If no disturbance is present, the passage of the light beam is shown by solid lines reaching the focus of  $L2$ , which has a diameter  $a_0$  [32]. These two dimensions are related [277]:

$$\frac{a_0}{a_s} = \frac{f_2}{f_1} \quad (3.11)$$

where  $f_1$  and  $f_2$  are the focal lengths of lenses  $L1$  and  $L2$ , respectively.

When the size of test region is large, necessarily the light beam must have a large diameter. In this case the use of spherical mirror is preferable to the one of lenses which are fairly expensive [161]. Figure 3.10 shows the classical schlieren system, called Z-type system, using spherical mirrors.

Z-type is the most popular schlieren system setup in practice. This is because the system allows a larger test region without needing to increase the size of the mirrors. In this configuration, light generated from a light source focuses on a condenser lens and goes through a slit. It is then directed to a parabolic mirror and collimated, resulting in uniform propagation through the test region. The collimated light is incident on another parabolic mirror,

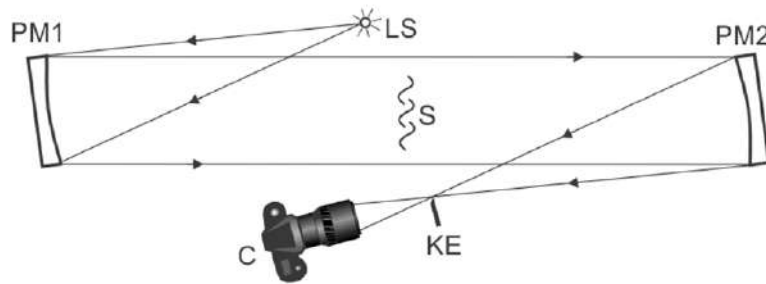


FIGURE 3.10: Typical schlieren apparatus: z-configuration.

which refocuses the light rays. The light passes through a cut-off (an edge or filter) and is refocused onto a screen or an image sensor of a camera. In general, light rays travel in a z-shaped, hence the title [187]. A minimum distance between the field mirrors of about  $2f$ , where  $f$  is the mirror focal length, is required to provide space for the test area [22].

Another important topic in the Z-type configuration is about aberrations as *coma* and *astigmatism*. Coma occurs when the direction of the light reflected from a mirror depends on the position of the point of reflection. This is a consequence of tilting the schlieren field mirrors of their optical axes [338]. The image of a point is focused at sequentially differing heights, producing a series of asymmetrical spot shapes of increasing size that result in a comet-like structure [187]. This aberration grows in proportion to the offset angle  $\theta_1$  (figure 64) but it is minimized by keeping  $\theta_1$  small. Fortunately, it is possible to cancel the effect of *coma* by tilting the mirrors at equal angles ( $\theta_1$  and  $\theta_2$ ) in opposite directions from the central optical axis, forming a "z" and using identical mirrors[338].

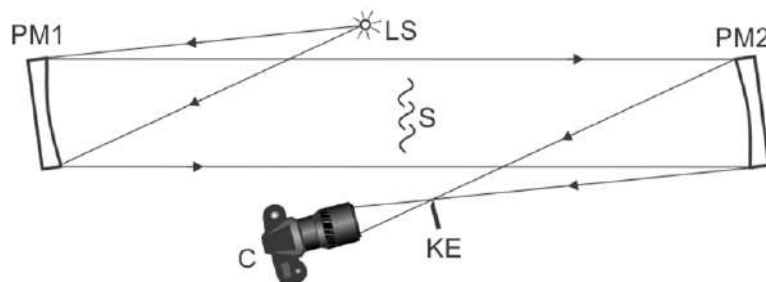


FIGURE 3.11: Geometric characteristics of z-type configuration

Unlike *coma*, *astigmatism* cannot be eliminated from the z-type schlieren or any off-axis mirror system. *Astigmatism* is the failure of focusing a point to a point, and the image is therefore not properly focused [28]. *Astigmatism* is shown to be proportional to the square power of the off-axis angle hence it can be reduced by reducing the size of the off-axis angle. The longer focal length obtainable with parabolic mirrors can also help reduce *astigmatism*[187].

Another schlieren configuration is *double-pass mirror system* (Figure 3.12).

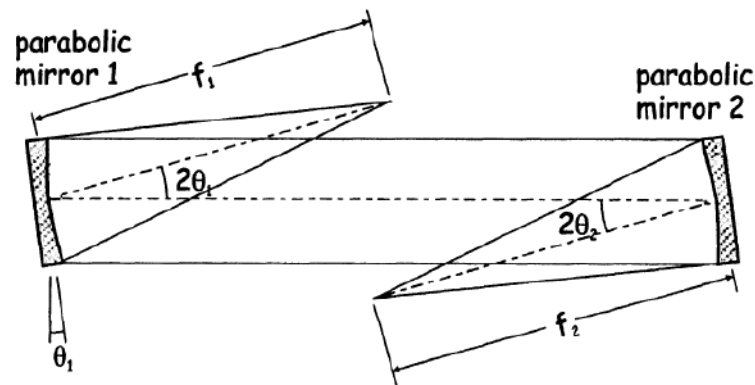


FIGURE 3.12: Configuration of double-pass mirror system [187]

The double-pass mirror system uses only one mirror, missing out on the advantages of collimating light rays. A single spherical field mirror with the light source on axis at the radius of curvature is used. Alternatively, a parabolic mirror with a corrector lens after the light source can be used. The schlieren object is positioned in front of the mirror. The principle is that, as the diverging light beam passes through the schlieren object, it hits the mirror and returns along a coincident path, forming an image. A reflecting knife-edge separates the returning rays from the source rays. These returning rays then carry the schlieren image to a camera. In this system, since the light passes through the schlieren object twice, the deflection of light rays occurs twice resulting in increased sensitivity. However, the double-pass setup requires a rather large, high-quality mirror which drastically increases the cost. Also, the light rays are not propagating parallel to each other and the schlieren object is close to the mirror, which is a disadvantage in some applications [187].

### 3.2.1 The razor-blade

The knife edge is a cut-off filter for intensity and the correct positioning of this will uniformly darken the image captured. In other words, if the razor blade was incorrectly positioned, it would be easily noticeable because of the partial darkening of the image and the apparent difference in brightness. The intensity of the light that arrives on image plane is a function of angular deflection of the light rays and this intensity is the fraction non-stopped by Schlieren aperture. It also depends on the geometrically shape of light source (Figure 3.13). The maximum intensity occurs when light image moves completely outside any aperture stop and the cone angle is large enough. It means that there is a minimum and maximum value of the deflection angle that can be measured as light intensity [33]. Some possible apertures can be used and if it is a circular geometry gives equal sensitive in x and y direction.

Figure 3.14 illustrates the difference of intensity of light with and without knife-edge.

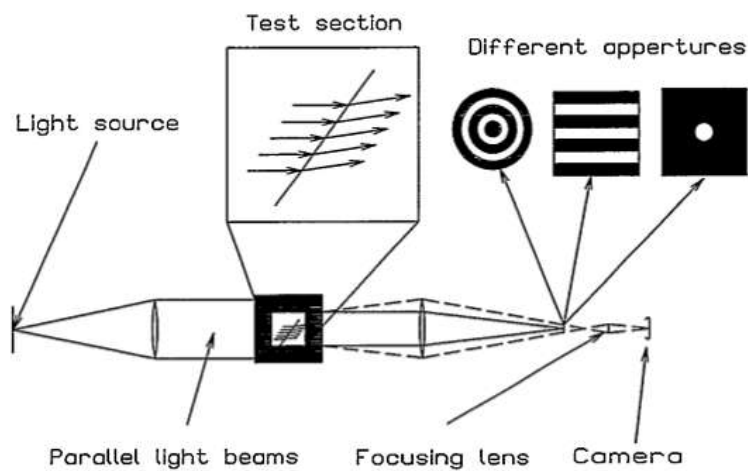


FIGURE 3.13: Schlieren system highlighting different apertures [187]

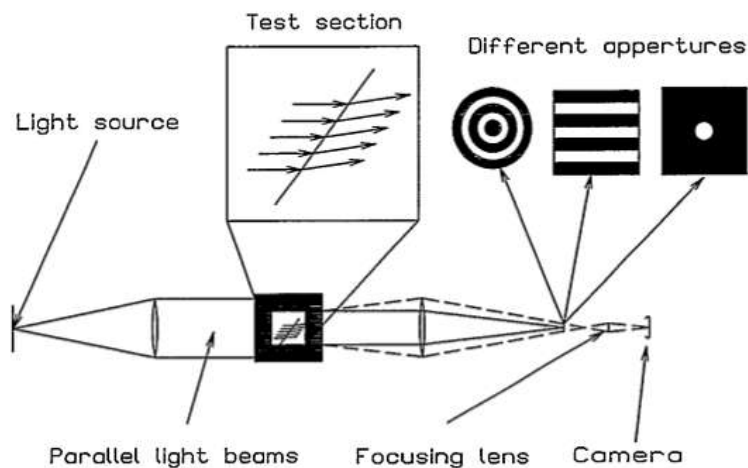


FIGURE 3.14: Sketch of the light paths in configuration with knife edge and without knife edge [187]

First configuration (top Figure 3.14) allows the light source to hit completely the screen, while the knife-edge in the second configuration (bottom Figure 3.14) blocks all rays and consequentially there is no intensity light on the screen. Some differences occur also when gradient of index changes (Figure 3.15).

First schlieren configuration in Figure 3.15 has a constant gradient, negative, of refraction index (the gradient is represented by the purple dashed line): light path is diverted, and, in this case, the light rays pass over the razor blade, up by  $\Delta y$  quantity, arriving completely on screen that is all illuminated. Second sketch shows the change of the index and the light passes over the knife edge (if gradient is negative) or the rays hit the razor blade and they are blocked (if gradient is positive) with no light onto the screen.

The adjustment of the knife-edge plays a significant role in the quality of

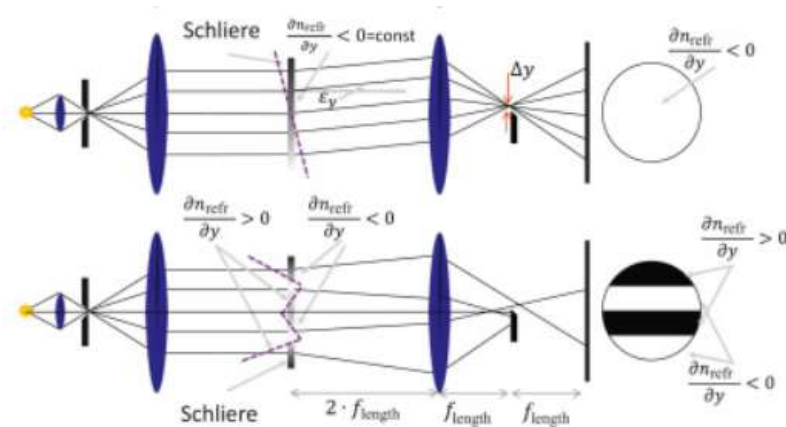


FIGURE 3.15: Sketch of schlieren with different index gradient

the schlieren image recorded: in Figure 3.15 the distribution of light intensity over the screen is shown for various positions of the knife-edge. Figure 3.16 (a) and (c) respectively show non-uniform distribution of light intensity when the knife-edge is either too close or too far away from the second concave mirror. Figure 3.16 (b) shows light intensity distribution for a correctly placed knife-edge [277].

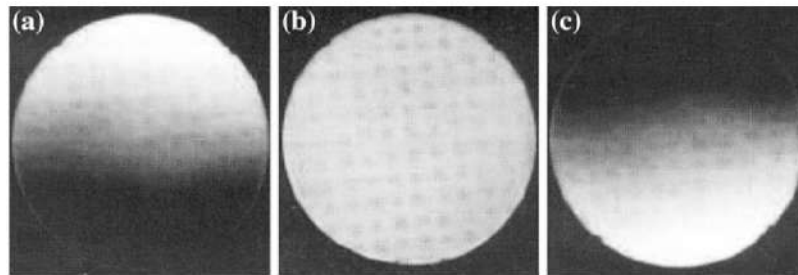


FIGURE 3.16: Effect of knife-edge movement on the schlieren image for a horizontal knife-edge cutting off the light beam from below. (a) Knife-edge is very close to the second concave mirror; (b) Knife-edge is correctly placed. (c) Knife-edge is beyond the focal plane of the second concave mirror

An important step in the alignment procedure is to adjust the percent cut off by the knife edge in order to obtain the desired sensitivity. If the cut off is small, a large amount of light passes over to the screen and results in poor contrast of the schlieren images along with the possibility of camera saturation. If the cut off is large, high images are possible, but the measurement may result in the loss of information in regions of low density gradient. If the sensitivity of the schlieren system is deliberately reduced, either by a lower intensity cut off by the knife-edge, or by whit a graded (grey-scale) filter, vibrations errors would be truly minimal [277].

### 3.3 Mie Scattering imaging

A scattering phenomenon is based on a wave that runs into a medium. Inside the medium there are charges that oscillate in response to the collision, part of the wave power is lost as a result of the Joules work into the medium and in order to overcome the force resistance. Another part of wave power is lost into a phenomenon called Scattering. Scattering of electromagnetic waves is due to an interaction between the incident electromagnetic wave and the atomic structure of scattering object: the wave is redirected when the light radiation hits a heterogeneous medium. The constituent molecules of matter have electric bound charges that when are perturbed from light radiation moving from their respective position. As a result, an unbalance and consequently polarization of particles occurs. This behaviour induces electric dipole moment and fluctuation of charges. The frequency of this oscillation is same as the frequency of incident electromagnetic waves. The oscillation of charges generates secondary electromagnetic waves that also radiate energy in the form of light radiation in different directions.

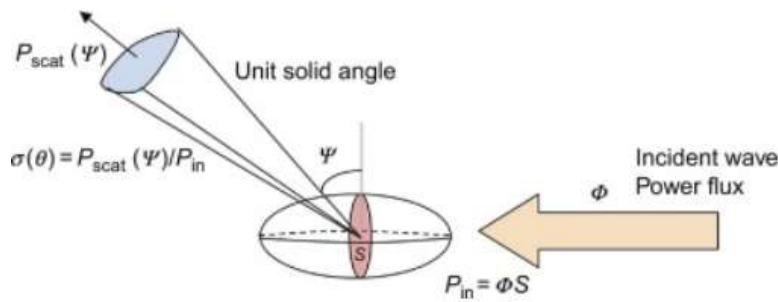


FIGURE 3.17: Scattering cross section [2].

In the Figure 3.17 a scattering cross section  $\sigma_s(\theta)$  for a electromagnetic wave is showed; particle scattered forms angle  $\theta$  with the direction of propagation and therefore angle  $\Psi$  with electric field of the incident wave. Scattering cross section is the ratio of the time-averaged scattered power per unit solid angle in that direction, per unit incident power, evaluated at the location of the scattering object. Thus, it is the fraction of the total power incident that is re-radiated by the scattering object in that particular direction per unit solid angle. To have a total scattering cross section is necessary integrate the directional scattering cross sectional area over all solid angles in all possible directions. The amount and nature of scattering depends on the relative value of the wave length and on the diameter of the scattering particle. Considering this last feature a differentiate in scattering phenomenon can be done: there may be the Rayleigh scattering or the Mie scattering. The Rayleigh scattering occurs when the dimension of the scattering particles is smaller than the wave length of the incident electromagnetic wave and there is no appreciable change in the phase of the electric field. A required condition for the Rayleigh scattering is:

$$\frac{2\pi}{\Lambda} \cdot d \ll 1 \quad (3.12)$$

where  $d$  is the diameter of spherical particles and  $\Lambda$  is the length wave. Physically it means that the time for penetration of the electric field is much less than the period of oscillation of the electromagnetic wave. The power radiate by the particle due to the scattering is [2]:

$$\sigma_{\text{scat}} = \frac{2}{3} \pi^5 \frac{d^6}{\lambda^4} \left( \frac{n^2 - 1}{n^2 + 2} \right)^2 \quad (3.13)$$

and it depends on the refractive index  $n$  and on the power re-radiated is in the same direction of the primary wave. Moreover, it is proportional to the sixth power of particle size and it is inversely proportional to the fourth power of wavelength  $\Lambda$ . This means that high frequencies are more scattered compared to lower ones and it is for this reason that scatter of sunlight results in blue colour on sky. The Mie scattering results from a solution to the Maxwell's equations and the phase of the incident signal can change considerably with the dimension of the scattering particle. Therefore, the condition (3.12) that is necessary for applicate the Rayleigh scattering must not be satisfied in this case. The scattering signal intensity is influenced by the ratio of the refraction index between the particle and the ambient medium, by the size, the shape and orientation of the particle. The light intensity in Mie scattering is higher than intensity in Rayleigh scattering. For all these characteristics, the Mie Scattering model is able to describe the light dispersion due to liquid particles. Therefore, through the interaction between light and particles with different dimensions using the Mie scattering is possible to visualize the liquid phase into a spray when it is illuminated by a continuous light.

## Chapter 4

# CFD Techniques for Spray Characterization

### 4.1 Governing Equation of a Mono-Phase Fluid Flow

Mono-phase fluid flows can be modelled mathematically using conservation equations. They are also called governing equations and regards mass, momentum and energy:

$$\frac{\partial \rho}{\partial t} + \nabla \cdot (\mathbf{u}\rho) = 0 \quad (4.1)$$

$$\frac{\partial(\rho\mathbf{u})}{\partial t} + \nabla \cdot [\mathbf{u}(\rho\mathbf{u}) + p] = \nabla \cdot \sigma \quad (4.2)$$

$$\frac{\partial(\rho e)}{\partial t} + \nabla \cdot [\mathbf{u}(\rho e) + p] = \nabla \cdot (\sigma \cdot \mathbf{u}) + \nabla \cdot \mathbf{q} \quad (4.3)$$

where:

- $p$  is pressure which is assumed to be coupled to density and temperature via the perfect gas state equation:

$$\frac{p}{\rho} = RT \quad (4.4)$$

- $e$  is the total energy given by the sum of internal  $U_i$  and kinetic energy :

$$e = U_i + \frac{1}{2}\|\mathbf{u}^2\|$$

with  $U_i$  expressed as:

$$U_i = c_v T$$

$c_v$  represents constant volume specific heat and T is temperature;

- $\sigma$  is the stress tensor that for a newtonian fluid is equal to:

$$\begin{aligned}\sigma &= \mu \left[ \nabla \mathbf{u} + (\nabla \mathbf{u})^T \right] - \left( \frac{2}{3} \mu \nabla \cdot \mathbf{u} \right) \mathbf{I} = \\ &= 2\mu \operatorname{dev}(\mathbf{D})\end{aligned}$$

with  $\mu$  dynamic viscosity computed by Sutherland's law as a function of temperature:

$$\mu = \frac{A_s \sqrt{T}}{1 + T_s/T} \quad (4.5)$$

$A_s$  and  $T_s$  are specific constants of the single specie.

$\mathbf{D}$  strain tensor:

$$\mathbf{D} = \frac{1}{2} \left[ \nabla \mathbf{u} + (\nabla \mathbf{u})^T \right]$$

- $\mathbf{q}$  is the heat flux vector computed as:

$$\mathbf{q} = -\nabla T$$

where  $T$  is the fluid temperature and  $\lambda$  is the heat conduction coefficient computed as:

$$\lambda = \frac{\mu c_p}{Pr}$$

with  $c_p$  being the constant pressure specific heat and  $Pr$  is the Prandtl number.

$c_p$  is computed as function of temperature from JANAF tables [59] with the following relation:

$$c_p = R \left( \left( \left( \left( a_4 T + a_3 \right) T + a_2 \right) T + a_1 \right) T + a_0 \right) \quad (4.6)$$

This function is valid between a lower and upper limit at temperature  $T_l$  and  $T_h$ , respectively. Two sets of coefficients  $a_0 \dots a_4$  are specified, the first set for temperatures above a common temperature  $T_c$  (and below  $T_h$ ), and the second for temperatures below  $T_c$  (and above  $T_l$ ).

In order to study the mixing of multiple species consequent to the injection process the set of governing equations (4.1-4.4) is completed by a transport equation for each specie:

$$\frac{\partial (\rho Y_i)}{\partial t} + \nabla \cdot \rho \mathbf{u} Y_i = \nabla \cdot (\rho D_i \nabla Y_i) \quad (4.7)$$

where, for the  $i$ -species,  $Y_i$  is concentration, and  $D_i$  is the diffusivity equal to:

$$D_i = \frac{\mu}{\rho Sc}$$

The above-mentioned governing equations of fluid flows (i.e. Equations 4.1,4.2,4.3) are in differential forms and are derived based on an infinitesimal small fluid element in the flow, with a differential volume. In fact, the fluid element (may be fixed in space or moving) is infinitesimal in the same sense as differential calculus; however, it is large enough to be viewed as a continuous medium (containing a huge number of molecules). It is worth mentioning that, the partial differential equations obtained directly from the assumption of fluid element fixed in space are the conservation form of the equations. On the other hand, particular partial differential equations which can be derived from the moving fluid element assumption are called the non-conservation form of the equations. When the conservation form is used, the computed flow-field is generally smooth and stable.

In a turbulent flow (like fuel sprays in ICE) governing equations are valid only if the spatial and temporal resolutions are fine enough to capture all scales of the flow. Unfortunately, at the present time conducting, such Direct numerical simulation (DNS) on complex fluid flows and specifically on complex domains is not computationally practical due to the technological restriction (high computational costs). Therefore, instead of solving full length of turbulent scales, various modelling techniques have to be used. In the next section of this chapter the ones used in this work are presented.

## 4.2 Turbulence Modelling

### 4.2.1 Physics of Turbulence

The observation of turbulent flows is a daily experience that we identify with the non-stationary, irregular and apparently chaotic motion of a fluid. The volutes formed by the smoke of a cigarette in its upward motion, the mixing of milk and coffee inside a cup or the irregular wake of a river downstream of a bridge pylon are just a few examples among an innumerable quantity ". The concept of turbulence is clear enough for everyone, the effect that turbulence has on the global characteristics of a flow is not so clear. Consider, for example, lighting a cigarette inside a room; It is common experience that after a few seconds the presence of smoke can be felt throughout the room, indicating that the smoke has "spread" everywhere. A naive interpretation could lead us to think that diffusion is the cause of this phenomenon but an estimate of the time scales unequivocally excludes this factor. However, it could be observed that since cigarette smoke is warmer than the surrounding air, natural convection plays an important role in the diffusion of the smoke. A dimensional estimate, however, provides speeds of the order of  $\text{cm s}^{-1}$  which, combined with the observation that the hot smoke rises upwards and does not propagate horizontally, still leads to times of hours in sharp contrast, with daily experience. The reason for the discrepancy between practical experience and the two quantitative estimates is that in both cases, the presence of turbulence was neglected. The velocity fluctuations induced in the fluid by turbulent motion, in fact, have the ability to transport a quantity (scalar or

vector) very rapidly even in the absence of average motion. This leads to assimilate the effect of turbulence with a notable increase in the diffusion of the fluid which is also two or three orders of magnitude greater than the value molecular. A more careful study of turbulent phenomena will however show that this is only the most visible effect of a very complex dynamics involving mainly the non linear terms of the Navier - Stokes equations.

Laboratory experiments on the flow inside circular cross-section tubes were carried out for the first time in a systematic way by O. Reynolds in 1883 who observed that by combining the mean velocity of the flow  $U$ , the diameter of the duct and the kinematic viscosity of the fluid  $\mu$  in the factor  $Ud/\mu$  (which later took the name of Reynolds number) it was possible to describe the flow dynamics in three different categories. For  $Re \leq 2100$  the flow remained stationary and behaved as if rectilinear sheets (hence the term laminar flow) were sliding on each other interacting only through tangential forces. This behaviour was noted by observing the evolution of a "streak-line" of ink released from a fixed position inside the duct; the dye line, in fact, remained straight, spreading very weakly as it moved away from the source. For  $2100 \leq Re \leq 4000$  the dye line lost its stationarity and propagated along a wavy trajectory with time dependent characteristics. In this transitional regime, however, the trace of dye preserved its spatial coherence by remaining confined to a thin line. On the contrary, for  $Re \geq 4000$ , after an initial stroke with oscillations of increasing amplitude, the ink trace was vigorously diffused throughout the cross section of the tube until it was evenly distributed throughout the flow. This latter regime is called turbulent and is characterized by a disordered, completely three-dimensional and non-stationary motion and by speed fluctuations with non-deterministic characteristics. These eddies breed new instabilities and hence smaller eddies. The process continues until eddies become sufficiently small which means fluctuating velocity gradient are sufficiently large, and viscous effects dissipate turbulence energy as heat. For instance within a mixing process the reduction of the velocity gradients due to the action of viscosity reduces the kinetic energy of the flow; in other words, mixing acts as a dissipative process that converts the energy irreversibly into internal energy of the fluid (heat). This process was first suggested by Richardson [307] and is called the turbulence energy cascade [294]. The first concept of the energy cascade is that the turbulence can be composed of eddies of different sizes. As explained by Richardson [307], breaking up of the large eddies (which are unstable) transfers the energy to rather smaller eddies. This break up process continues until the Reynolds number is sufficiently small that the eddy motion becomes stable, and the role of the molecular viscosity in dissipating the energy becomes effective.

### 4.2.2 Turbulence Numerical Simulation

The mechanism common to all turbulence phenomena is the cascade of energy from the largest structures of the body size that generates the turbulence up to the finest structures of the order of magnitude of the Kolmogorov scale

$\eta$ . The transfer of energy from large to small scales takes place through the non-linear and pressure terms with an essentially non-viscous process which therefore does not dissipate energy. Most of the flow energy is in the large scales, while the dissipation occurs at the small scales and the former are in constant equilibrium with the latter across the range - inertial [374]. Unfortunately, for flows with a high Reynolds number, the difference in size existing between the largest and smallest scales becomes huge and at some point in the cascade it is necessary to make a cut beyond which to use a model; the difference existing between the various calculation techniques consists precisely in the position of the 'cut' in the cascade or, in other words, in which motion scales one is willing to calculate and which ones to model.

### DNS Simulation

The most obvious technique is to apply no cut to the scales of motion and simulate them all, from the LG dimension of the body, around or within, the flow occurs up to the Kolmogorov scale.

It can be demonstrated that for performing a DNS of a cube of volume  $L^3$  are necessary  $N_{tot} = N \approx Re^{9/4}$  calculation points. Although this estimate grows rapidly enough with the Reynolds number advising to avoid this approach already for moderate values it worths underlying that it is an optimistic estimation. In fact, since the integration of the equations must be performed with a time step  $\Delta t$  discrete, this must be commensurate with the dynamics of the flow. As a rule of thumb we can state that, in the current state of things, the direct simulation of a flow at a Reynolds number of a few thousand already constitutes a challenge for modern supercomputers even if it is limited to a simplified geometry. If we then add the geometric complexities of industrial applications, and the inhomogeneities of the flow, we conclude that the direct simulation of turbulence, i.e. the solution of the Navier Stokes equations without any model, does not constitute a possibility of investigation of practical problems even in the coming decades. This continues to be true even assuming a growth in computing power similar to the past, ie with a doubling of the processing speed every 18 months, as has occurred in the last three decades (Moore's law).

### Reynolds averaged Navier Stokes (RANS) Modelling

RANS solves only for the mean flow quantities modelling all the details of turbulence. It is based on the statistical Reynolds decomposition which indicates that an instantaneous quantity  $\phi(x, t)$  certain point in a fluid domain can be defined as the sum of a mean averaged value and a fluctuation about that value as:

$$\phi(x, t) = \overline{\phi(x, t)} + \phi'(x, t) \quad (4.8)$$

where  $\overline{\phi(x, t)}$  and  $\phi'(x, t)$  denote averaged and fluctuation components of quantity  $\phi(x, t)$ , respectively. RANS formulation was originally developed for incompressible flows by replacing velocity and pressure terms of the Navier-Stokes equations with their Reynolds decompositions. Infact, for the

$i$ -th components of the velocity vector and for pressure,  $u = \bar{u} + u'$  and  $p = \bar{p} + p'$  are substituted in to the Navier-Stokes equations, respectively. The RANS formulation of the incompressible Navier-Stokes equations are well documented and are not included in the current thesis and the reader is referred to literature publications for further information [351, 374]. However, the current study mainly focuses on compressible flows in which density may vary significantly due to pressure variations hence it enters into the averaged form of Navier-Stokes equations. For the fluid flows with variable density, [112] developed statistical equations by applying a mass-weighted average method. This helped avoid the introduction of a number of extra terms in the governing equations. Favre separates a transport quantity  $n$  into a mass-averaged part (Favre-averaged)  $\tilde{n}$  and a fluctuation  $n''$  such that:

$$n \equiv \tilde{n} + n'' \text{ with } \bar{\rho}\tilde{n} \equiv \bar{\rho}\bar{n} \text{ and } \overline{\rho n''} \equiv 0 \quad (4.9)$$

where double prime denotes the fluctuating part with respect to the Favre averaging and over bar represents the Reynolds averaging. By substituting the Reynolds decomposition of density and pressure and the Favre decomposition of velocity and internal energy in to the governing equations (Equations 4.1, 4.2 and 4.3) the time averaged governing equations for density, momentum and energy are obtained as presented in Equations 4.10-4.12, respectively.

$$\frac{\partial \bar{\rho}}{\partial t} + \frac{\partial}{\partial x_i} (\bar{\rho}\tilde{u}_i) = 0 \quad (4.10)$$

$$\frac{\partial}{\partial t} (\bar{\rho}\tilde{u}_i) + \frac{\partial}{\partial x_j} (\bar{\rho}\tilde{u}_i\tilde{u}_j) + \frac{\partial \bar{p}}{\partial x_i} - \frac{\partial \bar{\sigma}_{ij}}{\partial x_j} + \overline{\rho u_i'' u_j''} = 0 \quad (4.11)$$

$$\frac{\partial}{\partial t} (\bar{\rho}\hat{E}) + \frac{\partial}{\partial x_j} (\bar{\rho}\tilde{u}_j\hat{H}) - \frac{\partial}{\partial x_j} (\tilde{u}_i\bar{\sigma}_{ij} - \tilde{u}_i\overline{\rho u_i'' u_j''}) + \frac{\partial}{\partial x_j} \bar{q}_j = 0 \quad (4.12)$$

The "hat" symbol in E and H in equation 4.12 indicates that the quantity is based on filtered variables as:

$$\hat{E} = \tilde{e} + \frac{1}{2}\tilde{u}_i\tilde{u}_i \quad (4.13)$$

$$A = \tilde{e} + \frac{1}{2}\tilde{u}_i\tilde{u}_i + \frac{\bar{p}}{\bar{\rho}} \quad (4.14)$$

The averaged equation of state for a calorically perfect gas may also be written as:

Term  $\overline{\rho u_i'' u_j''}$  is called Reynolds stress tensor. It should be noted that it is not actually a true stress in the conventional sense of the word and just represents the mean momentum fluxes induced by the turbulence.

Capturing the effects of these fluxes is achievable by pretending  $\overline{\rho u_i'' u_j''}$  is a stress. Trying to get an equation for  $\overline{\rho u_i'' u_j''}$  results in creating a new term,  $\overline{\rho u_i'' u_j'' u_k''}$  and a further unknown variable,  $u_k''$ . Attempting to find an

equation for the latter third-order correlation will result in a fourth-order correlation. The key point is that there are always more unknowns than equations in modelling turbulence with statistical description which means that the system of equations is not closed. This is known as the "closure problem of turbulence" which is a common characteristic of non-linear dynamical systems. In order to close the system, some additional information must be introduced. For almost a century, engineers have plugged this gap using the so-called eddy-viscosity hypothesis and this still form the backbone of engineering turbulence [294]. In fact, the Reynolds stress tensor can be estimated using the Boussinesq approximation for compressible flows as:

$$-\overline{\rho u_i'' u_j''} = \mu_t \left[ \left( \frac{\partial \tilde{u}_i}{\partial x_j} + \frac{\partial \tilde{u}_j}{\partial x_i} \right) - \frac{2}{3} \frac{\partial \tilde{u}_k}{\partial x_k} \delta_{ij} \right] - \frac{2}{3} \bar{\rho} k \delta_{ij} \quad (4.15)$$

where  $\mu_t$  is called turbulent viscosity and  $k$  is the turbulent kinetic energy defined as:

$$k = \frac{1}{2} \frac{\overline{\rho u_i'' u_i''}}{\bar{\rho}} \quad (4.16)$$

A suitable expression is required for  $\mu_t$  in order to close the set of the averaged governing equations. Various models were proposed to estimate  $\mu_t$ . Prandtl suggested that the turbulent viscosity might be considered to be directly proportional to a turbulent velocity scale and a turbulent length scale that is called the mixing length. However, there are two major drawbacks for this definition for  $\mu_t$ . First is that this definition is highly flow dependent and second is that it is not capable of estimating  $\mu_t$  in the absence of mean strain rate [374]. Later, in order to obtain a more realistic definition for the turbulent viscosity it was suggested that  $\mu_t$  could be considered proportional to the square root of  $k$  and a turbulent length scale. Then, in order to obtain  $k$  an additional transport equation is coupled to the aforementioned governing equations in order to create a determined set of equations hence this methodology is typically called "one-equation" eddy viscosity model. A drawback of this model is that the mixing length needs to be estimated using empirical assumptions that makes its application limited particularly for complex flows [294]. Therefore, "two-equation" models were suggested that a second transport equation is incorporated in order to calculate the aforementioned turbulent length scale. The choice of variable for the second transport equation is not restricted, however, the most validated models used either dissipation rate  $\epsilon$  or  $\omega = \epsilon/k$ , the dissipation rate per unit turbulence kinetic energy. In case of a two equation model based on the dissipation rate the turbulent viscosity is defined as:

$$\mu_t = C_\mu \frac{\rho k^2}{\epsilon} \quad (4.17)$$

where  $C_\mu$  the closure coefficient and is typically kept constant. One of the most famous two-equation eddy viscosity models, also used in this work was proposed by Launder and Spalding (1974) and is called the "Standard

k- $\epsilon$ ".

### Large eddy simulation (LES) Modelling

The concept behind the LES approach is to model the smaller scales, which are universal and not affected by the flow geometry, while explicitly solving the larger ones. This is performed by mathematically filtering the governing equations and introducing the so called Sub-Grid Stress (SGS) tensor ( $\tau_{sgs}$ ) [294].

Typically the filtering is performed adopting the low-pass filter introduced by Leonard (1974):

$$\overline{\mathbf{U}(\mathbf{x}, \bar{t})} = \int_D G(\mathbf{r}, \mathbf{x}, \Delta) \mathbf{U}(\mathbf{x} - \mathbf{r}, t) d\mathbf{r} \quad (4.18)$$

where the integration is over entire flow domain  $D$ , and  $G$  is the filter function (with filter width of  $\Delta$ ) which is typically associated with the grid spatial resolution (cube root) and satisfies the normalization condition as:

$$\int G(\mathbf{r}, \mathbf{x}) d\mathbf{r} = \mathbf{1} \quad (4.19)$$

Using the Favre averaging and applying the LES filtering to the Navier-Stokes equations results in formation of residual-stress tensor due to the existence of non-linear terms (Pope, 2000). The Sub-Grid Stress (SGS) tensor is defined as:

$$\tau_{SGS} = \bar{\rho} (u_i \tilde{u}_j - \tilde{u}_i \tilde{u}_j) \quad (4.20)$$

where  $\bar{\rho}$  denotes the filtered density. The deviatoric part of the Sub-Grid Stress (SGS) tensor is defined as:

$$\tau_{SGS}^D = \tau_{SGS} - \frac{2}{3} k_r \delta_{ij} \quad (4.21)$$

where  $k_r$  is the residual kinetic energy defined as

$$k_r \equiv \frac{1}{2} \tau_{ii}^R \quad (4.22)$$

In order to form a determined set of governing equations a Boussinesq type hypothesis may be used in order to model the deviatoric part of the residual stress tensor as:

$$\tau_{SGS}^D = -2\bar{\rho} v_{sgs} \left( \dot{S}_{ij} - \frac{1}{3} \delta_{ij} \dot{S}_{kk} \right) \quad (4.23)$$

where  $v_{sgs}$  is the sub-grid kinematic viscosity.

The SGS term modelling involves an eddy viscosity approximation. Smagorinsky [343] was the first to suggest an expression for  $v_{sgs}$  as:

$$v_{SGS} = C_s^2 \Delta^2 \sqrt{2S_{ij}S_{ij}} \quad (4.24)$$

where  $C_s^2$  is called the Smagorinsky constant and is calculated using the local equilibrium analysis and a Kolmogorov spectrum as  $C_s = \frac{1}{\pi} (3K_0/2)^{-3} / 4$ , where  $K_0$  typically equal to 1.4 which lead to a Smagorinsky constant of  $\sim 0.1$  be noted that  $K_0$  is flow dependant (a function of Reynolds num parameters) and can be interpreted as the ratio of the mixing len scale to the filter cut-off length  $\Delta = (\Delta_x \Delta_y \Delta_z)^{1/3}$  (Pope, 20 constant is normally ranged between 0.1 and 0.2 .

In this work a one-equation eddy viscosity model for compressible flows was adopted [147, 413]. This kind of approach, which is different from zero equations models, uses a transport equation to compute the local SGS kinetic energy  $k_{sgs}$ . Then, the sub grid scale eddy viscosity  $\nu_{sgs}$  is calculated using the  $k_{sgs}$  field and the filter dimension  $\Delta$  (usually evaluated from the grid size) according to the following relation:

$$\nu_{sgs} = C_k \Delta \sqrt{k_{sgs}} \quad (4.25)$$

where  $C_k$  is a model constant whose default value is 0.094.

Finally, using this parameter, an effective viscosity ( $\mu_{eff}$ ) is obtained and used for the solution of the governing equations (4.1-4.3) [134].

### 4.3 The Finite Volume Method

In order to solve the partial differential equations governing fluid flows they should be discretized on the computational domain. Discretization converts the partial equations into sets of solvable linear equations. Various discretization methods are available but Finite Volume (FV) method is the most practical and common approach for CFD applications [374].

All governing equations of fluid dynamics can be written in the form of general transport equation which for a generic property  $\phi = \phi(\mathbf{x}, t)$  considered continuous in space, given as:

$$\frac{\partial \phi}{\partial t} + \nabla \cdot (\mathbf{U}\phi) - \nabla \cdot (\Gamma_\phi \nabla \phi) = S_\phi(\phi) \quad (4.26)$$

where  $\partial \phi / \partial t$  is the unsteady term,  $\nabla \cdot (\mathbf{U}\phi)$  is the convection term,  $\nabla \cdot (\Gamma_\phi \nabla \phi)$  is the diffusion term,  $S_\phi(\phi)$  is the source term and  $\Gamma_\phi$  is the diffusivity. Diffusion term includes the second derivative of  $\phi$  therefore Equation 4.26 is a second-order partial differential equation. For accuracy it is necessary to have an equal or higher level of discretization than the order of equation that is being discretized. The FV method requires the integral form of Equation 4.26 is satisfied over the control volume  $V_P$  around point  $P$ . The integral form of Equation 4.26 can be derived as [160].

$$\begin{aligned} \int_t^{t+\Delta t} \left[ \frac{\partial}{\partial t} \int_{V_P} \phi dV + \int_{V_P} \nabla \cdot (\mathbf{U}\phi) dV - \int_{V_P} \nabla \cdot (\Gamma_\phi \nabla \phi) dV \right] dt \\ = \int_t^{t+\Delta t} \left( \int_{V_P} S_\phi(\phi) dV \right) dt \end{aligned} \quad (4.27)$$

Assuming the control volume is bounded by a series of flat surfaces a second-order accurate discretised form of the general form of Gauss's divergence theorem,  $\int_V \nabla \cdot a dV = \int_S a \cdot dS$ , can be formulated as:

$$(\nabla \cdot a)V_P = \sum_f Sa_f = \sum_{\text{owner}} Sa_f + \sum_{\text{Neighbour}} Sa_f \quad (4.28)$$

The subscript  $f$  implies the value of the variable  $a$  in the middle of the face and  $S$  is the outward-pointing face area vector. The face area vector  $S$  points outward from  $P$  only if  $f$  is owned by  $P$ . This forms the idea of 'owner' and 'neighbour' cells as stated in Equation 4.28 [160]. FV discretization of each term of Equation 4.27 are typically obtained as follows.

### 4.3.1 Convection Term Discretization

The discretized form of the convection term is obtained applying Equation 4.28 into the transport equation 4.27:

$$\int_{V_P} \nabla \cdot (\mathbf{U}\phi) dV \approx \sum_f S \cdot (\mathbf{U}\phi)_f = \sum_f S \cdot (\mathbf{U})_f \phi_f = \sum_f F_f \phi_f \quad (4.29)$$

where  $F$  represents the volumetric flux through the face  $f$ . In order to evaluate Equation 4.29 the volumetric flux  $F_f$  and the face value of  $\phi_f$  are required to be obtained by interpolating the values of  $\mathbf{U}$  and  $\phi$  at the centroids of neighbouring control volumes. The interpolation employed depends on the convection discretization scheme. There are several convection differencing schemes available which can be summarized as follows:

- Central Differencing (CD) is a second order accurate linear interpolation scheme. It assumes that the linear variation of  $\phi$  between the centroids of  $P$  and  $N$  is calculated as

$$\phi_f = w_f \phi_P + (1 - w_f) \phi_N$$

where the weighting factor is  $w_f = |S \cdot \mathbf{d}_{fN}| / |S \cdot \mathbf{d}_{PN}|$  and  $\mathbf{d}$  represents the vector connecting the centroids of two control volumes. It was noted that central differencing causes unphysical oscillations when convection is dominated hence violating the boundedness of the solution [374]

- Upwind Differencing (UD) was developed to overcome the problem of oscillatory solutions and make the convection term unconditionally positive (Jasak, 1996). The face value of  $\phi$  is calculated according to the direction of the flow. This discretisation practice first-order accurate and it requires high grid resolution to achieve accurate solutions.
- Blended (Gamma) Differencing was introduced as a linear combination of the central differencing and upwind differencing to preserve both boundedness and accuracy of the solution. Though none of these is

guaranteed because the behaviour of the scheme depends on the a priori definition of the blending factor

- Flux-Limited Schemes is a typically second-order accurate practice that developed based on a nonlinear combination of the first-order 'diffusive' bounded scheme (UD) and a 'limited' higher order unbounded scheme. The flux-limiters, that are designed to provide boundedness in the solution, must satisfy particular boundedness criteria with the most important one is the Total Variation Diminishing (TVD) criterion [374]. In order to comply with the TVD condition the flux-limiter should lie in the Sweby's diagram. Various flux-limiters of this type were developed including van Leer [358], Monotonic Upstream-Centred Scheme for Conservation Laws (MUSCL) limiter (van Leer, 1979) and Superbee limiter (Arora and Roe, 1997). Various other flux-limiter methodologies are also available which can be found in literature [160, 306, 374].
- Central Flux-Splitting Schemes such as central scheme of Kurganov and Tadmor (2001) are second order accurate non-oscillatory techniques in which the face interpolation method is split into two directions, one inward and one outward of the face. A TVD-based scheme may be used to evaluate each component of the associated flux.
- Advection Upstream Splitting Method (AUSM) is considered as a second order accurate technique developed based on the UD concept. AUSM uses a flux splitting principle similar to van Leer; specifically, AUSM splits the inviscid fluxes into two physically distinct parts *i.e* convective (associated with the flow speed) and pressure (associated with the acoustic speed). AUSM is relatively accurate in modelling flows with embedded shock wave and/or contact discontinuity. Various types of this scheme *i.e.* AUSM<sup>+</sup> and AUSM<sup>+</sup>-up were also developed [222]. The latter one is the most advanced type with the ability of modelling fluid flows with arbitrary velocity range.

### 4.3.2 Diffusion Term Discretization

The diffusion term is discretized in a similar way to the convection term. In fact, using the assumption of linear variation of  $\phi$  and applying Equation 4.28 gives discretised version of the diffusion term as:

$$\int_{V_p} \nabla \cdot (\Gamma_\phi \phi) dV \approx \sum_f S \cdot (\Gamma_\phi \phi)_f = \sum_f (\Gamma_\phi)_f S \cdot (\nabla \phi)_f \quad (4.30)$$

where  $\Gamma_\phi$  is the diffusivity and  $(\nabla \phi)_f$  is the face gradient of  $\phi$ .

All terms in general equation of transport (4.27) which cannot be expressed as convection, diffusion, or temporal terms are grouped into the source term. If the source term is dependent on  $\phi$  then linearization should be carried out as:

$$S(\mathbf{x}, \phi) = S_c(\mathbf{x}, \phi) + S_p(\mathbf{x}, \phi)\phi(\mathbf{x}) \quad (4.31)$$

Integration of Equation 4.31 on a control volume results in the discretized form of the source term as:

$$\int_{V_P} S_\phi(\phi) dV = S_c V_P + S_p V_P \phi_P + e_{\text{Source}} \quad (4.32)$$

where  $S_c$  and  $S_p$  may also be functions of  $\phi$ .

### 4.3.3 Temporal Discretization

The discretisation of time-dependent terms is performed on a semi-discretised form of transport equation where the spatial terms were already approximated by a proper discretization method. Temporal discretization on a semi-discretised transport equation can be written as:

$$\int_t^{t+\Delta t} \left[ \frac{\partial}{\partial t} \int_{V_P} \phi dV \right] dt = V_P (\phi_P^n - \phi_P^0) = \int_t^{t+\Delta t} f(t, \phi(\mathbf{x}, t)) dt \quad (4.33)$$

where the subscripts  $n$  and  $0$ , represent new and old time respectively and  $f(t, \phi)$  contains all spatial terms. The important part of the temporal discretization process is to approximate  $\int_t^{t+\Delta t} f(t, \phi) dt$  term which cannot be evaluated exactly. Based on this different temporal discretization practices are available that can be summarized as

- Euler Explicit method integrates the spatial terms by using the values at the beginning of the time intervals by assuming:

$$\int_t^{t+\Delta t} f(t, \phi(\mathbf{x}, t)) dt = f(t, \phi(\mathbf{x}, t)) \Delta t$$

this scheme is stable for Courant numbers ( $Co = |U| \Delta t / h$ ), less than 0.5. Here  $|U|$  is the velocity magnitude and  $h$  is the cell size [374].

- Euler Implicit method evaluates the spatial terms in  $f(t, \phi)$  using  $\phi^n$  which are obtained by solving a coupled system of algebraic equations. This is first order accurate but, unlike the explicit method coupling in the equation system is much stronger and the system is stable even if the Courant number limit is violated.
- Crank-Nicholson is a second order accurate time discretisation practice that requires evaluation of spatial terms for old and new time steps. Because the values of  $\phi^n$  are not known at the new time, a system of algebraic equations are solved in each time step. This method can be formalized as:

$$\int_t^{t+\Delta t} f(t, \phi(\mathbf{x}, t)) dt = \frac{1}{2} \left[ f(t, \phi(\mathbf{x}, t^0)) + f(t, \phi(\mathbf{x}, t^n)) \right] \Delta t \quad (4.34)$$

- Backward Differencing is a second-order accurate in time temporal discretization scheme. This method uses three time levels. The recent time

level is the second old time which can be derived using Taylor series, as:

$$\phi(t - \Delta t) = \phi^{00} = \phi^n - 2\frac{\partial\phi}{\partial t}\Delta t + 2\frac{\partial^2\phi}{\partial t^2}\Delta t^2 + O(\Delta t^3) \quad (4.35)$$

then the backward differencing temporal approximation can be derived as [160]:

$$\frac{\partial\phi}{\partial t} = \frac{\frac{3}{2}\phi^n - 2\phi^0 + \frac{1}{2}\phi^{00}}{\Delta t} \quad (4.36)$$

- Explicit Runge-Kutta (RK) is the standard approach for solving partial differential equations in form of  $d\phi/dt = g(t, \phi)$ . Various formulations of RK method are available, here the classical fourth order RK method (RK4) is discussed. Aforementioned equation can be rearranged as:

$$d\phi = dt[g(\phi, t)] \quad (4.37)$$

where  $g(\phi)$  includes all the aforementioned differential terms. The RK4 method estimates  $\phi^n$  as:

$$\begin{aligned} k_1 &= g(t^0, \phi^0) \Delta t \\ k_2 &= g(t^0 + \Delta t/2, \phi^0 + k_1/2) \Delta t \\ k_3 &= g(t^0 + \Delta t/2, \phi^0 + k_2/2) \Delta t \\ k_4 &= g(t^0 + \Delta t, \phi^0 + k_3) \Delta t \\ \phi^n &= \phi^0 + a_1k_1 + a_2k_2 + a_3k_3 + a_4k_4 \\ t^n &= t^0 + \Delta t \end{aligned} \quad (4.38)$$

#### 4.3.4 Solution Of The Algebraic Equations

Spatial and temporal discretizations produce an algebraic equation that relates face and cell values of  $\phi$  and  $\nabla\phi$  for both old and new time level around cell-centre  $P$  and the cell-centre of the neighbour cell  $N$ . This equation is formulated as [160]:

$$a_p\phi_p^n + \sum_N a_N\phi_N^n = R_p \quad (4.39)$$

The values of  $\phi_p^n$  depends on the values in the neighbouring cells therefore a system of algebraic equations are formed as:

$$[A][\phi] = [R]$$

where  $[A]$  is a sparse matrix with coefficients  $a_p$  on the diagonal and  $a_N$  off the diagonal, and  $[R]$  is the source term vector. Solving the set of equations (introduced as vector Equation 4.39) produces a new set of  $\phi$  values for the new time step.

Generally there are two main algorithms to solve the governing equations of fluid flow: pressure-based and density-based. Historically, pressure-based algorithms were proposed to simulate incompressible, low-Reynolds number flows. Originally these methods solved the equations of fluid motion

in a segregated fashion, but more recently were extended to couple solutions for high-Reynolds number and compressible flows as well. It worth mentioning that the solution procedures can be classified also in segregated and coupled algorithms. In the segregated approach the set of algebraic equations is solved sequentially which means once solving for one variable, other variables are treated as known. On the other hand, in coupled or simultaneous approach the system of equations are solved concurrently over the whole computational domain. After discretizing the momentum Equation 4.2 the pressure gradient term is written separately and not included in the source term  $S_\phi(\phi)$  as the pressure is treated as an unknown [374]. This means that velocity and pressure are coupled together with linear dependency. Therefore, in a segregated approach special treatments are required in order to establish the necessary inter-equation velocity-pressure coupling. Semi-implicit method for pressure-linked equations, known as SIMPLE algorithm [351, 374] and pressure implicit with splitting of operators (PISO) algorithm developed by Issa [351, 374] and their derivatives are the most popular methods in handling this inter-equation coupling. For the coupled approach the solution matrix include the inter-equation couplings and there is no need for a velocity-pressure coupling algorithm. In both pressure-based and density-based approaches velocity field is obtained from the momentum equation. Then for the pressure-based algorithm, pressure is obtained from a velocity-pressure coupling algorithm while in a density-based solver pressure is obtained from an equation of state and density (density is already obtained from the continuity equation). In low Mach conditions and particularly within the incompressible limits ( $Ma < 0.3$ ) the compressible governing equations become stiff. This is because, the variation of density becomes minute thus the pressure calculated using density and the equation of state is not associated entirely with the velocity field obtained from the conservation of momentum. Therefore, extra treatment is required if it is to develop a computational framework for arbitrary Mach number from the subsonic to the supersonic limits. For a coupled density-based approach 'preconditioning' in conjunction with 'dual time-stepping' is typically used in order to overcome the stiffness of the governing equations for low Mach number flows. Although implicit pressure treatment techniques such as SIMPLE and PISO were originally developed for incompressible flows, their concept were extended to the compressible flows and can be considered as solutions for obtaining a compressible numerical framework (segregated) for all flow speeds [].

## 4.4 Liquid Spray CFD Simulation

The simulation of a multi-phase flow can be performed using different approaches accordingly to the particular phenomenon considered. In typical fuel sprays the liquid fuel is disrupted into a number of droplets up to  $10^8$  with average diameters in the ten-micrometer range. These numbers suggest to choose a different approach rather than the classical FV method have

to be adopted. The established method uses a Lagrangian approach following the droplet's evolution within the computational domain. However, the large number of droplets presents in the computational domain make it prohibitive to resolve each single droplet in numerical simulations. Instead, some kind of statistical averaging technique becomes necessary with additional sub-models in order to describe the subscale processes.

Generally the problem can be defined by the so-called spray equation [401]. In this approach the probable number of drops per unit volume at time  $t$ , that are located between position  $\vec{x}$  and  $\vec{x} + d\vec{x}$  and characterized by a velocity between  $\vec{v}$  and  $\vec{v} + d\vec{v}$ , a radius between  $r$  and  $r + dr$  and a temperature between  $T_d$  and  $T_d + dT_d$  is described with the probability density function  $f$ . Since both the droplet position  $\vec{x}$  and its velocity  $\vec{v}$  have three spatial coordinates,  $f$  has a total of nine independent variables:

$$\frac{\text{probable number of droplets}}{\text{unit volume}} = f(\vec{x}, \vec{v}, r, T_d, t) d\vec{v} dr dT_d \quad (4.40)$$

It should be underlined, that the above formulation is based on the assumption that the droplets are ideally spherical and that their size or mass is thus explicitly defined by their radius  $r$ . However, this assumption is valid only if the relative velocity between gas and droplet is small, which is not generally the case in typical engine sprays. Especially, in the vicinity of the injection nozzle considerable relative velocities between liquid and gas phases are encountered, such that aerodynamic forces cause droplet distortion and even droplet breakup. Therefore, in most CFD-codes applied for engine simulations with spray combustion, two additional independent variables are included in the distribution function: the droplet distortion parameter  $y$  and its temporal rate of change  $\dot{y}$ . Thus,  $f$  becomes a function of eleven independent variables, and Equation 4.40 is:

$$\frac{\text{probable number of droplets}}{\text{unit volume}} = f(\vec{x}, \vec{v}, r, T_d, y, \dot{y}, t) d\vec{v} dr dT_d dy d\dot{y} \quad (4.41)$$

The temporal and spatial evolution of the distribution function is described by a conservation equation which can be derived phenomenologically in analogy to the conservation equations of the gas phase. It is commonly referred to as the spray equation and can be written as:

$$\begin{aligned} \frac{\partial f}{\partial t} = & - \frac{\partial}{\partial x_i} (f v_i) - \frac{\partial}{\partial v_i} (f F_i) - \frac{\partial}{\partial r} (f R) - \frac{\partial}{\partial T_d} (f \dot{T}_d) - \frac{\partial}{\partial y} (f \dot{y}) - \frac{\partial}{\partial \dot{y}} (f \ddot{y}) \\ & + \dot{f}_{coll} + \dot{f}_b \end{aligned} \quad (4.42)$$

$\vec{F}$  denotes a force per unit mass, i.e. an acceleration. Thus the component  $F_i$  is the acceleration along the spatial coordinate  $x_i$  ( $F_i = dv/dt$ ).  $R$ ,  $\dot{T}_d$  and  $\dot{y}$  are the time rates of change of droplet radius  $r$ , temperature  $T_d$  and oscillation velocity  $\dot{y}$ . The source terms  $\dot{f}_{coll}$  and  $\dot{f}_b$  account for changes in the distribution function due to droplet collision and breakup, respectively.

By solving the spray equation, the so-called source or exchange terms

can be obtained, that describe the interactions between the liquid and gas phases. In order to assure conservation of mass, momentum and energy of the total (two-phase) system, these terms need to be included in the gas phase conservation equations previously exposed. The source term accounting for mass evaporation of the liquid droplets is

$$\dot{\rho}' = - \int f \rho_l 4\pi r^2 R d\vec{v} dr dT_d dy dj \quad (4.43)$$

The rate of momentum gain due to droplet drag, body forces and evaporation is

$$\rho_s \vec{F}^s = - \int f \rho_l \left( \frac{4}{3} \pi r^3 \vec{F}' + 4\pi r^2 R \vec{v} \right) d\vec{v} dr dT_d dy dj \quad (4.44)$$

the energy transfer between gas and droplets by evaporation, heat transfer into the droplet and work due to turbulent fluctuations is

$$\dot{Q}' = - \int f \rho_l \left\{ 4\pi r^2 R \left[ u_d + \frac{1}{2} (\vec{v} - \vec{u})^2 \right] + \frac{4}{3} \pi r^3 \left[ c_{p,d} \dot{T}_d + \vec{F}' (\vec{v} - \vec{u} - \vec{u}') \right] \right\} \cdot d\vec{v} dr dT_d dy dj \quad (4.45)$$

and the dissipation of turbulent kinetic energy due to droplet dispersion is given by

$$\dot{W}^s = - \int f \rho_l \frac{4}{3} \pi r^3 \vec{F}' \cdot \vec{u}' d\vec{v} dr dT_d dy dj \quad (4.46)$$

In Equations 4.43 to 4.46 the superscript *s* indicates that the source terms are due to spray effects (as opposed to effects of chemical reactions that will be denoted by superscript *c*).  $\vec{F}'$  is the difference between  $\vec{F}$  and the gravitational acceleration  $\vec{g}$ ,  $(\vec{v} - \vec{u})$  is the relative velocity between droplets and gas phase, and  $\vec{u}'$  is the turbulent fluctuation of the gas velocity. Note, that in Equation 4.44  $u_d$  denotes the specific internal energy of the droplet and is not to be mistaken for the gas velocity  $\vec{u}$ .

The simulation solution of the spray equation can be performed using the continuum droplet model (CDM). CDM is the direct solution of such equation thanks to a finite volume (or difference) Eulerian scheme for both gas and liquid-droplets phases. Unfortunately such model requires huge computational resources and so it is not used [351]. Differently, the discrete droplet model (DDM) describes the spray's droplets with stochastic groups of particles called parcels. These parcels represent classes of identical droplets and they are tracked through the computational domain (Lagrangian approach). Coupling between the Eulerian and the Lagrangian fields is performed by solving the gas flow field and, initially, neglecting the presence of any spray particles in the flow. Using such gas phase results, the droplet trajectories together with the mass, momentum and energy exchanges between the two phases are calculated. Hence, the gas phase is recalculated, now including the source terms due to the spray particles, and the whole procedure is repeated iteratively until the convergence criterion is met [242, 351].

In this way, using a proper number of parcels, a discretised solution can be calculated and it becomes representative of the spray evolution.

Both methods do not directly solve the gas-droplet interface due to computational limitations and so additional sub-models must be used to describe these phenomena. In this regard can be mentioned:

- breakup model;
- turbulent dispersion-diffusion model;
- drop drag model;
- collision model;
- coalescence model;
- vaporization model.

Further details regarding all sub-models including the latest research activities performed in the field of liquid spray simulation are reported in chapter 5.



## Chapter 5

# Gasoline Direct Injection Engines - Latest Technologies and Trends

### 5.1 Overview of the Chapter Topics

In this chapter a quick and, as far as possible, complete reference guide to GDI engines, was reported. The intention was to highlight the most interesting topics and the most relevant works that have been done in these recent years. The idea is to follow the journey of a gasoline droplet through the engine, beginning from its breakup and ending at the exhaust duct when it becomes a pollutant particle. In this chain of events, the injection process plays a relevant role, and for this reason it is the common thread of this work.

Spark-ignition direct injection engines are widely recognised as a key technology to comply with the ever increasing emission standards limitations. In the past, gasoline engines exploited port fuel injection systems (PFI), but today gasoline direct injection (GDI) systems are becoming prominent, allowing a massive engine downsizing, a relevant emission reduction and significant operating performance enhancement. To implement such technique a deeper knowledge of the phenomena that take place during an engine cycle is fundamental. The gasoline jet breakup modality and distribution quality within the combustion chamber are the main factors that affect many events, such as mixture formation, combustion quality and emission amounts. For this reason, innovative experimental and numerical techniques have been used to study the spray breakup process. Mie scattering, schlieren and shadowgraphy imaging techniques allow the recording of the developed spray shape. With phase Doppler particle anemometry (PDPA), the particle speed and diameter can also be measured. The spray's near-nozzle flow field measurement is gaining interest, especially with the new multi-hole and high-pressure injectors. For this purpose, to highlight the fluid flow and local phenomena such as cavitation, X-ray imaging and instrumented injectors are used. Lately, still on the subject of experimental spray characterisation, the flash-boiling process is gaining attention. This occurs when the fuel is at high temperature and consists of a sudden phase change of the jet that can significantly improve the spray's atomisation quality. It is observed usually with ultra-fast X-ray and PDPA methods.

Alongside experimental activities, with the growth of computational resources available everywhere, physical sub-models that allow a consistent

simulation of the injection process are embedded into CFD codes. The classical methodology used to represent such process is called DDM which uses an Eulerian-Lagrangian statistical approach in acceptable timeframes. In this way the overall breakup process is well represented (especially in the far field) using the Kelvin-Helmholtz Rayleigh-Taylor and the Reitz-Diwakar models. DDM method has some limitations especially concerning the representation of the near-nozzle zone flow and so, recently, interesting new methods based on different approaches, are gaining attention. These are mainly VOF model, Eulerian-Eulerian method, level set method and ELSA model. The exact turbulent flow solution known as direct numerical simulation (DNS) must be mentioned and today we can report the first attempts to use DNS to study the injector's near-nozzle flow. This is a zone where experimental techniques often cannot provide measurement, and so the results of these simulations are becoming very important because they can be used to validate other models. The spray is usually studied by trying to reproduce engine-like conditions and highlighting the effects of thermodynamic parameters on the spray shape, penetration and pulverisation.

The relatively small dimensions of the combustion chamber and the jet's speed easily involve the spray-wall impact and the consequent formation of a liquid wall film. Avoiding the occurrence of wall impingement is recognised as a key requirement to obtain clean combustion, reduce fuel consumption and finally reduce emissions. These considerations, first raised years ago, led to the development of both mathematical modelling and experimental characterisation of these phenomena, but studies are always in development. The last experimental observations provide a new classification of the impact mechanisms. Smoothed particle hydrodynamics (SPH) and other models are used in CFD simulations that are today able to reproduce the wall impingement and permit a comprehensive study of this phenomenon.

In the past and over the years, many different mathematical models have been developed to study the various and complex events occurring during the combustion process and, recently, attention was paid to the ignition process and to anomalous combustion phenomena, knock and misfiring. The Swept Volume method and the Triangulated Lagrangian Ignition Kernel are examples of models used to provide a more accurate evaluation of early flame kernel development and to capture new features of the flame propagation. The variance equation and the Probability Density Function-based knock model, the Tabulated Knock Model based on a tabulated chemistry approach and on a RANS turbulence modelling framework, are example of different approaches to study the occurrence of knock. A better prediction of the in-cylinder airspeed fluctuation and, especially, of the instability of combustion and the consequent cycle-to-cycle variability (CCV) of turbulent flows, is obtained using LES turbulent combustion models, as the most appropriate approach for CFD simulations, made possible today by the ever increasing computational resources available. In GDI engines PM emissions are much higher than in PFI engines. So, PM reduction has become a relevant research topic. An examination of the literature on the subject reveals

that knowing the soot formation mechanisms and optimizing the thermodynamic processes, the engine design parameters and the composition and physical properties of fuels are fundamental issues to avoid large amounts of particulate emissions. Higher injection pressure values lead to a reduction of the PN and of their mass, due to a more uniform air–fuel mixing process and consequently the best vaporization. Injection and combustion (homogeneous or stratified) strategies, strongly affect particulate emissions. Very interesting is a multiple phase injection strategy that makes it possible to have the shortest fuel jet length, an improved mixture formation process, a reduced impact of the fuel on surfaces, and, finally, lower particulate emissions. Fuel blends more volatile with a lower content of aromatic and olefin components promote a good mixture formation and combustion and a reduction of particulate emissions. The addition of ethanol in the fuel reduces the gasoline vapor pressure, enhances evaporation and thus reduces the particulates.

In literature attention is paid to phenomena of deposits and fouling, extremely important in SIDI engines as the injection system is in direct contact with the combustion gases and exposed to high temperatures and pressures. Significant injector fouling can lead to engine misfiring and drivability problems and can shorten the vehicle life. Finally, a small space, certainly not exhaustive, was dedicated to some significant research activities concerning low-temperature combustion engines. The GDCI engine is one of the most promising technologies in this category, attracting a growing interest to respect the increasingly stringent emissions rules. Indeed, it merges the high efficiency of compression ignition engines with the low CO<sub>2</sub>, NO<sub>x</sub> and PM emissions of spark ignition engines.

Following this literature review the attention will be focused on the ECN Spray G injector's spray characterization. In chapter 6 a numerical-experimental investigation of the aforementioned spray is reported while in the chapter 7 the flash-boiling jets will be investigated. An innovative breakup model, developed by the author, is presented in details and validated, thanks experimental data, acquired at Istituto Motori - CNR - Naples.

## 5.2 Spray Breakup Process

The spray breakup process is a key element in internal combustion engines. Disintegration of the liquid fuel flow into millions of droplets promotes a rapid evaporation, produces a better air–fuel mixture and, finally, is an effective way to control the combustion process. So, the most relevant studies carried out to characterise the spray morphology and its behaviour in an environment like the combustion chamber are analysed here.

In the last few years, various experimental procedures have been developed to capture images of the injection process at different thermo-fluid-dynamic operating conditions which should be the most representative of the engine conditions. The combustion chamber is an unfriendly measuring environment: the turbulent gas phase, the flame itself and the particular thermo-dynamic conditions make it difficult to perform measurements without altering the environment's conditions. Experimental data are thus

used by researchers to tune and validate CFD (computational fluid dynamics) spray models that become powerful tools to understand such phenomena.

The experimental and numerical results provide a better comprehension of the operating condition's effect on the spray characteristics, allowing us to optimise the injection process and so to obtain low emissions and a more efficient combustion.

The two-phase liquid fuel flow, originated from the injector, is shown in Figs. 5.1 [39] and 5.2 [16] with some schematic representations.

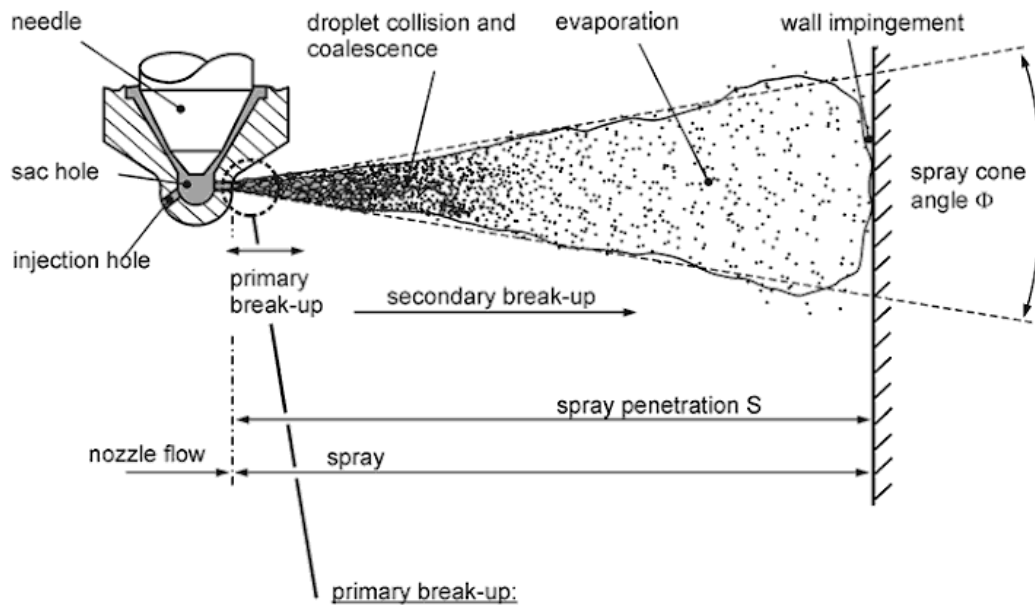


FIGURE 5.1: Schematic representation of a liquid fuel spray.

The parameters that allow us to describe the jet morphology are mainly the penetration length, cone angle and Sauter mean diameter (SMD), defined as:

$$SMD = \frac{\sum_{i=1}^{N_d} d_i^3}{\sum_{i=1}^{N_d} d_i^2} \quad (5.1)$$

where  $N_d$  is the overall number of droplets and  $d_i$  the  $i$ -th droplet's diameter.

As the fuel, thanks to the high injection pressure, exits from the injector's holes at high speed, the liquid flow breaks into ligaments and further into droplets (churning flow). In this dense or thick spray region, the jet assumes a cone shape and the liquid droplets occupy a considerable volume fraction with respect to the gas part. Going downstream (from left to right in Fig. 5.1) the distance between droplets increases due to the conical spray shape and the volume fraction occupied by the gas too. This is the thin spray region. Here, as in the thick zone, the small relative distance promotes droplet-droplet interactions such as collision and coalescence. Thus, the flow cannot be treated without taking into account these phenomena. Finally, there is the dilute or very thin region where the liquid mass fraction becomes negligible and there are just isolated droplets surrounded by gas [304].

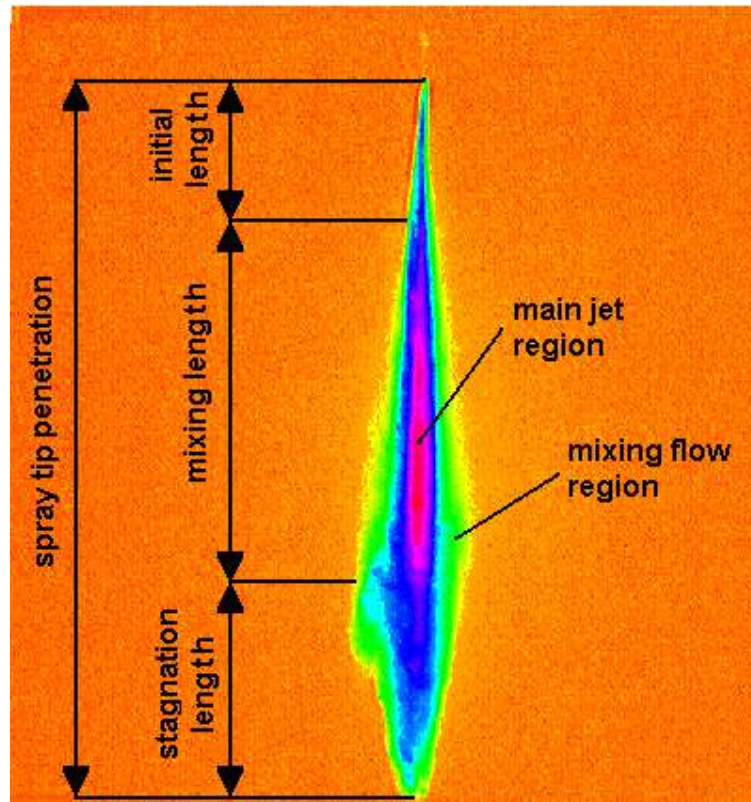


FIGURE 5.2: Structure and shape of the free spray.

The breakage of the fuel spray into these droplets and filaments occurs in two steps: primary and secondary breakup. Primary breakup takes place just outside the injector's hole and consists in the splitting of the intact liquid core into the first droplets. A relevant pressure drop, across the injector nozzle, accelerates the liquid flow and consequently generates high levels of turbulence at the gas-liquid interface that have a destabilising effect on the jet, creating the condition for having the droplets breakup. Furthermore, at the nozzle exit there is a reduction of the stream diameter (vena contracta) that, according to Bernoulli's law, leads to another static pressure reduction that could be lower than the fuel vapour pressure and create cavitation bubbles inside the nozzle. Once these bubbles are dragged out of the nozzle, they implode and contribute to the disintegration of the spray. Behind the breakup there is a last mechanism: on the droplet's surface aerodynamic forces also act, creating perturbations that end in rupture of the droplet [351].

Four different spray regimes can be identified depending on the values of the Reynolds ( $Re$ ) and Ohnesorge ( $Z$ ) numbers: Rayleigh, first wind-induced, second wind-induced and atomisation regimes [239, 271]. A more complete definition that takes into account the gas-phase thermo-dynamic properties was suggested by Reitz.

Rayleigh breakup, characteristic of low injection velocities, is driven mainly by liquid inertial forces and by its surface tension, and the child droplets have a diameter greater than the nozzle diameter. Gas-phase inertial forces becomes more and more important in the first wind-induced regime, where the

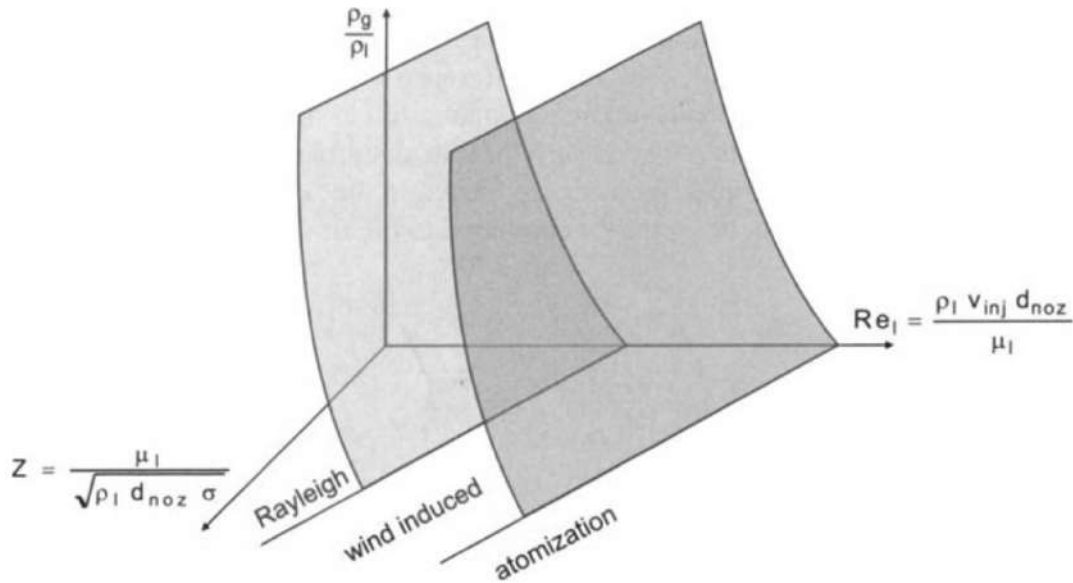


FIGURE 5.3: Breakup regimes as a function of  $Re$ ,  $Z$  and gas density

surface perturbations due to the gas-liquid interaction can lead to breakup, and in this case the droplet diameter is always greater than the nozzle dimension. A further increase of injection velocity brings the second wind-induced regime, where aerodynamic forces play a key role. On the liquid surface they generate disturbances with a shorter wavelength and so droplets with a smaller diameter. The atomisation regime, characteristic of high-pressure injectors, is reached with significant injection velocities and relatively high gas density. In this condition, the spray has a conical shape, the particle diameter is much smaller than that of the nozzle one, the breakup begins just outside the nozzle orifice or almost some diameter down-flow. A third variable, the gaseous to liquid density ratio ( $\rho_g/\rho_l$ ), was introduced to consider the gas-phase thermodynamic conditions and so provide a much more complete representation of different breakup regimes, as shown in Fig. 5.3 [302].

Secondary breakup happens later, down-flow, when the droplets are surrounded by the turbulent gas-flow, which creates aerodynamic forces on the droplet surface. Such forces may be able to overcome the superficial tension and distort the spherical shape breaking the droplet again into parcels of smaller dimensions. Quantitatively, the Weber number relates these two kinds of actions that act on the droplets. Depending on the  $We$  number ( $We$ ) the secondary breakup can be classified in different regimes [207]. Figure 5.4 summarises this [399].

After the spray has broken up into small particles, due to the energy exchange with the surrounding air, the droplet evaporates. This is a fundamental process to achieve the correct mixing between fuel and air. A poor or a too fast evaporation causes inefficient combustion and finally lead to the formation of different pollutant species (unburned hydrocarbons and nitrogen oxides) [301, 400].

The reduced space available and the great number of droplets present in

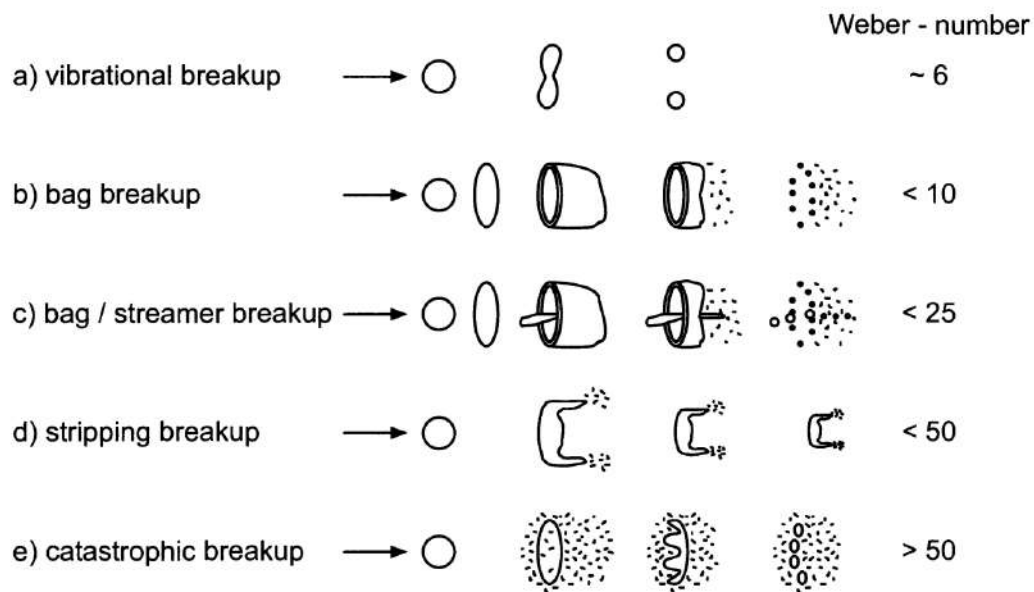


FIGURE 5.4: Secondary breakup regimes as function of We.

the combustion chamber easily creates the conditions to have several droplet collisions. This phenomenon inevitably has strong consequences on the mixture formation and finally on the combustion quality. The occurrence of droplets collision depends mainly on the directions of their velocity as well as on the local void fraction. Depending on the collision Weber number, different collision regimes can be identified: droplets can bounce apart elastically, they can coalesce, separate again or remain together and, finally, they can crumble into many tiny droplets [121, 297].

Table 5.1, in the follows, summarises the papers describing the spray's physical behaviour.

Process	Short Description	References
Breakup	Liquid core rupture in ligaments and droplets	[16, 39, 207, 304]
	Breakup regimes	[239, 271, 302, 399]
Evaporation	Droplet's phase change description	[6, 342]
Collision and coalescence	Impact between various droplets	[121, 297]

TABLE 5.1: Spray Physics Summary Table

### 5.3 GDI Spray Measurement Techniques

The set-up commonly adopted to study the injection process consists of an injector mounted on a vessel equipped with optical windows that allow pictures of the evolving spray to be captured. In this way, ambient conditions similar to the combustion chamber can be recreated in terms of temperature and pressure.

Spray measurement technologies can be classified depending on the spray's region of interest and the experimental technique used. Mie scattering, shadowgraphy and schlieren photography are the most common techniques used to characterise the spray. Other techniques are also used: laser-induced fluorescence, phase Doppler particle anemometry, X-ray phase-contrast imaging and plenoptic imaging.

Mie scattering is elastically scattered light from particles that have a diameter similar to or larger than the wavelength of the incident light. The Mie signal is proportional to the square of the particle diameter [141, 283].

Schlieren photography is like the shadowgraph technique and relies on the fact that light rays are bent whenever they encounter changes in density of a fluid [83]. Specifically, a schlieren image displays the deflection angle, while a shadowgraph displays the ray displacement resulting from deflection; besides, schlieren imaging requires a knife-edge object to cut the refracted light.

The Mie scattering technique is used mainly to visualise the developed spray liquid-phase shape (very thin or dilute region) and to measure the spray's penetration length or cone angle [151, 282]. The Mie scattering technique does not show the vapour phase of the spray, and so for this reason the schlieren technique is usually used in order to have a complete fuel spray representation [200]. The high-speed shadowgraph technique can also be used for dense-spray regions such as the near-nozzle zone [138].

Laser-induced fluorescence (LIF) exploits the temperature dependence of the absorption and emission spectra to measure the gas or liquid temperature [209]. The spray is excited with a single-wavelength laser light, and so the temperature is evaluated from the ratio of fluorescence intensity in two wavelength bands [402]. Lately, LIF is being used to characterise the evaporation of the different chemical components of gasoline [34, 158], the spray's temperature-induced stratification dynamics [290], and, thanks to its capability to record both liquid and vapour phases, it is also exploited to study the fuel's droplet surface impact [276]. The quantitative knowledge of a fuel's vapour distribution and concentration within the engine is critical to enhance the combustion process and evaporation modelling, which suffers of from a lack of experimental data.

The phase Doppler particle anemometry technique (PDPA) measures, simultaneously, the size, velocity and concentration of spray particles. The key feature of PDPA is its capability to provide quantitative values of such spray parameters. Simultaneous measurement of both size and velocity allows correlations to be made between these two quantities. The characteristics of moving particles are obtained by utilising the laser Doppler effect [8,

150].

PDPA has a physical limitation: it cannot be used in the near-nozzle field (thick region) due to the spray's high density. This problem was overcome by Payri R. et al. [285], making the measurement volume small enough to allow a single droplet to pass through it [69, 345]. The near-nozzle zone is very important because here primary breakup takes place [30]. However, it is really difficult to capture images of the individual spray plume due to the strong interaction effects with the surrounding air, persistent unsteadiness, a relevant liquid mass fraction present in the spray flow, cavitation and flash boiling [129, 337]. These conditions cannot be analysed with, for example, Mie scattering, due to the severe absorption and scattering of the laser light in the thick region [186, 217, 392].

Differently from the conventional laser methods, the main feature of X-ray phase-contrast imaging (XPCI) is the ability to capture the upstream internal nozzle flow region. XPCI records the interference fringe pattern formed along the liquid feature boundary. Thanks to the different densities or structures, it is possible to detect the inter-facial structures among the materials [256]. In the last decade, XPCI was performed to study mainly the near-nozzle spray behaviour with the final aim of correlating the injector's needle motion and nozzle geometry to the near-field flow characteristics [99, 186, 254, 255, 257].

Knowledge of the nozzle's internal geometry is obviously fundamental to studying internal and near-nozzle flows. Injector manufacturers rarely release such information and so X-ray-based techniques alongside transparent or instrumented injectors are often used to perform experimental campaigns [109, 316]. X-ray computed tomography (CT) allows researchers to measure exactly the injector's nozzle dimensions and study different aspects of near-nozzle flow such as plume-to-plume variations in the mass fluxes from the holes and their effects on the spray structure (especially the ECN Engine Combustion Network Spray G [100]).

Figure 5.5 shows several different images of a spiral spray hollow-cone nozzle [212].

Almost all the experimental pictures are 2D images, and only a few examples of 3D imaging techniques have been demonstrated. They are still a challenge for many researchers, and some of them used special optical-accessible engines. Plenoptic imaging is the first technique able to capture 3D structural information of a fuel spray [63]. A plenoptic camera records the light field of a scene and not the light intensity, as is more common. Chen H. et al. [62] used one to study the impact of engine operating conditions on spray development. Observations made in the 3D images are in full agreement with expectations and thus underscore the ability of plenoptic imaging to capture 3D structural information about in-cylinder sprays.

In the last few years, a strong interest was growing around the flash-boiling phenomenon. It consists in the sudden phase change of a fluid from liquid phase to vapour phase and occurs in GDI engines operating at high

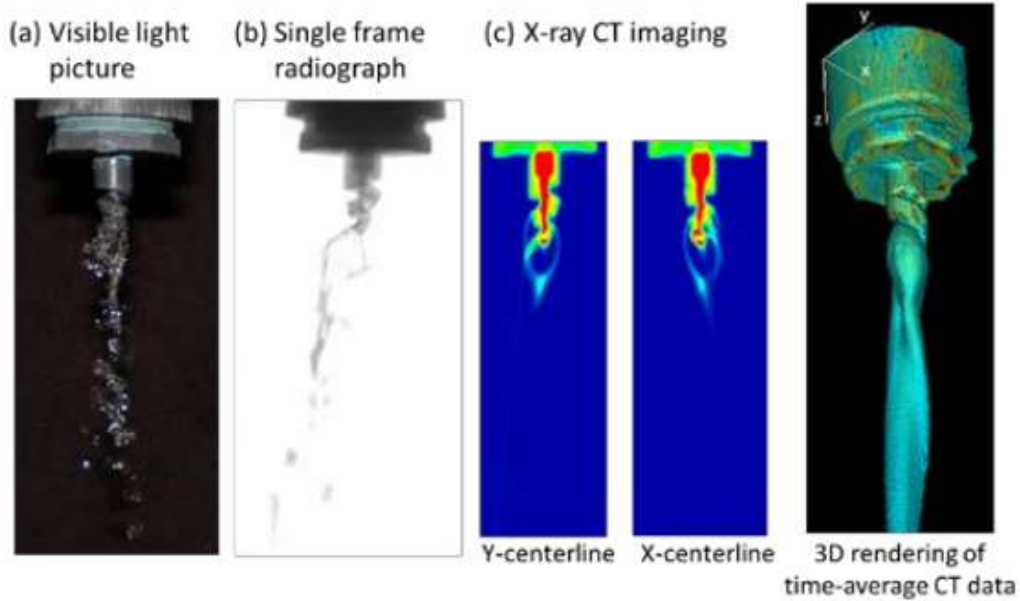


FIGURE 5.5: Visible light (a), single frame X-ray radiograph (b), X-ray CT images (c), and subsequent post-processing elaborations of a spiral spray hollow-cone nozzle.

temperature levels [303]. During the injection process, due to the subsaturation pressure conditions, the formation of vapour bubbles occurs in the liquid fuel flow. The consequent explosion of these bubbles results in sudden evaporation and catastrophic disintegration of the liquid jet. So, finally, flash boiling is a potential way to enhance the atomisation level [340]. Visualisation of flash boiling is thus attracting the attention of many researchers, and PDPA alongside ultra high-speed imaging techniques are widely used [10, 129, 167, 216]. Jiang C. et al. studied the impact of gasoline direct injection fuel injector hole geometry on spray collapse [163] using PDPA.

Table 5.2, in the following, summarises the papers on spray measurement techniques, broken down by research topic and technique type.

Research Task	Experimental Technique	References
Developed spray liquid phase	Mie scattering	[141, 151, 282, 283]
Developed spray both liquid and vapor phases	Schlieren, Shadowgraphy	[83, 200]
Developed spray temperature measurement	Laser induced fluorescence (LIF)	[34, 158, 209, 276, 290, 402]
Developed spray's particles size, velocity and concentration	Phase Doppler anemometry	[69, 285, 345]
Near-nozzle flow	X-ray Phase Contrast Imaging	[99, 186, 254–257]
Nozzle internal flow	X-Ray Tomography Instrumented/Transparent Injectors	[100] [109, 316]
3D imaging in optical engines	Plenoptic Imaging Camera	[62, 63]
Flash Boiling	PDPA Ultra-Fast Imaging	[129, 163, 167] [10, 216]

TABLE 5.2: Spray Measurement Techniques Summary Table

## 5.4 Mathematical Modelling of Liquid Spray

The simulation of an injection process involves the solution, besides the gas phase fluid-dynamic governing equations, of the so-called spray equation that describes the probable number of droplets in the unit volume as a function of eleven independent variables [401]. The continuum droplet model (CDM) is the direct solution of such equation thanks to a finite volume (or difference) Eulerian scheme for both gas and liquid-droplets phases. Unfortunately such model requires huge computational resources and so it is not used [351]. Differently, the discrete droplet model (DDM) describes the spray's droplets with stochastic groups of particles called parcels. These parcels represent classes of identical droplets and they are tracked through the computational domain (Lagrangian approach). Coupling between the Eulerian and the Lagrangian fields is performed by solving the gas flow field and, initially, neglecting the presence of any spray particles in the flow. Using such gas phase results, the droplet trajectories together with the mass, momentum and energy exchanges between the two phases are calculated. Hence, the gas phase

is recalculated, now including the source terms due to the spray particles, and the whole procedure is repeated iteratively until the convergence criterion is met [242, 351].

In this way, using a proper number of parcels, a discretised solution can be calculated and it becomes representative of the spray evolution.

Both methods do not directly solve the gas-droplet interface due to computational limitations and so additional sub-models must be used to describe these phenomena, such as the turbulent dispersion-diffusion model, and drop drag model, spray breakup model.

The central core of fuel injection processes simulation is undoubtedly the set of sub-models adopted. First of them to be mentioned is the breakup model

The primary breakup model's aim is to define the spray fluid-dynamic conditions at the nozzle exit [103, 221]. The predominant mechanism of the jet's breakup is the growth and development of perturbations on the liquid phase surface driven by aerodynamic actions, known as Kelvin-Helmholtz instabilities. The most important and consistent breakup model, based on such physical considerations, is the wave-breakup, or Kelvin-Helmholtz model (KH), developed by Reitz [302].

### Wave Breakup Model

The turbulent flow inside the nozzle creates perturbations on the jet's liquid surface of radius  $a$ . Such perturbations have an initial amplitude  $\eta_0$  and a spectrum of wavelengths  $\lambda$  with wave number  $k = 2\pi/\lambda$ . The infinitesimal axi-symmetric displacement is equal to:

$$\eta(t) = \Re(\eta_0 e^{ikx + \omega t}) \tag{5.2}$$

where  $\omega$  is the growth rate.

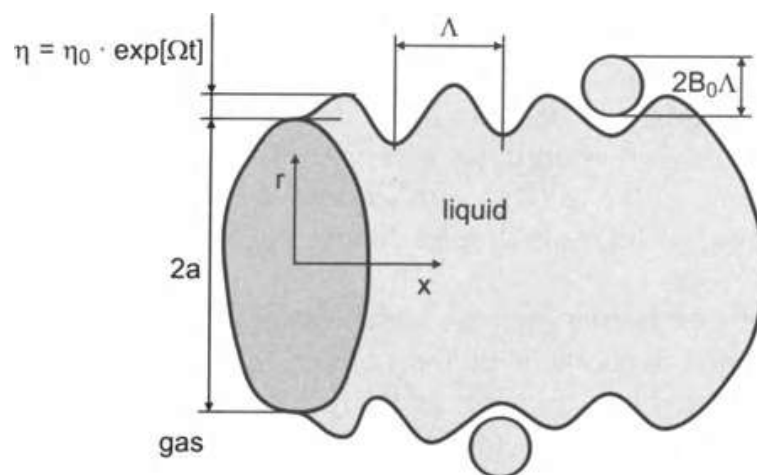


FIGURE 5.6: Schematic representation of surface perturbations in the wave-breakup model [304].

Assuming that the jet's radius is much bigger than the perturbation's amplitude ( $a \gg \eta$ ), free slip at the gas-liquid interface and gas phase as an

inviscid fluid from Eq. (5.2) a further relation called the dispersion relation can be obtained:

$$\omega^2 + 2\nu_l k^2 \omega \left[ \frac{I_1'(ka)}{I_0(ka)} - \frac{2kl}{k^2 + l^2} \frac{I_1(ka)}{I_1(ka)} \right] = \frac{\sigma k}{\rho_l a^2} (1 - k^2 a^2) \cdot \left( \frac{l^2 - k^2}{l^2 + k^2} \right) \frac{I_1(ka)}{I_0(ka)} + \frac{\rho_g}{\rho_l} \left( U - \frac{i\omega}{k} \right)^2 - k^2 \left( \frac{l^2 - k^2}{l^2 + k^2} \right) \frac{I_1(ka) \cdot K_0(ka)}{I_0(ka) \cdot K_1(ka)} \quad (5.3)$$

where  $\nu_l$  is the kinematic viscosity of the liquid phase;  $U$  the gas velocity at the liquid interface;  $I_n$  and  $K_n$  are the  $n^{\text{th}}$  order modified Bessel functions of the first and second kind, respectively.

Using a numerical solution of this equation, Reitz obtained the relation for the maximum growth rate  $\Omega$ :

$$\Omega \left( \frac{\rho_l a^3}{\sigma} \right)^{0.5} = \frac{0.34 + 0.38 \text{We}_g^{1.5}}{(1 + Z)(1 + 1.4T^{0.6})} \quad (5.4)$$

and its corresponding wavelength  $\Lambda$ :

$$\frac{\Lambda_{KH}}{a} = 9.02 \frac{(1 + 0.45Z^{0.5})(1 + 0.4T^{0.7})}{(1 + 0.87\text{We}_g^{1.67})^{0.6}} \quad (5.5)$$

where

$$Z = \frac{\text{We}_l^{0.5}}{\text{Re}_l}, \quad T = Z\text{We}_g^{0.5}, \quad \text{We}_l = \frac{\rho_l U^2 a}{\sigma},$$

$$\text{We}_g = \frac{\rho_g U^2 a}{\sigma}, \quad \text{Re}_l = \frac{Ua}{\nu_l}$$

The new droplets originated from the breakup have a radius that is linearly dependent on wave length  $\Lambda_{KH}$  modulated by constant  $B$ :

$$r_d = B\Lambda_{KH} \quad (5.6)$$

The spray cone angle is proportional to the wave growth rate:

$$\tan \left( \frac{\alpha}{2} \right) = \frac{4\pi}{A} f(T) \sqrt{\rho_g / \rho_l} \quad (5.7)$$

with  $f(T)$  a function of the temperature and  $A$  a nozzle geometry constant, while the intact core length is :

$$L_{KH} = \frac{ca}{f(T)} \sqrt{\frac{\rho_l}{\rho_g}} \quad (5.8)$$

### Blob injection model

Reitz improved the wave breakup model, specialising it for the internal combustion engine's high-pressure injectors. He assumed that during injection drops (so called blobs) are continuously injected, with a diameter comparable to the nozzle's hole dimension, subjected to Kelvin-Helmholtz instabilities. It accounts also for the generation of child droplets and parent drop diameter reduction.

The blob injection model calculates the maximum wave length and the corresponding growth rate as done in the wave model (Eq. (5.4) and Eq. (5.5)). Then the droplet radius is:

$$r_d = B_0 \Lambda_{KH} \quad (5.9)$$

with  $B_0 = 0.61$  (breakup size constant) and for the atomisation regime is given by the following relation [225]:

$$B_0 = 0.3 + 0.6P \quad (5.10)$$

where  $P$  is a random number in the range between zero and one.

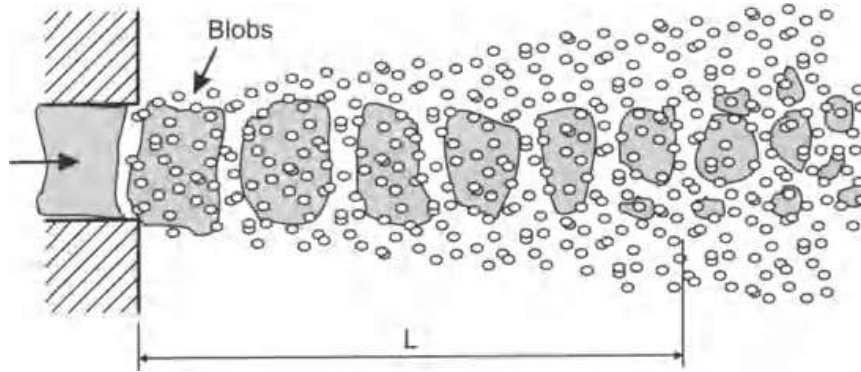


FIGURE 5.7: Schematic representation of blob injection model [300].

Differently from the wave model, these relations are valid if the calculated  $r_d$  is less than the parent droplet's diameter ( $r_d \leq a$ ). In the other case, one time only can be used:

$$r_d = \min \left\{ \begin{array}{l} (3\pi a^2 U / 2\Omega)^{1/3} \\ (3a^2 \Lambda / 4)^{1/3} \end{array} \right. \quad (5.11)$$

The parent droplets thus have a reduced radius described by

$$\frac{da}{dt} = -\frac{a - r_d}{\tau_{KH}} \quad (5.12)$$

where  $\tau_{KH}$  is the liquid breakup time equal to:

$$\tau_{KH} = 3.726 \frac{B_1 a}{\Lambda_{KH} \Omega_{KH}} \quad (5.13)$$

$B_1$  is the breakup time constant and it can vary from  $\sqrt{3}$  to 30 [284].

The KH model does not take into account the internal nozzle flow, but its turbulent nature and the occurrence of cavitation have an unavoidable effect on the primary breakup. Huh and Gosman's modified model [148] and the breakup model presented by Baumgarten C. et al. [40] try to take these effects into account. In particular, the latter divides the nozzle orifice's flow into two zones: a first with a liquid core and a second where there are cavitation bubbles and liquid filaments, and finally, exploiting energetic considerations, it calculates the droplets diameter and spray cone angle.

### LISA model

In order to achieve hollow-cone sprays, high-pressure swirl atomisers are often used in direct injection spark ignition engines. The situation is slightly different from conventional injectors: the inner fuel flow, now shaped initially as ligaments and then as droplets, is exposed to a centrifugal force. The LISA (linearised instability sheet atomisation) model was developed by Senecal PK et al. [334] to describe this situation, considering the growth and development of surface instabilities.

At the nozzle orifice of swirl injectors, a two-dimensional, viscous, incompressible liquid sheet of thickness  $2h$  moves with velocity  $U$  through a quiescent, inviscid gas medium. Similarly to the wave model, infinitesimal disturbances grow on the sheet surface and they can be described by Equation (5.2). In this case, there are two solutions of such equations, called sinuous and varicose mode, and the first is suitable to describe engine applications [334]. For modern swirl-injectors, it can be assumed that: the second order terms of viscosity can be neglected, the critical Weber number is exceeded ( $We_g = 27/16$ ) and the gas-to-liquid density ratio is small enough ( $\rho_g/\rho_l \ll 1$ ), giving the dispersion relation equal to:

$$\omega_r = -2v_l k^2 + \sqrt{4v_l^2 k^4 + \frac{\rho_g}{\rho_l} U^2 k^2 - \frac{\sigma k^3}{\rho_l}} \quad (5.14)$$

An analogy with a cylindrical liquid jet's breakup length allows us to estimate the ligaments breakup time:

$$\eta_b = \eta_0 \exp(\Omega \tau_b) \quad \Leftrightarrow \quad \tau_b = \frac{1}{\Omega} \ln\left(\frac{\eta_b}{\eta_0}\right) \quad (5.15)$$

where  $\eta_b$  is the critical amplitude at breakup. The relative breakup length can be calculated with the hypothesis of liquid sheet constant velocity:

$$L = U \tau_b = \frac{U}{\Omega} \ln\left(\frac{\eta_b}{\eta_0}\right) \quad (5.16)$$

while being  $\ln(\eta_b/\eta_0) = 12$  [94] the ligaments diameter is:

$$d_L = \sqrt{\frac{4}{\pi} \Lambda_s \cdot 2h} = \sqrt{\frac{16h}{K_s}} \quad (5.17)$$

where  $K_s$  is the wave number  $K_s = 2\pi/\Lambda_s$ . Further ligaments breakup in droplets is calculated using the analogy of Weber's result for growing waves on cylindrical, viscous liquid columns:

$$d_{drop} = \left( \frac{3\pi d_L^2}{K_L} \right)^{1/3} \quad (5.18)$$

with:

$$K_L d_L = \left[ \frac{1}{2} + \frac{3\mu_l}{2\sqrt{\rho_l \sigma d_L}} \right]^{-1/2} \quad (5.19)$$

### Rayleigh-Taylor model

The overall breakup process, both primary and secondary breakup, is well represented by the combination of the Kelvin-Helmholtz and Rayleigh-Taylor (RT) models used together, as proposed by Liu Z. et al. [224]. The principle behind the Rayleigh-Taylor model is that the liquid-gas interface becomes unstable when the density gradient and fluid acceleration have opposite directions [363].

The Rayleigh-Taylor model is based on the stability of the liquid-gas interface accelerated in a normal direction. Drag forces create an acceleration on the droplet surface equal to :

$$|\vec{F}| = \frac{3}{8} C_D \frac{\rho_g U_{rel}^2}{\rho_l r} \quad (5.20)$$

where  $U_{rel}$  is the relative velocity between the liquid and gas and  $r$  the droplet radius.

Considering the same approximation done for the wave model, negligible viscosity and a linear disturbance growth rate, the following relations can be obtained for the fastest growing wave's maximum growth rate:

$$\Omega_{RT} = \sqrt{\frac{2|\vec{F}|}{3}} \cdot \left[ \frac{|\vec{F}| (\rho_l - \rho_g)}{3\sigma} \right]^{1/4} \quad (5.21)$$

and wavelength

$$\Lambda_{RT} = 2\pi \sqrt{\frac{3\sigma}{|\vec{F}| (\rho_l - \rho_g)}} \quad (5.22)$$

The breakup time is equal just to the reciprocal of the frequency  $\Omega$ :

$$t_{RT} = \Omega^{-1} \quad (5.23)$$

while the child droplet's diameter is proportional to the wavelength  $\Lambda$ :

$$r_d = C_{RT} \Lambda_{RT} \quad (5.24)$$

The KH and RT breakup models are usually used in combination and the breakup mechanism to use is chosen time by time as the one that predicts the shortest breakage time. Usually in the near-nozzle zone the RT breakup is the governing mechanism, while farther away KH prevails.

### Reitz-Diwakar model

Another valid model for secondary breakup is the Reitz-Diwakar model [305]. It introduces bag or stripping breakup processes depending on the Weber number. In stripping breakup the liquid is stripped from the droplet's surface, while, with lower Weber number, a non-uniform pressure field leads to the bag breakup.

This model is based on the work of Nicholls [264] and is suitable for secondary breakup. Depending on the We number, there are two breakup mechanisms:

$$\text{Stripping breakup} \quad \frac{We}{\sqrt{Re}} > \frac{1}{2} \quad (5.25)$$

$$\text{Bag breakup} \quad We > 6 \quad (5.26)$$

The break times associate with stripping and bag breakup are respectively:

$$t_{strip} = C_1 \frac{r_d}{v_{rel}} \sqrt{\frac{\rho_l}{\rho_g}} \quad (5.27)$$

and

$$t_{bag} = C_2 \sqrt{\frac{\rho_l r_d^3}{\sigma}} \quad (5.28)$$

When the lifetime of unstable droplets reaches these values, breakup occurs. The new drop size is calculated using either (Eq. 5.25) or (Eq. 5.26) considered as an equality [300]. The unstable droplet diameter is allowed to change, conserving the liquid mass.

### Taylor-analogy model

The TAB model is based on a mass-spring-damper analogy. Supposing that the liquid viscosity acts as a damper and the surface tension as a restoring force, the motion equation is:

$$\ddot{y} + \frac{5\mu_l}{\rho_l r^2} \dot{y} + \frac{8\sigma}{\rho_l r^3} y = \frac{2\rho_g v_{rel}^2}{3\rho_l r^2} \quad (5.29)$$

where  $y = 2x/r$  is a dimensionless parameter that describes temporary droplet distortion with  $r$  the droplet radius. Solving Equation (5.29),  $y = y(t)$  can be calculated and if  $y$  exceeds unity, breakup occurs. So the characteristic

time is equal to:

$$t_{bu} = \pi \sqrt{\frac{\rho_l r^3}{8\sigma}} \quad (5.30)$$

for very low We numbers ( $We \approx 6$ ).

While:

$$t_{bu} = \sqrt{3} \frac{r}{v_{rel}} \sqrt{\frac{\rho_l}{\rho_g}} \quad (5.31)$$

for high We numbers.

Finally, through an energetic balance between the surface and distortion energy, the child droplet's radius can be calculated from the following relation:

$$\frac{r}{r_{32}} = \frac{7}{3} + \frac{\rho_l r^3}{8\sigma} y^2 \quad (5.32)$$

where  $r_{32}$  is the child droplet's SMD.

The latest scientific works permit us to achieve a consistent optimisation and improvement of such models. The KH-RT breakup model was applied on the Engine Combustion Network (ECN) Spray G injector with an LES (large eddy simulation) turbulence framework by Allocca L. et al. [15]. By means of schlieren and Mie-scattering images, they validated the overall simulation and they highlighted that: the minimum cell size required to obtain an accurate representation of spray-gas interactions is  $250\mu\text{m}$ ; a too high number of parcels lead to an overestimation of the liquid penetration due to an underestimation of the drag force; a higher content of turbulent kinetic energy is present in the larger scales of flow; the plumes boundaries are the areas of the spray where there is the highest probability of ignition.

Other simulations on the Spray G injector were performed by Paredi D. et al. [278] with OpenFoam/Lib-ICE (a library specifically developed for the internal combustion engine, within the OpenFoam open source-code). Huh-Gosman for atomisation and Reitz-Diwakar for secondary breakup models were adopted and tested over a wide range of injection pressures, ambient temperatures and density. A unique set of parameters suitable for each operating condition, with good accuracy, was found. Modification of the Reitz-Diwakar  $C_2$  constant is needed only for the lowest ambient temperature and density simulations.

Wang X. et al. [390] carried out a comparison of the Kelvin-Helmholtz Rayleigh-Taylor (KH-RT) and Reitz-Diwakar (RD) breakup models tuned with experimental data. They highlighted the differences of spray morphology obtained from changing specific calibration constant values and simulation parameters. Synthetically: the mesh sizes of 0.5 mm and 1.0 mm show similar penetration for both the KHRT and RD models; coarse mesh (1.5 mm or greater) results in a stronger breakup at the beginning of injection and a larger SMD at the end of injection; the time step has a soft impact especially at low back-pressures; the increase of the  $B_1$  and  $C_{RT}$  constants, respectively of the KH and RT models leads to a weaker breakup process and longer penetration. The same behaviour was found with the RD model's constants  $C_1$  and  $C_2$ .

A completely different physical approach underlies the Taylor analogy breakup model (TAB) [274]. This method is based upon Taylor's analogy between an oscillating and distorting droplet and a spring mass system [362] (further details in paragraph 5.4). With this model the child droplets are usually all the same size. However, a Rosin-Rammler or a chi-square probability density function is often used to achieve more realistic droplet dimensions [274].

In the last decade, the injector's internal and near-nozzle zones have received attention because in GDI engines the fuel injector nozzle design can strongly influence spray characteristics such as the breakup length, initial droplet size, cone angle and exit velocity [45, 341]. Alongside previously described breakup models there are other approaches that begin from different considerations than the ones used by DDM models, these not being suitable for the dense spray region [89]. Indeed, the liquid phase is initially a continuum (a liquid jet or film) and some basic hypotheses, such as low liquid volume fraction and homogeneously distributed parcels in the computational domain, are not valid until the primary breakup takes place [18]. Consequently, spray processes were studied by modelling the liquid-gas interface with different approaches. One of these is the VOF (volume-of-fluid). The principle of the volume-of-fluid method is that a two-phase system can be represented as a mixture of phases in which the phase-fraction distribution includes sharp, yet resolvable, transitions between the phases [43, 142]. This method describes the gas-liquid interface with a unique variable: the liquid volume fraction [18]. The VOF model is usually used with an LES turbulence framework, but it requires a very small mesh size in order to capture the smallest surface wave structures [44, 265]. It must be noted that in the nozzle zone, due to the high-pressure gradient, cavitation inevitably occurs. The VOF model, based on a two-phase flow, does not account natively for such phenomena [42, 43, 45]. A model capable of handling the interaction between liquid, vapour and gas is required. To achieve this task, some models present in the literature try to link the VOF method with a cavitation model, while others extend cavitation models to account for the gas phase [122, 123, 242].

As said previously, for internal and near-nozzle regions it is very difficult to obtain experimental data, because the liquid phase is too dense. So, the direct numerical simulation (DNS) approach is an attempt to obtain numerical data that are reasonably representative of the two-phase fluid dynamics at the orifice outlet. DNS simulations are then used to obtain data in order to build and to validate possible subsequent numerical approaches, such as, for example, the one obtained by coupling VOF and level set methods, first proposed by Sussman and Puckett [357] and then modified by Menard T. et al. [199, 237]. DNS simulations are very expensive, with minimum grid sizes of the order of 2-5  $\mu\text{m}$  in the near-nozzle regions and total cell counts of the order of 200 million. Therefore, they must be limited to very small domains. However, the primary breakup takes place in a quite small area which is often limited by few injector diameters in the downstream direction. Therefore,

it is actually very appealing to test such a method even with its inherent limitations. Figure 5.8 shows DNS simulations of a liquid jet with a mesh size of  $2.5 \mu\text{m}$  [237].

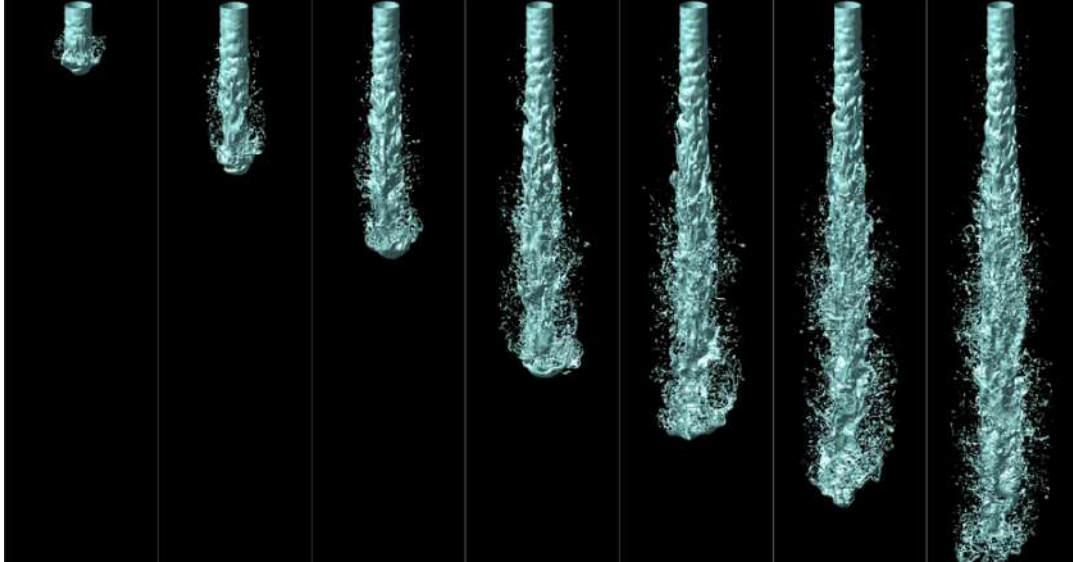


FIGURE 5.8: DNS simulation of a liquid jet.

The DDM's limitations on the spray's dense zone can be overcome also with another family of model to which belong eulerian lagrangian spray atomization (ELSA) and the Eulerian-Eulerian method belong. These treat both liquid and gas phases with the Eulerian approach in the near-nozzle dense spray region, then they switch the spray's modelling to the Lagrangian approach in the dilute region downstream of the nozzle [18, 265]. The application of such models reveals good agreement with experimental data and higher accuracy as a consequence of both higher resolution and a more suitable modelling approach [89, 377]. Other phenomena play a key role in the injection process. These are evaporation, collision and coalescence. The direct solution of the droplet heat transfer problem is not realisable due to the huge computational resources needed, so the droplet is usually assumed as spherical with averaged flow conditions. So different evaporation models were developed over the years, considering lumped, one-dimensional and multi dimensional approaches [6, 342].

Collision modelling is a very complex topic because there is a lack of experimental data with which such model can be validated. In consequence, there are few models present in the literature; the most important was developed by O'Rourke and Bracco, and it is implemented in many commercial CFD software systems [272]. It is based on energetic considerations and uses a statistical approach because in common spray simulations there is too large a number of droplets and so it is impossible to check collisions for each of them.

Table 5.3 summarises the papers on mathematical models, broken down by the research topic and model used.

TABLE 5.3: Mathematical Models Summary Table

Research Topic	Models Used	References
Primary Breakup	Wave breakup Blob Injection	[300, 302]
Primary breakup + internal nozzle flow	Baumgarten Model Huh Gosman	[40] [148, 278]
Swirl Injector's primary breakup	LISA	[334]
Secondary Breakup	Kelvin- Helmholtz/Rayleigh- Taylor Reitz-Diwakar Tab Model	[15, 224, 363, 390] [278, 305, 390] [274, 362]
Near-Nozzle Analysis	VOF VOF and Cavita- tion VOF-Level Set Method Hybrid Models (ELSA, Eulerian- Eulerian method)	[42–45, 142, 341] [122, 123, 242] [199, 237, 357] [18, 89, 265, 377]
Evaporation	Lumped, one and two dimensional	[6, 342]
Collision and Coalescence	O'Rourke and Bracco	[272]

#### 5.4.1 Influence of spray's thermodynamic parameters

Many authors have studied the influence of thermodynamic parameters on the spray morphology and breakup process. The injection pressure's influence on the spray morphology is widely studied: a higher injection pressure, obviously, determines a better atomisation and an increased jet penetration length [202, 366, 428]. Tian [366] and Lee [203] also made a comparison of some spray pictures taken at different pressure values, and a bigger penetration length is clearly visible, increasing the pressure. This behaviour is due to the entrainment of air, which closely relates to the relative velocity between the jet and the surrounding gas that facilitates the breakup of the jet. Therefore, the higher the injection pressure, the deeper the entrainment of air, and then a fully developed jet is produced more quickly.

Also, there are effects on the parcel diameter and spray cone angle, as

highlighted by [203, 215, 223]. Such researchers have captured and then post-processed spray images by means of different techniques. The measurement results showed a reduction in the droplet size with the increment of the pressure.

Fuel temperature was analysed by [223, 428]. With increased fuel temperature, the spray undergoes greater dispersion and becomes more transparent; substantial drop penetration and smaller droplets, with a more concentrated size distribution, are produced.

The effect of ambient pressure, which is directly correlated to density, on the parcel diameter is still not clear. According to some experimental studies conducted with the PDPA technique, the SMD diameter significantly increased at high ambient pressures, as reported by [215, 372], while the numerical simulations performed by Banerjee [31] highlighted the opposite trend. At elevated ambient pressure, as observed by Guo H. et al. [128], the spray collapses in the near field due to low-pressure zone formation (jet-induced spray collapse). Moreover, under flash-boiling conditions, this phenomenon also occurs in the far field [128]. Finally, the flash-boiling process is also strongly influenced by both ambient and fuel thermodynamics [216].

Zeng W. et al. [418] quantified the macroscopic characteristics of the spray plume using the dimensional analysis, obtaining some analytical relations between dimensionless numbers and the plume angle or penetration tip.

Hiroyasu H. et al. [144, 145] previously found some empirical correlation for diesel spray, but, due to different fuel viscosity, the results are not applicable to the gasoline spray [430, 431].

Table 5.4 summarises the papers on the influence of the spray's thermodynamic parameters, broken down by the parameter considered and its effects.

TABLE 5.4: Spray's Thermo-Dynamic Parameter Influence Summary Table

Parameter Considered	Effects	References
Fuel Injection Pressure $\uparrow$	Cone Angle $\uparrow$ $D_{\text{Drop}} \downarrow$ $L_{\text{Penetr}} \uparrow$	[202, 203, 223, 366, 428]
Fuel Temperature $\uparrow$	$D_{\text{Drop}} \downarrow$ $L_{\text{Penetr}} \downarrow$	[223, 428]
Ambient Density $\uparrow$	$D_{\text{Drop}} \uparrow\downarrow$ Spray's Collapse	[31, 215, 372] [128, 216]
Dimensionless Numbers		[418]

## 5.5 Spray-wall interaction

The fuel jet injected into the combustion chamber easily impacts on the surfaces of the piston head and cylinder liner. The spray wall-interaction is a very interesting research topic because it involves complex physical phenomena influencing the chain of events leading from secondary evaporation up to un-burned hydrocarbons and soot emissions [139, 258, 424].

Concerning diesel sprays, a wide analysis of such phenomena can be retrieved in the bibliography [84–86], while only lately, thanks to the ever increasing injection pressures (of the order of hundreds of bar), gasoline's jet impingement is assuming a greater scientific relevance and many aspects need deeper investigation: heat flux transfer, film boiling, splashing droplet production [220].

As described by Stanton [350] and O'Rourke [273], there are four different regimes for drop-wall interaction depending on the impact energy: stick, spread, rebound and splash. Rioboo R. et al. [308] inserted the occurrence of fingering in the spreading phase and also replaced the splash regime with four differentiated "disintegration" mechanisms, numbered as below: (iii-a) prompt splash, (iii-b) corona splash, (iii-c) receding break-up and (iii-d) partial rebound. Moita and Moreira [246] added (iii-e) finger breakup. Figure 5.9 shows the phenomena, classified by the impact energy (Fig. 5.9-a) and by an appropriate time scale (Fig. 5.9-b) [259].

With a very low impact velocity, droplets stick to the wall and, in the case of a slightly greater energy level, form a lamella which spreads and recoils, dissipating energy. Fingering occurs with moderate impact energies; in this regime the lamella is unstable and lead to the formation of fingers. Such structures grow ahead of the contact line and breakup during the last phase of spreading [11, 234, 412]. A broad explanation of the fingering process can be found in the work of Yanin [411]. Higher impact energy levels cause the droplet to disintegrate a few instants after the impact. Prompt splash is the mechanism that occurs at the spread/disintegration transition. It happens when the inertial forces overcome capillary effects [410].

Quantitative criteria to differentiate the impact regimes are provided by relations between the dimensionless groups of Reynolds, Ohnesorge, Laplace and Weber. Through different algebraic combinations of such parameters, a wide spectrum of impact situations can be described (wet or dry surfaces, roughness finish) [28, 71, 135, 262, 354, 373]. Most literature correlations uses the  $K_c$  parameter to recognise the onset of the splash regime. It is calculated as:

$$K_c = A \cdot Z^a \cdot We^b \quad (5.33)$$

The coefficients  $A$ ,  $a$ , and  $b$  assume different values depending on the impact conditions.

It must be pointed out that spray-wall interaction usually involves the impact of many drops with disparate velocities and diameters, directions and so also this aspect must be taken into account [311].

A relevant topic, strictly linked with direct injection spark ignition engine combustion optimisation and emissions reduction, is the impact of droplets

on heated walls like the piston surface. In this condition, four different heat transfer regimes occur as a function of wall temperature ( $T_w$ ) [219]:

- film-evaporation: at relatively low temperature there is no phase change, and heat transfer occurs principally by conduction and free convection;
- nucleate boiling: the heat flux reaches its maximum values, bubbles form on the wall's surface and the evaporation time decreases to the critical heat flux (CHF);
- transition boiling: as the heat flux increases an insulating vapour layer grows and partially divides the liquid and solid wall, and the heat flux reduces to its minimum at the Leidenfrost point;
- film boiling: with a higher surface temperature an insulating vapour layer divides liquid spray from the solid wall and in this way heat is transferred by conduction, and the evaporation time slightly decreases.

Figure 5.10 summarises this [220].

The wall temperature strongly influences the so-called secondary evaporation and consequently affect the mixture formation, combustion and emissions.

The wall impact regimes, too, are a function of wall temperature. Figure 5.11 [21] shows the transition conditions as a function of the impacting droplet  $We$  and wall temperature as reported by Bai and Gosman [28].

Once the impacting droplets have disintegrated by one of the previously described mechanisms, secondary droplets will be created with completely different characteristics. The knowledge of the quantitative correlations between the drop's morphology before and after impact form the basis of spray-impingement models. Such relations are widely present in the literature for non-heated walls while only a few of them are available for heated walls. Below, the features of the main models, capable of predicting the size, velocity and number of secondary droplets, are reported.

Bai and Gosman's [27] model, based on experimental data sets found in the literature, recognises the different regimes, stick, rebound, spread or splash, if the wall is wet, spread and splash for impinging on dry walls. The model uses transition criteria based on the drop's Laplace number ( $La$ ), taking also into account in dry conditions the surface roughness. Droplets produced from splash have a random size, while a modified version, from the same authors, adopts a chi-squared probability function [29]. Stanton and Rutland's model [350] considers wall-film covered surfaces and uses fixed  $We$  number values as the threshold between the stick, rebound and spread regimes. The model is also sensitive to impact of multiple drops. Mundo, Sommerfeld and Tropea's [262, 263] empirical model considers, as a transition criterion between regimes, a new critical parameter  $K$ , a function of the  $Re$  and  $Z$  numbers, independent of the surface structure. The Kuhnke model [190] uses the  $K$  parameter too and it is sensitive to the surface temperature as well as dry and wet walls. Senda and Fujimoto's model has the particular feature of dividing the impingement regimes into two groups depending on

the energy level [333]. Kuhnke's model gives reasonable results in terms of width and thickness: both the liquid thickness and width are over-estimated for high injection pressure, while the vapour thickness is slightly underestimated for high wall temperatures [291]. With high temperature, it was found [55, 250] that the  $k-\epsilon$  turbulence model diffuses gasoline vapour more quickly from the wall zone than the  $k-\zeta-f$  model. This behaviour offsets the previous model underestimation and gives results in accordance with experimental observations.

A comparison between the Kuhnke and Mundo models, implemented for a multi-hole injector (as reported by Montanaro A. et al. [250]), reveals, in particular, that the Kuhnke model is quite appropriate to reproduce the secondary evaporation, consequent droplet transient heating, and the liquid splashing and rebounding. Indeed it is sensitive to the wall temperature and the transient heating effects. An example of such comparison is shown in Fig. 5.12.

AVL Fire's thin-wall sub-model, taking into account transient cooling effects, also gives good results of the amount of wall-film mass and spray interaction [24, 291, 369]

Lately, an interesting new approach was developed. It is the smoothed particle hydrodynamics (SPH) method, initially developed for non-axial phenomena in astrophysics [247], and was modified to simulate the drop-surface impact in combustion devices [409]. This methodology, shown in Fig. 5.13, highlights a good agreement with the experimental data and can recognise the crown formation as well as the drop spreading.

Although it has already been mentioned, it should again be underlined that wall impingement has a great influence on many aspects of the direct injection spark ignition engine: the spray's impact over metallic surfaces (like the piston head) creates the liquid wall-film that influences all the consequent processes. The CFD analysis, incorporating impingement models, becomes a powerful tool to perform simulations that account for and link the effects of such phenomena to the subsequent ones like mixture formation, combustion, and pollutant emission, with the final aim of improving general GDI engine design.

As an example, Catapano F. et al. [55] considered a piston equipped with thermocouples to acquire the surface temperature values and validate a 3D model describing the spray-piston interaction in order to obtain further parameters not available from experimental observations. A complete temperature map of the piston shows that the gasoline has a cooling effect that strongly affects the evaporation process. Equivalence ratio maps of the mixture, at different time steps present near the piston head, highlights that the evaporation is enhanced by increase of the wall temperature and it influences the mixture formation process [1, 55]. The thickness of a smaller wetted area can be achieved, also increasing the excess-air ratio because in this way less fuel is injected and so soot emissions also diminish [335].

In the last few years, thanks to diagnostic techniques such as XPCI, PDPA, ultra-fast X-Ray imaging and schlieren, a wider comprehension of the wall-impingement process was achieved. To detect both impinging liquid and

vapour phases Mie scattering and schlieren are used in a quasi-simultaneous mode [253, 291]. Proper post-processing of images allows us to detect the liquid phase contour and so measure its width and thickness [13, 251]. The fuel adhesion thickness can be measured with infra-red (IR) refractive-index-matching (RIM) [96] and LIF, although this last method is limited to perfectly smooth impinging walls [230]. Through these experimental techniques, it was observed that a high wall temperature favours fuel evaporation that begins from the periphery [1, 229, 252] and so reduces the wall-film thickness. Also, an inverse proportionality is confirmed for the width except for some temperature values higher than the Leidenfrost point, as expected [252]. A high ambient pressure increases the fuel adhesion mass and leads to a uniform distribution [228], while higher injection pressures reduce the wall-film mass [324]. Instead, an opposite result was found, by means of schlieren-Mie scattering imaging, by Montanaro A. et al., who underlined a direct proportionality between the injection pressure and wall-film thickness [253]. Among the many parameters analysed by Schulz F. et al. [324], by means of RIM, it is interesting to observe how the spray's impact angle has a great influence on many of the wall-film's parameters, such as heat-flux, mass, width and height. IR measurement campaigns have also highlighted that a nozzle with a sharp inlet and an orifice length-to-diameter ratio of 1 is the best configuration to accelerate heat transfer and so evaporation [323].

PDPA observations of an impinging spray under engine conditions on a flat plate allow us to understand the droplet size distribution along the vertical distance and radial axis before and after the impingement. Before impingement, there are large droplets with an "M-type" probability distribution of droplet numbers and " $\wedge$ " distribution of SMD while later a vertical ">" curve type is recognisable [231].

Table 5.5 summarises the papers on spray-wall interaction, broken down by research topic with a useful short description.

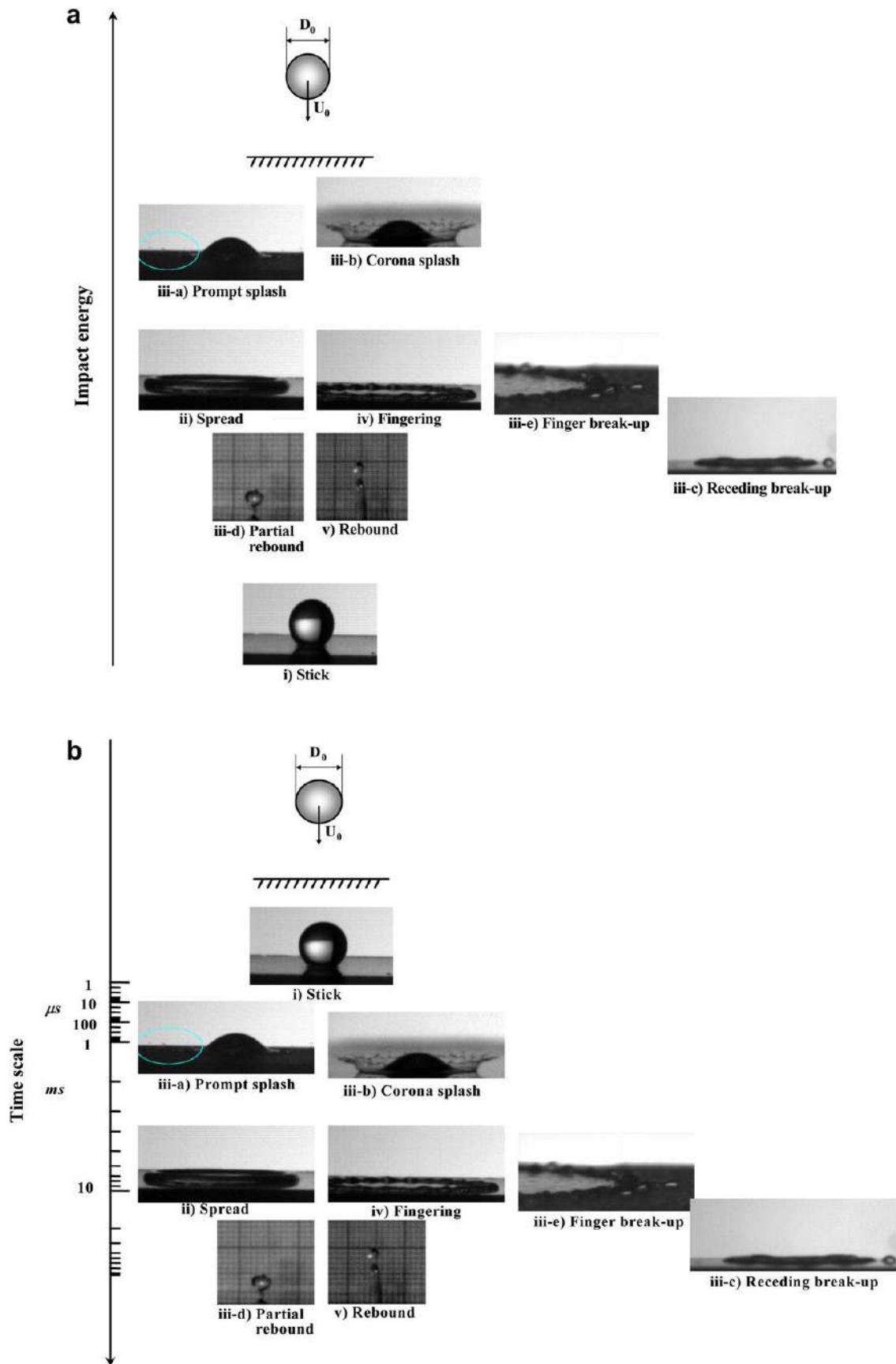


FIGURE 5.9: Classification of drop impact mechanisms.

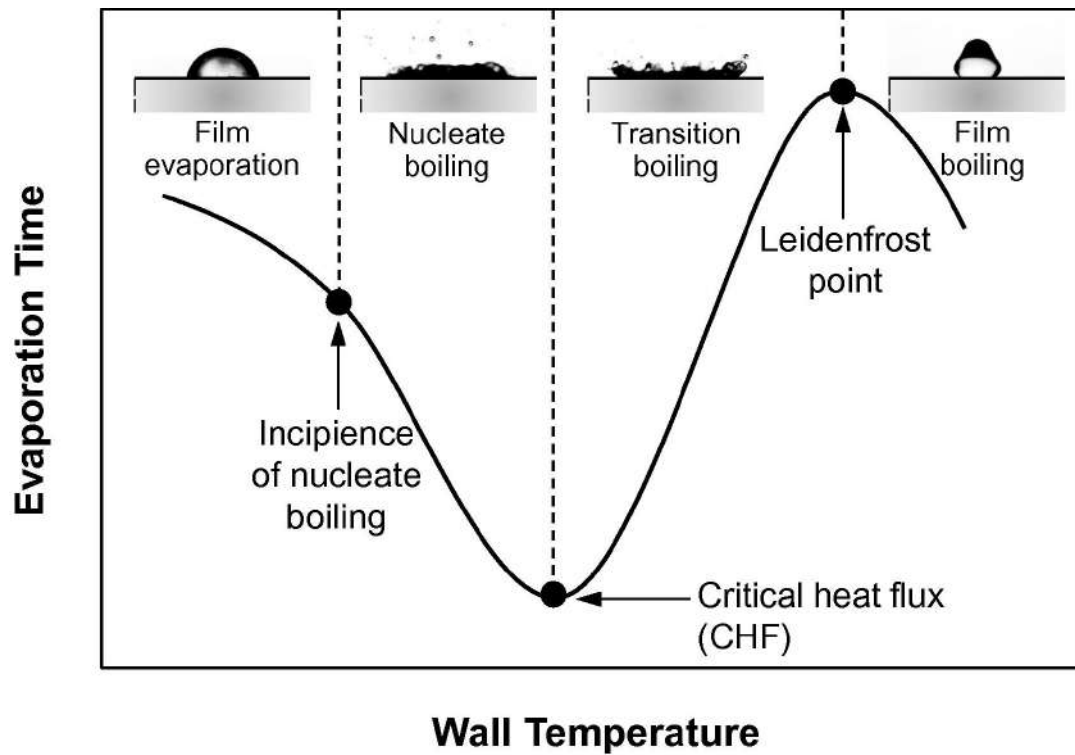


FIGURE 5.10: The heat transfer regimes of a droplet impinging an heated wall.

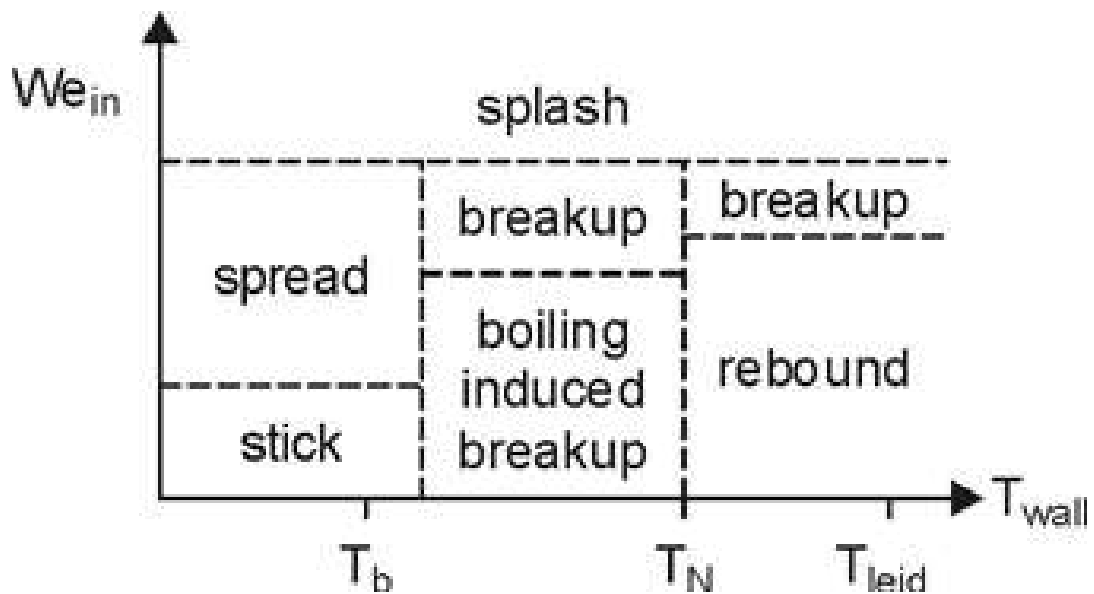


FIGURE 5.11: Impact regimes and transition conditions for heated walls.

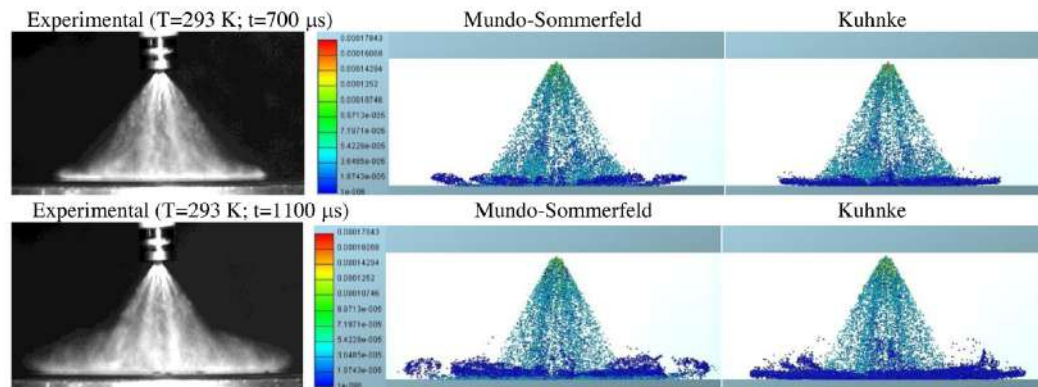


FIGURE 5.12: Experimental and numerical spray data from Montanaro et al.'s investigations.

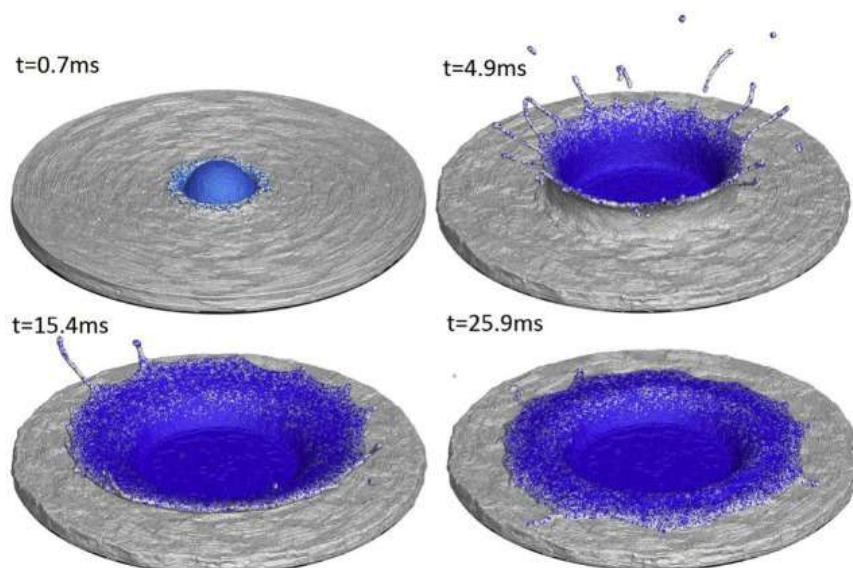


FIGURE 5.13: Water drop impact on a wetted surface as simulated with SPH method.

TABLE 5.5: Spray-Wall Interaction Summary Table

Research Topic	Short Description	References
Spray-wall interaction	General influence on internal combustion engines	[84–86, 139, 220, 258, 424]
Impingement regimes	Description of droplet-wall interaction mechanisms	[273, 350]
	Further classifications	[259, 308]
	Fingering Process	[11, 234, 246, 411, 412]
	Prompt Splash	[410]
	Transition criteria	[28, 71, 135, 262, 354, 373]
	Multi-droplet impact	[311]
	Impact on heated wall	[21, 28, 219]
Mathematical models	Bai and Gosman (based on experimental data)	[27, 29]
	Stanton and Rutland (uses We number fixed values)	[350]
	Mundo, Sommerfeld and Tropea (uses K parameter transition)	[250, 262, 263]
	Kuhnke (uses K parameter transition)	[55, 190, 250, 291]
	Senda and Fujimoto (uses energetic considerations)	[333]
	Thin-wall submodel	[24, 291, 369]
	SPH approach models	[247, 409]
Thermodynamics Parameters	Influence of the ambient and injection pressure	[228, 253, 324]
	Impact angle	[324]
	Nozzle design	[323]
	Heat transfer process	[55, 291]
	Temperature Influence	[1, 55, 229, 251–253]
Impingement and GDI engines design	Piston surface spray's interaction	[1, 55]
	Combustion and wall impingement	[335]
Experimental Visualization	Mie-Scattering/Schlieren	[13, 251–253, 291]
	PDPA imaging	[231]
	Infra-red RIM	[96, 228–230, 323, 324]

## 5.6 Mixture Formation and Combustion

Once injected, the fuel droplet continues its journey in the combustion chamber where the whole injection process fulfils a first-importance role in the chain of events that begins from the air-fuel mixing phase, passes through combustion, and ends with generation of the pollutant.

The key-innovation of Spark Ignition Direct Injection (SIDI) engines is that the air-fuel mixture formation process takes place directly in the combustion chamber [371]. This makes it possible to overcome the limits of PFI and, at the same time, to adapt the in-chamber mixture composition to the engine's operating conditions, in order to improve the fuel consumption and, in general, the performance [5, 76]. Traditional PFI engines were modified and improved, developing advanced and dedicated direct injection systems, new intake ports, new combustion chambers and new piston head shapes [426]. Such engine configuration (GDI) determines radical changes in both the mixture formation process and combustion dynamics and strategies (stratified or homogeneous charge), requiring deepened studies. In this respect, engine geometric models are used together with experimentally tuned spray models, to reproduce in-cylinder air motion and to develop thermo-fluid dynamic simulations of the entire engine cycle. It is thus also possible, without having to investigate a real engine, to optimize the air/fuel mixture and combustion, saving time and money [72, 312]. As a consequence of the aforementioned, the researches that analyze the effects of the engine's operating and design parameters (injection pressure, fuel temperature, plunger geometry, injection strategies, ignition timing, ...) on the mixture formation are of fundamental importance.

### 5.6.1 Effects of Engine Design Parameters on Mixture Formation

#### Injection Pressure

The most important index used to evaluate air/fuel mixture quality is the Equivalence Ratio (ER): the local air/fuel ratio over the stoichiometric one.

As shown by Piock W. F. [292], Addepalli S. et al. [4] and Reddy A. et al. [299], higher fuel injection pressure leads to more uniform ER in-cylinder distribution due to better atomization and faster evaporation of fuel droplets. Because of the transfer of momentum from the injected fuel to the surrounding air, the turbulent kinetic energy (TKE) increases too, while the tumble ratio (TR) does not seem to be affected by the injection pressure due to the symmetry of the used injector's holes [4, 183, 299].

#### Fuel Temperature

The fuel temperature strongly affects the mixture formation process. Jing D. et al. [165] demonstrated how high temperature values lead to spray collapsing due to stronger jet-air interaction. The consequent short penetration promotes a more homogeneous mixture distribution. As described in more

detail in the previous review (Part 1), the occurrence of flash boiling is greatly enhanced by a relatively high fuel temperature.

### **Injection Strategies**

It is interesting to understand the crucial role played by the injection strategies. An homogeneous charge can be obtained injecting the fuel during the intake stroke as a high, favourable, dispersion of fuel droplets occurs. A delayed injection timing, during the compression stroke, does not give enough time to reach a uniform-distributed mixture within the combustion chamber leading to the formation of a stratified mixture, [76, 166, 180].

A double injection strategy, injecting a small amount of fuel right before the spark timing, increases the engine power thanks to the additional turbulence induced by the second injection [166, 182, 348].

CFD simulation coupled with a Simplex optimization algorithm was performed by Costa M. et al. on a single cylinder, four valve, four stroke engine. [72, 73]. They developed a fully automatic procedure to tune the sub-model of direct injection spray and a 3D numerical model of the engine (developed within the AVL Fire environment) to select the best injection strategy. It was found that the start of injection (SOI) placed at  $475^\circ$  (being  $0^\circ$  the beginning of the expansion stroke) and spark ignition (SI) at  $680^\circ$  maximize the engine performances, in the case of a single injection strategy. In the case of two events injection the optimal values are: SOI equal to  $450^\circ$ , dwell equal to  $80^\circ$ , spark ignition remaining at  $680^\circ$ . In another publication Costa M. et al. [74, 76] studied the flame initiation and early propagation, both experimentally, in a optically accessible engine, and numerically, by a 3D engine model capable to follow the evolution of the asymmetric flame front consequent to the flow motion in the combustion chamber. The authors highlight that changing the injection and ignition timings leads to a different flame propagation modality. Indeed, for example, mixture inhomogeneity, caused by a late injection, was found, responsible of asymmetric flame front propagation, self-ignitions and poor combustion efficiency.

Besides, Xie F. et al. [404], working with a stoichiometric mixture and under medium and low load engine operating conditions, highlight the crucial importance of the injection and ignition parameters to reduce particulate emissions.

### **Injector and Spark-Plug Positions**

Optimizing the position of the injector and spark-plug have great influence, especially, on the performances of wall-guided GDI engines [408]. In these engines, operating with late injection, spark-plug and fuel injector position, such as injection pressure and timing, are fundamental to create a combustible mixture near the spark plug. Besides, the piston top surface is designed in such a way that the injected fuel is directed towards the spark plug to form a combustible mixture at the time of ignition (stratified charge). Karaya Y. [171] and Saw O. P. [319] investigated spark plug position and orientation with respect to the injector. For both the authors the final relative position of

the injector and spark plug is almost the same: the spark plug is placed on the engine head's centre and the fuel injector between the two intake ducts. In such configuration the mixture is ideally stratified as desired, the combustion is faster (as demonstrated by the highest value of heat release rate) and the in-cylinder-pressure is higher too.

### Spark Advance

Reddy A. et al. [299], in their detailed parametric study on a GDI engine operating in lean stratified mixture condition, highlight as a spark advance variation from 7.5 to 20 crank angle degrees (CAD) before the TDC determines increase of the indicated thermal efficiency and the indicated mean effective pressure (IMEP). Instead, because of similar fuel injection pressure (110 bar) and inlet boundary conditions, not significant TR and TKE changes occur and values of the equivalence ratio in the flammability range, at the spark plug location, can be observed. Similar results were shown by Costa M. et al. [76]: the advance of the start of spark advance (SOS) produces an increase of work until the phenomenon called "arrested phasing" occurs.

### Piston Shape

The piston shape also affects the mixture stratification. Harshavardhan B. et al. [137] analysed in-cylinder air flows and air-fuel interaction created by different piston shapes, understanding that the flat-with-centre-bowl piston gives higher cylinder air speed. The TR and TKE with the flat with centre-bowl piston engine are higher compared with other piston shapes. Zheng Z. et al [427] confirmed these results and underlined how this shape helps the formation of a combustible mixture around the spark plug at the time of ignition. Figure 5.14 shows four different piston shapes [427]. It is highlighted that the D configuration shows the best distribution of the equivalence ratio, a higher turbulent kinetic energy at the ignition time and also a thinner gasoline liquid film.

### Valve Position and Orientation

The inlet valve's orientation strongly influences the TKE and TR of in-cylinder airflow as well as the overall combustion process. It is known that the swirl intake port design improves the mixture formation in compression ignition engines, but lately studies conducted by Karaya Y. et al. [170] have demonstrated how it could do the same for GDI engines, enhancing the indicated mean effective pressure (IMEP) in stratified operating mode. Unfortunately, this also leads to higher emissions of  $\text{NO}_x$  and HC for high values of ER.

Saw O. P. [320] used CONVERGE CFD software to analyze a single-cylinder wall-guided four-stroke GDI engine, concluding that a  $14^\circ$  cylinder head pent roof angle is the best compromise between the engine's performance and  $\text{NO}_x$  emissions.

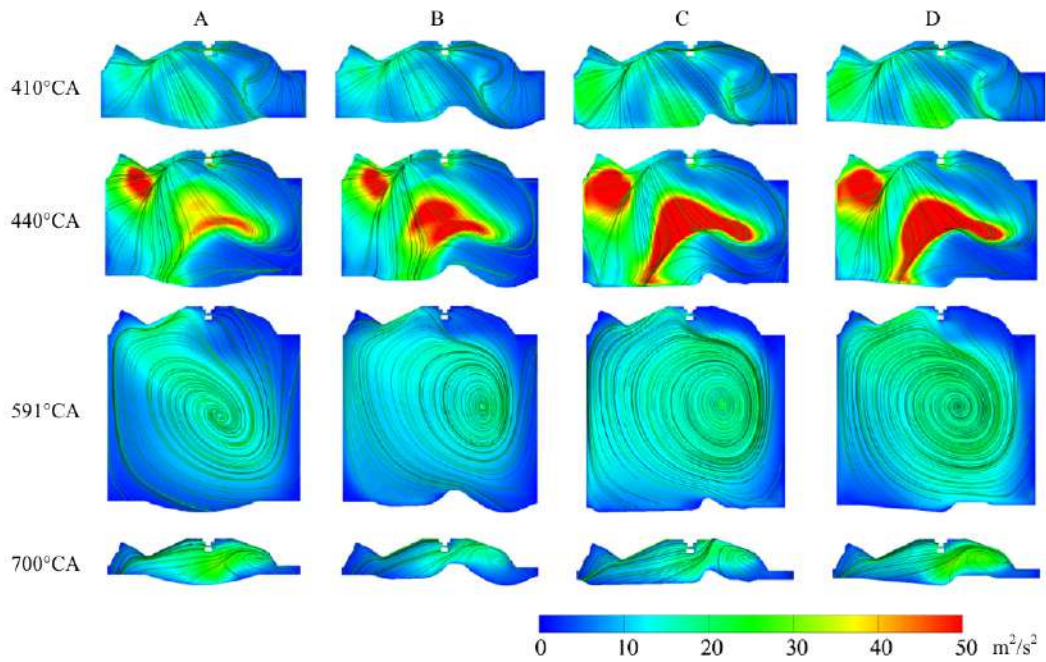


FIGURE 5.14: Effects of piston shape on turbulent kinetic energy.

### 5.6.2 Other Parameters

The compression ratio (CR) does not influence the flow structure inside the combustion chamber and so the ER's map remains more or less the same [3]. Instead, the TKE decreases because the reduced space available for the parcels restricts air motion inside the cylinder, which results in the reduction of the magnitude of fluctuating and mean components of velocity [4]. Another parameter that strongly affects in-cylinder air motion is the engine speed: both TR and TKE significantly increase with the increment of this parameter [3, 4, 188].

Table 5.6 summarizes the papers regarding the mixture formation process available in the literature with a short comment.

TABLE 5.6: Mixture Formation Process Summary Table

Studied Parameter	Comment	References
Injection Pressure	Direct proportionality with ER and TKE. Bulk air motion not affected	[4, 299]
Injection Strategy	Enhancement of turbulence, atomization and flame propagation; particulate reduction Parametric Optimization	[74, 76, 348, 404] [72]
Injector position	Improvement of mixture, reduction of emissions	[171]
Spark Advance	Significant Role for IMEP and Thermal Efficiency	[299]
Piston Shape	Design Optimization	[137, 427]
Inlet Valve	Best Orientation and Swirl Design	[170]
Cylinder's Head	Design Optimization	[320]
Compression Ratio	TKE decrease, Same Flow Structure	[3, 188]
Operating Speed	Effects on mixture stratification, TKE and TR	[3, 4]

## 5.7 Combustion Modelling

The in-cylinder mixture distribution significantly affects the combustion dynamics and make it possible to have two operating modalities of GDI engines (Addepalli S. et al. [5]). As illustrated in Figure 5.15, the combustion can be classified as stratified or homogeneous depending on the air-fuel charge distribution [57].

At the partial load conditions, a stratified charge (late injection) is used. The fuel is injected during the compression stroke (Figure 5.15 on the right) to obtain a stratified charge near the spark plug at the instant of ignition. A homogeneous charge (early injection) is preferred for the higher load conditions. The fuel is injected during the intake stroke (Figure 5.15 on the left) to provide a homogeneous mixture. The engine operates under stoichiometric or a slightly rich condition at full load [349]. This has strong implications also for the engine's emissions.

During the combustion process, various and complex events occur, such

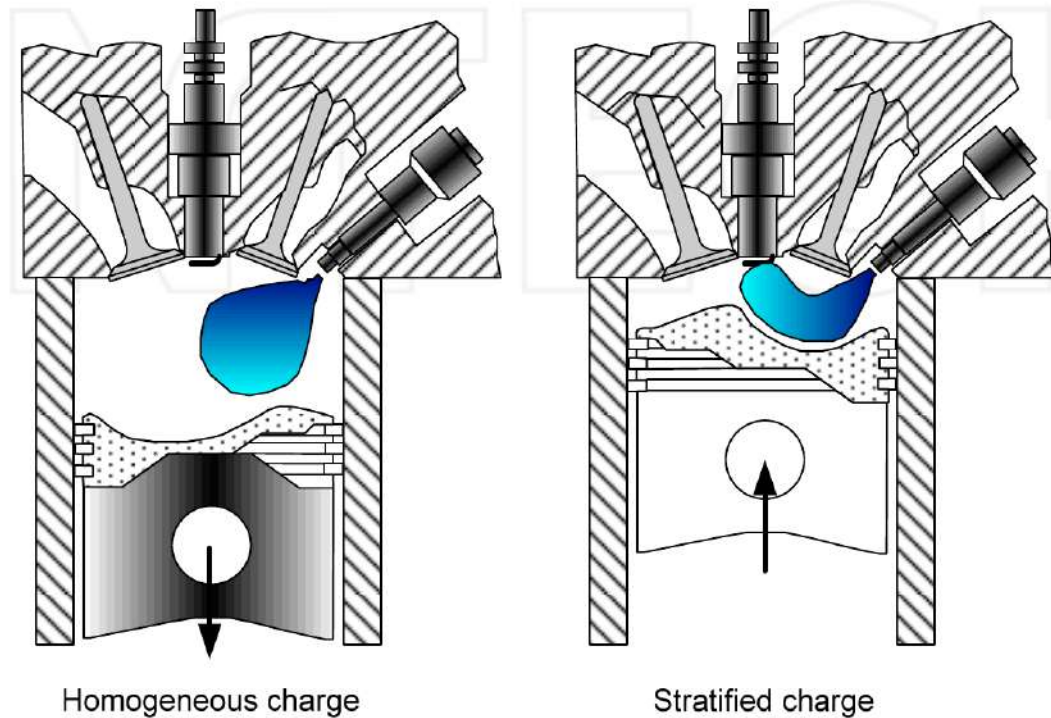


FIGURE 5.15: Operating modes of a GDI engine.

as the ignition, turbulent flame propagation, multiple chemical reactions, maybe knock, and so, consequently, in the past and over the years many different mathematical models were developed [110, 211, 289, 317, 359, 368].

Recently, particular attention was paid to the ignition process and to anomalous combustion phenomena, such as knock and misfiring. The main recent researches on these topics are discussed below. The ignition process has a great influence on the kernel development and flame propagation [143]. The Swept-Volume method developed by Zhu G. et al. [429] provides a more accurate evaluation of the volume swept by the flame within a time step. Usually this is approximated with the turbulent flame speed, but the authors demonstrated that this hypothesis is not accurate and so they decided to develop this new model. It captures new features of the flame propagation, and also the values of the indicated pressure and heat release rate are in good agreement with experimental data.

The Triangulated Lagrangian Ignition Kernel Model (TLIK) developed by Perini F. et al. [287] shows the sub-grid features of the early flame kernel development that the former Discrete Particle Ignition Kernel model (DPIK) does not capture [111]. DPIK simulates a spherical kernel development without the necessity for a fine grid resolution close to the spark plug, while TLIK simulations showed that the early flame kernel development is significantly far from the spherical shape that is supposed by the DPIK model. Sforza L. et al. [339] developed a Eulerian-Lagrangian model for premixed spark ignition combustion systems capable of describing the flame stretch effects. It was highlighted that they are negligible after the combustion's early propagation stage.

The occurrence of knock is a critical issue and a limiting factor in the development of spark ignition direct injection engines [365]. Knock onset, knock intensity, super-knock and pre-ignition are all phenomena strictly linked with knock itself [168]. The stochastic nature of engine knock, the instability of combustion and the consequent cycle-to-cycle variability (CCV) of turbulent flows would suggest LES as the most appropriate approach for CFD simulations. However, valid results could be obtained also with RANS-based models. The use of a variance equation and a Probability Density Function-based knock model (PDF) make it possible to overcome these problems [79]. Lately, the Tabulated Knock Model is the one used most due to the relatively small computational effort required. It relies on a tabulated chemistry approach and on a RANS turbulence modelling framework [52]. Usually optically accessible engines are used to validate these numerical models and to study the effects on the knock tendency of various parameters such as spark and intake valve timings [54, 153, 227, 241]. On the other hand, the ever increasing computational resources available allow the implementation of the first LES turbulent combustion models, which showed, as expected, a better prediction of the in-cylinder air-speed fluctuation and especially the combustion cycle-to-cycle variations (CCV) [41]. CCV could lead to misfire or knock, limiting the engine's operating regime [60, 114–116].

As already discussed, due to direct fuel injection, GDI technology permits a stratified charge operating mode. The preparation of the air/fuel mixture is quite challenging and requires a rich composition confined near the spark plug and ultra-lean composition elsewhere in the cylinder. To achieve this goal, both RANS and LES simulations are used and three different mechanisms of mixture formation could be retrieved: spray-guided, air-guided and wall-guided [157, 281, 356, 383].

Table 5.7 summarizes the papers regarding Direct Injection Spark Ignition Combustion Models available in the literature with a short comment.

TABLE 5.7: Combustion Modelling Summary Table

Topic	Analysis	References
Engine Operating Modality	Stratified and Homogeneous Charge	[5, 57, 349]
Combustion Process	Chemistry Models Available in literature	[110, 211, 289, 317, 359, 368].
Ignition Process	Ignition Models For Kernel Development	[111, 339, 429]
Knock Tendency	Knock Occurrence: Limiting Factor, Models Available	[52, 168, 365]
	Design Parameters Influence	[54, 79, 153, 227, 241]
Cycle-To-Cycle Variations	Models With LES Framework	[41, 60, 114–116].
Stratified Combustion	CFD Analysis and A/F Mixing Mechanisms	[157, 281, 356, 383]

## 5.8 Emissions Studies

The most relevant features of the direct injection spark ignition engines can be summarized as follows: fuel consumption is reduced, specific power is higher and limited CO<sub>2</sub> tailpipe emissions. Indeed, as showed by various authors in literature, due to the higher fuel efficiency, CO<sub>2</sub> emitted by GDI engines are averagely lower than diesel and PFI engines [268, 296, 315].

The stratified charge operation mode, characteristic of the GDI engines, involves complex production dynamics of pollutants like HC, CO and NO<sub>x</sub>.

The NO<sub>x</sub> emissions depend on many factors, ad example, optimizing the injector and spark-plug positions they can be reduced, but, engine performances decrease [319]. The same consideration can be pointed out for the adoption of the intake swirl port design [320]. Another effective way to reduce the NO<sub>x</sub> production is the adoption of a delayed injection which implies a lower peak temperature [204]. The NO<sub>x</sub> emissions are higher at higher fuel injection pressures because the improved atomization produces finer fuel droplets, an enhanced combustion and finally higher in-cylinder gas temperature [299]. Such emissions can be reduced adopting exhaust gas recirculation systems (EGR) [293, 425]. However a too high EGR rate leads to unstable combustion and so a trade-off relationship must be found to avoid such phenomenon occurrence [204].

HC and CO emissions are dependent on the completeness of combustion and on the mixture formation process [97]. Splitting injection is one technique to reduce HC emissions [75, 270]. Unburned hydrocarbon emissions are insensible to spark timing and fuel injection pressure while are higher for an open valve injection due to interaction of the fuel spray with the intake

valve. [310] The production of unburned hydro-carbons seems to increase also adding an higher EGR amount [421, 425] while there is not a strong correlation with piston temperature and no noticeable difference between swirl and multi-hole injectors [204].

From the discussions above the necessity of finding a trade-off condition between the reduction of different kind of pollutants arises. It can be well underlined with the case of the CO which decreases with the increase of fuel injection pressure. Reddy A. et al. [299] found that the CO emissions decrease by about 92.9% and 94.6% respectively at 150 and 200 bar fuel injection pressures, compared to that at 110 bar. So, if on the one hand, an higher fuel injection pressure leads to a faster and complete combustion, and hence less CO formation, on the other, as seen previously, increases  $\text{NO}_x$  production.

Anyhow at this point, it is important to underline, that no great differences between GDI and PFI engines gaseous emissions result from literature analysis [315] and, besides,  $\text{NO}_x$  are definitively lower compared to the diesel ones [268].

The main issue of the direct injection spark ignition engines is broadly recognized being the production of particulate matter caused by the internal mixture formation and the possible spray-wall impingement. The soot emissions of a GDI engine are consistent and especially much higher than a PFI engine, therefore, exhaust gas treatment systems, such as gasoline particulate filters (GPF), must be used and are in continuous development in order to meet the emissions regulations [58, 403]. For all these reasons, lately, the study of GDI engines soot emission has become a relevant research topic as shown by the broad literature about it [26, 64, 298, 370].

The soot particles are different in concentration, size, morphology and chemical composition compared with those produced by diesel engines [172, 193, 336]. As shown by Seaton A. et al. [325], alveolar, fine and ultrafine particles are more dangerous to the human respiratory system than larger particles because they have a greater penetration depth. They reach the lung's alveoli, where the self-cleaning process by macrophages fails [159]. It is important to focus attention on the particle formation process. It can be divided into six steps: pyrolysis, nucleation, surface growth, coalescence (or coagulation), agglomeration and oxidation [119, 120, 175, 260]. Thermal pyrolysis involves alteration in the molecular structure of hydrocarbons under high temperature without significant oxidation despite the presence of oxygen [201]. After temperature peaks have faded out, the nucleation particles coagulate into bunches of particles (70–100 nm). However, the nucleation phase remains poorly understood [119]. Surface and spatial growth increases the volume of particles. Then the particles collide and merge into bigger spheroids reducing the overall number but obviously keeping the mass constant. This is the coalescence or coagulation phase. Finally, the existing particles stick together to form large groups of soot aggregates, typically with fractal-like structures [367]. Knowing the soot formation mechanisms is fundamental to optimize thermo-dynamic processes and engine design parameters, in order to avoid high amounts of particulate emissions.

### 5.8.1 Effects of Injection Parameters and Combustion Strategy

Higher injection pressure values lead to a reduction of the number and mass of particles, due to the more uniform air–fuel mixing process and consequent best vaporization [80, 286, 292, 389].

The soot emissions, injection timing and fuel impact on surfaces are together strictly correlated. A late injection, typical of stratified combustion, causes the fuel to have insufficient time to completely mix with air, promoting higher amounts of particulate emissions. Instead, an early injection, typical of homogeneous combustion, increases spray-wall interactions, so, the fuel, remaining as liquid phase on the solid surfaces of the piston and liner, produces a number of particles greater than one or more orders of magnitude [139, 422]. One solution to this problem is a multiple phase injection strategy that makes it possible to have the shortest fuel jet length, to reduce the fuel's impact on surfaces, to improve the mixture formation process and so, finally, to reduce particulate emissions [49, 164, 269, 355, 404].

Zhang M. et al. [421] carried out an experimental investigation using the Taguchi method to highlight the mutual influences of various engine parameters, concluding that adding a proper amount of air and EGR diluents, retarding the ignition timing and rising injection pressure, all help to reduce the particulate number (PN) concentration.

Combustion, too, obviously has a great influence on the particulate emissions. Combustion and emissions models are often linked together in order to understand the quality and quantity of particulate created during the engine cycle [50, 388]. A rich mixture composition, compared to the stoichiometric one, leads to a higher number of particles. On the other hand, a too lean mixture entails an incomplete combustion and, thus, an increment of the particulate mass [74, 164].

The ignition timing has a great influence on the number of particles. An early timing leads to a longer combustion, leaving more time for particulate oxidation [280, 395].

So-called pool fires, in other words the combustion of liquid fuel, are another source of PM emission. Pool fires often occur on metallic surfaces and for this reason proper design of the piston and head surfaces is essential. Optical engines are usually used to capture images of the bright yellow flame's characteristics of this combustion dynamic [35, 48, 232].

### 5.8.2 Effects of Fuel Characteristics

The composition and physical proprieties of fuels are relevant factors that strongly affect particulate emissions [7, 184]. Further than the engine's design parameters optimization, a very recent research topic is the development of new fuels that are able to substantially reduce particulate emissions. Fuel blends with an high aromatic content lead to high PN emissions. PN and PM benefit from the reduction of olefin components [65, 391, 405]. A more

volatile fuel promotes a good mixture formation and combustion and, finally, a noticeable reduction of particulate emissions [176].

Six different Chinese phase IV and V gasolines composed with various percentages of ethanol, sulphurs, aromatic hydrocarbons and olefin were tested on a GDI engine by Wang Y. et al. [391], confirming the above statements. Finally, it is possible to highlight that ethanol has a low energetic density, but its addition reduces the gasoline's vapour pressure, enhancing evaporation and thus reducing particulates [36, 56, 66, 218, 233, 389]. Ethanol has a 34.8% oxygen gravimetric content that makes more complete combustion and a more efficient post-flame oxidation possible [37]. Differently to ethanol, methanol effects on particulate emissions are not directed to their reduction because it has a relative high vapour pressure (referred to ethanol) and it involves a local cooling in the air-fuel mixture within combustion chamber caused by the higher vaporization enthalpy [197, 198, 245].

Table 5.8 summarizes the papers regarding the emissions studies available in the literature with a short comment.

TABLE 5.8: Emissions Studies Summary Table

Topic	Comment	References
Emissions in GDI engines	CO <sub>2</sub> emissions and PFI comparison	[268, 296, 315]
	NO <sub>x</sub>	[204, 293, 299, 319, 320, 425]
	HC and CO	[75, 97, 204, 270, 299, 310, 421, 425]
	Particulate matter problem, exhaust gas treatment devices	[26, 58, 64, 296, 298, 370, 403]
Particulate characterization	Differences among diesel particles, formation process description	[119, 120, 159, 172, 175, 193, 201, 260, 325, 336, 367]
Effects of injection parameters on particulate matter	Injection pressure	[80, 286, 292, 389]
	Injection timing	[139, 422]
	Multi-phase injection	[49, 164, 269, 355, 404]
Effects of Combustion strategy on particulate matter	Stratified-lean combustion	[50, 74, 164, 388, 421]
	Ignition timing	[280, 395]
Pool fires Effects of fuel composition on particulate matter	Liquid fuel combustion	[35, 48, 232]
	Aromatic content	[65, 391, 405]
	Olefin content	[391, 405]
	Fuel volatility	[176]
	Ethanol content	[36, 37, 56, 66, 218, 233, 389]
	Methanol content	[197, 198, 245]

## 5.9 Injector Deposits and Fouling

Unlike PFI engines, in gasoline direct injection engines, because the mixture formation process takes place directly in the combustion chamber, the injection system is exposed to high temperatures and pressures and comes into direct contact with the combustion gases. Therefore, the phenomena of deposits and fouling on the injector become extremely important. So, as this has a strong impact on the air/fuel mixture distribution and on the vehicle emissions, it becomes central to understand how the deposits affect the injection process [19]. There are two places where deposits grow: at the nozzle exit and inside it, consequently modifying the fuel flow rate and spray pattern. It

is widely recognized that a relevant injector fouling can lead to engine misfiring and drivability problems and, most importantly, it can shorten a vehicle's life [20, 424].

The injector fouling process can be experimentally visualized using different techniques. First, imaging methods such as optical and scanning electronic microscopy (SEM) are used to analyze the deposits structure [81]. X-ray micro-tomography and thermo - gravimetric analysis (TGA) are, also commonly used, respectively, to reconstruct a 3D geometric surface that represents the injector's fouled tip and to define the chemical composition of deposits formations [417]. Figure 5.16 shows three micrographs of injectors, representing three different conditions: clean, fouled and cleaned-up [140].

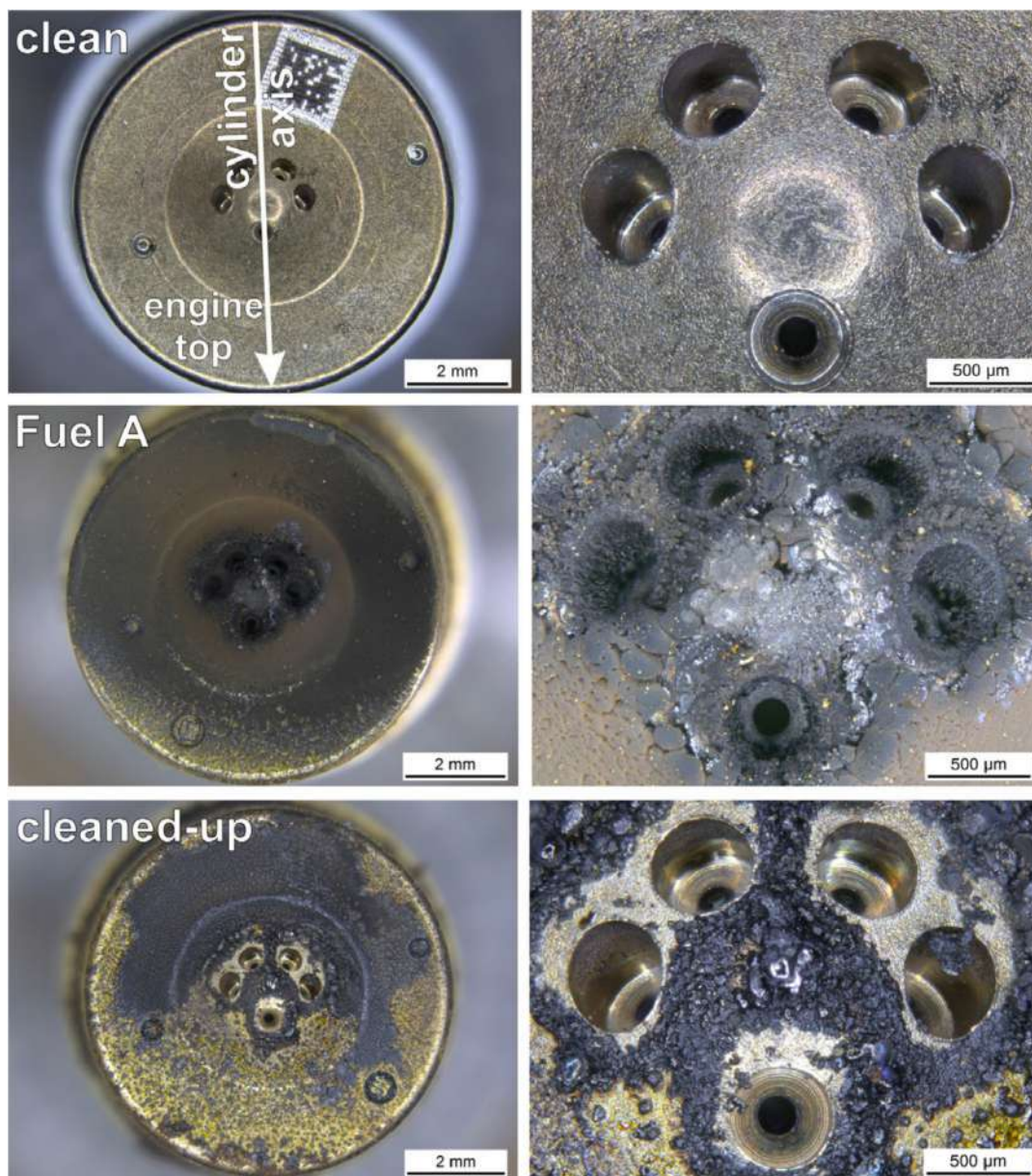


FIGURE 5.16: Injector's micrographs in three different conditions: clean, fouled and cleaned-up.

The impact factors such as nozzle geometry and injector tip temperature are discussed in [156]. The spray pattern is strongly modified by injector fouling [25, 384]. The restriction of the effective flow area leads to a reduction of the mass flow rate. Furthermore, in the injector's counter-bore there are air re-circulation zones which, in the fouled injector, are not effective, causing poor atomization and a smaller spray cone angle [162, 385, 386]. The deposits act as an extension of the inner hole constraining, the air entrainment. The Single Injection Fuel Quantity (SIFQ) decreases by around the 10% due to the smaller diameter of the nozzle's orifice caused by the fouling process [347].

Both computational and experimental studies can be found in the literature. First of all the fouled injectors are analyzed with the already mentioned techniques and from this data a CAD geometric model of the fouled surfaces is created in order to implement CFD simulations of the sprays. The results showed smaller spray angles, longer penetrations, higher droplets velocity and smaller size of the fouled injector [162, 385, 386, 397].

The fuel composition plays a relevant role in the injector fouling processes. Common gasoline is composed of olefins, sulphur, aromatic hydrocarbons, alcohol and metallic salts. These last ones are insoluble, and it seems that they do not affect the fouling process: the injector lifetime remains almost the same using gasoline with or without MMT (Methylcyclopentadienyl manganese tricarbonyl, an additive used to enhance the gasoline octane number) [51, 236]. The most important alcohol specie is the ethanol, which has only a single bond in its chemical structure and also one oxygen atom. These features make this substance relatively thermally stable and mainly it supplies oxygen during combustion avoiding relevant soot emissions [360, 389]. Olefins are highly chemically reactive substances, so they play a key-role in the deposition process, while the effects of aromatic hydrocarbons are still not clearly understood [406]. Tests of different gasolines highlight that detergent components lead to a reduced deposit formation and consequently pollutant emissions [140, 423].

Table 5.9 summarizes the papers regarding injector deposits studies available in the literature with a short comment.

TABLE 5.9: Injector Deposits and Fouling Summary Table

Topic	Comment	References
Injector fouling process	Effects on performance and emissions	[19, 20, 424]
Experimental visualization	Imaging techniques mostly used	[81, 140, 417]
Effect of fouling process	Spray characteristics Injected mass	[25, 162, 384–386, 397] [347]
Effect of fuel composition	Orifice design	[33, 156]
	MMT additive	[51, 236]
	Ethanol	[360, 389]
	Olefins	[406]
	Detergent components	[140, 423]

## 5.10 New Frontiers

At the end of this work, it seemed appropriate to dedicate a small space, certainly not exhaustive, to some significant research activities concerning low temperature combustion engines (LTC), that, in the last years, in order to respect the increasingly stringent emissions rules, are attracting growing interest. The Gasoline Direct Injection Compression Ignition (GDCI) engine is one of the most promising technologies in this category. GDCI engines merge high compression-ignition efficiency with the low CO<sub>2</sub>, NO<sub>x</sub> and PM emissions of spark ignition (SI) engines [185, 329, 416]. The auto-ignition is controlled with the injection timing: it takes place late, during the compression stroke, and, differently from Homogeneous Charge Compression Ignition (HCCI) engines, a stratified charge distribution within the cylinder is created [131, 169]. This is important because a homogeneous charge is a relevant issue in controlling the start of auto-ignition [77]. The compression ratio of the GDCI engines is, of course, much higher than classical SI.

Sellnau M. et al. developed three generations of GDCI engines, optimizing different aspects [326, 327, 331]. Engine dynamometer tests showed that the GDCI engine's brake specific fuel consumption (BSFC) is better than diesel and SI engines, it is comparable with hybrid vehicles, and the emissions targets of combustion noise, NO<sub>x</sub> and smoke are met [327]. The second generation of GDCI engine [331] uses, in all operating conditions, Partial Premixed Compression Ignition combustion to avoid the use of spark-plugs and combustion switching systems. Relevant improvements to the injection system and, EGR after-treatment have been implemented to meet stringent US Tier 3-Bin 30 emissions standards. Engine tests showed that these limits have been respected and BSFC is 11.8 % better than the first generation. The third generation [326] features wet-less technology to avoid wall impingement. The new engine has a special cylinder head with a shallow pent roof to achieve a high compression ratio.

Various researchers consider multiple injections during the compression stroke as the best strategy to achieve the desired mixture stratification [179, 181, 329, 330]

An efficient mixture stratification can be obtained also with an optimized piston bowl geometry and a variable valve train system, as simulated by Crancknell R. et al. [77]. The use of a glow-plug is another solution used to enhance combustion.

The most important consequence of a low temperature combustion is that the GDCI engine's NO<sub>x</sub> and particulate emissions are significantly lower than other combustion systems, even allowing the complete elimination of relative after-treatment devices [332]. On the other hand, the GDCI engine's HC and CO emissions are relatively high and for this reason various studies have been conducted especially regarding fuel composition [328]. Storey J. et al. [353] analyzed RON 80 E0 and RON 92 E10 gasolines with the Fluorescent Indicator Adsorption (FIA) method and they tested them on a light-duty GDCI vehicle, understanding that a more reactive gasoline like RON 80 E0 has a overall lower HC emission. Another problem of such engines is combustion noise and ringing intensity; studies in this field conclude that injection timing can strongly reduce this phenomena [88, 330, 332].

Table 5.10 summarizes the new frontiers regarding gasoline direct injection engines.

TABLE 5.10: New Frontiers Summary Table

Topic	Analysis/Comment	References
LTC combustion	GDCI engines general information	[169, 185, 329, 416]
GDCI studies	Tests of the three generations developed	[326, 327, 331]
	Injection strategies	[179, 181, 329, 330]
	Combustion and emissions	[77, 131, 169]
	Fuel composition optimization	[328, 332, 353]
	Combustion noise	[88, 330, 332]

## Chapter 6

# ECN Spray G Experimental-Numerical Characterization

### 6.1 Investigation Methodology

The main goal of the investigation is to simulate a higher-pressure spray, consistent with the experimental observations, aiming to bring a broader comprehension of the spray characteristics, attempting to understand the correlation present between the injection parameters and the occurrence of such phenomenon. In fact, due to the small size of the injector nozzle diameters and the high fuel injection velocities, it is difficult to obtain a complete understanding of jet evolution by relying only on experimental observations and measurements. Specifically referring on the mass and heat transfer process in a flashing spray, optical techniques such as schlieren and Mie scattering do not provide information regarding temperature and mass concentration of the spreading jet [213]. For this reason, a numerical reconstruction of the spray injection should be performed. An experimental campaign was conducted at the Istituto Motori CNR laboratories. The Engine Combustion Network (ECN, an international collaboration project involving researchers from all over the world) Spray G injector (8-hole gasoline direct injector) was investigated by means of Mie-Scattering and schlieren imaging technique. The liquid and vapour envelopes of the injected spray was evaluated in ECN standard condition (Table 6.1). The numerical model was so validated by comparing the images of the jet morphology and the axial penetration length

Fuel Temperature (K)	363.15
Ambient Temperature (K)	573.15
Ambient Density (kg/m <sup>3</sup> )	3.5
Injection Pressure (MPa)	20
Injection Duration ( $\mu$ s)	680

TABLE 6.1: Case study therm-dynamic parameters

in both experimental and numerical investigations. The experimental penetration length represents the distance between the nozzle exit and the furthest point on the spray contour, measured along the axis of the jet, as shown in Figure 7.14. The acquisition of the penetration length ends off as the jet overcomes the vessel window acceptance.

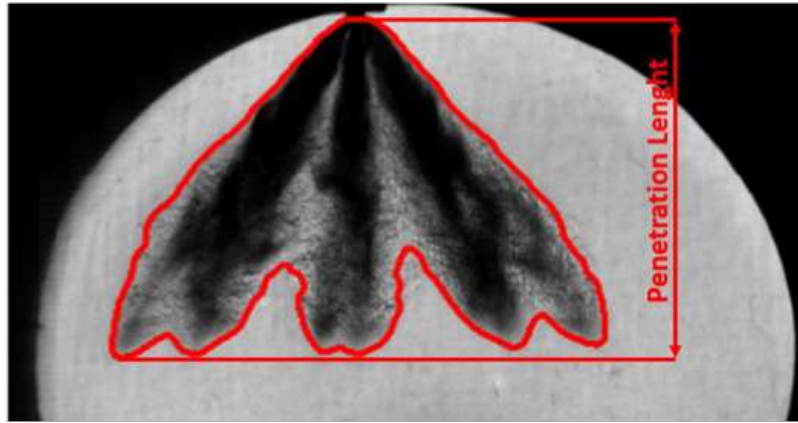


FIGURE 6.1: Axial Penetration Length Measurement.

Liquid and vapour numerical penetration values were respectively computed as the axial distance from the injector where 99% of the liquid mass and a mixture fraction of 0.005 were found [15]. Once the numerical model was validated, it was possible to obtain a quantitative measure of the above-mentioned parameters.

## 6.2 Experimental Apparatus

The experimental investigations were carried out injecting iso-octane in a heated, optically accessible, constant volume chamber (CVC) filled with pressurized nitrogen. The Engine Combustion Network (ECN) Spray G injector [104] consists in a 200-bar maximum pressure 8-hole gasoline direct injector, manufactured ad hoc by Delphi, following the specifications provided by the ECN circuit. The geometry and the main characteristics of the Spray G injector are reported in Figure 6.2 and Table 6.2 respectively.

Isooctane fuel was chosen as fluid ( $\rho=690 \text{ kg m}^{-3}$  at  $25 \text{ }^\circ\text{C}$ ), according to "Spray G Operating Conditions" supplied by ECN [104]. A pneumatic pump was used to introduce the fuel inside a common rail device at the required operating pressure. An electrical resistance was adopted for heating the fuel contained in the rail and the temperature was controlled by a J-type thermocouple. The injector nozzle temperature was also controlled by mounting a coolant jacket around the injector. The injection process was driven by a programmable Electronic Control Unit (PECU) for energizing the current necessary to activate the needle lift. For all the experimental conditions, the energizing time was set to  $680 \mu\text{s}$ , according to ECN specifications. The tests were performed in the CVC, optically accessible through three quartz window, 80 mm in diameter, surrounding the cylindrical test chamber which permits the

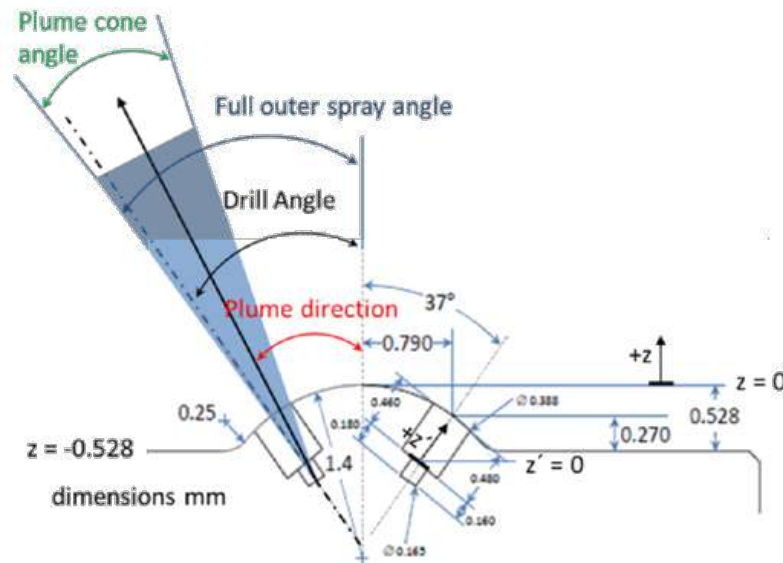


FIGURE 6.2: Spray G Injector Geometry [21].

access to a wide area of the spray under investigation. The injector was located at the top of the vessel in a customized holder, paying attention to the “plume directions” with respect of the camera lens. The eight plumes of the Spray G injector were distributed in three groups as shown in Figure 6.3

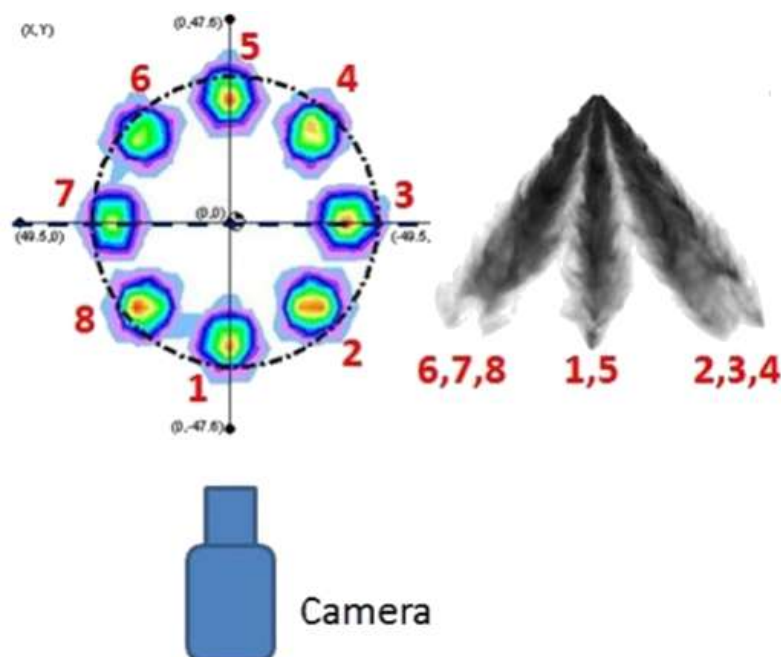


FIGURE 6.3: Schematic of plume directions with respect of camera line-of-sight [21].

Gas pressure conditions in the vessel ( $N_2$ ) was varied by gas addition, while the temperature was increased up to the required value through a system of electrical heaters integrated in the chamber. To reduce heat losses

Fuel Injector	Delphi solenoid-activated
Number of holes	8
Spray shape	circular
Nozzle type	Valve-covered orifice (VCO)
Nozzle shape	Step hole
Orifice diameter	0.165 mm
Orifice length	0.16 - 0.18 mm
Orifice drill angle relative to nozzle axis	37°
Full outer angle	80°

TABLE 6.2: Spray G Injector Characteristics.

through the chamber walls and to ensure a homogeneous temperature inside it, the inner surfaces of the vessel were coated with insulating material. More details of the above-mentioned setup are reported in [14, 253]. For the characterization of the fuel spray evolution both the liquid and the vapour phases have to be discerned. So, with the aim of capturing the peculiarities of a multi-phase fluid, an approach that combines two different non-intrusive optical techniques, working in alternative and quasi simultaneous mode, was proposed at Istituto Motori [249]. The schlieren optical technique is sensitive to the gradient of the density generated by the fluids flow along the optical path and resulting in variations of the refractive index of the fuel. For this reason, this optical technique is suitable for visualizing transparent media, such as gases, and it was recently adopted by the authors for an experimental characterization of a methane injection. So, the multiple phase liquid/vapour mixture was investigated by the schlieren technique, while, on the other hand, the high-speed Mie scattering imaging was used to visualize the liquid phase. By superimposing the Mie scattering images onto the schlieren one it was possible to highlight the differences between the two phases. The optical setup is schematically shown in Figure 6.4.

Schlieren setup was realized according to the traditional Z-type configuration. The schlieren source is a high-power pulsed LED lamp (Omicron LED MOD V2) that emits a light radiation at the wavelength of 455 nm. The beam is collimated through a first off-axis mirror (500 mm parent focal lens). The generated collimated beam crosses the spray in the chamber, and it is deflected and focused by a second off-axis mirror (same characteristics of the former). A knife-edge, mounted orthogonally to the spray propagation direction, is placed at the focus of the second mirror. Finally, a biconvex lens converts the images in the camera through its objective. The Mie scattering images were generated by a high-frequency copper vapour laser at the rate of 12.5 kHz. Both the schlieren and the Mie scattering images were acquired along the same optical path, by using a high-speed C-Mos camera (Photron

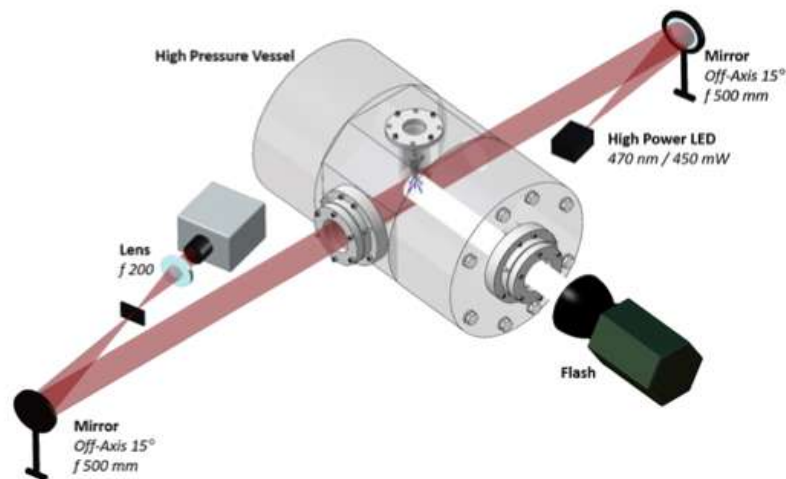


FIGURE 6.4: Optical setup for quasi-simultaneous Mie scattering and schlieren imaging technique..

FASTCAM SA4), working at a rate of 25,000 frames per second (fps) and realizing an image window of 384x352 pixels. The camera was equipped with a 90 mm focal lens resulting in a spatial resolution of 4.5 pixel/mm. Mie scattering and schlieren images were captured in a nearly simultaneous fashion using a TTL triggering signal generated by a pulse generator. The differences between the liquid and gas phases were highlighted by a customized algorithm of image processing. A complete description of this procedure is reported in [249].

### 6.3 Numerical Background

The numerical activities were performed on CONVERGE software suite. It is a general-purpose CFD tool that features also mesh movement, forced embedding and an adaptive mesh refinement algorithm (AMR). AMR refines mesh where high specific field gradients are calculated without significantly increasing the total number of computational cells. The grid dimensions and the refinement strategies were chosen accordingly to ECN Spray G information available on the website [104], the work done by Allocca L. et al [15] and CONVERGE reference material [306]. In particular the base grid dimensions are of 1 mm x 1 mm x 1 mm and the near nozzle zone were refined with a mesh up to 0.125 mm. Finally, the AMR is enabled by the velocity gradient and level adopted is three giving a 0.125mm x 0.125mm x 0.125mm grid around the jet. The modelling of the spray with the surrounding air was performed thanks to the Eulerian-Lagrangian coupling approach and a RANS Standard k- $\epsilon$  turbulence model. The liquid phase was modelled with a DDM (discrete droplet model) framework using the combination of KH-RT (Kelvin Helmholtz - Rayleigh Taylor) models to describe both primary and secondary breakup, Frossling correlation for general vaporization. The other sub-models are reported in Table 6.3. Kelvin Helmholtz (KH) – Rayleigh Taylor (RT) model well describes the overall injection process including both

Breakup	Kelvin-Helmholtz Rayleigh Taylor
Turbulence	Standard k- $\epsilon$
Turbulent Dispersion	O'Rourke Model
Evaporation	Frossling
Collision	NTC collision model
Drop Drag	Dynamic Drop Drag

TABLE 6.3: CFD sub-models used.

	Kelvin - Helmholtz	Rayleigh- Taylor
Breakup size constant	0.61	0.6
Breakup time constant	7.0	1

TABLE 6.4: Breakup models constants

primary and secondary breakup [152]. The breakup mechanism is chosen time by time as the one that predicts the short breakage time [102]. Usually KH model acts as the droplets leave the nozzle, while the RT model, characterized by a faster reduction rate of the droplets size, is applied only beyond a certain distance from the injector [278]. [278]. The parameters adopted for the breakup models are reported on Table 6.4. The two breakup mechanisms act in a competitive manner as the liquid exits the nozzles (liquid core length equal to zero). The parameters values were chosen relying on bibliographic material such as [278] and, especially, what suggested from ECN network . The numerical code uses two angle values as input: the plume direction and the plume cone angle. Their values are reported on Table 6.5.

Basically, the vaporization of the spray droplets is governed by two physical phenomena:

- Heat transfer from the hotter gas to the colder drop.
- Convective and diffusive mass transfer from the droplet surface to the gas environment, resulting in a variation of the liquid droplet radius over time.

CONVERGE contains vaporization models to take into account of the radius variation (Frossling correlations or Chiang correlations) and two difference methods for computing the heat transfer to a drop [306]. About the

Plume Direction	37 °
Plume Cone Angle	30 °

TABLE 6.5: Spray angles used for the numerical simulation

thermal transfer, for all the droplets whose radius is smaller than or equal to a specified value, the droplet temperature is assumed uniform and the temperature field is solved using two ordinary differential equations (Uniform Temperature Model). For the droplets whose radius is larger than the specified value, the droplet temperature is assumed spherically symmetric and temperature is solved using a partial differential equation (Discretized Temperature Model). To describe the evaporation of the liquid droplet into gaseous vapour, the Frossling correlation was chosen in this work. It allows to determine the time rate of change of droplet size as:

$$\frac{dr_0}{dt} = -\frac{\alpha_{\text{spray}} \rho_g D}{2\rho_l r_0} B_d Sh_d \quad (6.1)$$

where: -  $\alpha_{\text{spray}}$  is the user-specified scaling factor for the mass transfer coefficient; -  $D$  is the mass diffusivity of liquid vapor in air; -  $Sh_d$  is the Sherwood number, here defined as:

$$Sh = \left(2 + 0.6Re^{0.5} Sc^{0.33}\right) \frac{\ln(1 + B_d)}{B_d}$$

Where:  $Re$  and  $Sc$  are Reynolds and Schmidt number, respectively;  $B_d$  is defined as:

$$B_d = \frac{Y_1^* - Y^1}{1 - Y_1^*}$$

where  $Y_1^*$  is the vapor mass fraction at the drop's surface and  $Y^1$  is the vapor mass fraction. Finally, for the droplet collision processes the No Time Counter (NTC) method was adopted. The "plume direction" and "plume cone angle" were defined referring to experimental investigation performed. The injected fuel mass-flow profile is available due to specific measurement and is shown in Figure 6.5. The discharge coefficient and velocity coefficient were calculated using the information available on ECN website [104].

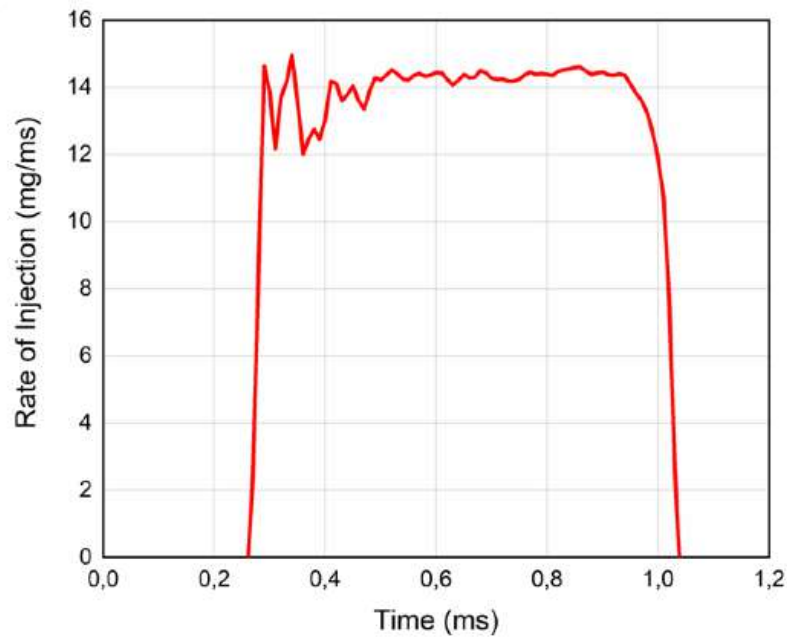


FIGURE 6.5: Mass-Flow Rate.

## 6.4 Results

The main results obtained in this work feature:

- The validation of the numerical model of the spray against the experimental data, for both ECN standard and flash boiling conditions.
- The investigation of the causal factors that influence the spray behaviour.

In order to evaluate the model reliability, numerical results were validated against experimental data in terms of general spray shape and penetration length. The spray shape was represented plotting a rendering of the simulated spray and comparing it with the experimental images. Figure 6.6 shows such comparison for both ECN standard at different time-step, with the schlieren pictures on the right and the numerical reconstruction on the left. The schlieren technique captures both spray's liquid and vapour phases. The simulated spray was obtained by overlapping a volume rendering of the iso-octane vapour mass fraction with a visualization of the liquid droplets. The map colour goes from white to black accordingly with increasing values of vapour mass-fraction. For the whole injection duration and for both analysed conditions, the numerical model is capable to describe the jet behaviour and to replicate the spray shape recorded experimentally. By observing the evolution of the spray in standard condition the single jet plumes are clearly recognizable, (sequence in Figure 6.6).

Figure 6.7 illustrates a comparison between numerical and experimental vapour (Figure 7-6.7) and liquid (Figure 7-6.7) penetration for ECN Standard case. On the experimental penetration curve the error bars were reported. The results show a general good agreement. Small differences are recognizable, for the liquid penetration, near the end of the acquisition window.

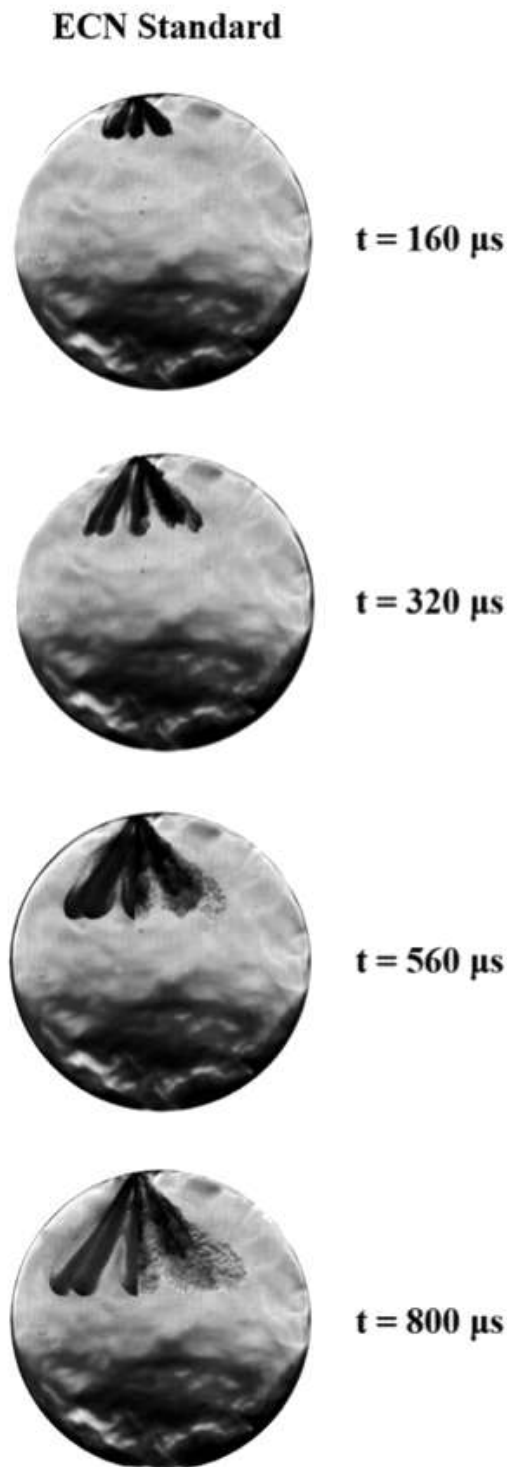


FIGURE 6.6: Comparison between experimental schlieren images (right half circle) and numerical computed iso-octane mass fraction (left half circle) for ECN Standard condition.

However, it worth noting that the major differences between the numerical and the experimental results are bounded by the error bars. The following Figure 6.8 and Figure 6.9 provide a further validation of the reliability of

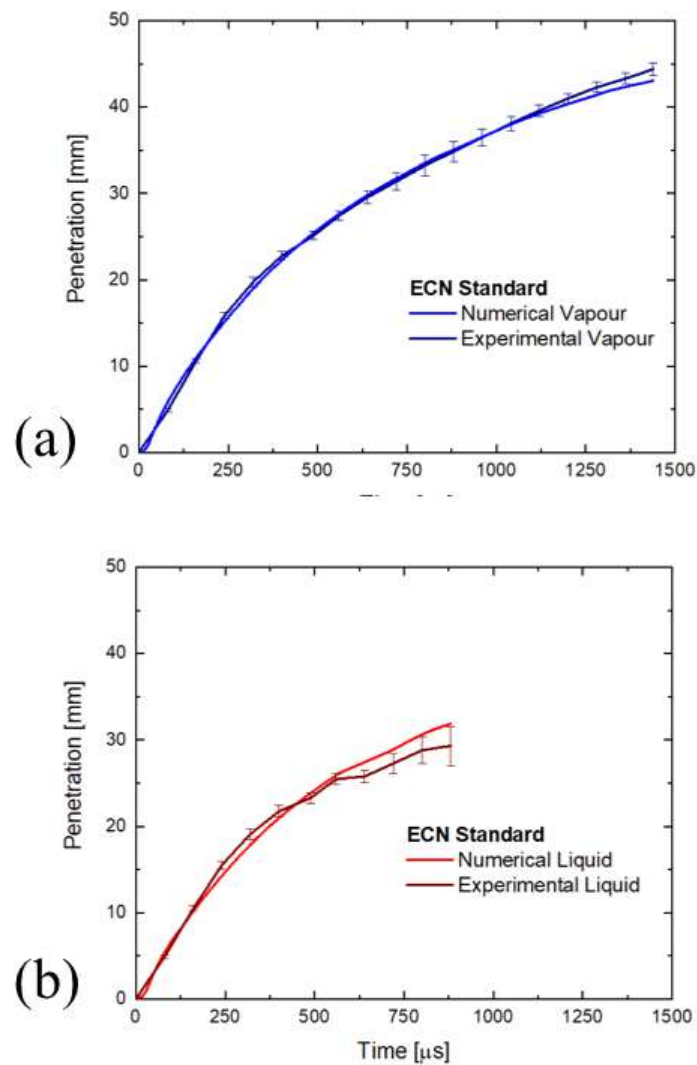


FIGURE 6.7: Numerical and experimental penetration for ECN Standard case.

the developed model in describing the spray breakup and its general evolution. In particular, Figure 6.8 shows a comparison between the centerline axial velocity, computed (using the numerical results) at a distance of 15 mm from the injector's nozzles, and experimental PIV measurement regarding the ECN Standard condition available in literature [104, 278]. The temporal evolution shows a good agreement between the two datasets. The velocities are negative and this means that there is a recirculation zone where the air flows from the bottom to the top of the injection environment.

Indeed, numerical results provide information regarding the air circulation around the spray too. Figure 6.9 represents a vertical cross-section of the spray where the air entrainment was represented overlaying the velocity vectors over the vapour mass fraction colour map. The direction of velocity vectors underline that the air enters from the bottom of the spray and go back

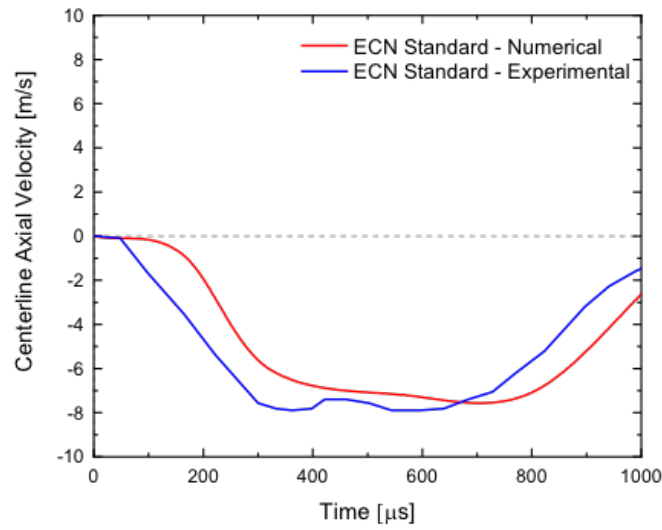


FIGURE 6.8: Temporal evolution of the centerline axial velocity at a distance of 15 mm from the nozzles of the injector. Experimental and numerical data were plotted against the injection period.

up to the nozzle [178].

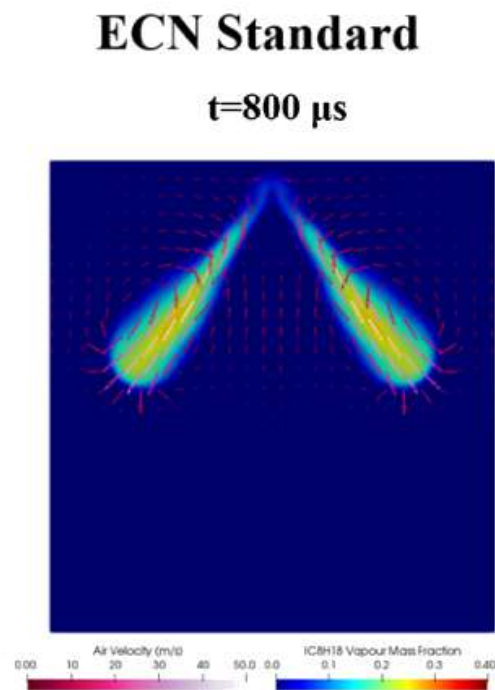


FIGURE 6.9: Iso-octane vapour mass fraction and velocity vectors at  $t=800 \mu$ s

Figure 6.10 represents the Sauter Mean Diameter (SMD) evaluation at distance of 15 mm from the nozzles of the injector. The SMD, computed from the numerical results [39], was compared against the phase-doppler interferometry measurement performed by researchers of the ECN community [104]. The SMD diameter computed does not perfectly match the measurements. This misbehaviour could be fixed properly setting the velocity coefficient as suggested by Paredi et al [278]. Indeed, a greater velocity coefficient lead to a reduced liquid droplets velocity and consequently to a higher average SMD.

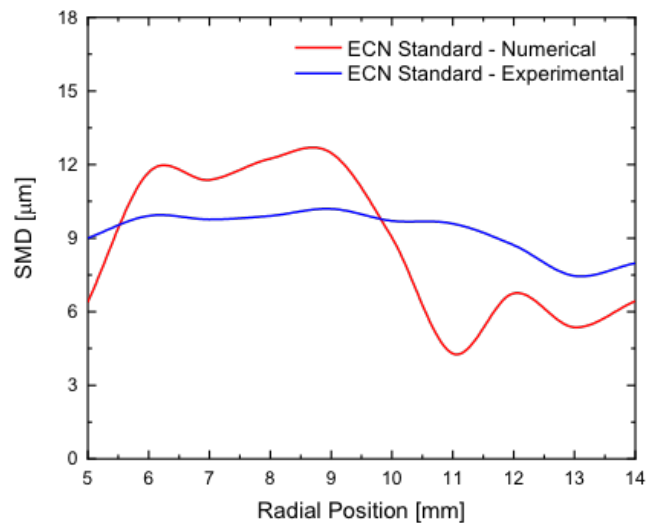


FIGURE 6.10: Sauter Mean Diameter (SMD) evaluation at a distance of 15 mm from the nozzles of the injector. Experimental and numerical data were plotted against the radial distance from the injector axis.

Finally figure 6.11 shows the time evolution of iso-octane vapour mass fraction for ECN Standard case which reaches values approximately equal to 0.3 highlighting the fact that the relatively high ambient density ( $3.5 \text{ kg m}^{-3}$ ) inhibits the fuel vaporization.

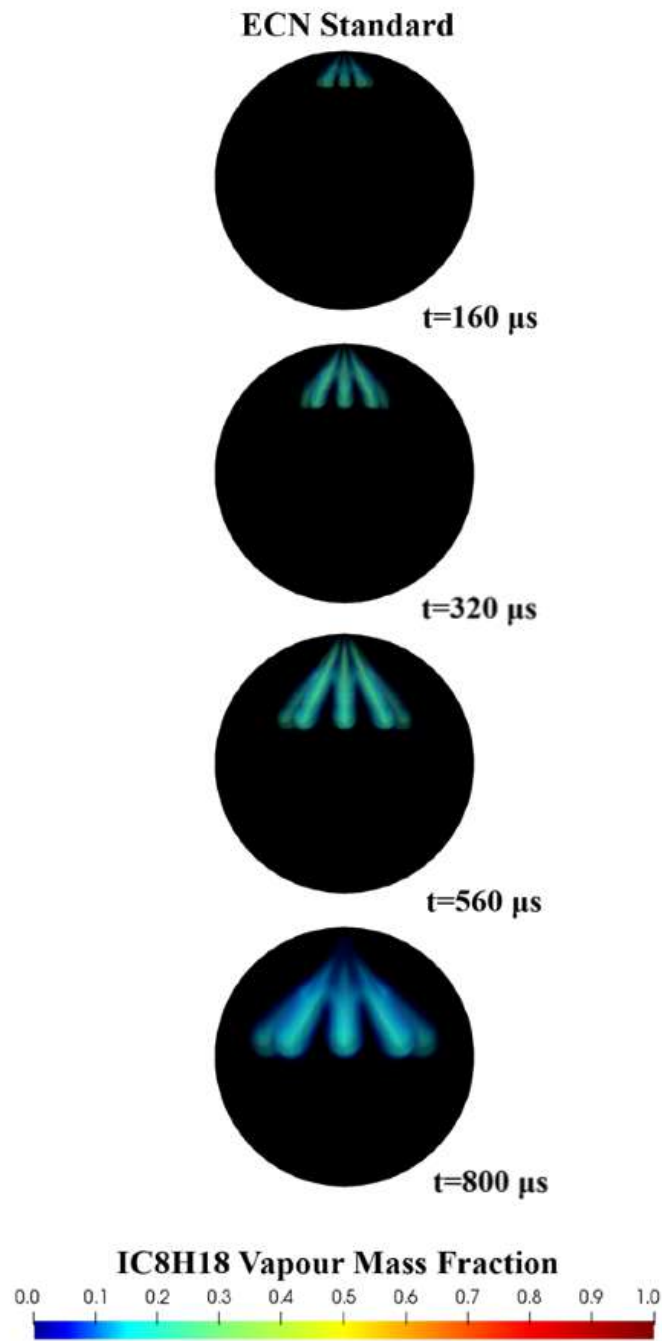


FIGURE 6.11: Iso-octane vapour mass fraction time evolution



## Chapter 7

# Numerical modelling of flash-boiling breakup and spray collapse

### 7.1 Flash Boiling in GDI engines

In gasoline direct injection engines, the flash-boiling phenomenon usually occurs when the fuel is injected directly into the combustion chamber very early during the intake stroke (sub-atmospheric conditions) to promote the formation of a homogeneous mixture [295]. Moreover, for such engines, multi-hole injectors are commonly used due to the flexibility of plume targeting, precise control of the injection timing and quantity, high spray velocity and enhanced air entrainment [205]. However, under flashing conditions, depending on the degree of superheat and the number and proximity of the injection holes, the enhanced radial dispersion of the single plumes may increase the jet-to-jet interaction, leading to the collapse of the spray [418]. The higher axial momentum of the collapsed spray may lead to increased piston wall-wetting, which in turn can cause the formation of exhaust soot [387].

Typically, the fuel breakup caused by flash boiling occurs inside or in the close vicinity of the nozzle exit, where it is very difficult to obtain measurements on the single spray plumes, due to the presence of a dense and complex liquid–vapour flow field [9]. For this reason, experimental investigations can only provide limited information regarding the breakup process and the collapse of the sprays. However, this data is essential to develop and validate numerical models capable of reproducing such a complex phenomenon and capturing the interaction of near-nozzle plumes and the consequent spray collapse.

There have been considerable efforts made to model the whole flash-boiling process from its initiation (bubbles nucleation) to its completion (bubble burst), passing through the bubble-growth step. The common approach is to adjust the model according to the experimental observations. Nevertheless, such “empirical models” fail to explain the physics behind the process and are not capable of predicting the collapse of the spray [46]. For this reason, it would be advisable to use a numerical predictive model which, once validated against experimental measurements, is able to automatically capture not only the spray morphology, but also the flash-boiling characteristics,

such as drop shattering due to bursting of the vapour bubbles (breakup criterion), and the radial velocities and sizes of the subsequent smaller droplets (child droplets).

The present study deals about the development, within the OpenFOAM library, of an innovative breakup model to describe the superheated spray. The Engine Combustion Network (ECN) Spray G injector was chosen as a case study. The model was tested and validated using experimental data collected at the Istituto Motori of CNR in Naples, for different operating conditions.

## 7.2 Thermophysical description of flash boiling

Flash boiling is the liquid-to-vapour phase transition that occurs when high-temperature liquid fuel is injected into an environment where the pressure is lower than the fuel saturation pressure. The spray morphology drastically changes, modifying the air–fuel mixing with consequences on the combustion quality and, therefore, pollutant emissions and engine performance. A deep understanding of this complex phenomenon is required to develop consistent numerical models to properly exploit the flash boiling in GDI engines. Flash boiling involves the nucleation, rapid growth, and subsequent bursting of vapour bubbles, producing a catastrophic disintegration of the liquid droplets inside or immediately outside the injector nozzle. Figure 7.1 shows the vaporisation process of an initially sub-cooled liquid (state A) through an isothermal transformation that leads it to a state D, located below the saturation line, meaning that the fluid has a pressure lower than its saturation value. A liquid in the state D, superheated fluid, is in a metastable condition. It can maintain its metastable state for a significant period, until local fluctuation of pressure or a nucleation site triggers the phase change process [226].

The transition from a metastable to a stable phase (point C) starts from the nucleation of a vapour bubble in a metastable equilibrium with the surrounding liquid. At the equilibrium condition, the pressure inside the bubble is greater than the pressure of the liquid, while the temperature of the latter is greater than that of the vapour inside the bubble. Two parameters are frequently used to describe the superheat level [195]. The first, the defined degree of superheat, is the difference between the liquid temperature,  $T_0$ , and the saturation temperature at ambient pressure,  $T_{sat}(p_\infty)$ :

$$\Delta T = T_0 - T_{sat}(p_\infty) \quad (7.1)$$

The second is defined as the ratio between the ambient pressure and the saturation pressure at the liquid temperature:

$$R_p = \frac{p_\infty}{p_{sat}(T_0)} \quad (7.2)$$

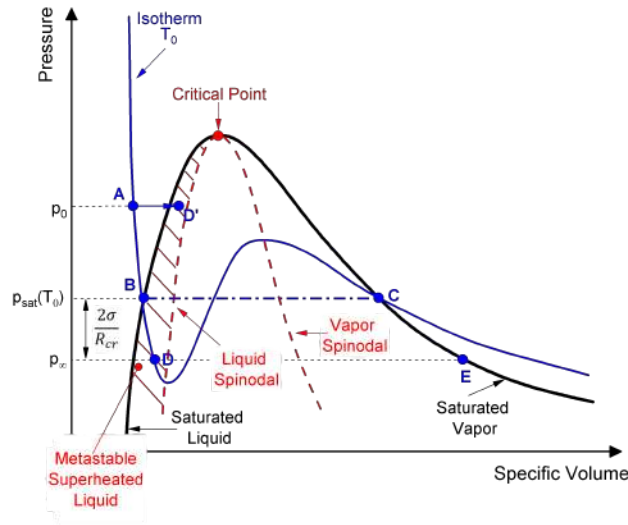


FIGURE 7.1: Typical pressure vs specific volume curve for a pure substance. Dashed area indicates the metastable superheated liquid region.

Flash boiling is expected to occur when this ratio assumes a value less than unity and three regions can be identified according to the  $R_p$  value: full flash boiling, a transition region and a non-flash-boiling region as shown in Table 7.1

$R_p < 0.3$	Full flash boiling
$0.3 < R_p < 1$	Transition region
$R_p > 1$	Non-flash-boiling

TABLE 7.1: Ambient to saturation pressure ratio ranges

The initial radius,  $R_{i,0}$ , of a vapour bubble arises from the equilibrium between the liquid surface tension ( $\sigma$ ) and the pressure forces inside the bubble–droplet system, as described by Equation 7.3

$$R_{i,0} = \frac{2\sigma}{p_{sat}(T_0) - p_\infty} \quad (7.3)$$

Vapour bubbles with a smaller radius than this value cannot be formed because they collapse under the force of the surface tension. Any variation of the pressure difference " $p_{sat}(T_0) - p_\infty$ " will cause the bubble to grow or collapse and for this reason it is called the critical radius.

The growth is then driven by the difference between the bubble vapour pressure,  $p_v = p_{sat}(T_0)$ , and the ambient pressure,  $p_\infty$ , while the surface tension, liquid inertia and fluid viscosity are opposed to bubble growth [275]. During this process (path C-E in Figure 7.1), the fuel on the bubble surface evaporates. The bubble's superficial temperature drops and the latent heat

of evaporation is transferred from the liquid to the bubble, causing the formation of a thin thermal boundary layer from the bubble wall towards the liquid. The vapour pressure drops to the ambient pressure and growth of the bubble results, driven by thermal conduction. The last stage of a flash-boiling injection is the atomisation process, which consists in the micro-explosion of the droplets [275]. During such shattering, the liquid jet increases its plume cone angle due to the intense radial momentum acquired by the droplets. A proper representation of the flash-boiling process should consider all the phenomena here exposed.

### 7.3 ECN Spray G: Numerical characterisation of flash-boiling conditions

In this study, the Spray G of the Engine Combustion Network is considered (injector serial 19). Spray G is a stepped-hole valve-covered orifice (SVCO) type injector, having an  $80^\circ$  outer cone angle with 8 holes. The main characteristics of such device are reported in Table 7.2

The principal topics of the latest ECN workshops were the investigation of the internal and near-nozzle flow of a Spray G injector and the optimisation of the fuel–air mixing process, with particular attention paid to the experimental and numerical characterisation of the flash-boiling phenomenon [104].

The details of the dense and multi-phase flow inside or in the close vicinity of the nozzle orifices are fundamental for predicting the occurrence of flash boiling. Neutron imaging, backlit microscopy and X-ray radiography represent the most innovative techniques capable of providing information on the internal geometry and pintle motion of the injector and visualising the plume-to-plume interaction at the nozzle exit. These data contribute to the numerical reconstruction of the flow inside the injector. The most recent efforts in modelling the internal and near-nozzle flow in the context of a Spray G injector were reviewed in [244]. These models all involve a purely Eulerian approach, which treats both gas and liquid droplets with transport equations to account for the phase distribution. The two-phase flow can be modelled by

<b>Spray shape</b>	Circular
<b>Nozzle type</b>	Valve-covered orifice (VCO)
<b>Nozzle shape</b>	Stepped-hole
<b>Orifice diameter</b>	0.165 mm
<b>Orifice length</b>	0.16 – 0.18 mm
<b>L/D ratio</b>	1.4
<b>Orifice drill angle</b>	$37^\circ$ relative to nozzle axis
<b>Full outer angle</b>	$80^\circ$
<b>Flow rate</b>	15 cc/s @10 MPa

TABLE 7.2: Main characteristics of the Spray G injector

either a volume-of-fluid (VOF) or a homogeneous relaxation model (HRM) [261].

Due to the huge computational resources required, a purely Eulerian approach is not suitable for modelling the spray mixing process, which mainly occurs far from the nozzle. For this reason, a combined approach of a Eulerian scheme for the gas phase and Lagrangian particle-tracking methods for the liquid droplets must be used. To properly reproduce the physics involved in a flashing multi-hole spray injection and predict the radial expansion of the plume, specific spray sub-models must be used and calibrated. Furthermore, using the Lagrangian approach for initialising the velocity of the injected droplets, the plume cone angle value represents a mandatory input parameter.

Conventional breakup models, such as the Kelvin Helmholtz– Rayleigh Taylor (KH-RT) or the Reitz–Diwakar (RD) models, coupled with the RANS turbulence framework, are not capable of reproducing the different flash-boiling conditions without changing specific constants and, especially, tuning the plume cone angle with values that may not be consistent with those experimentally measured. Furthermore, such approach tends to overestimate the intensity of the collapse, assuming that the spray has an “umbrella” morphology and providing unrealistic droplet diameters [101, 240]. Only a few studies illustrating methodologies capable of predicting flashing sprays correctly are present in the literature. The Rutland diameter reduction technique was used by Paredi et al. [279], the secondary breakup parameters under flash-boiling conditions. Recently, Tao et al. [361] proposed a correlation that is a function of the pressure ratio and the fuel properties, for an automatic prediction of the spray cone angle for flash-boiling spray initialisation at the nozzle exit. The CFD code was implemented in ANSYS Forte and the KH-RT breakup model was modified to account for the catastrophic droplet shattering at the nozzle exit under flash-boiling conditions. The model was validated against several experimental data from different injectors, including the Spray G injector, showing a good ability to capture the global spray morphology and plume interactions, under a wide range of flash-boiling conditions.

Another approach for modelling the spray dynamic, used for the flash-boiling condition too, is the so-called Eulerian-Lagrangian spray atomisation (ELSA) method. Typically, it consists in a purely Eulerian description of the multi-phase flow inside the nozzle which provides the boundary conditions for Lagrangian-Eulerian simulation of the spray for the downstream flow field (“one-way coupling”) [243, 266]

In order to offer a contribution to better simulate the spray evolution of the ECN G injector operating in flash-boiling conditions, the authors decided to use the Eulerian-Lagrangian modelling approach that accounts for a different flash-boiling breakup mechanism based on bubble growth within the droplets. It describes more properly the shattering of the droplets and considers the spray expansion that modifies the velocity vectors.

## 7.4 Numerical methodology

The new breakup model, **fbBreakup**, was developed in OpenFOAM's Eulerian-Lagrangian solver, **sprayDyMFoam**. The model simulates the flash-boiling breakup of the bubble-droplet system, shown in Figure 7.2, and the secondary aerodynamic breakup with the Reitz-Diwakar model.

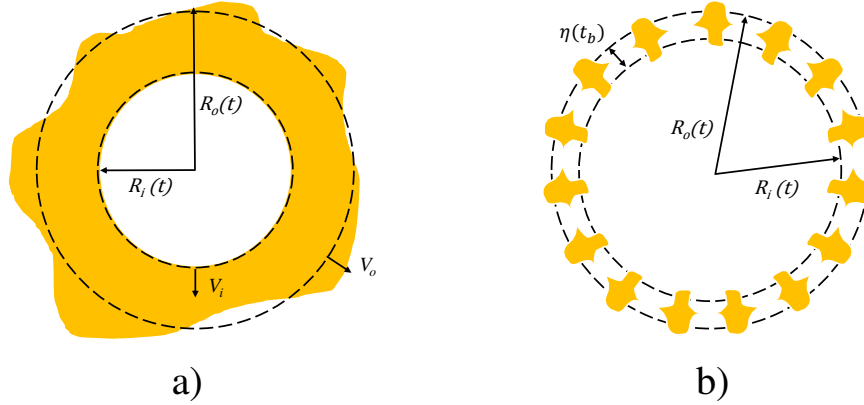


FIGURE 7.2: Time evolution of bubble-droplet system.

Flash-boiling breakup is due to the oscillations that are established along the droplet and bubble surfaces (Figure 7.2-a). The atomisation occurs when the instability amplitude grows larger than a characteristic length of the spray (Figure 7.2-b) [300]. For the bubble-droplet system, the disturbance,  $\eta$ , growing with a rate  $\omega$ , is given by:

$$\ln \left( \frac{\eta}{\eta_0} \right) = \int_0^t \omega dt \quad (7.4)$$

and the characteristic length can be chosen as the film thickness, the time-varying difference between droplet radius  $R_o(t)$  and bubble radius  $R_i(t)$  (outer and inner radius of the bubble-droplet system). Assuming the initial disturbance  $\eta_0$  proportional to the initial droplet radius,  $\eta_0 = 0.05 \cdot R_o(t_0)$ , a breakup criterion, for bubble-droplet systems under thermal non-equilibrium, can be expressed as:

$$\frac{\eta_0 e^{\int_0^t \omega dt}}{R_o(t) - R_i(t)} = k_b(t) \quad (7.5)$$

After a time  $t_b$ , when the instability amplitude equals the film thickness ( $k_b(t_b) = \bar{k}_b = 1$ ), breakup occurs.  $\bar{k}_b$  is a potential parameter for model gatimisation to take into account the complexities found in real bubble-droplet systems. As a first approximation, usually and within the context of the current study, it is assumed equal to one. The instability growth rate  $\omega$  is the largest real root of

the following normalised growth rate equation:

$$(\Delta - \Delta^2 - \psi_o \Delta) \Omega^2 + (-1 + \Delta^4 + \psi_o) We_o^{1/2} \Omega + 2\Delta^2 + 2\Delta^{-2} - 3\psi_i \frac{We_i}{Ma_i^2} \frac{\Omega}{\Omega + 3We_i^{1/2}} \Delta^2 = 0 \quad (7.6)$$

where:

$$\begin{aligned} \Omega &= \sqrt{\frac{\rho_\ell R_i}{\sigma}} \omega, \quad \rightarrow \quad We_o = \frac{\rho_\ell V_o^2 R_i}{\sigma}, \quad \rightarrow \quad We_i = \frac{\rho_\ell V_i^2 R_i}{\sigma}, \quad \rightarrow \quad Ma_i = \frac{V_i}{c} \\ \Delta &= \frac{R_o}{R_i}, \quad \rightarrow \quad \psi_o = \frac{\rho_{go}}{\rho_\ell}, \quad \rightarrow \quad \psi_i = \frac{\rho_{gi}}{\rho_\ell} \end{aligned} \quad (7.7)$$

$V_i$  and  $V_o$  are the bubble and droplet growth rate, respectively. Indeed, as previously mentioned, the model considers a bubble growing within each superheated droplet.

The initial bubble radius can be computed using Equation 7.3, while the bubble growth rate was computed from the Rayleigh-Plesset equation, assuming spherical 'symmetry:

$$R\ddot{R} + \frac{3}{2}(\dot{R})^2 = \frac{1}{\rho_l} \left( p_v - p_\infty - \frac{2\sigma}{R} - \frac{4\mu}{R} \dot{R} \right) \quad (7.8)$$

where  $R$ ,  $\dot{R}$  and  $\ddot{R}$  are respectively the bubble radius and its first and second derivatives,  $\rho_l$  is the liquid density and  $\mu$  is the dynamic viscosity. Solving the Rayleigh-Plesset equation, the bubble growth rate is equal to:

$$V_i = \sqrt{\frac{3}{\rho_l} (p_{sat} - p_\infty)} \quad (7.9)$$

The droplet growth rate can be expressed as a function of the bubble growth rate [419]:

$$V_o = V_i \cdot \Delta^2 \quad (7.10)$$

The expansion of such bubble leads to the explosion of the droplet. This kind of breakup is responsible for expansions of the spray plume and the eventual further collapse. In order to account for this behaviour once the breakup occurs, a radial velocity component is added to the original velocity of the droplet as shown in Figure 7.3

The magnitude of the radial velocity ( $U_r$ ) is thus equal to:

$$U_r = k_v \frac{3R_i^2 V_i (R_o - R_i)}{R_o^3 - R_i^3} \quad (7.11)$$

In this way, the new droplet acquires further velocity components:

$$U_x = U_{x,old} + U_{x\tau} \quad U_y = U_{y,old} + U_{y\tau} \quad U_z = U_{z,old} + U_{z\tau} \quad (7.12)$$

The orientation of  $U_r$  is random, while  $k_v$  is a constant for the spray expansion. The new Sauter mean radius of the droplets ( $SMR_{32}$ ) is expressed by

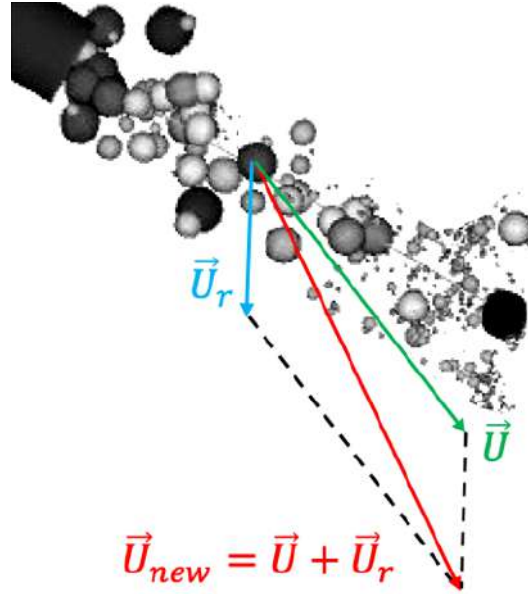


FIGURE 7.3: Droplet velocity after breakup updating.

the following relation:

$$SMR_{32}^{-1} = \frac{1}{2} \frac{R_0^2 + R_i^2}{R_0^3 - R_i^3} + \left( \frac{3}{2} \frac{R_i^4 (R_i^{-1} - R_o^{-1})}{R_0^3 - R_i^3} V_i^2 - \frac{U_r^2}{2} \right) \frac{\rho_\ell}{3\sigma} \quad (7.13)$$

The model iterates all the parcels present in the domain, checking the conditions for breakup and, eventually, updating the velocity. Each parcel undergoes only one time to the flash-boiling breakup, and then to the aerodynamic breakup. Differently from the flash-boiling breakup, the Reitz-Diwakar breakup model can be applied more times to a single particle. The following relationship ensures the mass conservation after breakup:

$$n_{new} d_{new}^3 = n_{old} d_{old}^3 \quad (7.14)$$

where  $n_{new}$  and  $n_{old}$  are the number of particles, respectively, in the current parcel system, after and prior to the breakup process.

## 7.5 Case study setup

The ECN Spray G was studied in four flashing conditions as reported in Table 7.3.

The injection environment is filled with nitrogen while iso-octane is the fuel injected. In the first column of Table 3, the test cases are indicated with the acronym “G\_SFBxxx” (G strong flash boiling), while “xxx” reveals the injection pressure (bar). These conditions, not included among the ECN ones, were investigated to better highlight the effects of flash boiling on the spray structure. The newly developed solver, named **fbprayDyMFoam**, was used. The integration domain is a cylinder with a diameter of 90 mm and height

Case	Fuel temperature [K]	Ambient temperature [K]	Ambient density [kg m <sup>-3</sup> ]	Injection pressure [bar]	Injection duration [μs]	Rp
G2	363.15	333.15	0.5	200	680	0.55
G_SFB200			0.2			150
G_SFB150				100		
G_SFB100						

TABLE 7.3: Case study summary

of 74.8 mm that reproduces the internal geometry of the CVC (constant volume chamber) used in the experimental campaign. Geometry discretisation is performed using a structured mesh of 1 mm in each direction and an adaptive mesh refinement (AMR) based on the velocity gradient. Three meshes were adopted: a base grid featuring an AMR of level 2 up to a dimension of 0.25 mm, a fine grid with AMR of level 3 and coarse mesh with AMR of level 1. The Eulerian framework of the model uses the PIMPLE algorithm for governing equations solution, the RANS Standard k- $\epsilon$  turbulence model and the Euler time integration method with a variable time step. The Lagrangian framework features the discrete droplet method (DDM) and the physical sub-models, as reported in Table 7.4.

<b>Injection model</b>	Flow rate + discharge
<b>Injection droplet distribution</b>	Rosin–Rammler
<b>Breakup</b>	fbBreakup
<b>Heat transfer</b>	Ranz–Marshall
<b>Vaporisation</b>	Adachi
<b>Collision</b>	O’Rourke (with coalescence)
<b>Dispersion</b>	Stochastic dispersion

TABLE 7.4: Lagrangian framework physical sub-models.

Mass flow rate profiles vs time are reported in Figure 7.4 for the different injection pressures at the ECN set energising time of 680 μs. The profiles overlap in the common part, during the opening and closing phase, while the stationary level increases coherently with the injection pressure. Hence, the corresponding amount of the injected fuel moves from 7.0 mg/str @ 100 bar to 10.0 mg/str @ 200 bar.

Further spray geometrical and hydraulic parameters are shown in Table 7.5. The discharge coefficient was computed using the information available on the ECN website [104].

	G2	G_SFBxxx
<b>Plume injection direction</b>	30°	25°
<b>Discharge coefficient</b>	0.64	

TABLE 7.5: Geometrical and hydraulic injection parameters.

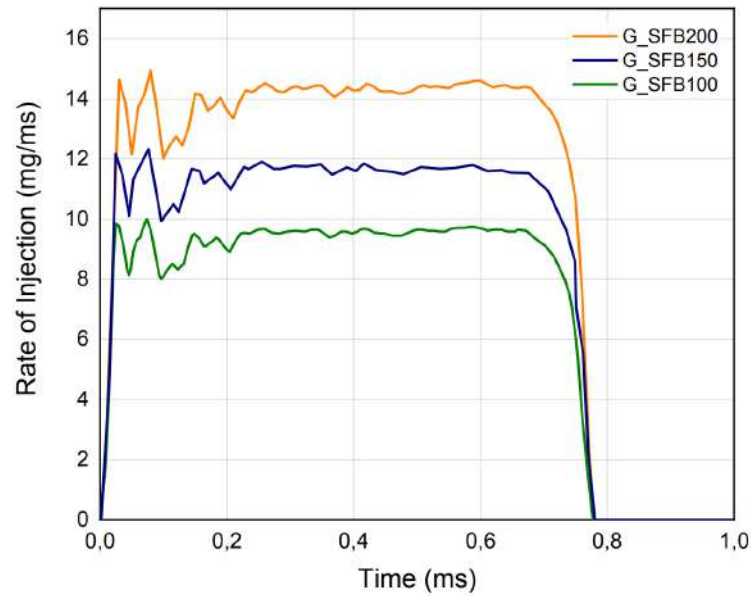


FIGURE 7.4: Mass flow-rate profiles corresponding to the three injection pressures.

The plume injection direction is defined as the inclination of the plume axis with respect to the injector axis. For further details see [105]. These values were obtained from the experimental campaign carried out taking into account the spray orientation and thus performing the proper measurement procedure. Table 7.6 reports the breakup parameters for both flash-boiling and aerodynamic atomisation.  $C_{bag}$ ,  $C_b$ ,  $C_{strip}$  and  $C_s$  are the Reitz–Diwakar breakup model constants, the latter chosen according to the literature references [240].

	G2	G_SFBxxx
$k_b$		1
$k_v$	1	2.5
$C_{bag}$		2
$C_b$		0.785
$C_{strip}$		0.5
$C_s$		1

TABLE 7.6: Breakup parameters.

The validity of the adopted numerical approach was proved using experimental data of the spray acquired at the Istituto Motori – CNR of Naples. The characterisation of the fuel spray evolution for both liquid and vapour phases required the adoption of different optical techniques. The spray morphology was investigated by the two techniques of schlieren and Mie scattering and acquiring the images along the same line-of-sight. The optical setup is the same described in paragraph 6.2 of Chapter 6 and so not repeated. For all the investigated conditions both the nozzle and fuel temperatures were kept at 363 K.

## 7.6 Results and discussion

The comparison between the experiments and computations was performed in terms of the liquid and vapour fuel penetration and distribution. The experimental and computed penetration lengths of the G\_SFB200 case are reported in Fig. 7 for the liquid and Fig. 8 for the vapour phases, respectively. Both the numerical and experimental liquid and vapour penetrations were computed as the axial distance from the injector where 99% of the liquid mass and a fuel mass fraction of 0.001 were found, respectively. Ten repetitions of each experimental configuration were performed for each injection event to account for cycle-to-cycle variations, and the uncertainty bars in the figures depict the variance from the average value. The uncertainty of the numerical results is assessed in accordance with the criterion illustrated by Roache in [309], where the assessment procedures adopted by the AIAA, ITTC and IEEE are described and discussed in detail. The apparent convergence order was calculated for the liquid penetration, resulting as approximately equal to the value of unity. Adopting an upwind first-order scheme ensures that the solution is convergent. Therefore, uncertainty was estimated by Richardson extrapolation.

Figures 7.5 and 7.6 show an excellent agreement between the liquid and vapour penetrations all along the injection event, also taking into account the uncertainty bars.

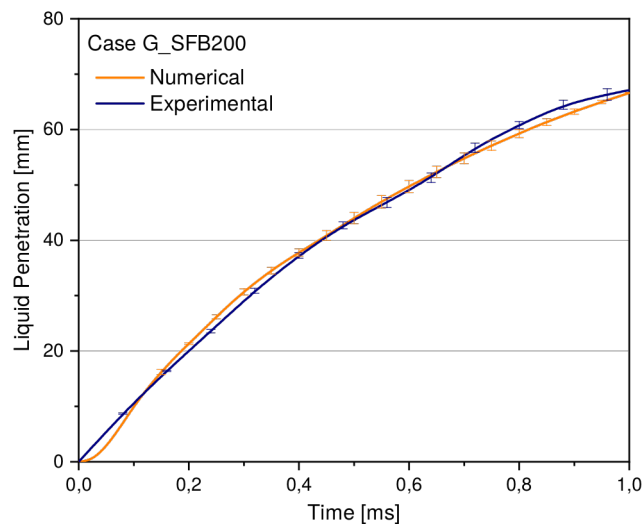


FIGURE 7.5: Numerical and experimental liquid penetration for G\_SFB200 case.

In Figure 7.6 the numerical uncertainty is relatively small until 0.5 ms. Then, as the injection goes on, the magnitude of the bars increases slightly. This behaviour is probably due to the turbulence modelling. Indeed, while the penetration is initially ruled by the jet's momentum, in the latest phases of the injection the air entrainment significantly influences both the liquid

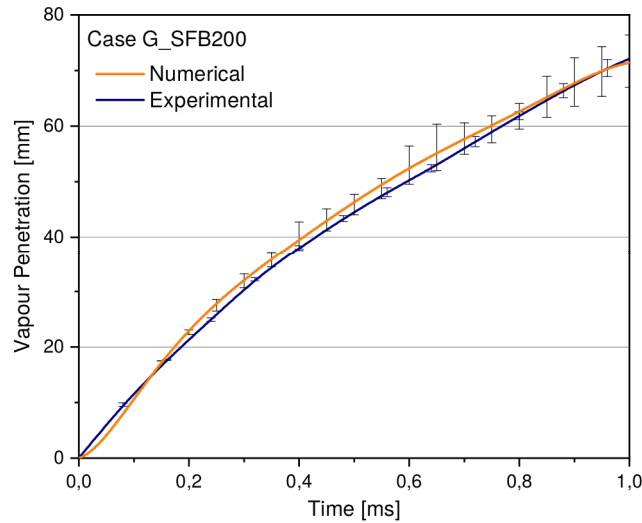


FIGURE 7.6: Numerical and experimental vapour penetration for G\_SFB200 case.

droplets and the fuel vapour penetration. A further grid refinement will likely reduce the level of uncertainty.

Figure 7.7 shows the simulated spray shape compared with the schlieren images at different times after the start of injection (SOI). For each time-frame, the image is divided in two semi-circles: on the left hand there is the simulated spray, plotted overlapping a volume rendering of the iso-octane vapour mass fraction with a visualization of the liquid droplets, while, on the right, the schlieren picture.

Differently from the ECN standard condition [104], where the plumes are clearly distinguishable, now they interact with each other and bend towards the central region, creating the spray collapse, with vortexes observed all along the spray edges. It is not possible to distinguish the profiles of the individual plumes and the spray appears as a single large jet. Because of the phase transition, the formation of the steam bubbles entails a greater compactness of the spray. At this condition, a rupture of the intact liquid core occurs soon after the SOI. The greyscale distribution of the computed images goes from white to black according to the increasing values of the fuel mass-fraction. For the whole injection duration, the numerical model is capable of describing the jet behaviour and replicating the spray shape experimentally recorded. The typical multi-hole flash-boiling spray structures, including plume interaction and spray collapse, are well predicted by the flash-boiling breakup model. Indeed, the radial velocity component (computed as approximately equal to 20 m/s), added to the droplets after the breakup, creates the condition for having the initial plume expansion.

The G2 condition is the standard ECN flash-boiling case. The computational procedure developed is capable of providing reliable results in this condition, too. Figure 7.8 and 7.9 show the corresponding penetration lengths

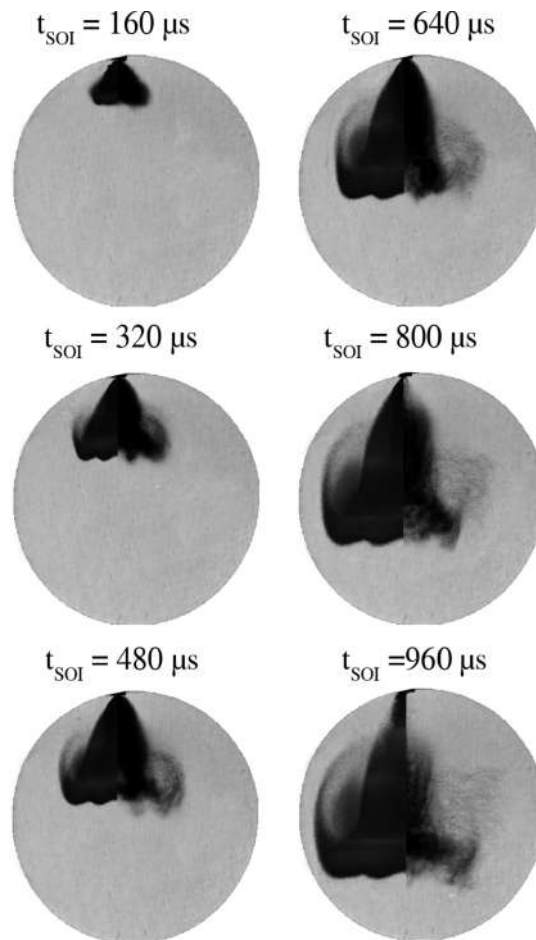


FIGURE 7.7: Comparison between experimental schlieren images (right half of each circle) and numerical iso-octane mass fractions (left half of each circle) for G\_SFB200 condition.

for the liquid and vapour phases. In the G2 case, the uncertainty was estimated always relying on Richardson extrapolation but using two grids with a refinement factor of two (0.5 mm and 0.25 mm). Furthermore, given the two-grid assessment procedure, the most pessimistic safety factor suggested in [309] was used, i.e. the estimated uncertainty was multiplied by a safety factor of 3. Speaking about the liquid penetration, a good agreement is recognisable until 1 ms after SOI, when the liquid length reaches a quasi-steady value due to the vaporisation process becoming dominant.

Figure 7.10 reports a computed (left circles) and experimental (right circles) spray sequence at different times from the start of injection for the condition G2. This is a transitional phase where the global spray starts to collapse and a discontinuity of the spray cone angle begins to appear, especially from the experimental images. Some plumes from different holes are widely separated and can be clearly identified, while others located on the same line-of-sight partially overlap. Also for this case, the numerical model demonstrates a good capability to reproduce the corresponding experimental spray shape, including the mixed area surrounding the liquid dense core.

In this case, the spray's shape is different from the case of G\_SFB200 in

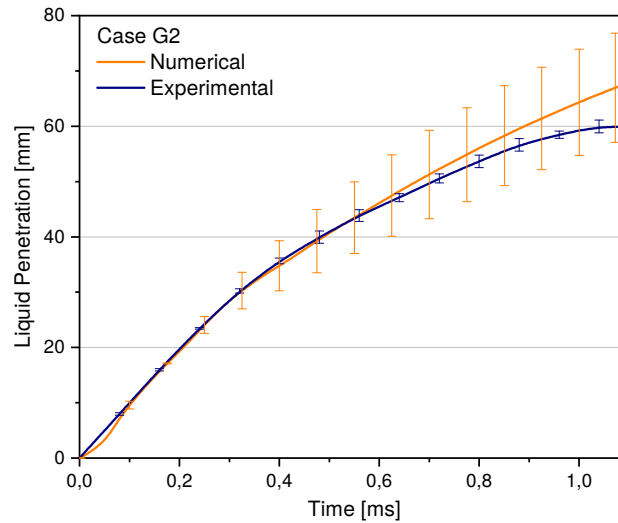


FIGURE 7.8: Numerical and experimental liquid penetration for G2 case.

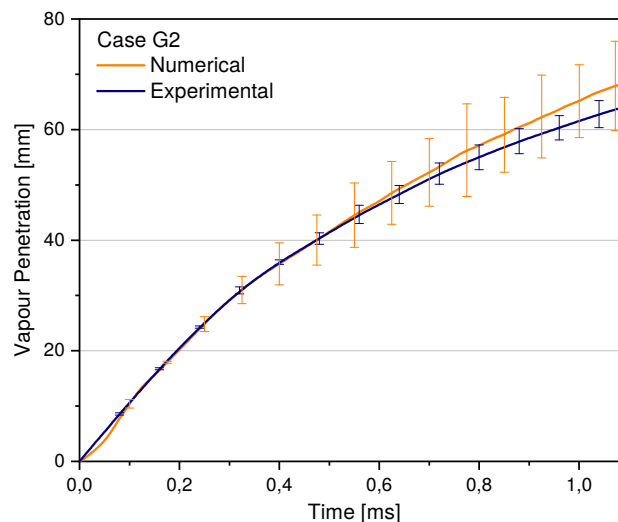


FIGURE 7.9: Numerical and experimental vapour penetration for G2 case.

Figure 7.7. Indeed, there is not a strong spray collapse, but instead expansion of the spray (the radial components are in the range of 5 m/s). The single plumes are clearly recognisable, and the flash boiling is weaker compared to the previous situation.

The spray's non-collapse can be explained by plotting an  $R_p$  map of the G2 and G\_SFB200 sprays 480  $\mu$ s after SOI (Figure 7.11).  $R_p$  was defined

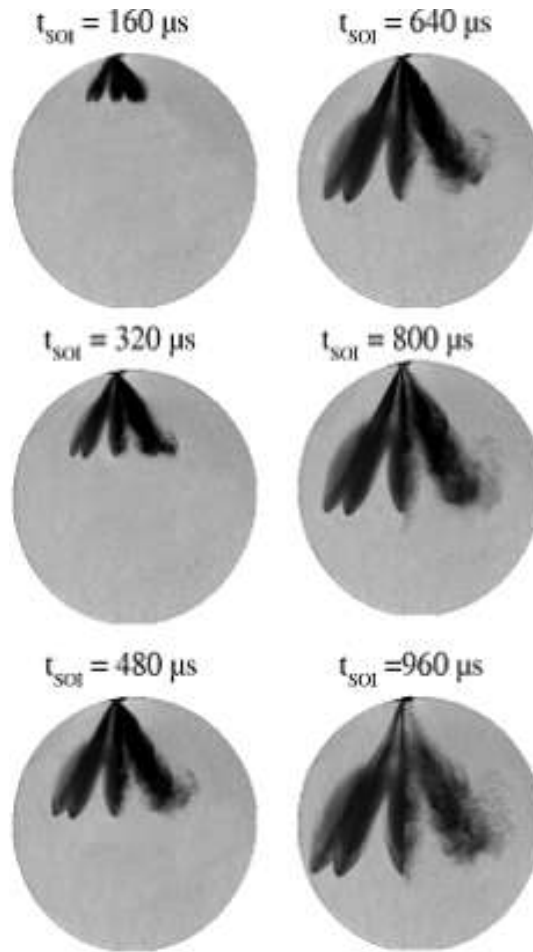


FIGURE 7.10: Comparison between experimental schlieren images (right half of each circle) and numerical results representation (left half of each circle) for G2 condition.

(Equation 7.2) as:

$$R_p = \frac{p_\infty}{p_{\text{sat}} (T_{d,i})}$$

where:

- $p_\infty$  is the ambient pressure;
- $p_{\text{sat}}$  is the saturation pressure computed, for the single spray droplet
- $T_{d,i}$  is the  $i$ -droplet temperature expressed in [K].

In Figure 7.11 the droplets of G2 and G\_SFB200 sprays are coloured from blue to red according to the increasing values of  $R_p$ . The near-nozzle red region identifies the full flash-boiling area while downstream the spray is in sub-cooled conditions and no further flash boiling takes place. The tendency of the G\_SFB200 plot towards red colour in the near-nozzle zone demonstrates the fact that a stronger flash boiling is happening in this case with respect to the G2 case.

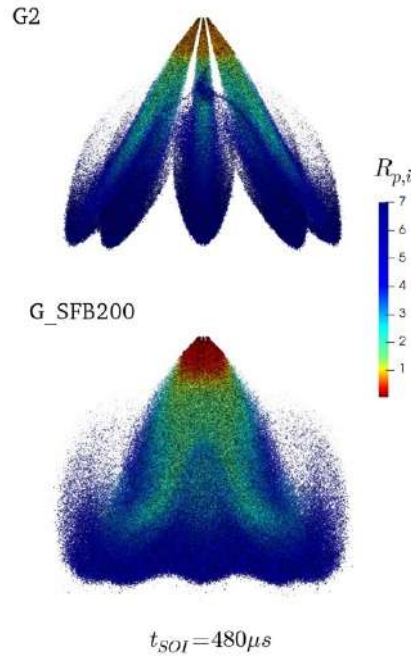


FIGURE 7.11:  $R_p$  map of the flash-boiling spray at  $480 \mu s$  after SOI for the G2 (top) and G\_SFB200 (bottom) conditions.

The spray collapse of the G\_SFBxxx cases can be physically explained by analysing the relative pressure drop. Figure 7.12 depicts the relative difference between the nominal ambient pressure ( $p_{amb}$ ) and the local computed pressure ( $p$ ) for both the G\_SFB200 (left) and G2 (right) cases, defined as:

$$\frac{\Delta p}{p_{amb}} = \frac{p_{amb} - p}{p_{amb}} \quad (7.15)$$

Higher values of the relative pressure drop mean lower pressure zones. In the G\_SGB200 case, an extended lower pressure zone is present around the vertical axis of the spray (left part of figure), while this is not present in the G2 case (right part of Figure 7.12). As widely reported in the literature, the pressure drop is the main reason for the spray collapsing in the flash-boiling conditions [130, 214]. The flow expansion of the fluid creates low-pressure cores in between the flashing jets and the whole spray collapses toward its centre. A further validation of the breakup model is given by Figure 7.13, which reports, still for the G2 case, the Sauter mean diameter ( $SMD_{32}$ ) evolution vs time in a plane orthogonal to the injector axis at a distance of 15 mm from the tip. The numerical  $SMD_{32}$  was compared against that obtained by phase-Doppler interferometry measurements, performed by researchers of the ECN community [104], for the whole injection duration. The numerical  $SMD_{32}$  was computed by collecting, for each time-step, all the parcels belonging to a plane 15 mm from the injector tip (within a tolerance of  $\pm 3\%$ )

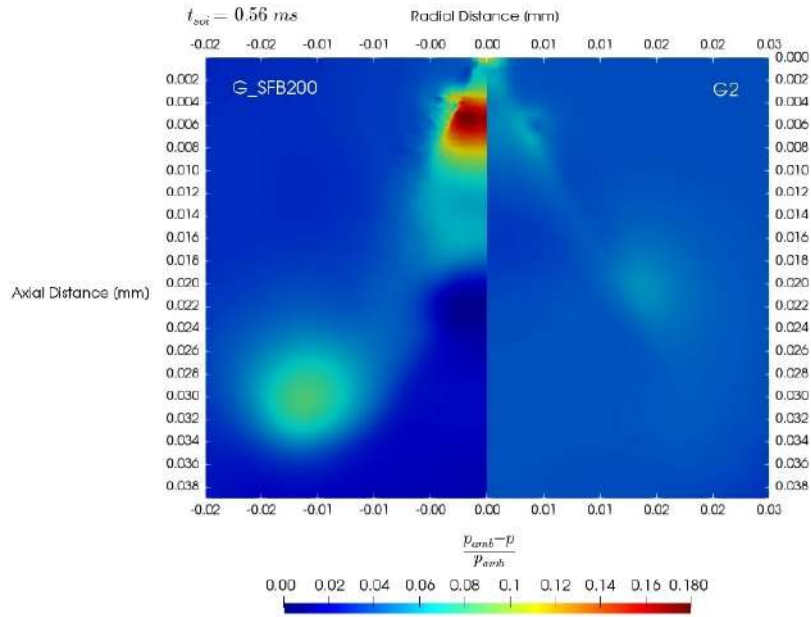


FIGURE 7.12: Representation of the relative pressure drop for G\_SFB200 and G2 conditions. The low-pressure zone, in red, causes the spray to collapse.

and applying the following relation:

$$SMD = \frac{\sum_{i=1}^{N_d} d_i^3}{\sum_{i=1}^{N_d} d_i^2} \quad (7.16)$$

The initial droplet sizes are smaller than the nozzle orifice diameter due to cavitation effects [295]. Similarly to literature works, applying reduction factors to the nozzle orifice diameter (nominally equal to 0.165 mm), two different Rosin–Rammler distributions were adopted. The resulting mean diameters are represented in Table 7 and they were used to determine the initial values of the injected parcels. It is worth mentioning that OpenFOAM limits the distribution within a minimum and a maximum value [126]. For this study the distributions were bounded within  $\pm 20 \mu\text{m}$  of the mean diameter.

	<b>Rosin–Rammler 1</b>	<b>Rosin–Rammler 2</b>
<b>Mean diameter <math>\mu\text{m}</math></b>	120	100
<b>n</b>	3	

TABLE 7.7: Parameters used for the two Rosin–Rammler distributions.

The behaviour of both the experimental and numerical curves highlights an initial decrease of  $SMD_{32}$  which reaches a minimum after which, due to droplet coalescence [127], it increases. The different values of the two numerical curves of Fig. 15 show how the choice of the initial diameter distribution strongly affects the resultant diameter distributions of the droplets. It follows

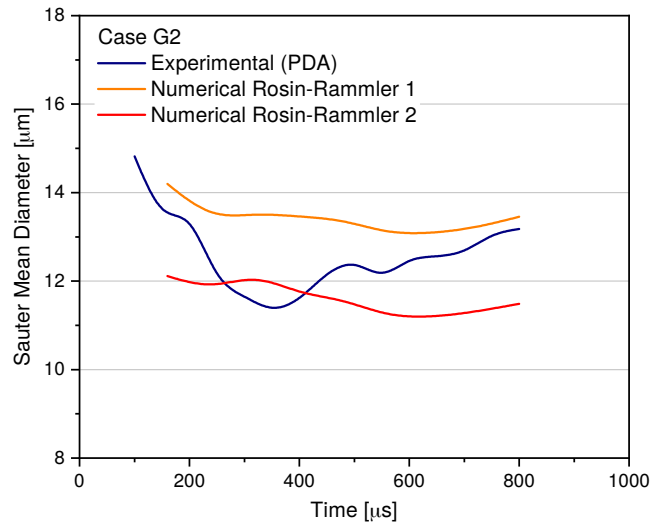


FIGURE 7.13: Sauter mean diameter ( $SMD_{32}$ ) evolution at a distance of 15 mm from the nozzles. Experimental [104] and numerical data were plotted against the time after SOI.

that, in order to provide a valid initialisation of the parcels' diameters, a specific injection model should be implemented taking account also of cavitation and flash boiling occurring within the injector ducts.

Figure 7.14 shows the  $SMD_{32}$  and  $k_b(t)$  (breakup criterion) values, at 720  $\mu\text{s}$  after SOI, plotted versus the axial distance from the injector tip. After approximately 8 mm, the  $SMD_{32}$ 's value decreases rapidly by about one order of magnitude and, in the meantime, the  $k_b$  value reaches approximately the value of unity. Flash-boiling breakup (primary breakup) occurs almost completely within this zone (the near-nozzle zone). Downstream, a further light reduction in  $SMD_{32}$  takes place, due to aerodynamic breakup (secondary breakup).

Figure 7.15 shows the time evolutions of the instantaneous liquid film thicknesses, respectively for the G2 and G\_SFB200 cases. The liquid film thickness has to be considered as the difference between the droplet and bubble diameters,  $(R_o(t) - R_i(t))$ . It changes over time according to both the bubble and droplet growth rate. The breakup for the G\_SFB200 case occurs earlier due to a faster bubble growth as a consequence of the lower back-pressure. The breakup time for the G2 case is double that of the G\_SFB200 one, while the thickness values are almost the same at the instant of breakup.

Changing the injection pressure (G\_SFB100, G\_SFB150 and G\_SFB200 cases), keeping the ambient conditions constant, the spray morphology does not change significantly, as shown in Figure 7.16 where the experimental schlieren images (right column) and the numerical reconstructions (left column) of the spray are shown at 640  $\mu\text{s}$  after SOI. Indeed, the spray morphology depends strongly on the flash-boiling phenomenon that occurs in all three cases. The

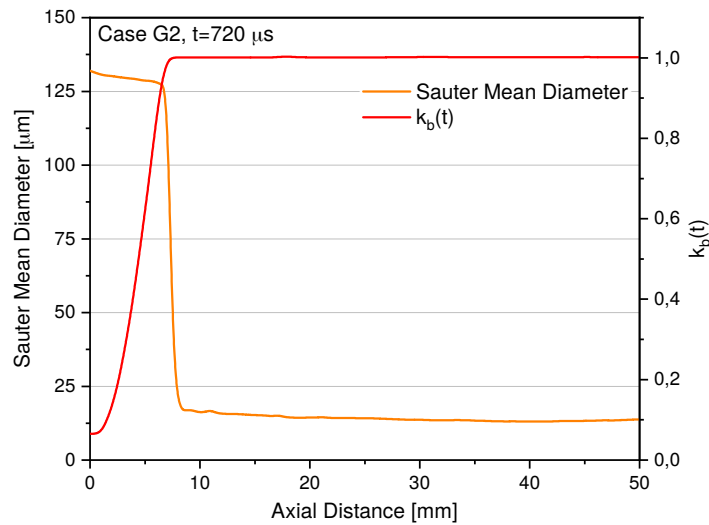


FIGURE 7.14: Sauter mean diameter ( $\text{SMD}_{32}$ ) and breakup criterion ( $k_b(t)$ ) plotted against axial distance from injector tip.

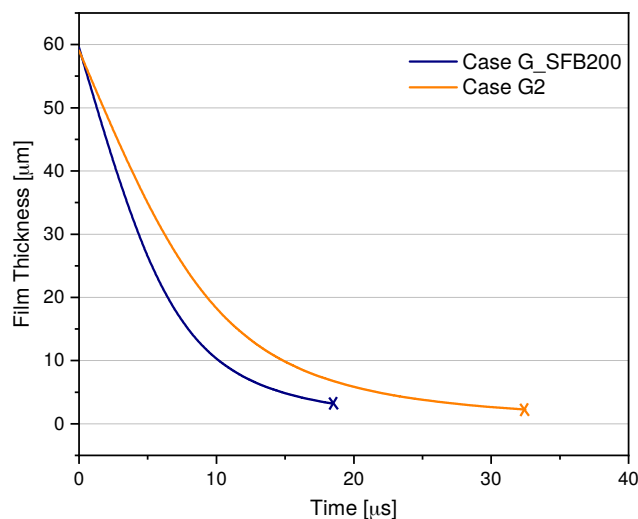


FIGURE 7.15: Droplet film thickness plotted against time since breakup has occurred.

code seems capable of describing well the spray behaviour and development under flashing conditions, thus reproducing the global spray shape.

Figures 7.17 and 7.18 show the experimental liquid (Figure 7.17) and vapour (Figure 7.18) spray penetrations, compared to the numerical ones, for all the tested injection pressures. The solid and dotted lines represent the experimental and computed results, respectively. The overlapping of the profiles at the same injection pressure confirms the accuracy of the code in capturing the spray structure during the entire injection process for both the liquid and

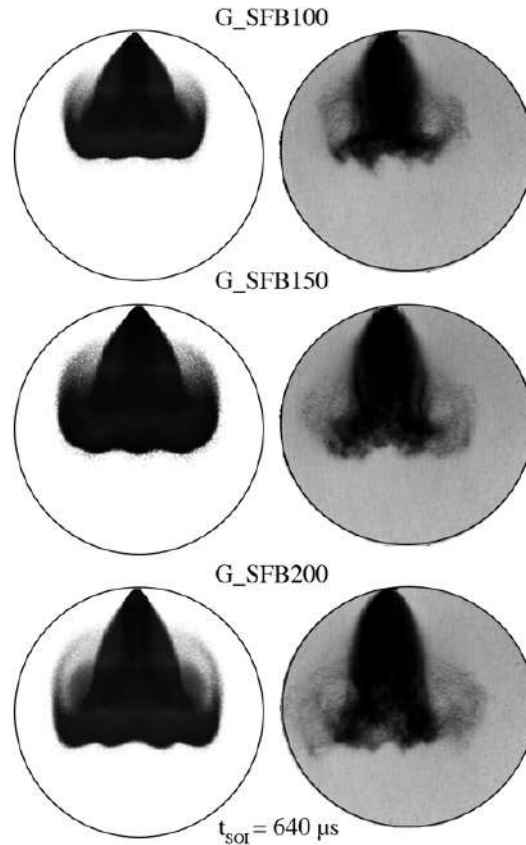


FIGURE 7.16: Comparison between the experimental schlieren images (right) and the numerically computed iso-octane mass fraction (left) for three different injection pressures: 200, 150 and 100 bar at  $640 \mu\text{s}$  from the SOI.

vapour phases. It is worth underlining that the adopted approach is capable of reproducing these different cases without changing any parameter in the model, but only updating the amount of mass injected in accordance with the experimental measurements.

Finally, Figure 7.19 shows the droplets'  $SMD_{32}$  as a function of the axial distance, for the three injection pressures. The higher the injection pressure is, the greater the flash-boiling breakup zone becomes. This is reasonable because a higher injection pressure means higher jet momentum and thus faster penetration, which leads to the extension of the zone where flash-boiling breakup occurs.

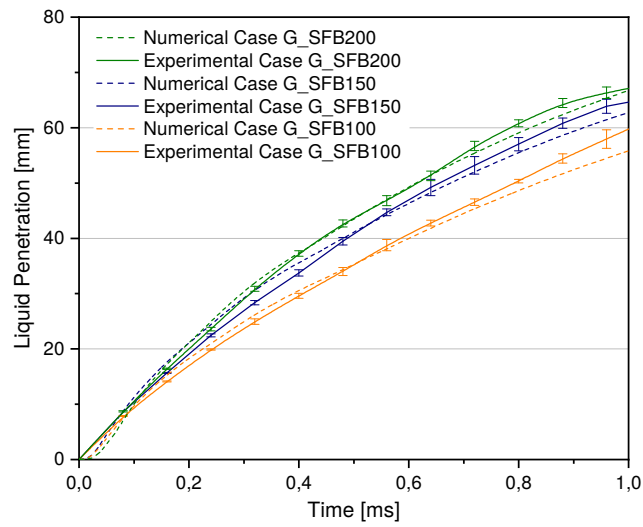


FIGURE 7.17: Numerical and experimental liquid penetration for the three injection pressures 100, 150, and 200 bar, G\_SFBxxx cases.

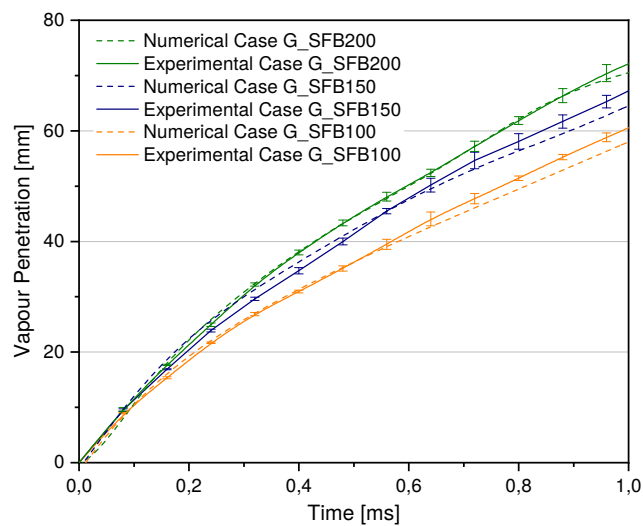


FIGURE 7.18: Numerical and experimental vapour penetration for the three injection pressures 10, 15, and 20 MPa, G\_SFBxxx cases.

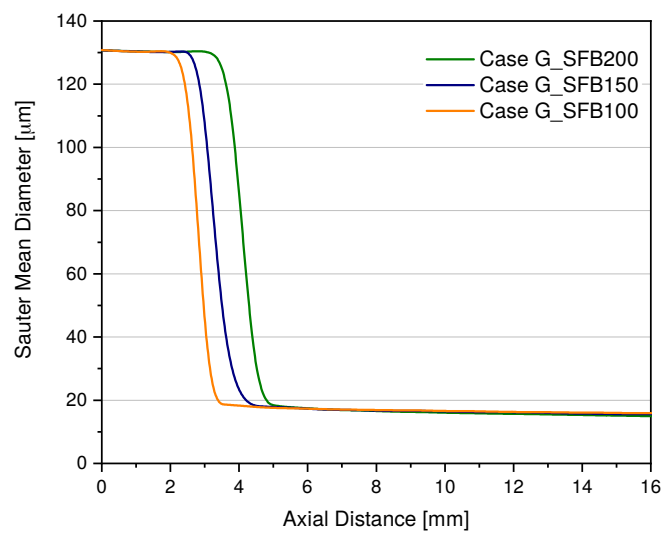


FIGURE 7.19: SMD plotted against axial distance from injector tip for the three injection pressures of 100, 150, and 200 bar.

## 7.7 Conclusions

A breakup model was developed in the OpenFOAM environment and embedded in the **sprayFoam** Eulerian-Lagrangian solver. It aims to capture the droplet shattering mechanism present in the flash-boiling of fuel sprays using linear stability analysis, bubble growth and conservation laws. A radial velocity component was added to the child parcel in order to account for the spray expansion after breakup in the near-nozzle zone. Secondary breakup was then simulated using the classical Reitz-Diwakar model. This new methodology was used to simulate the ECN Spray G injector in various flash-boiling conditions. A qualitative and quantitative validation of this modelling approach was performed, relying on experimental data collected using schlieren and Mie scattering imaging techniques. The main findings are as follows:

- The model is capable of reproducing correctly the spray liquid and vapour penetrations for different environmental conditions and injection pressures.
- Numerical uncertainty estimation, performed based on the classical procedure, ensures convergence of the solution with further grid refinement.
- The spray morphology is well reconstructed. Spray expansions, caused by flash boiling occurring in the near-nozzle zone, were reproduced thanks to the addition of the radial velocity component.
- Spray collapse, occurring only in strong flash-boiling conditions, was captured too. The reason for such spray behaviour is the formation of an extensive low pressure zone right downstream from the injector tip in the axial direction and inside the plume rose.
- Comparison of the numerical results of  $SMD_{32}$  with experimental data acquired by [104] using the PIV technique highlights that the implemented breakup mechanism correctly estimates the diameter dimensions, but, in the meantime, great sensitivity was found with respect to the droplet's injection diameter distribution.
- The flash-boiling breakup model predicts the breakage of droplets in the near-nozzle zone where an important reduction of the parcels' diameter is present.
- The results of the evolution of the liquid film thickness within the bubble-droplet system are very similar for the different analysed conditions, while flash-boiling droplet explosion occurs faster in the presence of a lower ambient density.

Future developments of this numerical approach should consider the implementation of a specific injection model accounting for cavitation and flash boiling occurring within the injector's nozzles. This is required in order to correctly initialise the parcels' diameter.



## Chapter 8

# Natural gas as an alternative energy carrier

### 8.1 Compressed natural gas: points of strength and drawbacks

One relatively quick way to reduce vehicular emissions with little change to overall transportation infrastructure is switching to gaseous fuels like natural gas (NG). The widespread usage of NG is likely going to be an effective step in the transition towards efficient and sustainable transportation. The adoption of NG as transport fuel can be implemented in vehicles in two ways depending on the fuel aggregation state:

- gaseous state, compressed natural gas (CNG), with pressurized tanks for on-board storage pressures up to 250 bar;
- liquid state liquified natural gas (LNG), with cryogenic tanks for on-board storage and after been cooled below -160 .

The second option is undoubtedly more technologically complex and economically more expensive, although it allows to solve problems inherent to the vehicle range autonomy. In this work will be considered CNG

The main advantage offered by CNG engines is represented by the low carbon / hydrogen ratio which means lower CO<sub>2</sub> emissions; moreover, the particulate matter and unburned hydrocarbons emitted are significantly lower. Furthermore, it was estimated that carbon dioxide emissions per kilometre travelled are reduced by more than 25%, compared to the petrol counterpart [210].

CNG is produced by compressing the conventional natural gas and it is stored in a tank at a pressure of 200-250 bar. The use of compressed natural gas such as a fuel for transport were discovered in Italy in 1930. By 1995 to 2015, the natural gas vehicles have increased speedily at an annual rate of 24% (Figure 8.1) and the majority of this vehicles are light duty car [177]. The octane number of natural gas is in a range from 120 to 130 and it means that the engine has a compression ratio up to 16:1 without knock effect. This high octane number and consequently a high compression ratio improve the engine thermal efficiency of about 10% than that of gasoline engine. The compressed natural gas engine may have the efficiency up to 35%, while the

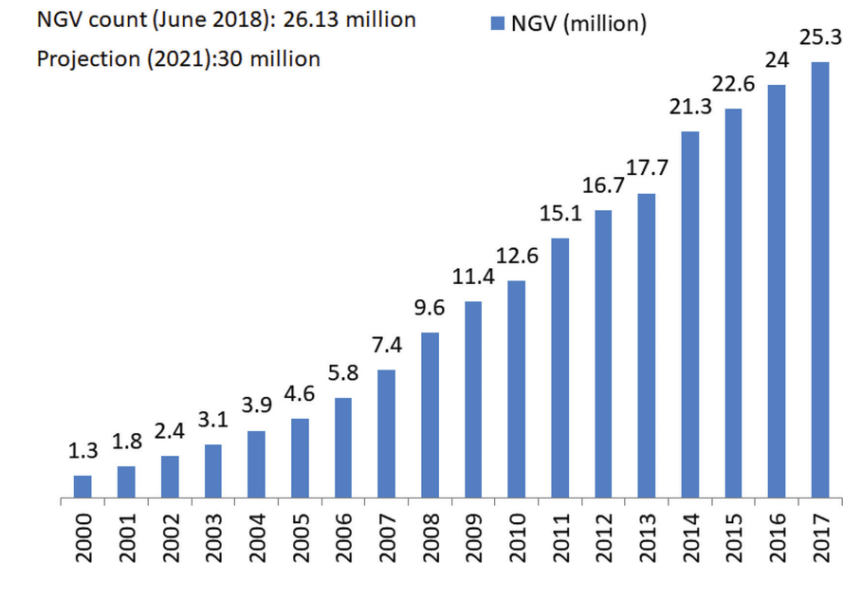


FIGURE 8.1: Number of natural gas vehicles worldwide by years [154].

efficiency of gasoline engine reaches a 25%. The molar mass of natural gas is 16 g/mol, while that of gasoline is 114,23 g/mol: the lower molar mass and the light weight of natural gas produce a better homogeneous air-fuel mixture. A high level of miscibility and diffusion with air is crucial for good combustion and in fact compressed natural gas being a gaseous fuel at normal temperature conditions while liquid fuels need time for complete vaporization. Natural gas vehicles have lower cost of maintenance and prolongs useful life engine than traditional fuelled vehicles. For example, natural gas does not contaminate engine oil and the life of lubricant is longer. In the other hand, gasoline comes into the engine as spray and washes down the oil from the piston rings, leading to wear of the engine. There is not a lead concentration and it means that compressed natural gas avoids lead fouling of spark plugs and the life of plugs and piston rings is extended. In this engine, oil changes occur from 5000 to 10000 kilometres depending how the vehicle is used. Brake specific fuel consumption is 12% to 20% lower than of gasoline and it is due to speed range. This can be attributed to higher heating value and to lean and slow burning of compressed natural gas. The heating value of compressed natural gas is 47,5 MJ/kg while that of gasoline is 43,5 MJ/kg. For this reason, natural gas engine has 5-12% higher brake thermal efficiency than gasoline engine. About economic system, in most countries, the compressed natural gas is cheaper than diesel and gasoline despite the compression costs. Figure 8.2 shows a comparison between the price of natural gas and the price of diesel and gasoline. Furthermore, is less vulnerable to the fluctuations of price, besides the fact that its resources are more distributed over the earth comparing to oil. This means that in countries with a good natural gas vehicles penetration, the pump price has an average 50% less than gasoline and diesel price.

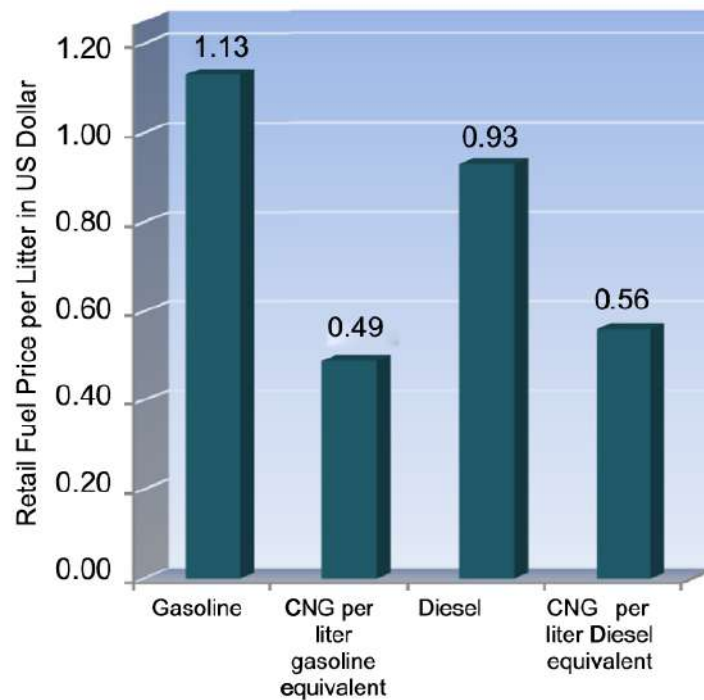


FIGURE 8.2: CNG price compared to gasoline and diesel.

LCA analysis, among the others, can be performed for vehicles and for fuels too. Comparing LCA of CNG and diesel light duty vehicles, some studies done were showed a high efficiency and reduction of CO<sub>2</sub> emissions for natural gas. A model studied in Argonne National Laboratory's revealed that compressed natural gas emits approximately 6-11% less of greenhouse gases than gasoline, during the fuel life cycle. Finally, in 2007 a study for the California Energy Commission declared that light and heavy duty vehicles have produced less greenhouse gases emissions in their life cycle than gasoline and diesel vehicles [177]. Naturally the fundamental component of natural gas is methane and so the emission factors of this vehicles can be reduced by installation of an exhaust catalyst.

However, natural gas has some negatives aspects, such as flame speed and volumetric efficiency, that are balanced with very low emissions linked to this kind of engine. Natural gas has a slow flame propagation speed, and this conduces to prolongation of total combustion duration compared with gasoline or diesel engines. Energy losses are increased, and engine power is reduced from 5% to 10%. Slow flame propagation speed issue can be solved mixing natural gas with fuels having fast burning speed and one solution can be the hydrogen. It is considered the best additive because it has a fast flame propagation speed, 265-325 cm/s. Moreover, the volume occupied by natural gas is larger than that occupied by gasoline or diesel engine in a stoichiometric air-fuel mixture : when liquid fuels enter in the cylinder the liquid particles vaporize and this increase the inlet pressure of the cycle, while compressed natural gas is just gaseous and the rise of inlet pressure is not present. A way to improve the volumetric efficiency can be increasing the number of

intake valves per cylinder, a lift valve optimization using turbocharged engine and modifying the design of intake valve. But in this case, costs and reliability must be taken into account. Despite this, the emission performance of natural gas engine leads to a potential benefit for the environment, for the air quality and for noise. Compressed natural gas is one of the cleanest vehicle fuels. An interesting case study is the town of Delhi. Delhi has the biggest public transport system based on compressed natural gas engine. A comparison made between the levels of environmental pollutants before and after the adoption of natural gas vehicles showed the decrease of CO, SO<sub>2</sub> and NO<sub>x</sub>. Indeed, the aspect that decreases the efficiency engine, as a low flame propagation speed, reduces the maximum temperature into combustion chamber and this behaviour involves dissociation from CO<sub>2</sub> to CO. Also CO<sub>2</sub> emissions of compressed natural gas vehicles are lower and can be decreased by 20% respect those of gasoline because natural gas has high hydrogen to carbon ratio that is 4:1 while gasoline ratio is 2,3:1 and diesel ratio is 1,95:1. Taking into account the value of CO<sub>2</sub> produced by methane combustion and comparing this emission with that of other fuels, at the same heat, the result is that other fuels leads to an higher value, as shown in Figure 8.3.

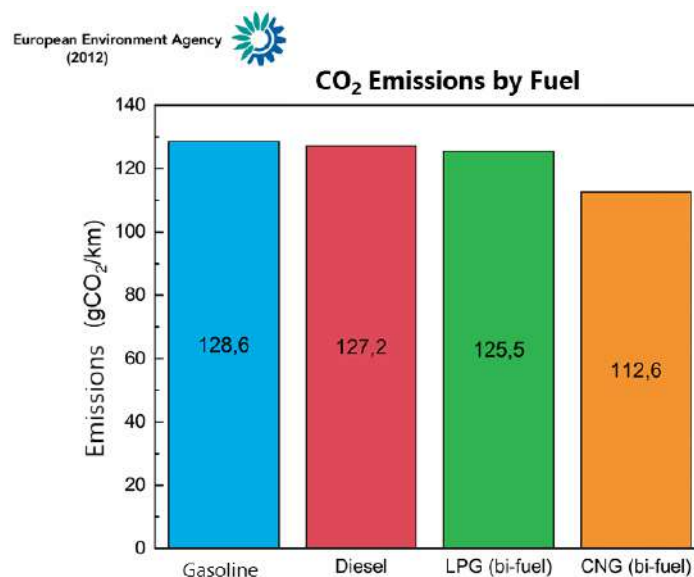


FIGURE 8.3: Reduction in CO<sub>2</sub> emissions [108].

Compressed natural gas burns at a low adiabatic flame temperature due to leans air-fuel mixture with the excess of air that reduces the peak of combustion temperature and the result is low NO<sub>x</sub> emissions. Another positive aspect of natural gas concerns particulate matter emissions: it not has aromatic compounds and it has less sulphur compounds than petroleum fuels. This means that PM emissions are significantly reduced. The high hydrogen to carbon ratio with a few aromatic compounds content is responsible for the reduction of volatile organic compounds species (VOCs). It is important to

consider also the safety of compressed natural gas vehicles. Safety benefits compared with gasoline and diesel were found because physical properties make compressed natural gas safer. It has a restricted flammability range that is 4,3% to 15,2% by volume in air and it means that natural gas will not burn in presence of a spark, if its concentrations in air is below 4,3% and above 15,2% [173]. Moreover, natural gas is lighter than air (the density of compressed natural gas is 0,68 kg/m<sup>3</sup> while the density of air is 1,12 kg/ m<sup>3</sup> ,at atmospheric condition) and in case of leakage natural gas rises and disperses rapidly don't forming some pools on the ground that are formed in case of gasoline and diesel leakage. This fact reduces the probability to have a fire in case of tank breached. The possibility of accidental ignition of this fuel is low because, in addition to the flammability range, natural gas has a high auto ignition temperature that is 540 °C, in contrast to auto ignition temperature of gasoline (258 °C) and of diesel (316 °C).

All these aspects discussed above, combined with positive results from studies of compressed natural gas engine, are increasing the interest of researchers to approach experiments of natural gas jets in combustion chamber.

## 8.2 Compressed Natural Gas in ICE

Besides than DI systems CNG can be implemented on ICE using other kinds of technologies. For the sake of completeness, a quick overview, of the principal solutions is reported in this paragraph.

### 8.2.1 Bi-Fuel Engines

CNG/gasoline bi-fuel engines are refitted from gasoline engines, by adding a NG supply and injection system. On average bi-fuel engine reduced CO emissions by around 80%, CO<sub>2</sub> by 20% and HC by 50% and increases NO<sub>x</sub> emissions by around 33%, with CNG compared to gasoline. Bi-fuel vehicles fuelled with CNG also have the potential to reduce the PM emissions compared to gasoline operation under NEDC emission certification mode. For port injection of CNG, partial air space is occupied by NG and thus the volumetric efficiency reduces. Furthermore, the maximum burning velocity of methane is 37 cm/s, and it is less than that of gasoline. As a result, power output of bi-fuel engine fuelled with NG is lower than with gasoline [61]. On the other hand, with PFI the mixture quality and the homogeneity are better than DI because air and fuel have more time and space to mix each other. NO<sub>x</sub> emissions of bi-fuel engines are higher than the pure-gasoline ones due to the combustion temperature that is higher for bi-fuel systems.

### 8.2.2 Dual-Fuel Engines

The "Dual Fuel" technology is based on compression ignition engines. The operating mode provides that a homogeneous mixture of natural gas and

air (previously introduced in the combustion chamber) is burned by a pilot injection of diesel, just before the end of the compression stroke. At load level, these engines operate exclusively with diesel; as the load increases, CNG replaces diesel in percentages of the order of 60-90%. This technology still suffers from the high pumping losses due to intake regulations and does not solve the problem of particulate emissions, typical of diesel engines [396].

### 8.3 Compressed Natural Gas Direct Injection Engines

CNG-DI provides that the fuel is introduced directly into the combustion chamber (at very high pressures) during the compression stroke. The advantages of such technology can be summarized as follows:

- compensates the reduction of volumetric efficiency associated with PFI;
- increases thermal efficiency;
- reduces the CO<sub>2</sub> emissions by 22-25% with respect of diesel engine and 30% less than gasoline engine [396];
- reduces in fuel consumption;
- provides higher torque.

The main advantage of DI technique consists in having available two engine operation modalities: homogeneous mixture and stratified mixture. The homogeneous charge operation, designed for medium-to-high engine loads, is a consequence of early fuel injection. This charge strategy increases the indicated efficiency reducing losses in exchange process and the injection starts at the end of inlet stroke to minimize the influence of volumetric efficiency. A very good mixing is obtained with adaptation of advanced injection timing because if the fuel is injected early, there is a time for fuel air-mixing before the ignition. It must be highlighted that there is a limit on lean operation because, for further lean conditions (equivalence ratio lower than 1.25), incomplete combustion occurs with result of excessive HC emissions. On the other hand, the stratified charge operation occurs with a late fuel injection close to compression stroke and when there is a high amount of fuel (rich mixture) close to spark plug, in the remaining area of the combustion chamber there is a lean mixture. Stratified operation of CNG engine improves the indicated efficiency and fuel consumption. The nozzle shape and the characteristics of the injector have great influence on stratification capability.

Converting a gasoline engine to operate with CNG requires modifications as redesign of cylinder head to improve the position of direct fuel injector. Nowadays research is focused on various solutions developed for implementing DI of CNG.

The requirements of a gas injector are quite different from common liquid ones. First of all, unlike injectors for liquid fuels, the gas injector is not

lubricated by the fuel itself and, therefore, to extend its life requires ad hoc lubrication systems. To inject a sufficient quantity of fuel during the compression or intake stroke (depending on the operating conditions) it is necessary to have either sufficiently large passage sections and/or high pressure values. In the absence of a compressor, the maximum injection pressures are a function of the pressure of the fuel in the tank. In CNG PFI systems, for example, injection pressures are about 8 bar with a 96% use of cylinder fuel. With the same injection pressure in a CNG DI engine the power would be significantly limited; on the other hand, if the pressure were increased, for example, to the value of 30 bar, there would be a 9% decrease in the range of the vehicle, since a smaller amount of gas contained in the tank can be used. The optimal injection pressure is, therefore, the result of a trade-off between the output power required from the engine and the range of the vehicle. Figure 8.4 shows the different kind of injectors:

- "outwardly-opening", with opening towards the outside;
- "inwardly-opening", with inward opening.

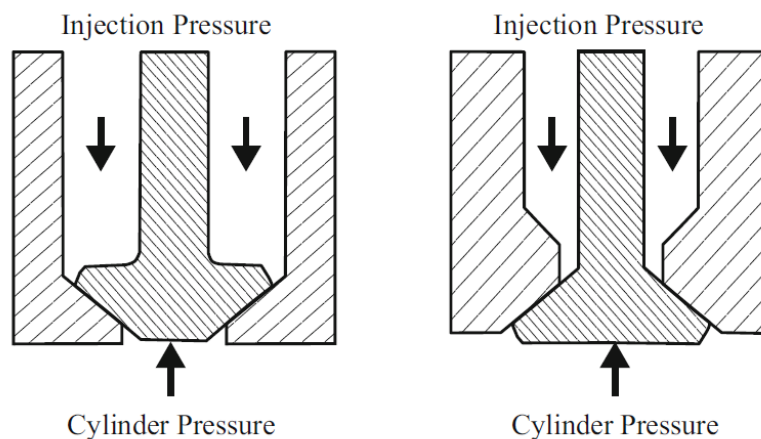


FIGURE 8.4: Schematic representation of inwardly and outwardly opening injectors [91].

Considering that the injection pressure in a CNG-DI can be of the order of 30 bar, an "inwardly-opening" injector could inadvertently open due to the back pressure in the cylinder. This suggests that the best choice for a CNG-DI engine should be to use an "outwardly-opening" injector.

Further than the classical configuration for DI, it can be mentioned "Two Stage Combustion Systems" that consist in the use of a pre-chamber with the goal to improve lean mixture combustion process and consist in two parts, main chamber and pre-chamber. The main chamber is filled with lean mixture, while into the pre-chamber there is a rich mixture. During the compression stroke, lean mixture is forced into the pre-chamber to weakening the rich mixture. In this applications, direct injection of fuel into the combustion chamber occurs to avoid the knock, spark plug is as an ignition source

when the fuel is mixing with air and the control of the engine power is done varying the amount of fuel injected per cycle. For this application, there is a reduction of NO<sub>x</sub> but also the increase of HC emissions. However, the positive aspect of this configuration is that the pre-ignition chamber has the potential to overcome ignition problem of direct injected gaseous jets.

CNG is regarded as fuel also for CI engines. Advanced combustion and injection techniques are present in literature and are being deepened by researchers. To overcome the problem of CNG misfiring a CNG/diesel injection procedure was developed in which the gaseous fuel is injected into combustion chamber as the primary fuel, while the pilot diesel injection, with a small quantity of fuel (usually limited at 20%), works for ignition only. This technique is called High Pressure Direct Injection (HPDI) and it is shown in Figure 8.5, left side. This system features a dual-needle and dual-actuator fuel injector, natural gas and diesel are injected through separate sets of holes. This type of operated mode was found to reduce PM and NO<sub>x</sub> and it produces a relatively higher torque and efficiency. Another solution to CNG

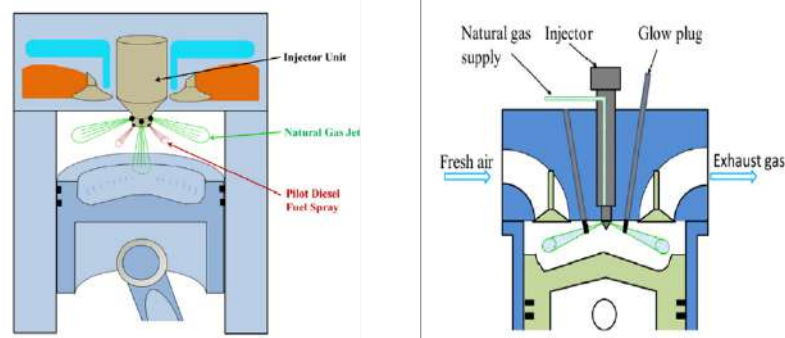


FIGURE 8.5: Diagram of high pressure direct injection system (left) and diagram of hot surface assisted compression ignition (right) [396].

is called "Hot Surface Assisted Compression Ignition" (Figure 8.5 right) in which a smaller amount of natural gas is injected directly into the cylinder close to a hot surface at the end of the compression. The hot surface is generally a glow plug with a temperature of about 1400 K. This type of engine has high thermal efficiency and specific power but the problem is the durability of the hot surface due to the high surface temperature required.

## 8.4 Physics of High Pressure Gaseous Jets

The simplest theory for representing the evolution of gaseous jets resemble the injector's ducts as a DeLaval nozzle. Such analysis involves a number of concepts and assumptions:

- the ideal gas law is valid;

- the gas flow is isentropic (i.e., at constant entropy). It follows that the flow is reversible (frictionless and non-dissipative) and adiabatic (no heat are gained or lost);
- the gas flow is constant (i.e., steady);
- the gas flow is along a straight line from gas inlet to gas outlet section (i.e., along the nozzle's axis of symmetry)

It follows that from the conservation of energy, with the further hypothesis of mono-dimensional flow, it is possible to obtain the following relations:

$$\frac{d\Omega}{\Omega} = (Ma^2 - 1) \frac{du}{u} \quad (8.1)$$

$$\frac{d\Omega}{\Omega} = \frac{1 - Ma^2}{Ma^2} \frac{du}{u} \quad (8.2)$$

where,  $Ma = u/a$  is the Mach number,  $a$  is the speed of sound,  $p$  is pressure and  $\Omega$  is the transversal area. From the analysis of these expressions, the following conclusions can be drawn:

- for  $Ma < 1$  (subsonic flow), an expansion process have to be performed in a convergent duct;
- for  $Ma > 1$  (supersonic flow), an expansion process have to be performed in a divergent duct;

The pressure value reached at sonic condition is called critical pressure and it is equal to:

$$p_c = p_0 \left( \frac{2}{\gamma + 1} \right)^{\frac{\gamma}{\gamma + 1}} \quad (8.3)$$

where  $p_0$  is the upstream pressure and  $\gamma$  is the constant heat ratio.

Therefore, considering an expansion to a downstream pressure lower than critical pressure, first it is necessary to expand the gas within a convergent and, once the sonic conditions were reached, the expansion continues in a divergent. Gaseous injection process takes place in a nozzle and, here, the fluid itself creates a convergent-divergent duct expanding. The section where sonic condition are reached is called "throat section" and it features the minimum diameter. Here, the choking phenomenon takes place too. Indeed, the mass flow is generally proportional to upstream-to-downstream pressure ratio but, once the sonic conditions were reached, it remains constant for further pressure reductions. In this way the downstream conditions are re-established by different kind of shock-waves.

A shock wave represents a sudden change in the properties of the flow field (speed, pressure, temperature, ...) they occurs only for supersonic flows since the information, propagating as pressure waves, travels only downstream, failing to rise upstream of the disturbance. A shock wave is exclusively a compression wave and can be normal or oblique; the latter are also called expansion fans. The shock wave perpendicular to the flow direction

is defined as "normal"; such a wave is comparable to a plane of infinitesimal thickness. Consider a plane wave that translates perpendicularly to itself within a compressible fluid (similar to a perfect gas) at rest; assume as the reference system the one integral with the wave (so as to make the motion permanent) and indicate with subscript 1 and 2 the conditions of the fluid respectively upstream and downstream of the wave (Figure 8.6):

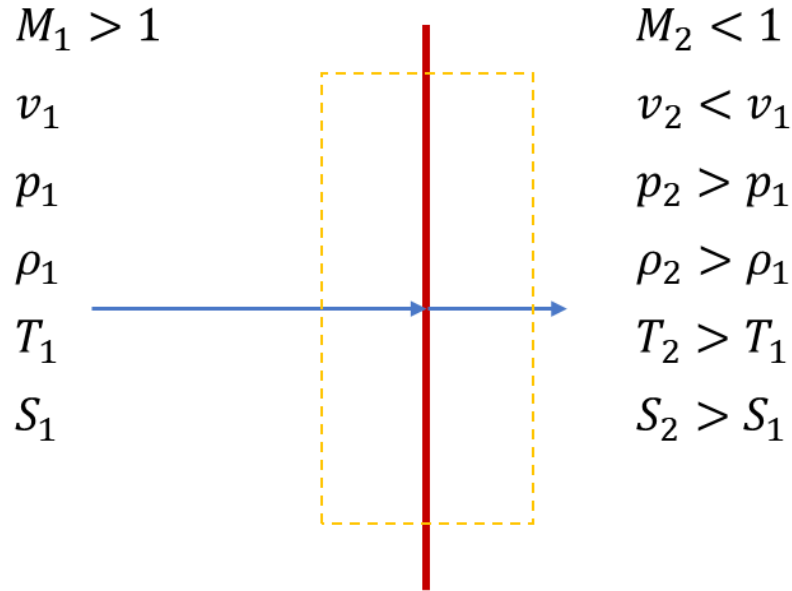


FIGURE 8.6: Normal shock wave.

Considering the dashed control volume in Figure 8.6, it is possible to write the governing equations for the fluid (with reference to an adiabatic flow):

$$\text{Continuity equation : } \quad \rho_1 v_1 = \rho_2 v_2 \quad (8.4)$$

$$\text{Momentum conservation equation : } \quad p_1 + \rho_1 v_1^2 = p_2 + \rho_2 v_2^2 \quad (8.5)$$

$$\text{Energy conservation equation : } \quad h_1 + \frac{v_1^2}{2} = h_2 + \frac{v_2^2}{2} \quad (8.6)$$

$$\text{Ideal gas equations : } \quad \begin{cases} h = c_p T \\ p = \rho R T \end{cases} \quad (8.7)$$

Combining such equations, introducing the definition of Ma and  $\gamma$ , the normal shock equation can be derived:

$$M_2^2 = \frac{1 + \left(\frac{\gamma-1}{2}\right) M_1^2}{\gamma M_1^2 - \left(\frac{\gamma-1}{2}\right)} \quad (8.8)$$

$$\frac{\rho_2}{\rho_1} = \frac{u_1}{u_2} = \frac{(\gamma+1)M_1^2}{2 + (\gamma-1)M_1^2} \quad (8.9)$$

$$\frac{p_2}{p_1} = 1 + \frac{2\gamma}{\gamma+1} (M_1^2 - 1) \quad (8.10)$$

$$\frac{T_2}{T_1} = \frac{h_2}{h_1} = \left[ 1 + \frac{2\gamma}{\gamma+1} (M_1^2 - 1) \right] \frac{2 + (\gamma - 1)M_1^2}{(\gamma + 1)M_1^2} \quad (8.11)$$

Equation 8.8 states that the Mach number downstream the shock wave is a function exclusively of the Mach number upstream. Therefore, the supersonic flow, crossing the shock wave, dissipates energy and, downstream, becomes subsonic. Equations 8.9, 8.10 and 8.11 demonstrate that the other thermodynamic parameters too are function of upstream and downstream Mach number. So from the entropy equation:

$$s_2 - s_1 = c_p \ln \frac{T_2}{T_1} - R \ln \frac{p_2}{p_1} \quad (8.12)$$

it can be deduced that the variation of entropy through a shock wave is a function exclusively of the Mach number upstream of the wave itself. The second law of thermodynamics states :

$$s_2 - s_1 > 0 \quad (8.13)$$

so it is possible to conclude that the condition  $M_1 < 1$  is not acceptable and, therefore, a normal shock wave can exist only in the case of supersonic flow.

Regarding to the total thermodynamic parameters, it is possible to verify that crossing the shock wave [17]:

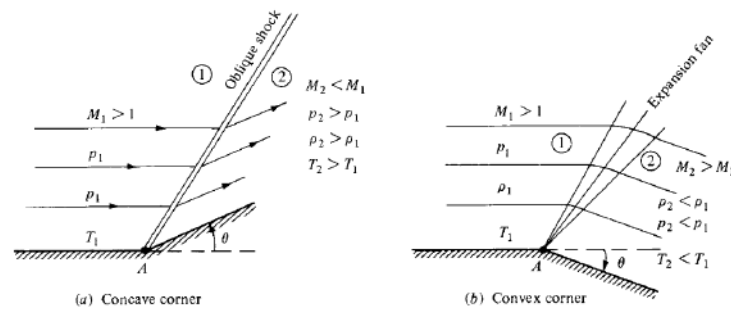
- the total temperature remains constant  $T_{0,1} = T_{0,2}$ ;
- the total pressure decreases  $p_{0,1} > p_{0,2}$ , although the static pressure increases.

It follows that, crossing the shock, there is partial dissipation of the kinetic energy which degrades in irreversibilities.

An "oblique" wave is a discontinuity in the flow-field with a direction that is not perpendicular to flow-field velocity; unlike normal shock waves, oblique waves can occur both in the form of compression waves (oblique shock waves), through which a non-gradual increase in pressure occurs, and in the form of expansion waves (expansion fans), through which the pressure gradually decreases.

Figure 8.7 shows a supersonic gas flow along a wall with a concave or convex angle at point A. The flow is tangent to the wall and, therefore, the streamline at the corner is deviated (to comply with the physical boundary imposed by the wall). If the angle is concave (a) the flow lines are deflected upwards, i.e. within the main flow: in this situation an oblique shock wave occurs. The streamlines behind the wave remain parallel each other, while, following the wave crossing, they are deflected upwards with an inclination. Similarly than a normal wave, crossing an oblique shock, the Mach number decreases, while pressure, density and temperature increase.

For an oblique shock wave, similar considerations of to those formulated for a normal wave apply. It is also possible to demonstrate that, defined  $\beta$

FIGURE 8.7: Supersonic flow along a corner of  $\theta$  angle [17].

as the angle between the direction of the undisturbed flow and the oblique shock wave, crossing the shock, only the normal velocity component (i.e. the one indicated in Figure 8.8) becomes subsonic ( $M_{2,n} = M_2 \sin \beta < 1$ ), while the parallel component ( $w$ ) is conserved, resulting in a decrease in the flow velocity. Furthermore, for a given Mach number upstream of the deviation, there is a maximum deflection angle  $\theta_{max}$ , beyond which the impact will no longer be oblique, but curved and detached from the vertex (Figure 8.9). On

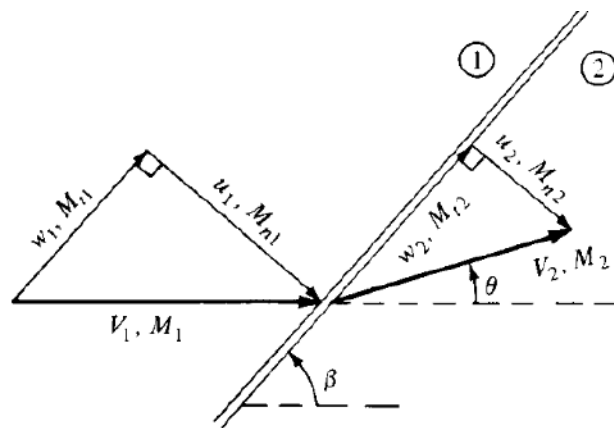


FIGURE 8.8: Geometric characteristics of an oblique shock [17].

the other hand, if the angle is convex (Fig. 8.7-b), the flow line is deflected downwards, away from the main flow: in this situation an expansion wave, or rather, a fan of oblique waves, appears (or even Prandtl-Meyer expansion fan), centred at point A, which progressively widens as the distance from the wall increases. The initially horizontal and parallel streamlines behind the expansion wave are gradually deflected downwards by the fan itself with an angle  $\theta$ . Crossing the expansion fan determines an increase in the Mach number and a decrease in pressure, density and temperature. Unlike the oblique shock waves, a gradual and isentropic transformation (expansion) of the gas takes place. The flow at the outlet of an expansion Meyer fan is in the direction of the deflection angle  $\theta$ , related to the Prandtl-Meyer function,  $\nu(M)$  through the relationship:

$$\theta \nu(M_2) - \nu(M_1) \quad (8.14)$$

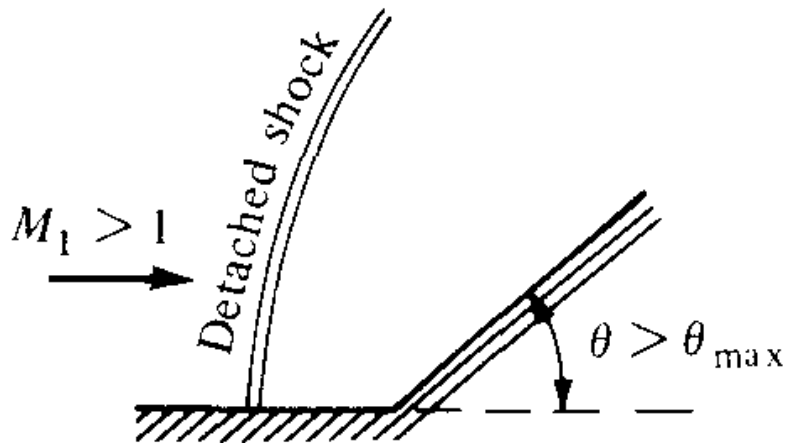


FIGURE 8.9: De-attached and oblique shock [17].

The shock waves can interact each other (compression or expansion), with the solid walls of the ducts, with the boundary layers and with vortex. First, consider an oblique shock wave incident on a wall (Figure 8.10):

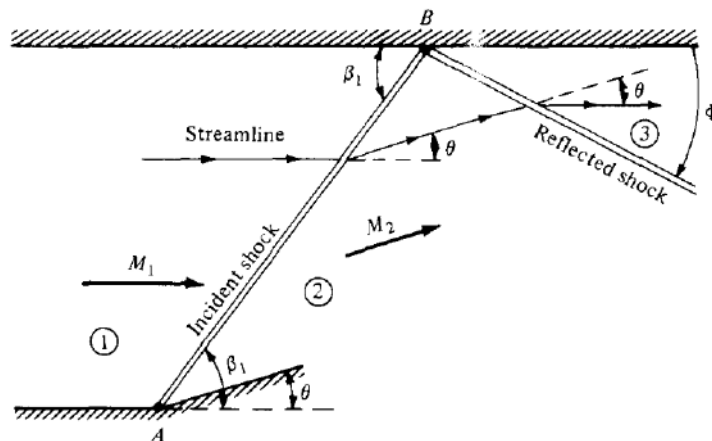


FIGURE 8.10: Oblique shock reflection on a wall surface [17].

The streamline, before the vertex [A], proceeds undisturbed with inclination  $\beta = 0$  and Mach number  $M_1$ . After the wall deflection of angle  $\theta$ , the flow deviates (to remain parallel to the wall) and an oblique shock wave is formed, inclined by  $\beta_1$  angle, defined as an *incident shock wave*. The *incident shock wave*, generated starting from point A, hit the wall at point B. The flow in region 2 is inclined of the deflection angle  $\theta$  and have a Mach number  $M_2 < M_1$  (due to the properties of compression waves). To comply with the boundary condition imposed by the presence of the upper wall, the flow has to further deviate by an angle  $\theta$ : this determines the birth of a further shock wave, at point B, called the *reflected shock wave*. The inclination of the reflected shock wave is lower than the inclination of the incident shock

wave. Even if the deviation of the flux is the same (i.e.  $\theta$  is unchanged), the reflected wave is not specular to that incident one: the angle  $\Phi$  is different from  $\beta_1$ . The properties of the reflection wave are uniquely defined by  $M_2$  and  $\theta$ . Since  $M_2$  is, in turn, a function only of  $M_1$  and  $\theta$ , the properties in region 3 and, therefore, the angle are easily determined starting from  $M_1$  and  $\theta$ . This is called regular reflection. When the value of  $\theta$  is high enough or the value  $M_1$  small enough, the flux line cannot be kept parallel to the upper wall and the regular reflection cannot occur: the reflected wave is no longer perfectly straight and the so-called Mach reflection occurs (Figure 8.11).

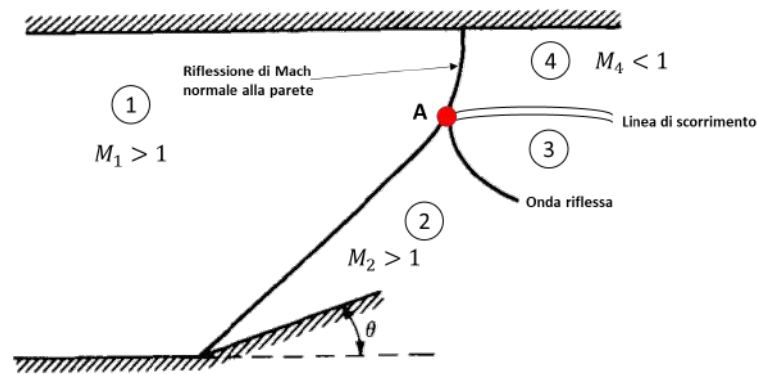


FIGURE 8.11: Mach reflection [17].

The tangent condition can only be verified if the impact is normal, resulting in zero deviation. The incident shock wave, initially inclined and rectilinear, tends to curve as it approaches the upper wall, becoming a normal shock wave. At point A (triple point) the incident collision, the Mach reflex collision and the reflex collision (which no longer originates from the wall, but from inside the field) meet. In regions 3 and 4 the flow direction and pressure are the same, while the temperature, entropy, velocity and Mach number are different (the streamline in 3 crossed two shock waves): consequently, the two regions are separated by a surface of discontinuity, called "slip line" or "vortex sheet". In particular, since at the same pressure the dissipation is greater in the passage through a single impact, above the sliding line the entropy is greater, the total pressure is lower and consequently the velocity is also lower. The phenomena of reflection of compression and expansion waves also occur when they interact with constant pressure contours. A typical example, in this regard, is represented by an over-expanded jet released within a region with a greater pressure (Figure 8.12). Crossing the oblique impact generated by the geometric edge at the outlet of the duct, an increase in pressure occurs, so in region 2 there is  $p_2 = p_b$ . Through the wave reflected from the plane of symmetry, a further increase in pressure occurs, so  $p_3 > p_b$ . At the interface of the jet, however, the condition of constant pressure must exist and consequently an expansion wave is generated on the contour, through which the pressure decrease occurs. In particular, a Prandtl-Meyer fan is created at the

point of intersection of the oblique impact reflected with the contour of the jet.

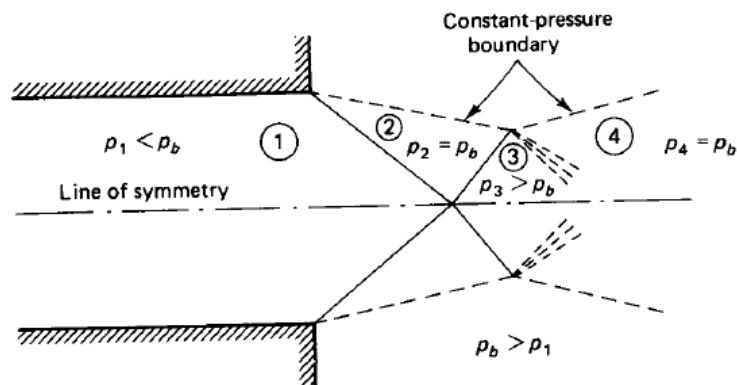


FIGURE 8.12: Oblique shock wave reflection from a constant pressure boundary [17].

A similar situation occurs when an under-expanded jet is released within a lower pressure region (Figure 8.13). Another possible interaction is that

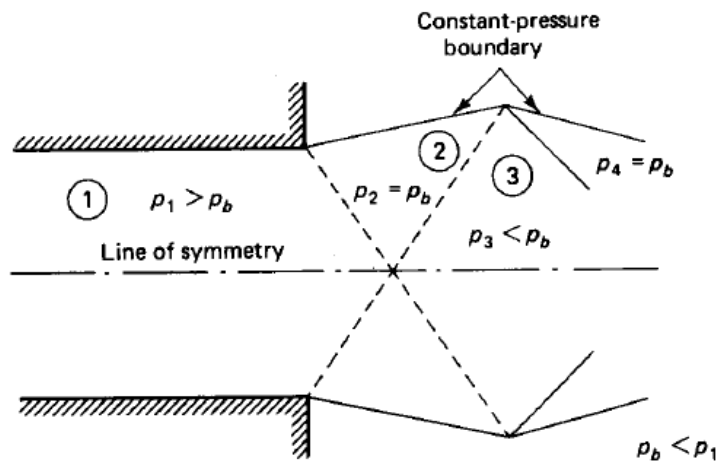


FIGURE 8.13: Oblique shock wave reflection from a constant pressure boundary [17].

determined by the intersection of two shock waves (Figure 8.14):

Due to the different angle of deflection, the two shock waves generated by the vertices G and H, have different length. The intersection of the two waves occurs at the point denoted by the letter E in Figure 8.14, from which two further shock waves emanate, separated by a sliding line. Through the streamline and in the two regions the pressure is constant and, consequently, the direction of the velocity (but not necessarily the modulus), in 4 and 4' is the same (parallel to the slip line). All the other properties in regions 4

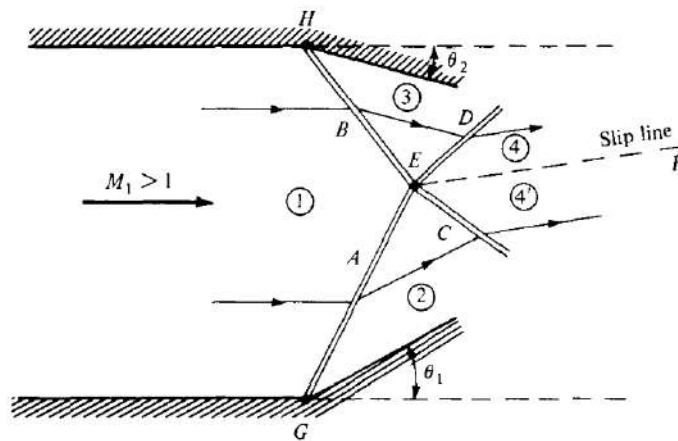


FIGURE 8.14: Intersection of two shock waves with different length [17].

and 4' are different. If the two incident waves were of the same intensity, at the point of intersection two further shock waves would still emanate but, finally, the distribution of the two would be symmetrical. The expansion of a free jet, when the Mach number upstream of the incident wave is small or the back pressure of the environment is high, brings to a Mach intersection as shown in Figure 8.15.

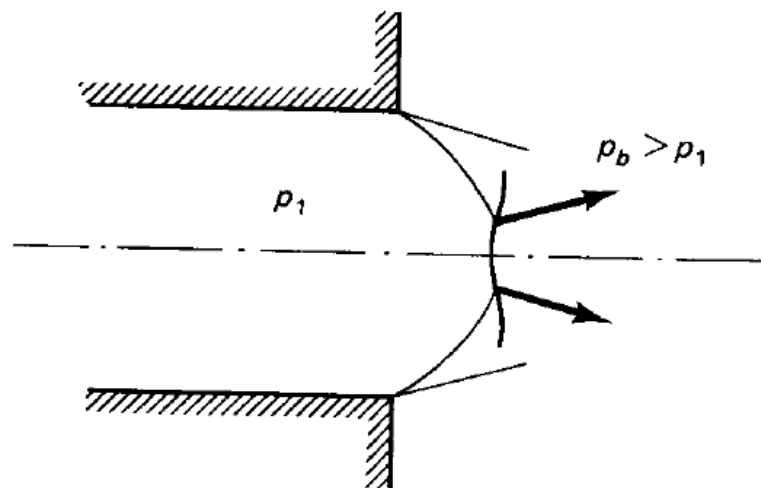


FIGURE 8.15: Mach intersection of two shock waves [17].

Summarizing what were reported:

- a shock wave (normal or oblique) born only in supersonic flows;
- a supersonic flow that crosses a normal shock wave becomes subsonic;
- an oblique shock wave reflects from a solid boundary as an oblique shock wave;

- an oblique shock wave reflects from a free boundary as an expansion fan;
- an oblique shock wave reflects from a free boundary as an expansion fan;
- two oblique shock waves can interact with each other: the intersection of the oblique shock waves can be regular or Mach.

The domain of existence of an under-expanded jet can be evaluated adopting the following pressure ratio:

$$\eta_0 = \frac{p_0}{p_{\text{inf}}} \quad (8.15)$$

The appearance of an under-expanded jet is only possible if:

$$\eta_0 > \frac{p_0}{p_{cr}} \quad (8.16)$$

When a free jet is introduced into an environment with a stagnant fluid, due to the speed gradient, a mixing layer is formed in the radial direction at the interface between the two fluids. The jet structure can so divided into three different regions (Figure 8.16):

- *near-field* zone;
- *transition* zone ;
- *far-field* zone.

The *near-field* is in turn divided into two regions: the central core *potential core* and the *mixing layer* in which the gas is mixed with the surrounding fluid. In the first region, the flow is isolated from the ambient fluid and its behaviour is mainly related to its compressibility. This conical area is characterized by a practically constant fluid velocity and extends for a length of some diameter of the outlet section in the direction of the axis of the jet. In the second region, also called *shear layer*, the injected gas is mixed with the surrounding fluid, with the formation of vortex structures that grow regularly downstream of the flow, due to the high velocity gradient ( Kelvin-Helmholtz instability). The *near-field* ends where the constant pressure line intersects the axis and therefore the mixing zone occupies the entire jet: this determines the beginning of the transition zone, in which there is a better mixing of the two fluids with consequent homogenization of the pressure field. In the *far-field* zone, the jet is fully expanded and the flow developed. The axial velocity, moving in radial direction decreases continuously with the maximum on to the jet's axis (the profiles are called "self-similar").

Depending on the pressure ratio  $\eta_0$  values there are three different kind of jet:

- subsonic jet;

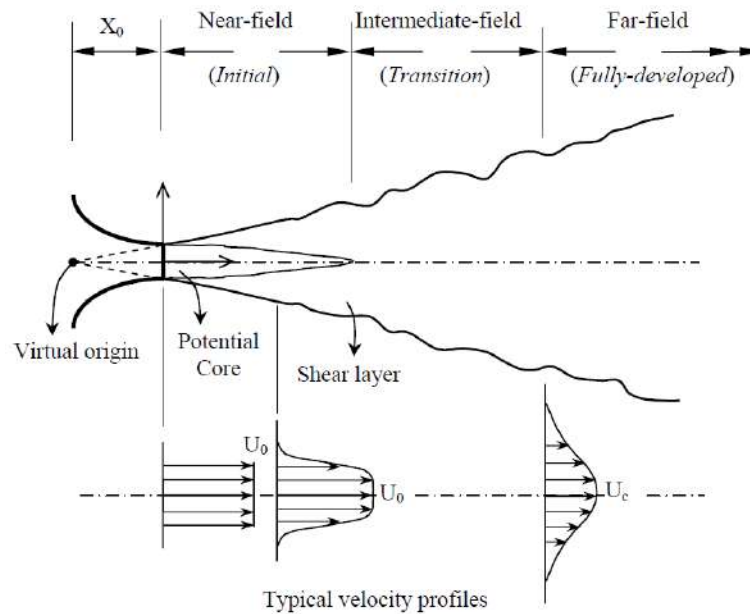


FIGURE 8.16: Schematic representation of an under-expanded jet flow regions.

- moderately under-expanded jet;
- strongly under-expanded jet

These three configurations cause different effects mainly in the near-field zone. In the case of subsonic jet, no shock waves occur and the flow trend is that shown in Figure 8.17:

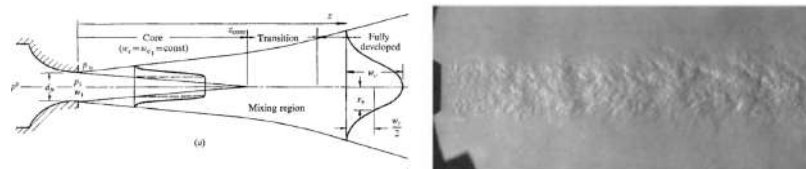


FIGURE 8.17: Structure of a subsonic jet (left) and Schlieren image (right) [344]

At a distance from the gas outlet section of the order of some nozzle diameter, the mixing region reaches the central line, sanctioning the exhaustion of the core. Beyond this point, the mixing layer continues to spread and the velocity varies due to the conservation of the axial momentum. At the end of the transition zone one enters the zone away from the field with fully developed motion, in which the profiles of the normalized flow variables such as average velocity, turbulence intensity, etc., become similar in various axial positions.

When the pressure ratio reaches critical conditions, a weak shock wave is formed in the normal direction (Figure 8.18).

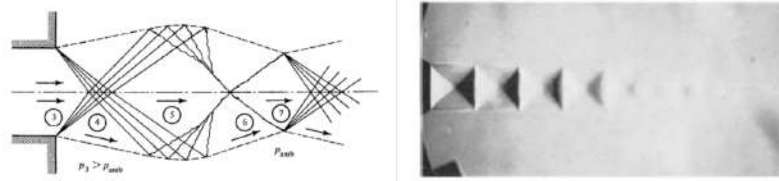


FIGURE 8.18: Structure of a moderately under-expanded jet (left) and Schlieren image (right) [344]

In the outlet section (3), given the presence of a convex angle, an expansion occurs with a Prandtl-Meyer fan: an infinite number of expansion waves are generated starting from the vertex. The fluid expands to the edge of the jet, where the expansion waves are reflected in the form of compression waves. The latter converge within the jet, merging to form an oblique shock wave ("intercepting shock"). The oblique waves incident on the axis are then reflected to form a further oblique compression wave, defined as a "reflected shock". The reflected wave can again reach the line at constant pressure, triggering a new expansion of Prandtl-Meyer (6), so as to replicate the same structure of the downstream flow. The jet is moderately expanded when the total pressure ratio is between the following values:

When the pressure ratio increases, the reflection of the "intercepting shocks" on the axis no longer occurs (Figure 8.19) and, consequently, a normal shock wave is formed, called Mach disk).

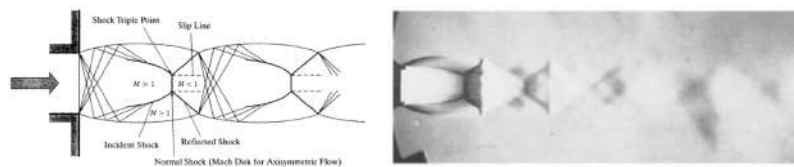


FIGURE 8.19: Structure of a strongly under-expanded jet (left) and Schlieren image (right) [344]

The intersection between the intercept wave, the Mach disk and the reflected wave is called the triple point; a streamline emanates from the latter which separates the flow upstream the Mach disk (which is supersonic,  $Ma \gg 1$ ) from the flow downstream of the reflected wave (subsonic,  $Ma < 1$ ). The structure thus created is called "barrel shock" and propagates until the jet returns to being overall subsonic.

Several studies were conducted to characterize under-expanded gaseous jets [117, 174, 267, 313, 432] and, in the next, the main findings regarding Mach discs are summarized. In particular, the location of the Mach disc:

- is mainly a function of the pressure ratio;
- increases with the Mach number in the outlet section of the nozzle;
- is independent of the type of gas;

- a good estimate of the Mach disc position is given by the following relation:

$$\frac{H_d}{D_e} = 0.67\sqrt{\eta_0} \quad (8.17)$$

with,  $H_d$  Mach disc height  $D_e$ , outlet section diameter.

The Mach disc diameter:

- mainly depends on the pressure ratio;
- decrease as the Mach number in the output section increases;
- depends on the type of gas and is inversely proportional to the ratio between specific heats (polytropic constant);
- is highly dependent on the shape and geometry of the nozzle;

The presence of Mach discs, barrel shock and other under-expanded structures influences the air/fuel mixing process. Indeed, considering the short time available for the mixture formation in DI, it is fundamental to achieve a deep knowledge of the characteristics of a turbulent pulsed jet and of the effects of shock waves on the turbulent mixing.

## 8.5 The Under-Expanded Jets in CNG Injection Processes

Many engine researchers investigated the under-expanded jet structure (such as jet penetration and jet cone angle) using different optical diagnostic techniques: Schlieren, Shadowgraphy, [68, 107], PLIF [68, 189, 208], and visualization by injection in liquid ambient.

J. Yu et al. [415] conducted an experimental campaign on a high pressure gaseous fuel jet, using the optical technique of laser induced fluorescence (LIF) in planar fashion (PLIF). This technique allows to determine not only the macroscopic parameters, such as the penetration and the cone angle, but also have information regarding the mixing process. The injection was performed in a CVC with two devices whose nozzle's diameters are of 0.5 mm and 1.4 mm respectively. A mixture of nitrogen and acetone, the latter used as tracer, was adopted for the measurement. The duration of the actuation was kept constant and equal to 4 ms for each test condition. The acquired pictures (Figure 8.20) testifies to the presence of the aforementioned under-expanded structures, during the jet's evolution:

- at the beginning of the injection, the pressure ratio is relatively small and a subsonic jet appears (Figure 8.20-a). In the near-field zone the jet is characterized by an high momentum. The core region is clearly identifiable, characterized by constant average speed and there is no turbulent mixing inside it. The core is then surrounded by a region in which there is a strong variation of the velocity gradient, a symptom of turbulent mixing (this area is defined "shear layer", due to the presence of viscous shear).

- as the injection goes on the jet becomes moderately under-expanded (Figure 8.20-b), it is possible to observe the shock cell structure, located inside the core region, which tends to gradually extinguish. The pressure energy owns by the jet is dissipated every once the flow passes through the compression and expansion waves and so dissipated , with the effect that the size of the shock cells gradually decreases until the jet becomes subsonic. The alternation of compression and expansion areas are equivalent, respectively, to areas of high density and areas of lower density;
- turning to the end of the injection the net pressure ratio is greater than 4 and the jet becomes strongly under-expanded (Figure 8.20-c). In the near nozzle zone it is possible to observe barrel shocks and the formation of the Mach disc.

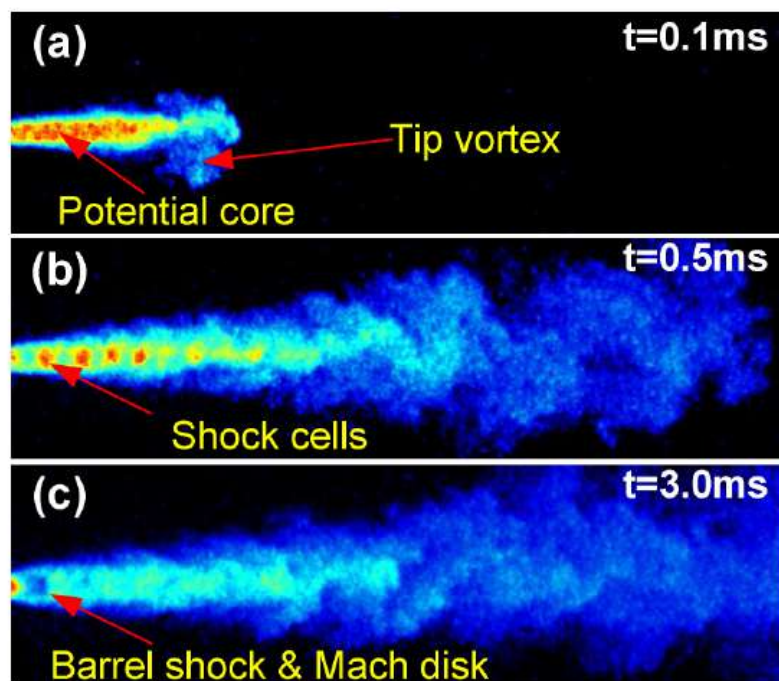


FIGURE 8.20: PLIF images of a gaseous jet, at different advance times. A) subsonic jet; B) casting moderately under-expanded; C) strongly under-expanded casting. False colors indicate the density distribution in the jet.

The authors then highlighted the effects of the variation in pressure ratio. The increase in injection pressure brings to an improvement in mixing (induced by shock waves), as shown in Figure 8.21. With an injection pressure of 5 bar, the jet is subsonic and the turbulent structures, where air/fuel mixing takes place, occurs only after the core area. On the other hand, with a pressure of 30 bar, the mixing occurs just after the Mach disc just few diameters far from the inlet section of the jet. The effect of the injection and environment condition on the characteristics of under-expanded structures was broadly

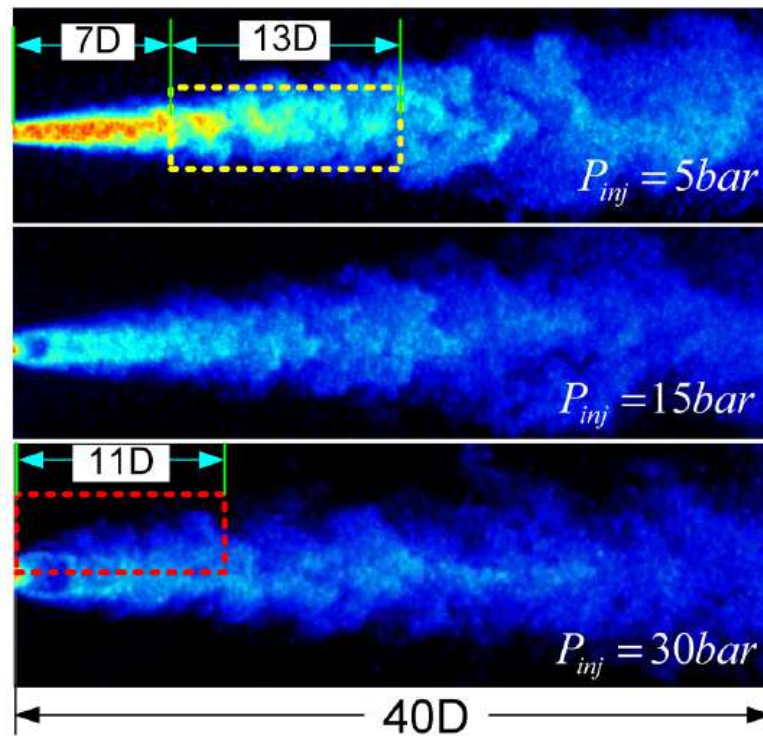


FIGURE 8.21: Effects of injection pressure on turbulent mixing

investigated. Dong et al [95] studied the Mach disks width and height evolution within time for different pressure ratio finding that the height of the Mach disk initially has a transient behavior: initially it increases and then, when the pressure at the inlet of the orifice is stabilized, remains constant till to the end of the simulation.

A digital image processing technique is required for the analysis of the jet's macroscopic features. For sake of completeness tip penetration length and cone angle definition for a gaseous jet are reported in the following:

- tip penetration length: the distance between the tip of the injector and the tip of the spray;
- cone angle: the angle between the vertical to the jet and its external edges. The edges of the jet are drawn at a specific distance from the injector tip (usually 20 mm).

Various authors observed that increasing the injection pressure or decreasing the environment pressure results in a faster jet penetration [107, 318, 415] while an higher fuel temperature does not affect significantly such parameter [194]. The jet cone angle during the first phase of the injection, gradually decreases until it assumes an almost constant value. The jet cone angle increases as the counter pressure in the chamber increases, while it decreases as the injection pressure increases [95, 107].

The quantitative measurement of air/fuel mixing is not always available by experimental investigations. In this regard, the improvement in the computing power allowed the use of CFD as a helpful diagnostic tool for investigating under-expanded jets. The CFD simulations allow not only to obtain information otherwise not available with certain experimental optical techniques, but also to reduce costs associated with variations in test rigs. In the last years, there were several numerical studies of under-expanded jets. The Pressure Implicit Split Operator (PISO) algorithm, initially developed for incompressible flows, was modified to be suitable in describing compressible high-speed jets. Such approach together with a LES turbulence framework, is capable to reproduce the macroscopic characteristics of under-expanded jets [92]. However, it was shown that density-based algorithms provide a better representation of such processes with a complete reconstruction of the shock structures and the compressibility effects [378, 380]. Yosri et al. [414] and Hamzehloo et al. [132, 133] verified that those approaches, featuring a LES turbulence framework, are capable to capture the initial vortex ring, formed at the beginning of the injection, the Mach disks location and dimensions, the macroscopic characteristics such as penetration length and volumetric growth (Figure 8.22). Banholzer et al. [32] investigated under-expanded methane jets taking into account the condensation phenomena that may occur at nozzle exit after the expansion of a very high-pressure jets. They combined a pressure-based solver with a vapor-liquid equilibrium model and a moving mesh methodology, and have carried out several RANS simulations in order to investigate the injection of methane at 30 MPa pressure into air at different pressure levels. Also, they have considered the effect of the fuel changing and the temperatures of the air. Furthermore, for the lower gas and air temperatures two additional simulations were performed including the needle opening process. They found that a decrease in fuel temperature such as an increase in NPR leads to a more significant phase separation. The numerical results were then compared with experimental measurements obtained from schlieren (for vapor phase) and Mie-scattering (for liquid phase) images. This comparison has shown a very good agreement between the experimental and numerical results both in length and width of the potential core and in their structures. A comparison between RANS and LES turbulence models results was performed by Hamzehloo et al. [134]. It has been found that using the same spatial resolution, the LES model leads to a wider subsonic region after each shock compared to those of RANS. Moreover, both RANS and LES models predicted similar penetration and spreading rate results. Deshmukh et al. [90] characterized a hollow-cone helium jet in terms of several macroscopic parameters such as axial penetration length and volume of jet, by LES and URANS simulations with both a fixed needle lift and a moving needle approach. They also have investigated the air/helium mixing in terms of mass-weighted probability density function (PDF) of the injected gas within the jet volume. They found that the transient needle opening law strongly influences the initial stages of the gas jet formation.

The local mixing activity of the flow field, as high concentration gradients, are typically estimated using Scalar dissipation rate (SDR) It is an important

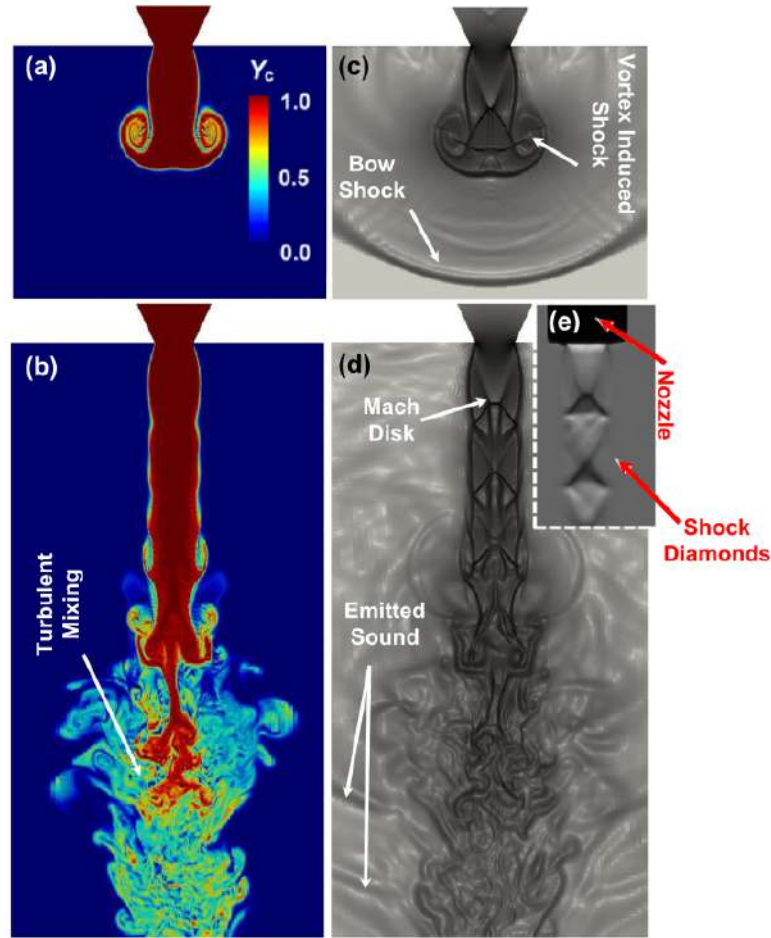


FIGURE 8.22: Under-expanded jet simulated by [134] . (a), (b) Instantaneous LES prediction of the mass fraction of the passive scalar at  $t=15$  and  $110 \mu\text{s}$ , respectively; (c), (d) Instantaneous LES prediction of the density gradient at  $t=15$  and  $110 \mu\text{s}$ , respectively, (e) time-averaged Schlieren image

parameter in combustion applications because it is fundamentally related to the structure of turbulent non-premixed flames and appears directly or indirectly in most turbulent combustion models. The scalar dissipation  $\chi$  is defined as [380, 415]:

$$\chi = 2D_c \left[ \left( \frac{\partial c}{\partial x} \right)^2 + \left( \frac{\partial c}{\partial y} \right)^2 + \left( \frac{\partial c}{\partial z} \right)^2 \right] \quad (8.18)$$

where  $D_c$  is the mixture fraction diffusivity;  $c$  is the passive scalar concentration;  $x, y, z$  are the position variables of the jet. Figure 8.23 reports a plot of the SDR for three pressure ratios of a mono-hole injector investigated by Vu et al. [415]. For higher pressure ratios, the scalar dissipation function decreases, reflecting lower concentration gradients and, therefore, better mixing.

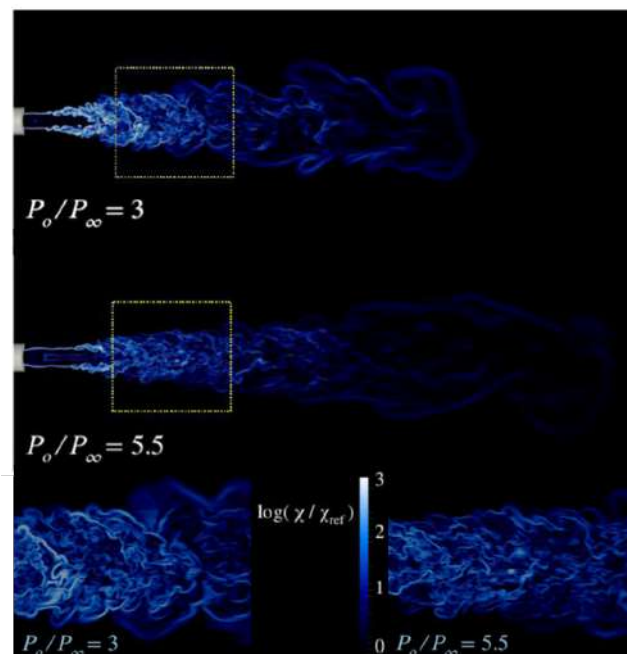


FIGURE 8.23: PLIF images of a gaseous jet, at different advance times. A) subsonic jet; B) casting moderately under-expanded; C) strongly under-expanded casting. False colors indicate the density distribution in the jet.



## Chapter 9

# Gaseous Jet Characterization: Single-Hole Injector Case Study

### 9.1 Investigation Methodology

The investigations carried out are finalized to characterize a gaseous injection in a constant volume, optically-accessible chamber at different thermodynamic conditions of a single hole injector. The jet studied has a transient evolution indeed, accordingly to up to downstream pressure ratio, changes during injection. The physics of under-expanded jets are fundamental for engine application because the phenomena influence the air/fuel mixing process and so, obviously the combustion. A deep knowledge of such processes can be achieved only through proper theoretical and experimental activities. In this optic, an experimental campaign was conducted at the Istituto Motori-CNR-laboratories by the schlieren imaging technique. A commercial injector, with injection pressure up to 1.2 MPa, was modified to be used as a direct injection device. Different operating conditions were investigated changing injection pressure, ambient pressure and temperature. The initial conditions for the experimental analysis are reported in Table 9.1. The jet was characterized in terms of penetration length, cone angle and Mach disk height.

TABLE 9.1: Experimental parameters

Parameter	Value
Ambient Temperature (K)	293.15, 363.15
Ambient Pressure (MPa)	0.1, 0.4
Gas Injection Pressure (MPa)	0.6, 0.9, 1.2
Injection Duration(ms)	5

Penetration length represents the distance between the nozzle exit and the furthest point on the contour of jet, measured along the axis of the spray. The acquisition of the penetration length ends off as the jet overcomes the vessel window acceptance. In this work, cone angle is defined as the angle between the tangents to the outside edge of the spray. The lines are drawn on the spray contour, from 1% up to 50% of the axial penetration: their intersection determines the origin of the angle itself [149]. Finally, Mach disk height, is measured as the maximum displacement of the disk in the direction of the jet evolution, with respect to the injector tip (Figure 9.1). The measure error of

Mach disk height is half of pixel's height, 166  $\mu\text{m}$ . Then, for further information, not available by the images measurement, a CFD model was developed.

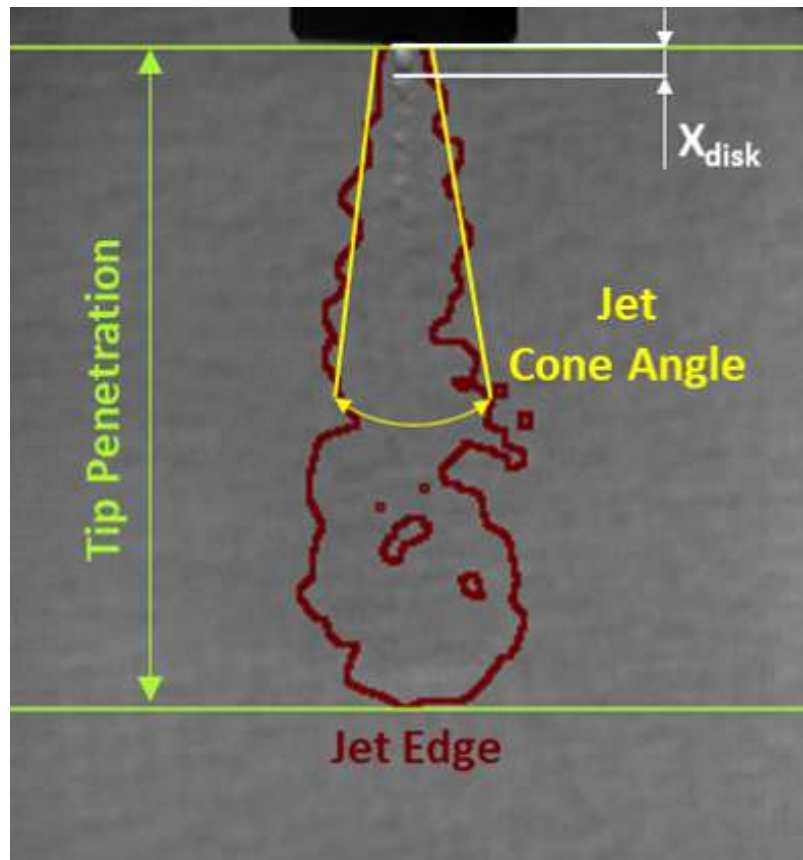


FIGURE 9.1: Definitions of measured parameters.

## 9.2 Experimental Activities

The experimental setup includes a fuel supply system, an injection apparatus for a CNG Direct Injection and an optically accessible constant volume chamber (Figure 9.2).

The fuel supply system consists of a tank filled with methane gas (99.95%) up to 17.5 MPa. A pressure regulator is used to realize the desired value per each condition. A transducer ensures an accurate reading of the gas pressure just upstream the injector connection.

The fuel was delivered using an inwardly opening single-hole commercial injector, suitably modified to inject gas directly into the constant volume chamber. The same injector was adopted in a revised PFI engine for research purpose at the CNR laboratory. To provide the direct injection of the gas, both the engine and the injector were suitably modified. For this reason, a special adapter 1 mm in diameter orifice was designed and mounted both in engine and CVC investigations. Further details of the adapter are shown in Figure 9.3, while the geometrical parameters of the adapter are reported in Table 9.2.

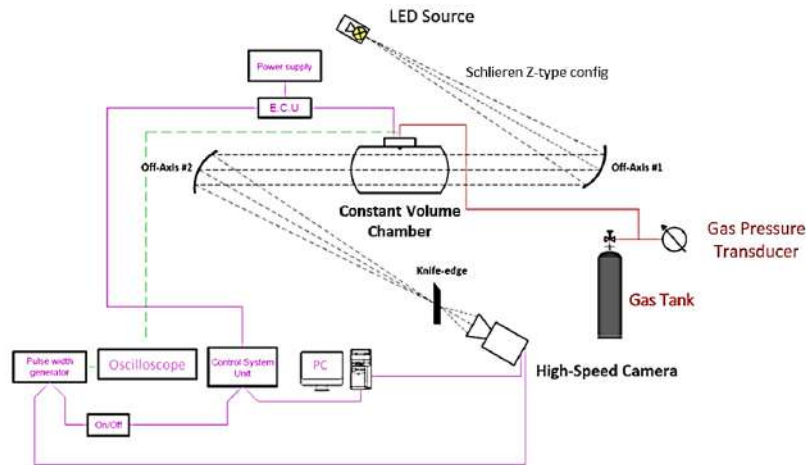


FIGURE 9.2: Experimental Setup.

The injection process was controlled by a programmable Electronic Control

TABLE 9.2: Adapter nozzle geometrical parameters

Parameter	Value
Adapter Length (mm)	42.6
Nozzle Length (mm)	0.9
Nozzle Angle (degree)	130
Nozzle Diameter (mm)	1

Unit (PECU) for energizing the current necessary to activate the needle lift. The injection duration was set at 5.0 ms for all the experimental conditions. Five repetitions were carried out to ensure repeatability of the measurements and define a minimum of records.

The injection and acquisition process started in synchronous mode by a TTL triggering signal generated by a pulse generator.

The tests were performed in the CVC, optically accessible through three quartz window, 80 mm in diameter, permitting the access to a wide area of the spray under investigation. The injector was located at the top of the vessel in a customized holder. Gas pressure conditions in the vessel ( $N_2$ ) was varied by gas adduction, while the temperature was set through a system of electrical resistances integrated in the chamber.

The structure of gaseous spray was investigated by the schlieren technique, sensible to the gradient densities generated by the fluids flow along the optical path and resulting in variations of the refractive index of the gas. Schlieren setup (Figure 9.2) was realized according to the traditional Z-type configuration, and further details are reported in [248]. A high-power LED lamp (Omicron LED MOD V2) emits a light radiation at the wavelength of 455 nm. The beam is collimated through a  $15^\circ$  off-axis mirror, with a focal length of 500 mm. The generated collimated beam passes through the spray in the chamber and is deflected and focused by a second off-axis mirror, with analogous characteristics. A knife-edge, mounted orthogonally to the spray propagation direction, is placed at the focus of the second mirror. Finally, a biconvex

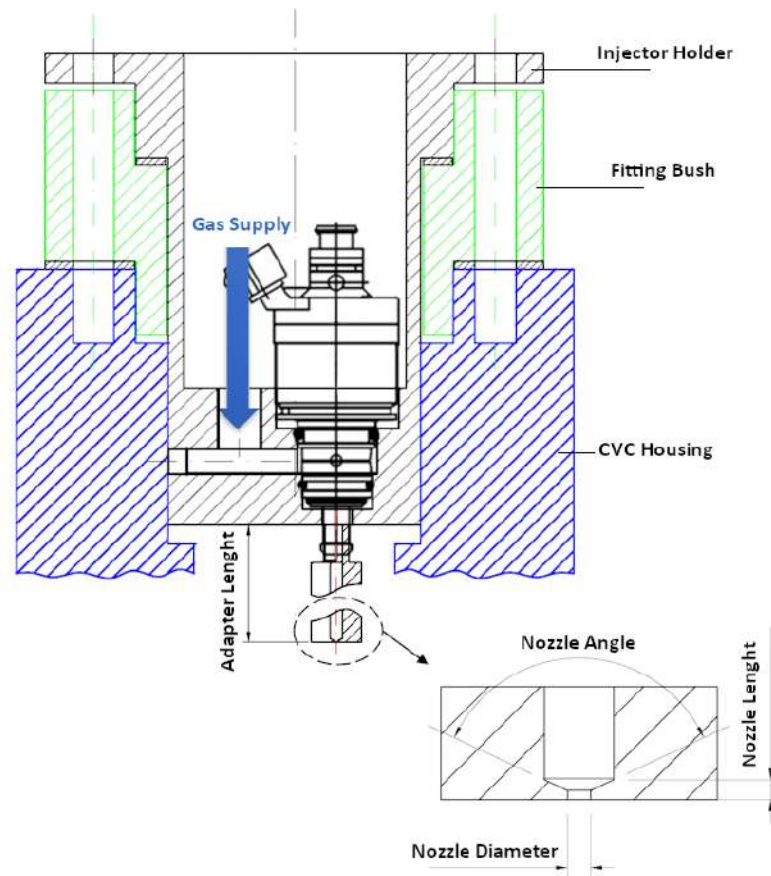


FIGURE 9.3: Sketch of the gas injection system.

lens converts the images in the camera through its objective. The detector is a high-speed C-Mos camera (Photron FASTCAM SA4), working at a rate of 27,000 frames per second (fps) and realizing an image window of 256x432 pixels. The camera was equipped with a 90 mm focal lens realizing a spatial resolution of 6 pixel/mm.

### 9.3 Image Processing Procedure

As stated above, the schlieren technique is sensitive to the gradients of density of the media under examination. Due to the expansion of a gas into a surrounding ambient made of gas, comparable density gradients realize between methane and nitrogen making the methane jet boundary difficult to detect. For this reason, a customized procedure was implemented to process the images and ensure a proper contrast in order to allow the measurement of macroscopic characteristics of the jet. The thread of this process can be found in [375].

Figure 9.4 reports the steps of the processing algorithm applied to the schlieren images.

The routine begins with the extraction of the background, through an average of its images, caught just before the start of the fuel injection (Figure 9.4-a).

Once injected in the chamber, the methane jet looks very feeble against the background (Figure 9.4-b); to attenuate undesirable noise, the background is removed (Figure 9.4-c). Subsequently, in an iterative way, a subtraction of one image and the previous one is carried out, to highlight differences in two consecutive steps during the evolution of the jet (Figure 9.4-d); images 9.4-c and 9.4-d are superimposed obtaining a better contrast with respect to the background (Figure 9.4-e). In the next step, an improvement in brightness and contrast (Figure 9.4-f) was obtained, followed by a blurring of the image, according to a Gaussian function (Figure 9.4-g). Then, the image was binarized, through the "OTSU threshold" operator (Figure 9.4-h) [352]. The spray outline was extracted from the binarized image by means of a contour recognition filter (edge detector, Figure 9.4-i), through which the measure of the spray penetration was possible. Figure 9.4-l shows an overlay of images "a" and "i", where the two lines determine the axial penetration.

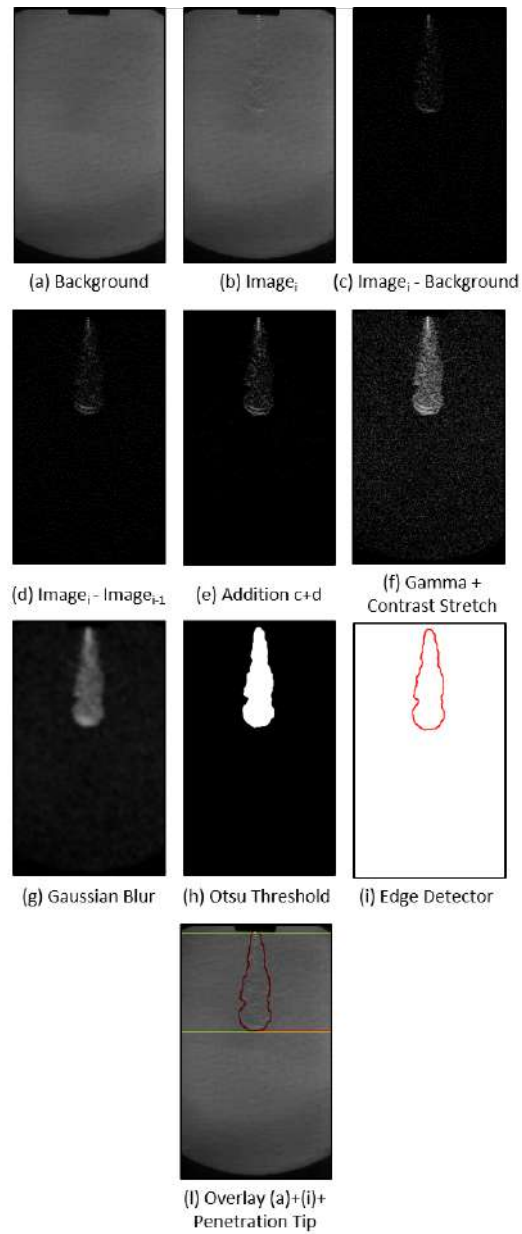


FIGURE 9.4: Image Processing Procedure.

## 9.4 Numerical Approaches

The numerical activities carried out in this study consist in a set of CFD simulations performed by CONVERGE software suite. It is a general purpose CFD tool that features also mesh movement, forced embedding, and an adaptive mesh refinement algorithm (AMR). AMR refine mesh where high specific field gradients are calculated without significantly increasing the total number of computational cells. The injected mass from the injector is unknown. The known parameters are the injection pressure, the injector's internal geometry and the pintle lift (Figure 9.5). The pintle lift law was provided by the manufacturer.

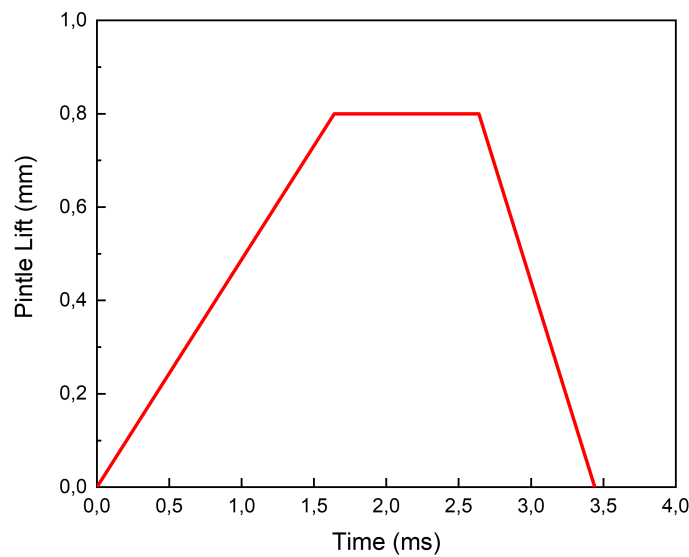


FIGURE 9.5: Pintle Lift.

In this way the simulation involves both inside and outside's flows. The pintle lift was simulated thanks to a mesh movement. The injector's exiting flow is free to expand in a constant volume cylinder of diameter and height respectively of 30 mm and 70 mm. The operating conditions reported in Table 9.3 were simulated and then validated using the data from the experimental campaign.

TABLE 9.3: Operating conditions numerically simulated

Case	Ambient Temperature (K)	Ambient Pressure (MPa)	Gas Injection Pressure (MPa)
Case 1	293.15	0.1	1.2
Case 2	293.15	0.4	1.2

The dynamics of the gaseous injection were described solving the typical equations of a fluid-dynamic problem: conservation of mass, momentum, energy and the specie's transport equations. To couple density, pressure and temperature the Redlich Kwong (RK) cubic equation was used:

$$P = \frac{RT}{v-b} - \frac{a}{v^2 + bv} \quad (9.1)$$

With  $a$  and  $b$ :

$$a = \frac{\alpha_{rk} p_c v_c^2}{\sqrt{T_r}}$$

$$b = \beta_{rk} v_c \quad (9.2)$$

$$\alpha_{rk} = 0.42748, \quad \beta_{rk} = 0.08664$$

where  $\alpha$  represents the attractive forces between molecules  $\beta$  represents the molecules volume while  $v_c$  is the critical volume, given by the critical temperature, the critical pressure and the universal gas constant. The equations were discretized using a central differencing scheme which Taylor series truncation errors is second-order [374]. The solution algorithm relies on the PISO method with converge criteria based on density, being the flow compressible [38, 306].

The grid dimensions were selected relying on bibliography references [90, 380, 415]. Specifically, the base mesh's dimension is of 4 mm with a local embedding of level 4 for the internal flow and for the flow just outside the nozzle. The AMR level was set to 6 based on the density and pressure gradients (minimum grid size = 62.5  $\mu m$ ). In this way, the model's computational weight was lowered and the cell usage optimized as shown in Figure 9.6.

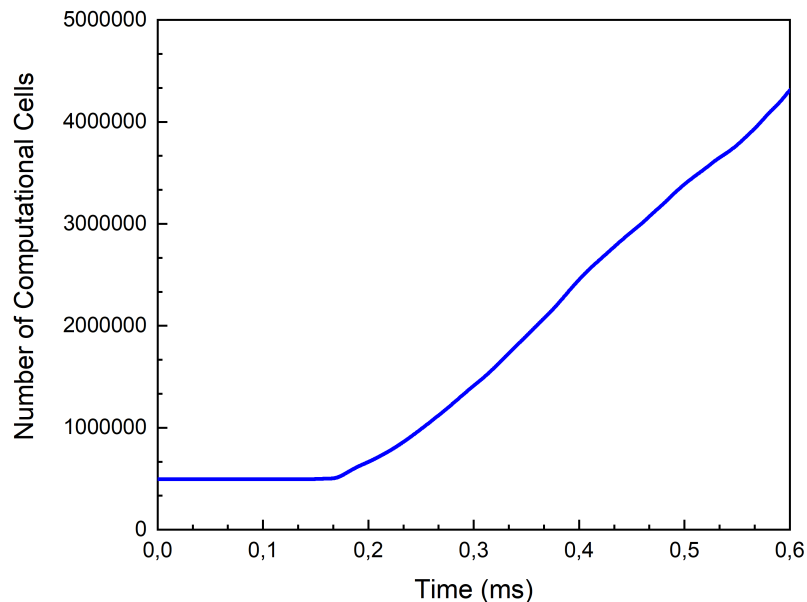


FIGURE 9.6: Computational cells over time.

The turbulence model selected is a LES-Viscous One Equation model in order to solve the flow field till to the smallest computable vortices. This is unavoidable to make qualitatively and quantitatively considerations concerning air-fuel mixing process that is fundamental in a possible subsequent

engine application. The point-wise successive over-relaxation (SOR) algorithm, with relaxation factor, was adopted to integrate solution over time [306]. The used time step was varied accordingly to the CFL convective and diffusion numbers so as not to exceed the unity in first case and two in the second one.

Three fluid regions were identified (Figure 9.7). The initial conditions at each region are the follow:

- High Pressure Region (Region 2): this is the high pressure zone filled with fuel at the injection pressure (methane). It is delimited by injector's internal surfaces and the pintle. However, when the pintle lifts, this region is connected to the Low Pressure Region and the methane flow.
- Low Pressure Region (Region 3): this zone belongs to the cylinder connecting the high pressure region to the bulk one. Its pressure and temperature are equal to the ambient ones. The species present are unknown. Indeed, after some cycles of injection, a fraction of methane, added to the nitrogen, is present in this region and there are no ways to estimate the relative fractions.
- Bulk Region (Region 1): this zone represents the injection volume, likely it is filled by nitrogen  $N_2$  at the ambient pressure and temperature.

The boundary conditions are the follows (Figure 9.8):

- High Pressure Inlets: these are the four holes where the combustible is supplied to the injector; their surfaces are treated as fixed pressure inlets;
- Moving Pintle Surface: this surface reproduce the movement of the pintle through a mesh movement;
- Injector Wall Surfaces: they consist of some internal faces of the injector and the bulk faces. Their boundaries conditions are velocity and temperature law of wall functions [306].

All the simulations were performed on 36 cores of a Fujitsu Siemens Workstation equipped with two Intel Xeon Gold 6140. Numerical results were post-processed by Paraview software. In particular, methane mass fraction and density gradient fields were plotted with proper color maps in order to compare them with the experimental images.

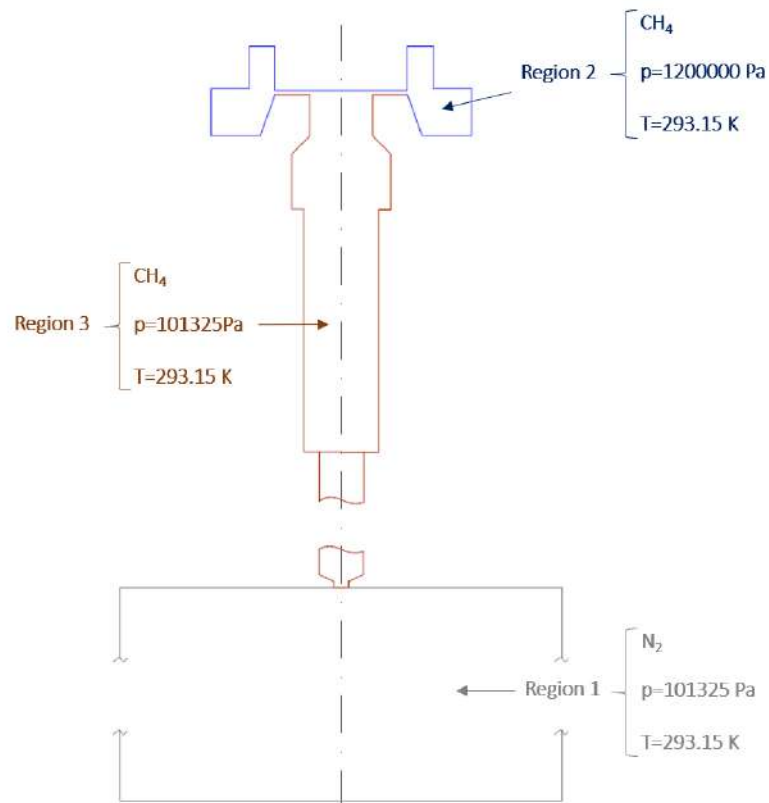


FIGURE 9.7: Sectional view of the computational domain and assignment of initialization regions.

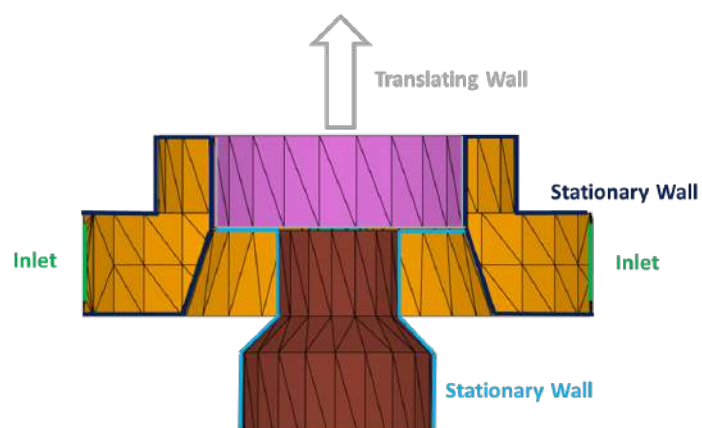


FIGURE 9.8: Detail of injector's upper part with related boundary conditions.

## 9.5 Experimental Results

The analysis of schlieren images has provided information regarding evolution and structure of the gaseous jet, tip penetration, cone angle, and Mach disk height allowing to measure them. A comparison of the experimental results was conducted in order to evaluate:

- effect of injection pressure variation at constant pressure and temperature in the chamber;
- effect of chamber back-pressure fixed the injection pressure and chamber temperature;
- effect of chamber temperature at fixed injection pressure and density of nitrogen in the vessel.

### 9.5.1 Effect of Injection Pressure

The effects of injection pressure on the evolution of the gaseous jet are shown in Figure 9.9, where the chamber pressure and temperature are maintained constant. Each sequence starts at the instant  $t_{SOI}$ , i.e. the time-frame just before the gaseous jet exits from the nozzle and appears in the chamber; the next images of the sequences are collected at a predetermined time interval from  $t_{SOI}$  function of the camera acquisition rate. Once fixed the solenoid excitation duration at 5.0 ms, the total injection durations up to 11 ms was measured. This is attributed to the compressibility of gas, despite being the pintle in the closed position, due to the continues flowing toward the chamber of the gas located in the adapter pipe.

For each of the injection pressure, the jet undergoes an evolution of its structure passing from subsonic to moderately under-expanded up to strongly under-expanded with appearance of Mach disk. As the pintle begins closing, the jet returns subsonic. Since Mach disk appearance and its length are correlated to NPR, it can be inferred that the pressure upstream the nozzle varies due the pintle lift transitory and gas compressibility. Figure 9.10 shows the variation of the Mach disk height during the injection process, as the injection pressure varies.

Mach disk height increases in time, up to about 1 ms; then assumes a constant value up to about 5 ms, indicating that the pressure upstream the nozzle stabilized. For longer times, the disk height gradually decreases, following the closure of the injector. Furthermore, the maximum Mach disk height increases for higher injection pressure. Figure 9.11 and Figure 9.12 show the effects of injection pressure on the jet tip penetration being constant the back pressure in the chamber (0.1 and 0.4 MPa respectively) and the temperature (293.15 K).

The graphs show values of axial penetration averaged on five successive injections per each test. Error bars reported on the graphs give the filling of the standard deviation in the complete measurements cycle. Increase of the tip penetrations correspond to higher injection pressures. This effect is

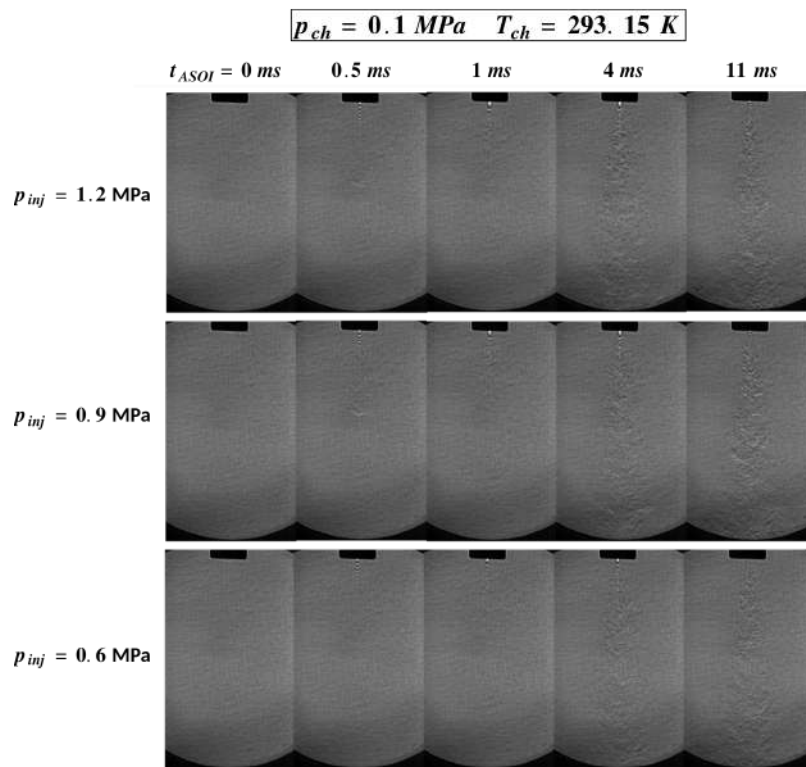


FIGURE 9.9: Evolution of the gaseous jet structure at the varying of the injection pressure

stronger for higher back-pressures. At 0.1 MPa pressure condition in the chamber (Figure 9.11) and injection pressure of 1.2 MPa, the jet takes 1.33 ms to cover the window clearance; as the pressure decreases down to 0.6 MPa, the flying time of the jet increases up to 1.48 ms. The growth in axial penetration is marginal within the analyzed time window. Jet cone-angle is weakly influenced by the injection pressure. On one side, the increase in injection pressure determines a greater quantity of injected fuel, with a consequent widening of the cone-angle. On the other hand, the spray would tend to penetrate more quickly, causing a self-narrowing. These two aspects tend to compensate each other, producing a negligible influence of the injection pressure, as shown in Figure 9.13.

### 9.5.2 Effect of Pressure in the Vessel

The effects of ambient pressure on the evolution of gaseous jet are shown in Figure 9.14, where the injection pressure and chamber temperature were kept constant.

The figure shows that, for the injection pressure of 1.2 MPa and the chamber pressure of 0.4 MPa, the Mach disks do not occur. The jet, initially subsonic, becomes moderately under expanded, with the appearance of shock diamonds figures. Then, the evolution again becomes subsonic. Figure 15 shows the effects of vessel back-pressure on the tip penetrations for  $p_{inj}$  1.2

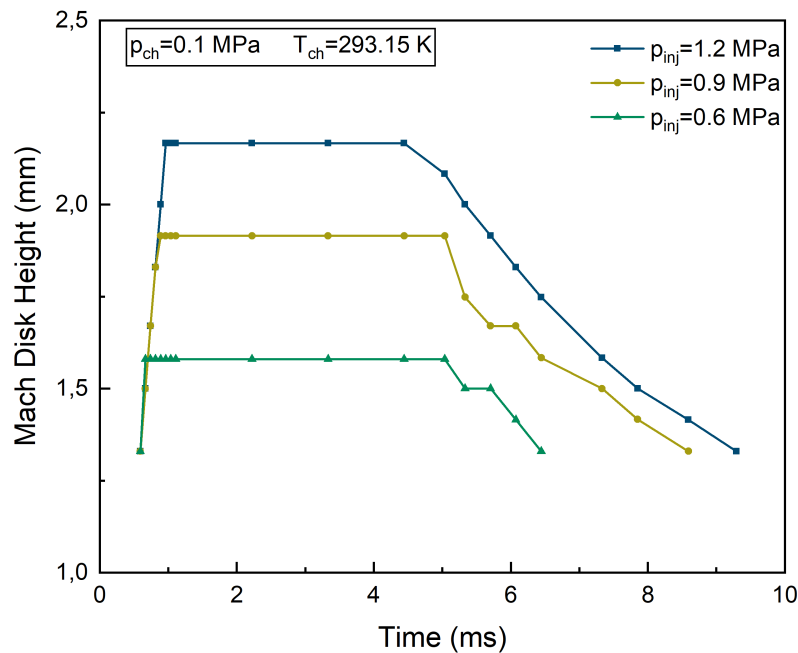


FIGURE 9.10: Effect of injection pressure on Mach disk height

MPa and the gas temperature of 293.15 K. At higher pressure of the gas in the vessel, the tip penetration decreases due to its brake action on the methane propagation. The vessel pressure of 0.1 MPa determines a tip elongation of 54.1 mm at 1.0 ms from the SOI while, at the same instant, the jet has covered 39 mm at the chamber pressure of 0.4 MPa. Similar trends are registered for the two other injection pressures.

Summarizing, the tip penetration of methane jet is more sensitive to changes in the vessel pressure than to the variation of the injection pressure. In the same way, jet cone-angle is mostly affected by the variations in chamber pressure, as pictured in Figure 9.16.

### 9.5.3 Effect of the gas Temperature in the chamber

The effects of the  $N_2$  temperature in the vessel on the evolution of gaseous jet are shown in Figure 9.17, where the injection pressure is kept constant, against a fixed ambient back-density obtained acting on the pressure and temperature of  $N_2$ . This condition realizes a constant resistance of the gas vs. the jet motion, regardless of the temperature values. Figure 9.17 highlights that, for the injection pressure of 0.6 MPa and the nitrogen density of 1.12 kg/m<sup>3</sup>, Mach disks still occur for both temperature values. This is due to the fact that the occurrence of Mach disks depends mainly on the pressure ratio, rather than on the temperature [118]. In both cases, the thermodynamic conditions are such that the ratio between the pressure, upstream of the nozzle, and the chamber pressure is such that the jet becomes under-expanded. For the same reason, no substantial differences on disk height were observed by varying chamber temperature. Figure 9.18 shows the effects of the gas

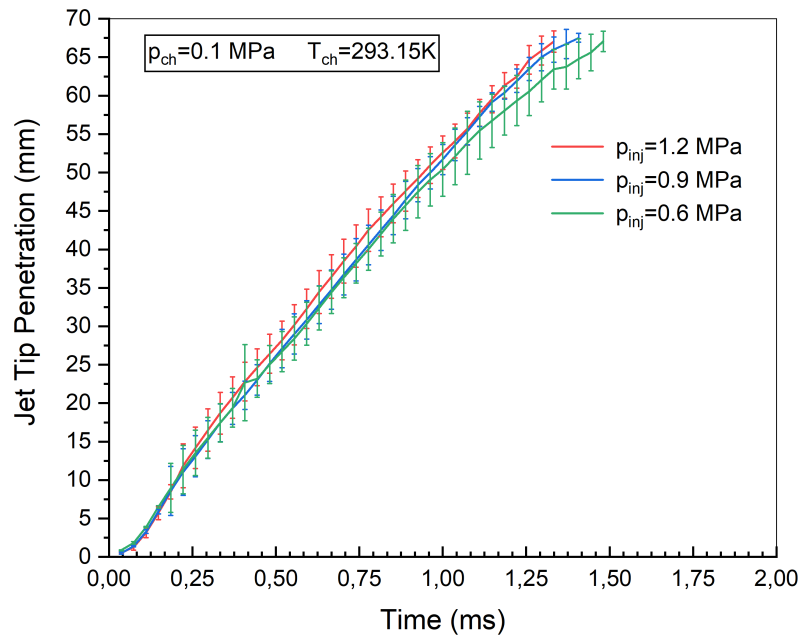
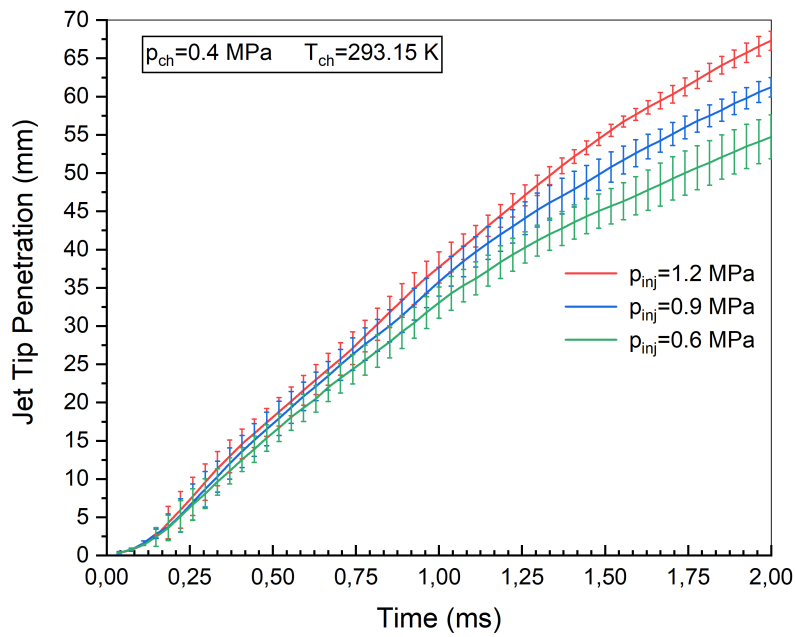
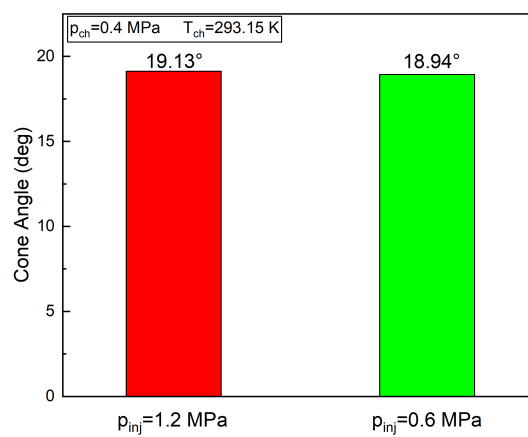


FIGURE 9.11: Axial jet penetration over time for  $p_{ch} = 0.1$  MPa.

temperature in the chamber on the tip penetration of the jets for the injection pressure of 0.6 MPa, at constant back-density of the gas. Variation in chamber temperature does not seem significantly affecting the axial penetration. Error bars are significantly larger at the chamber temperature of 363.15 K where the convective motions in the gas produce complex background figures making the image processing complex and hard for distinguishing the actual methane contours.

FIGURE 9.12: Axial jet penetration vs. time at  $p_{ch} = 0.4$  MPa.FIGURE 9.13: Variation of jet cone angle vs. injection pressure at  $p_{ch} = 0.4$  MPa.

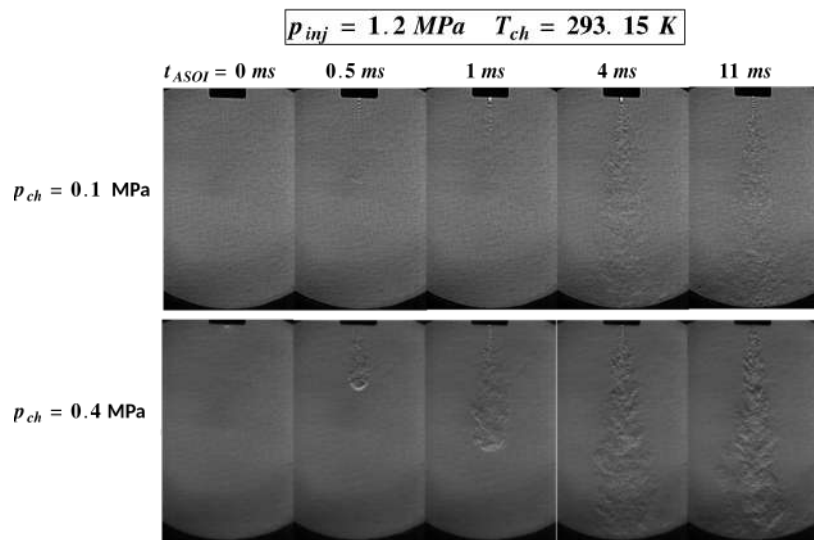


FIGURE 9.14: Evolution of the gaseous jet structure at the varying of the chamber pressure.

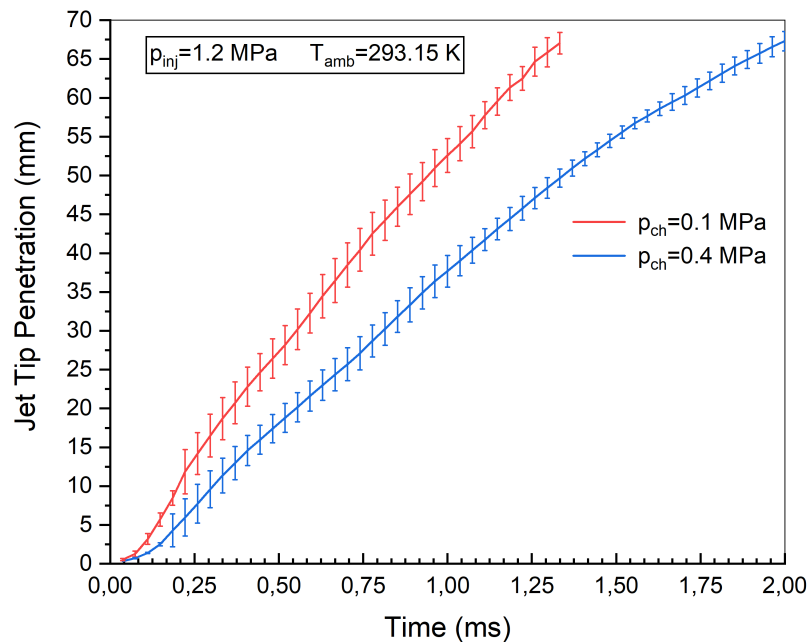


FIGURE 9.15: Axial jet penetration vs. time for  $p_{inj} = 1.2$  MPa.

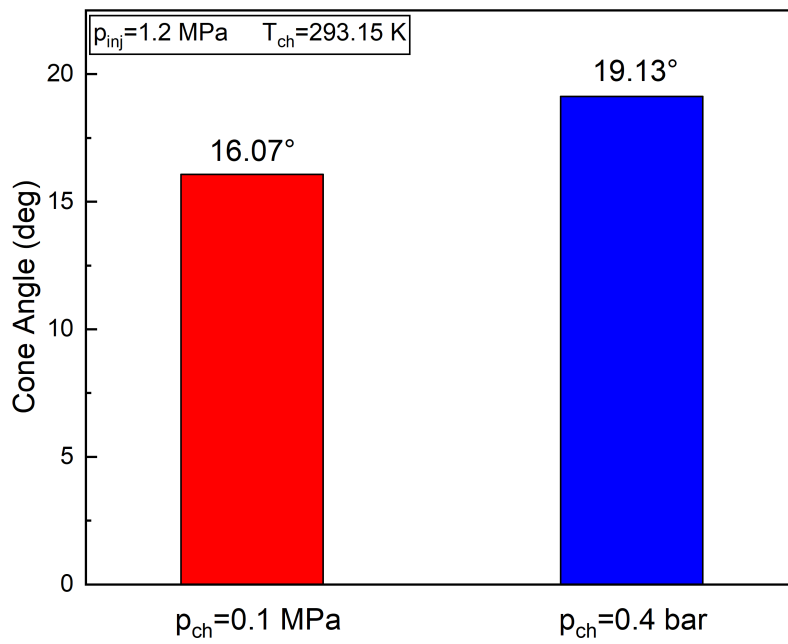


FIGURE 9.16: Variation of jet cone angle vs. chamber pressure at  $p_{inj} = 1.2$  MPa.

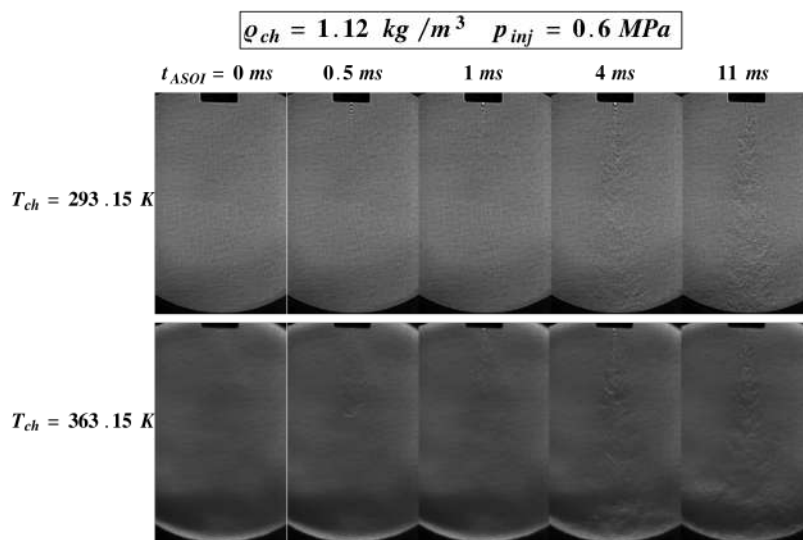


FIGURE 9.17: Evolution of the gaseous jet structure at the varying of the temperature of the gas in the chamber

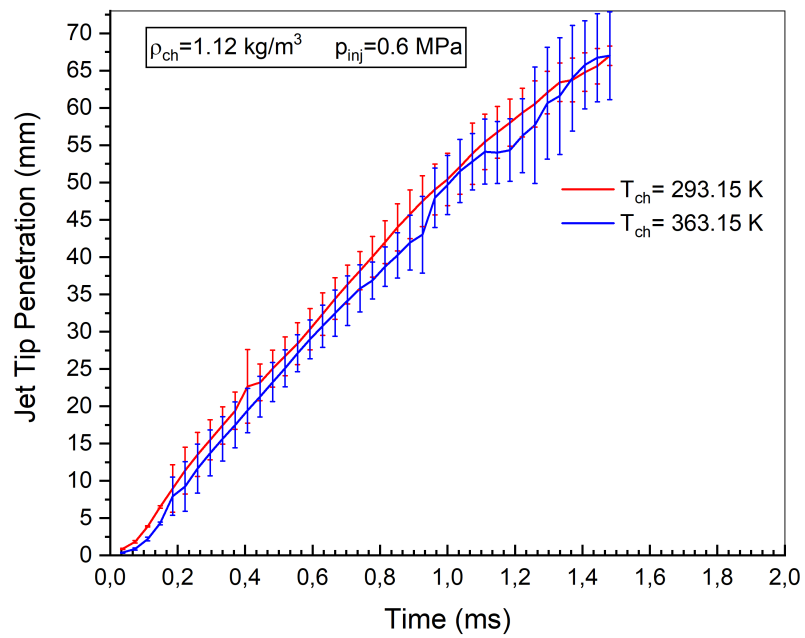


FIGURE 9.18: Axial jet penetration vs. time for  $p_{inj} = 0.6 \text{ MPa}$ .

## 9.6 Numerical Results

The results obtained by the developed numerical model were compared with the experimental data previously exposed. Figure 9.19 represents a 3D visualization of the simulated jet aiming to highlight the capacity of the numerical reconstruction to reproduce qualitatively the jet morphology.



FIGURE 9.19: 3D visualization of the simulated jet.

In the numerical investigation, the axial penetration length was computed as the distance between the farthest point on the contour of the jet and the top of the wall region, by using a threshold for the mass fraction of methane of 0.001, similarly to the definition of Deshmukh et al. [90].

Figures 9.20 and 9.21 show the comparisons between the numerical and experimental jet penetrations plotted as function of the time for the selected cases (Table 9.3 for further details).

The results between the experimental and numerical datasets catch the trends in both cases and highlight a good agreement toward the last part of the simulated time-frames while, at the beginning of the injection, small differences are registered. A possible motivation could be imputable to the

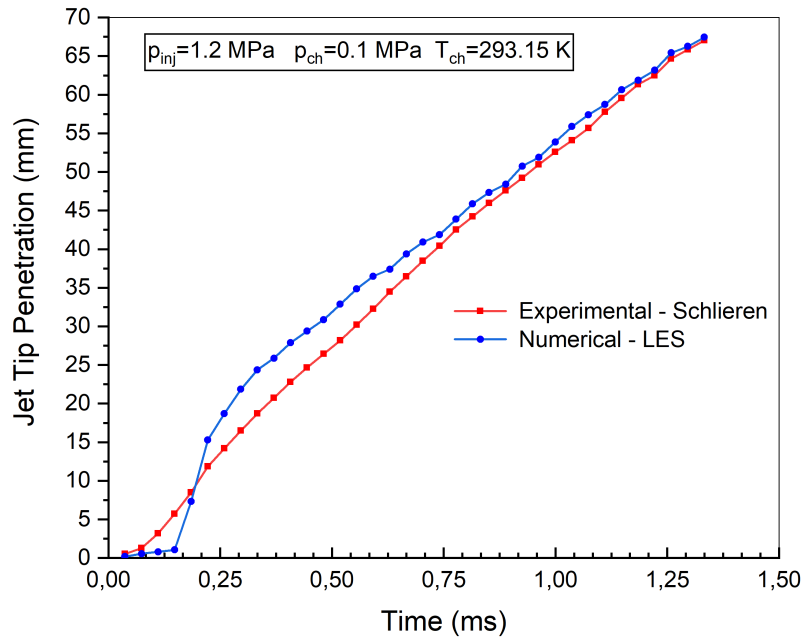


FIGURE 9.20: Experimental and numerical axial jet penetration vs. time for Case 1 ( $p_{inj} = 1.2$  MPa and  $p_{ch} = 0.1$  MPa).

uncertainty on the transient of the injector opening.

The adopted model is capable to reproduce qualitatively the jet morphology and its temporal evolution. Its characteristic normal shock is clearly visible plotting the density gradient, shown in Figure 9.22. At the first stage of the injection, the jet exits from the nozzle creating a tip vortex structure, Figure 9.22a. The pressure ratio is relatively low and the flow is subsonic Figure 9.22b. Then, at increasing of the NPR, critical conditions are reached: the jet becomes under-expanded and shock cells grow (Figure 9.22c). A further increase of the pressure brings to the formation of the Mach disk (Figure 9.22d).

As further confirmation of the model reliability, the Mach disk height was measured from numerical data for the Case 1 and compared with the experimental one. Again, numerical and experimental results are in a quite-good agreement. Just small differences appear during the first phase of the injection (Figure 9.23).

The Case 2 is not suitable for such analysis due to the  $NPR \ll 3.85$  [415] (Figure 9.24). Indeed, the model reveals the presence of shock cells as it is expected from the theory and observed from the experimental images.

The value of the Mach disk height,  $X_{disk}$ , is related to the upstream pressure ( $p_i$  in Figure 9.25) through the empirical relationship [118]:

$$\frac{X_{disk}}{D} = 0.67 \sqrt{\frac{p_i}{p_\infty}} \quad (9.3)$$

with:

- $D$  orifice diameter;

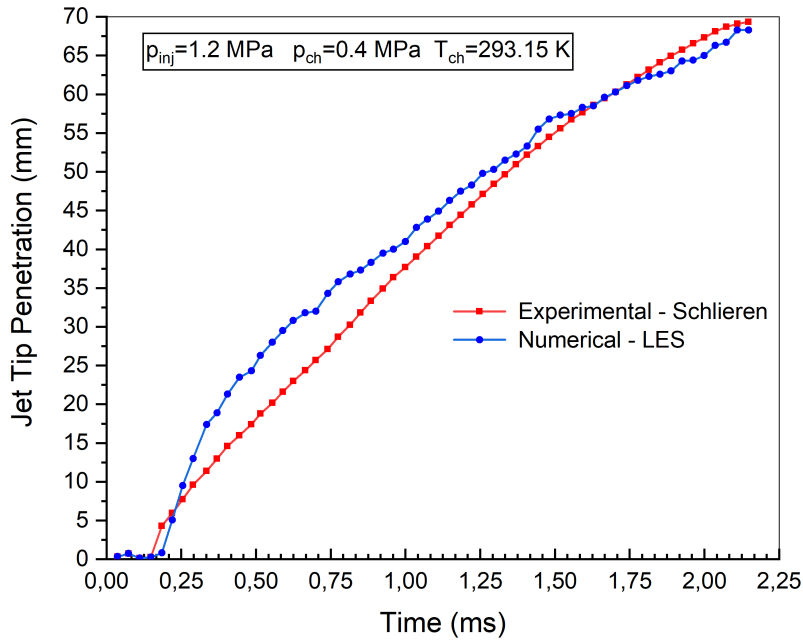


FIGURE 9.21: Experimental and numerical axial jet penetration vs. time for Case 2 ( $p_{inj} = 1.2$  MPa and  $p_{ch} = 0.4$  MPa).

- $p_{\infty}$  downstream pressure;

Handling Eq. 9.3, it is possible to compute  $p_i$ , as:

$$p_i = p_{\infty} \left( \frac{1}{0.67} \cdot \frac{X_{\text{disk}}}{D} \right)^2 \quad (9.4)$$

$X_{\text{disk}}$  can be measured from the numerical results as shown in Figure 9.26 and whose precision is related to the mesh size.

For example, at 0.81 ms the computed Mach disk height is equal to 2.05 mm. Inserting the ambient pressure of 0.101325 MPa and the diameter of the nozzle (1 mm) into the Eq. 9.3,  $p_{i,emp}$  is equal to:

$$p_{i,emp} = 0.101\,325 \text{ MPa} \left( \frac{1}{0.67} \cdot \frac{2.05 \text{ mm}}{1.000 \text{ mm}} \right)^2 = 0.94 \text{ MPa} \quad (9.5)$$

This value can be compared with that obtained from CFD model, at the position illustrated in Figure 9.25, computing the average value over the axial section ( $p_{i,cfd}$ ):

$$p_{i,cfd} = 0.97 \text{ MPa} \quad (9.6)$$

The two results are in good accordance with differences around 3%. The behaviour of both  $p_{i,cfd}$  and  $p_{i,emp}$  as function of the simulation time can also be easily computed. Figure 9.27 shows the comparison between the pressure  $p_{i,emp} = p_{i,emp}(t)$  calculated with the empirical relation (Eq. 9.3) and the one estimated from the CFD model  $p_{i,cfd} = p_{i,cfd}(t)$ .

From the analysis of Eq. 9.4, a quadratic relationship is recognizable between  $p_i$  and  $X_{\text{disk}}$ . This is indicative of how strong the impact of the  $p_i$  computation

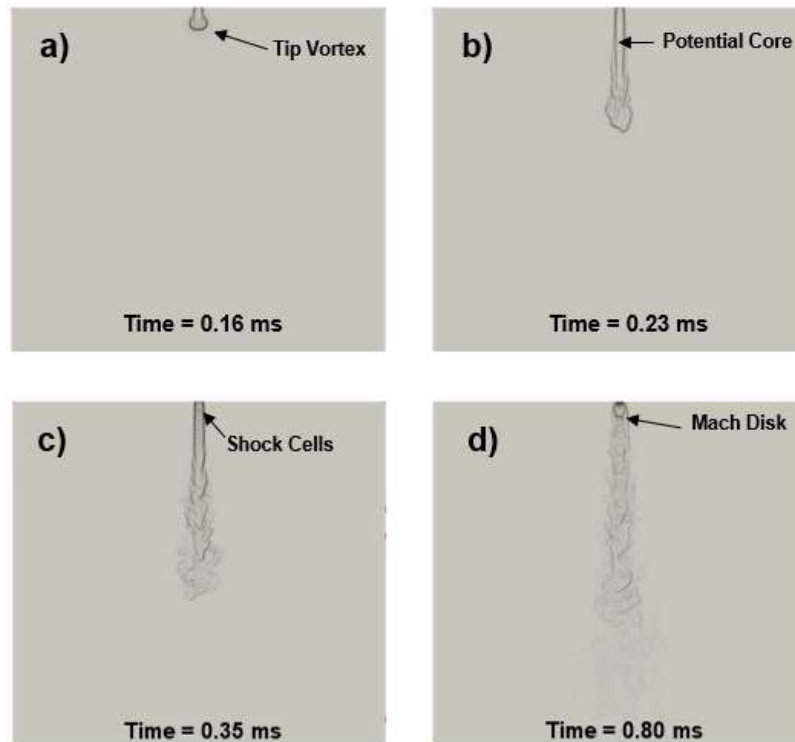


FIGURE 9.22: Gaseous jet structure's evolution at different time-step for Case 1 ( $p_{inj} = 1.2$  MPa and  $p_{ch} = 0.1$  MPa) obtained plotting the density gradient.

is against small uncertainty on the  $X_{disk}$ . The precise measurement of  $X_{disk}$  is clearly related to the mesh dimension that in our case is  $62.5 \mu\text{m}$ .

Evaluation of the methane/air mixing process is a relevant topic especially in terms of the effects on the combustion in engine applications. The image sequence reported in Figure 9.28 shows the methane mass fraction ( $y_{CH_4}$ ) at different instants from the SOI.

The analysis of the images makes clearly recognizable a zone, around the jet axis, composed predominantly by methane ( $y_{CH_4} \approx 1$ ) called potential core. As the injection goes on, the length of such zone grows in a first phase but, then, it begins to recede at the end of the simulation. This methane core is surrounded by a mixing layer of the two species (methane and nitrogen) on both the sides.

Downstream the potential core, the jet is characterized by a zone where the methane's mass fraction is significantly lower than the one present within the potential core.

Besides, to quantitatively estimate the mixing characteristics of the gaseous jet, an already established statistical approach was adopted [90, 378, 380]. The probability density function (PDF) of mass weighted methane fraction was computed within the jet volume ( $\rho_i Y_{CH_4, i} V_i$ ), obtained using a threshold value for the mass fraction of  $Y_{CH_4, i} > 0.001$ . The influence of the injected specie and the injection pressure on mixture formation in gaseous jets were analysed by Vourinen et al. [380] while, in this study, attention was focused on the effects of varying chamber counter-pressure. The probability density

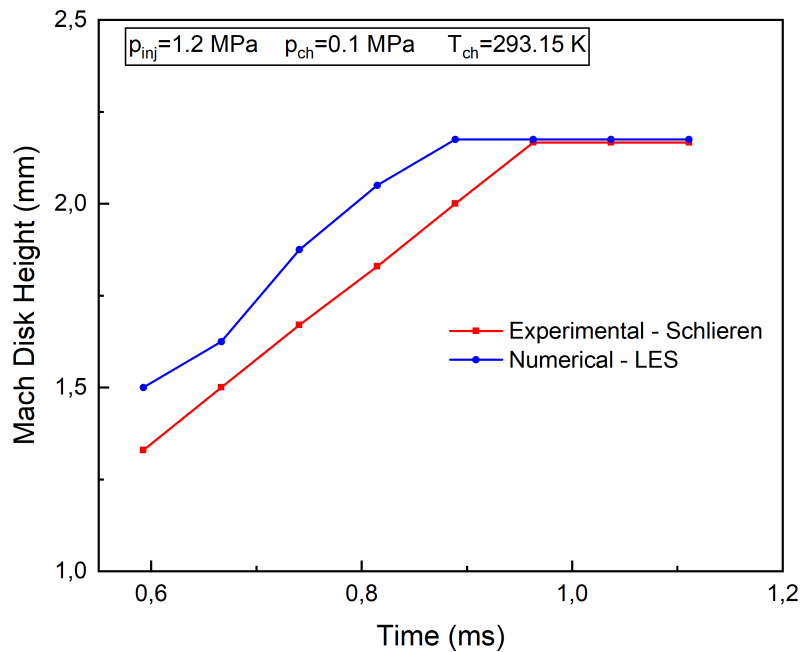


FIGURE 9.23: Experimental and Numerical Mach Disk Height vs. time for  $p_{inj}=1.2$  MPa and  $p_{ch}=0.1$  MPa

function allows to obtain the distribution of instantaneous methane concentration in each cell, thus providing information about global air/gas mixture. In Figure 9.29 the mass-weighted PDFs of the methane mass fraction, for Case 1 and Case 2, at  $t_{ASOI} = 0.75$  ms after the start of the injection, are shown.

The two vertical grey lines delimit the flammable zone defined by a methane mass fraction between 0.044 and 0.15. In both considered cases, the most probable value, greater of about the 24 % for Case 1 than Case 2, belongs to the flammable zone. Furthermore, the probability of finding methane mass with a  $y_{CH_4}$  in the flammable zone is greater for the counter-pressure of 0.1 MPa. Finally, for the selected timeframe, it can be observed another peak value for a  $y_{CH_4} \approx 1$  representatives of the potential core zone where almost only methane is present.

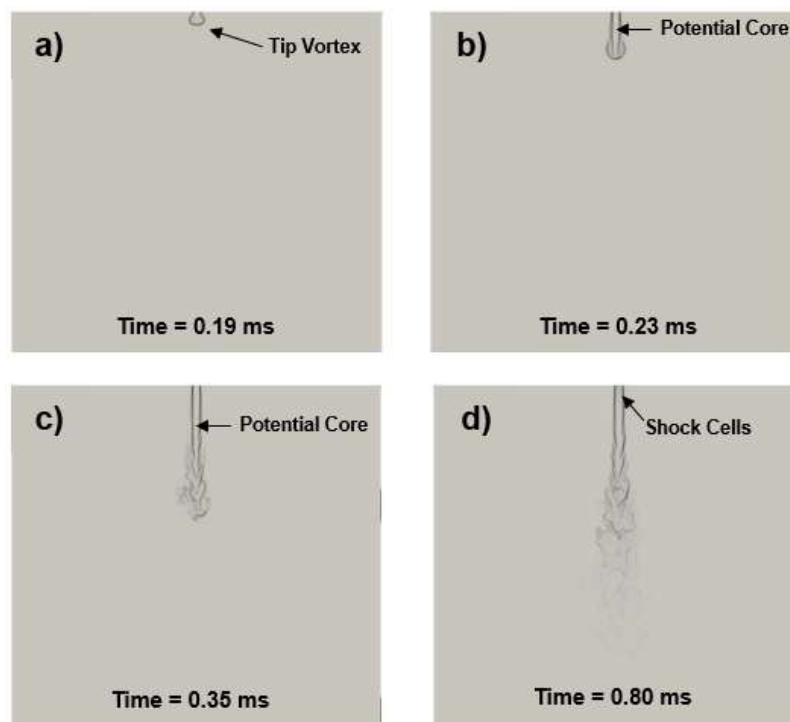


FIGURE 9.24: Gaseous jet structure's evolution at different time-step for Case 1 ( $p_{inj} = 1.2$  MPa and  $p_{ch} = 0.4$  MPa) obtained plotting the density gradient.

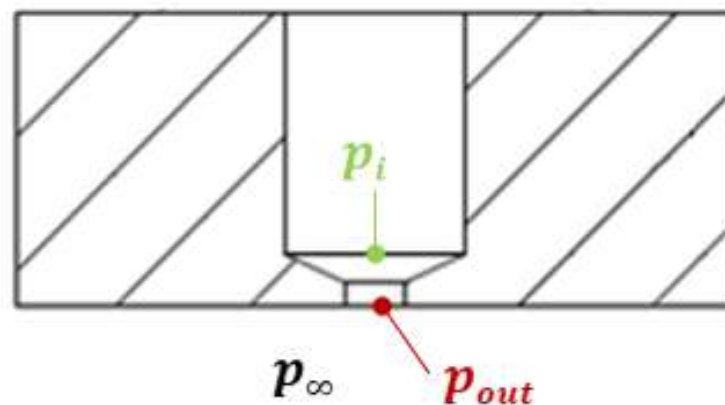


FIGURE 9.25: Nozzle Pressure Definition

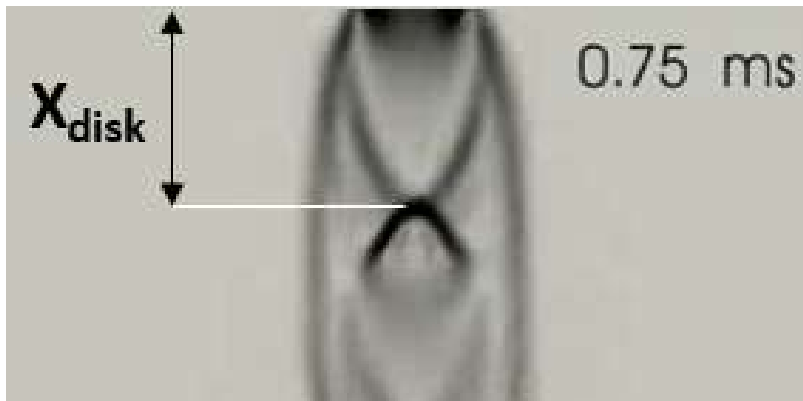


FIGURE 9.26: 2D-map of Density Gradient - Mach Disk particular

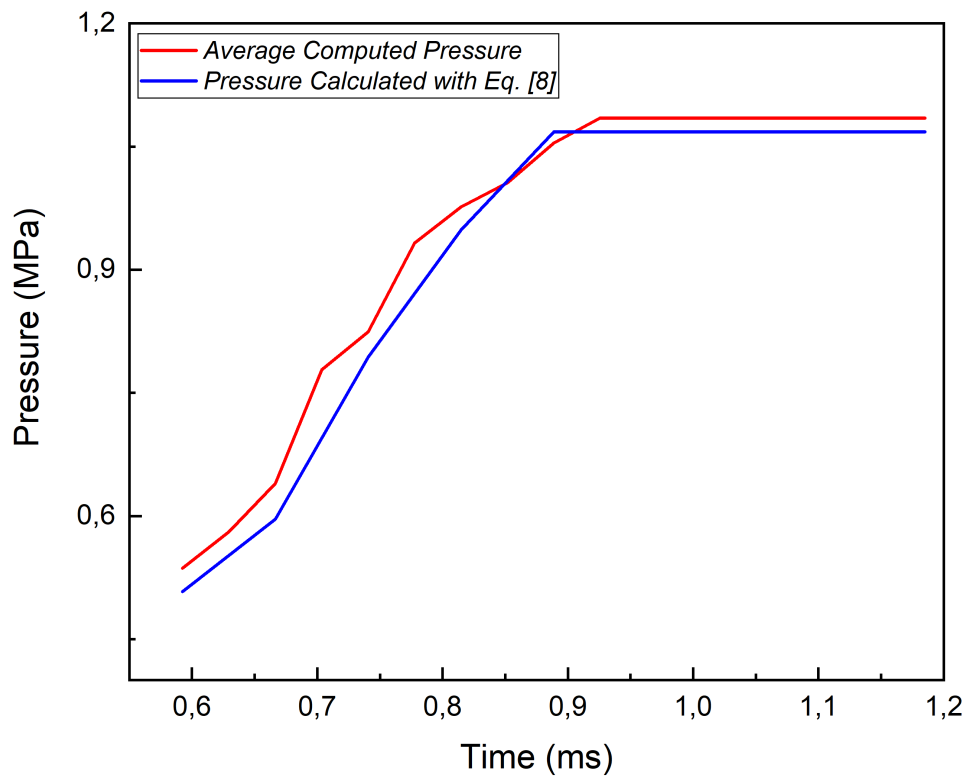


FIGURE 9.27: 2D-map of Density Gradient - Mach Disk particular

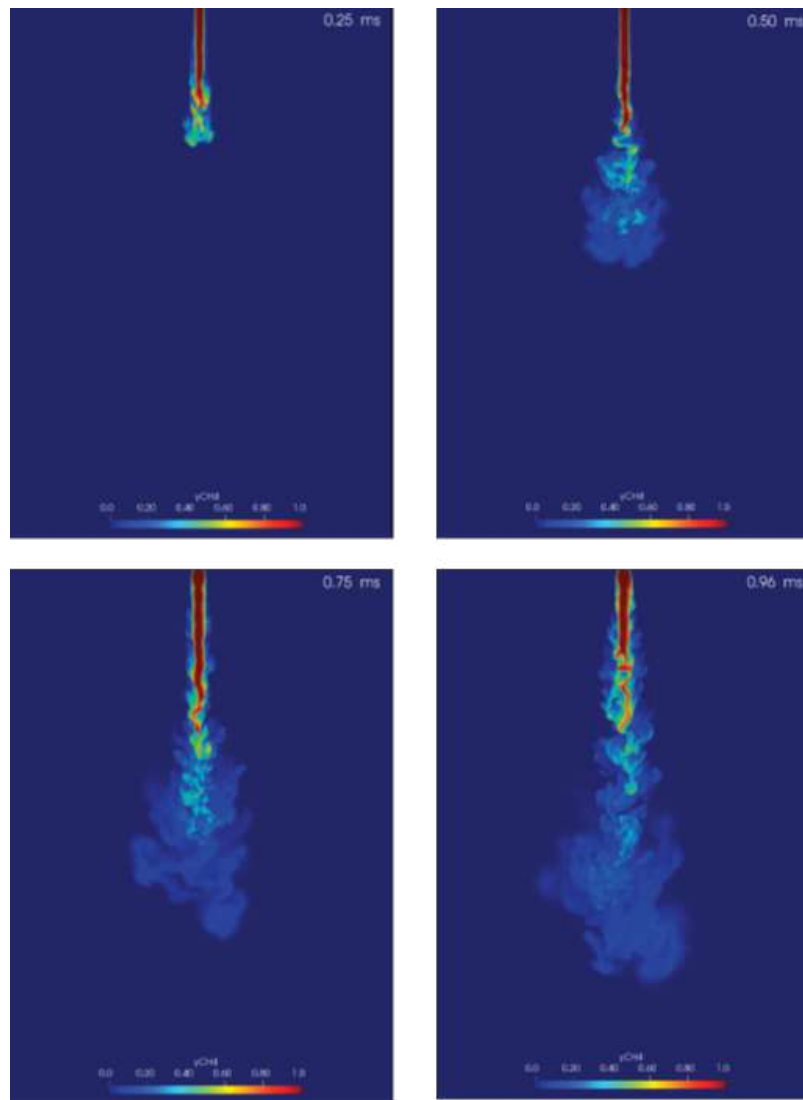


FIGURE 9.28: Evolution of the gaseous jet structure in term of  $y_{CH_4}$  2D-map -  $p_{inj} = 1.2$  MPa and  $p_{ch} = 0.1$  MPa

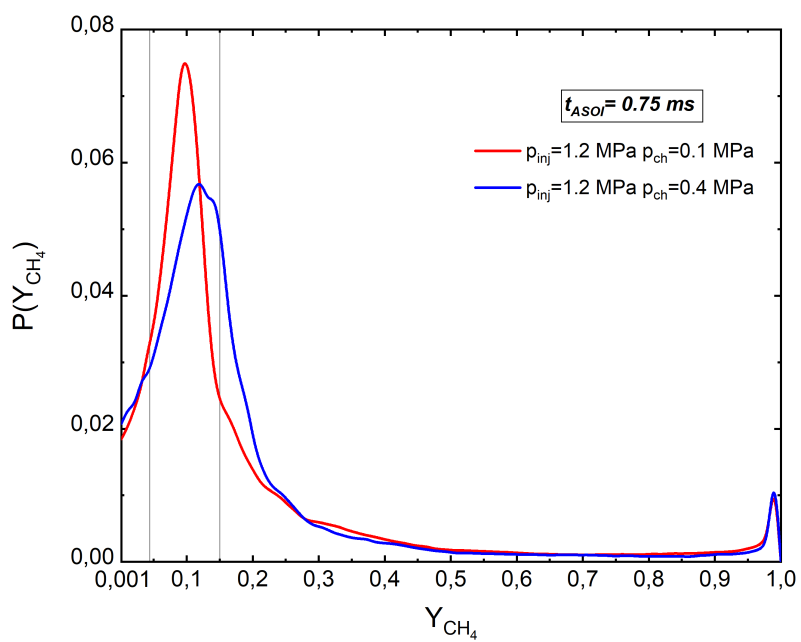


FIGURE 9.29: Probability distribution of mass fraction  $y_{CH_4}$  for Case 1 and Case 2 at  $t_{ASOI} = 0.75$  ms.



## Chapter 10

# Gaseous Jet Characterization: Multi-Hole Injector Case Study

### 10.1 Multi-Hole Injector and Gaseous Jets

The latest research indicated that multi-hole injectors are suitable for application in CNG-DI engines. Chiodi et al. [67] investigated the characteristics of a CNG jet issuing from both single and multi-hole GDI injectors, by means of experimental measurements into a single-cylinder engine and numerical simulations. They have shown that a multi-hole injector is more suitable for mixture homogenization or stratification than single-hole injectors. They have also found that mixture formation strongly depends on turbulence level in the mixture. A numerical investigation on the effects of combustion chamber geometry, injection parameters, cylinder head shape and injector type on mixing of air-methane in a CNG-DI engine was conducted by Yadollahi et al. [407]. They found that a multi-hole injector delivers a slightly more flammable, stratified mixture than a single-hole injector. The larger flammable mass fraction in multi-hole injection can be attributed to a wider jet spread and thus higher levels of mixing. Erfan et al. [106] used the schlieren photography technique to investigate the effect of varying injection parameters on the structure of a CNG jet issuing from a multi-hole injector. They also calculated the mass flow rate, using Dalton's law, showing that this is independent of chamber pressure because the natural gas flow is choked at the nozzle exit. Furthermore, mass flow rate increases at higher injection pressures.

The investigations of jet issuing from a multi-hole injector is challenging due to the interaction of the individual plumes and the complex physical phenomena that occur in the near-nozzle zone for under-expanded jets. Salazar et al. [314] studied the evolution of the mixing process of nitrogen/hydrogen mixture for several multi-hole injectors by means of Planar Laser-Induced Fluorescence (PLIF). For a 13-hole nozzle, they observed that all jets merged into a single collapsed jet, immediately downstream of the under-expanded zone. This phenomenon is called the Coanda Effect and it stems from a lack of air entrainment due to the close proximity of interacting individual plumes. The data from such experimental studies were used by Scarcelli et al. [321] to validate numerical results obtained with a CFD-RANS simulation. While CFD results accurately predicts the jet penetration and the

fuel distribution for all the multi-hole nozzles where no jet-to-jet interaction was observed, a worse agreement with experimental data was recorded for the 13-hole nozzle. This is due to the strong influence that the presence of under-expanded structures exerts on the mixing process and on the plume-to-plume interaction. They concluded that increasing the grid resolution and performing a Large Eddy Simulation (LES) could improve the accuracy of numerical prediction.

The present case study reports the experimental and numerical characterization of high-pressure jets for direct injection applications. The injector used is a prototypal device featuring an innovative hole's pattern and suitable for CNG direct injection with pressure up to 5.0 MPa. Methane was injected into a constant volume chamber filled with nitrogen. Schlieren imaging technique was employed to evaluate the effects of the injection pressure and ambient thermodynamic conditions on jet penetration length. In order to allow the measurements of macroscopic characteristics of the jet, a customized procedure for processing the images was adopted. Then the injection process was simulated with a fully explicit, density-based solver featuring Runge-Kutta 4th order time discretization and the central flux splitting scheme of Kurganov. An LES turbulence framework, multi-species transport model and variable thermo-physical properties were adopted in order to properly represent the fuel-air interaction. The results show the jet evolution inside the injector nozzle, the formation of shock waves and the evolution of the under-expanded, down-flow structures, in the near nozzle zone, achieving a deeper understanding of the air-fuel mixing process that strongly influences the combustion and pollutant emissions.

## 10.2 Investigation Methodology

The activities performed in the current study, dealt with an innovative high-pressure multi-hole injector, specifically developed for the direct injection of gaseous fuels with an innovative maximum pressure of 50 bar (Figure 10.1).



FIGURE 10.1: Silhouette of the high-pressure injector.

The device has an interchangeable terminal nozzle which drives the flow into a particular multi-hole spray configuration. Such a component was analyzed by means of X-Ray tomography, in order to define the exact internal geometry. Figures 10.2 and 10.3 show a cross section and a bottom view of the region of interest, respectively. This information was used to create a CAD model of the nozzle geometry.

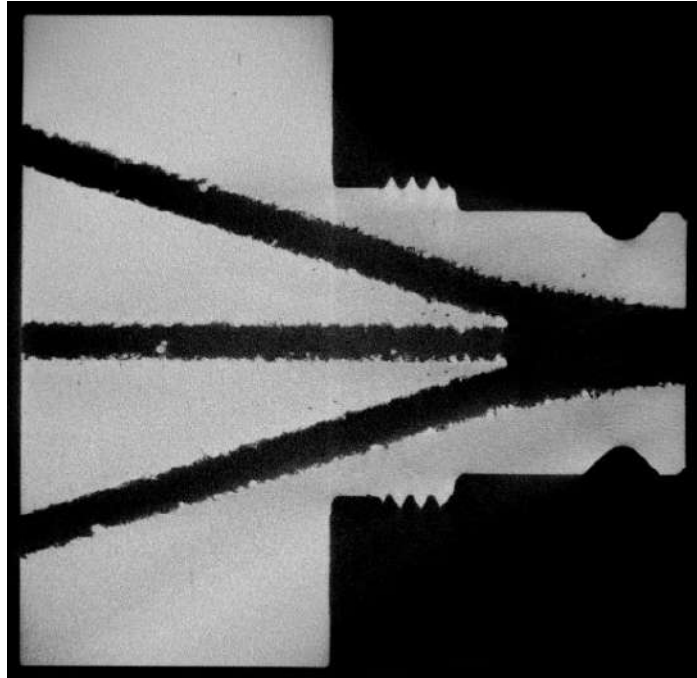


FIGURE 10.2: X-Ray tomography of the injector showing its internal geometry.

The injection process was controlled using a programmable Electronic Control Unit (PECU) with the energizing current profile shown in Figure 10.4 (blue curve). Following magnetic and mechanical opening delays, the injector needle begins to lift and the pressure at the nozzle inlet increases. The time behaviour of such a parameter was measured and provided by the injector manufacturer. It is represented by the red curve in Figure 10.4.

The experimental campaign features the recording, thanks to schlieren imaging technique, the time-evolution of the jet within a constant volume chamber (CVC) optically-accessible, filled with pressurized nitrogen. In order to reproduce the engine-like conditions and study their effects on the jet behaviour, different thermodynamic conditions were investigated including different injection pressures. Table 10.1 summarizes the investigated experimental conditions.

The injected gas is methane ( $\text{CH}_4$ ). The acquisition of the large amount of experimental data defined in Table 10.1, alongside with the time-history of the injection pressure and the nozzle geometry, poses the basis to start developing a numerical model capable to reconstruct the overall injection process. Besides, the numerical results provide further information concerning the air/fuel mixing process, the development of the under-expanded structures



FIGURE 10.3: X-ray bottom view of the injector showing the nozzle pattern.

Parameter	Values
Injection Pressure [MPa]	1.0 – 3.0 – 5.0
Ambient Pressure [MPa]	0.05 – 0.1 – 0.5 – 1.0
Ambient Temperature [K]	293
Injection Electric Duration [ms]	8.0

TABLE 10.1: Adopted experimental parameters.

of the jet, not available from the experimental images. The numerical simulations regards the condition reported in Table 10.2. Further details regarding the numerical model will be provided in the relative section.

From the experimental images, the jet was characterized both qualitatively and quantitatively in terms of penetration length, defined as the distance between the nozzle exit and the furthest point on the contour of jet along the axis of the spray. Numerical penetration was measured plotting the density gradient, or more precisely  $\log_{10} |\nabla \rho|$ , being  $\rho$  the density of the methane, keeping in mind the congruence with the schlieren technique that

Parameter	Values
Injection Pressure [MPa]	5.0
Ambient Pressure [MPa]	0.1
Ambient Temperature [K]	293

TABLE 10.2: Adopted experimental parameters.

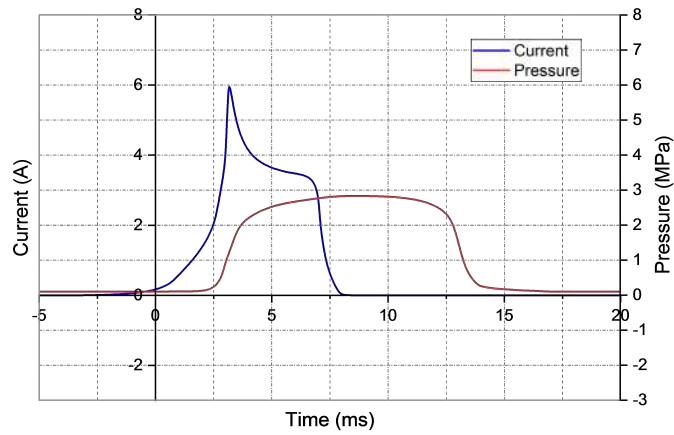


FIGURE 10.4: Current command signal and nozzle inlet pressure time behaviour.

just measures density gradients.

### 10.3 Experimental Activities

The experimental apparatus was built up at the Istituto Motori laboratories of the National Research Council (CNR). The tests were carried out injecting methane in a CVC, 4.5 liters, optically accessible through three quartz windows, 80 mm in diameter, orthogonally disposed, which permit the access to a large area of the investigated spray. The fuel supply system consists of a 20 MPa tank, filled with methane gas (99.5% purity). A high-pressure single-stage regulator (maximum outlet pressure 10 MPa) is used to realize the desired value per each condition. A piezo-resistive pressure transducer (0 - 6 MPa gauge pressure) ensures an accurate reading of the methane pressure just upstream the injector connection. A prototype multi-hole CNG-DI inwardly opening injector was used for introducing the fuel inside the CVC. The injection process was driven by a PECU for energizing the needle lift. At all the conditions, the energizing time was set to 8.0 ms. Five repetitions were carried out to check the repeatability of the measurements and define a minimum of spread. The PECU ensured the synchronization and delaying between the injection and acquisition chain by transistor-transistor logic (TTL). The injector was mounted in a customized holder, placed on the top of the CVC. The desired counter pressure inside the vessel was varied introducing nitrogen ( $N_2$ ) at the required value, while a vacuum pump was used for cleaning-up the measuring volume or for obtaining sub-atmospheric conditions in the CVC. Schlieren optical technique, in the classic Z-type configuration (Figure 10.5), was adopted to depict the spray spread, registering the images of the evolving fuel on a high-speed CMOS camera. Schlieren technique is sensitive to the gradient of the gas density generated by the fluids flow along the optical path and resulting in variations of the refractive index of the fuel, suitable for transparent media such as CNG.

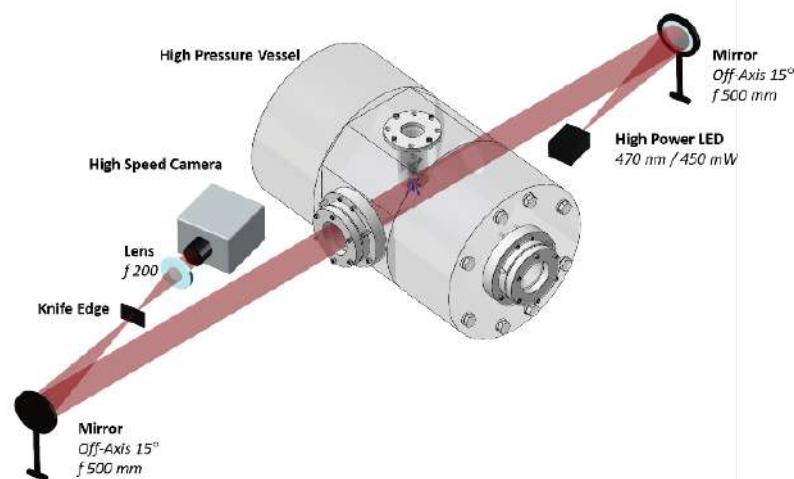


FIGURE 10.5: Optical setup for schlieren technique in Z-type configuration.

The schlieren setup used a high-power LED lamp (Omicron LED MOD

V2) as source, emitting radiation at the wavelength of 455 nm. The extended parallel beam is generating utilizing two  $15^\circ$  off-axis mirrors, 500 mm focal length. A knife-edge, mounted orthogonally to the spray propagation direction, is placed at the focus of the second mirror. Finally, a biconvex lens, 200 mm focal length, transfers the images on the camera through its objective. The detector is a high-speed CMOS camera (Photron FASTCAM SA4), working at a rate of 18,000 frames per second (fps) with an image window of  $448 \times 416$  pixels. The camera, equipped with a 90 mm focal lens, realized a spatial resolution of 5.5 pixel/mm and a time-resolution of 55  $\mu\text{s}$ .

## 10.4 Image Processing Procedure

The images, acquired at the different operating conditions (see Table 10.1), were analysed by means of a customized post-processing procedure to outline the contours of the gas and ensure a proper contrast, allowing the measurement of the parameters of interest such as the axial penetration of the jet. Figure 10.6 reports the steps of the implemented treating algorithm.

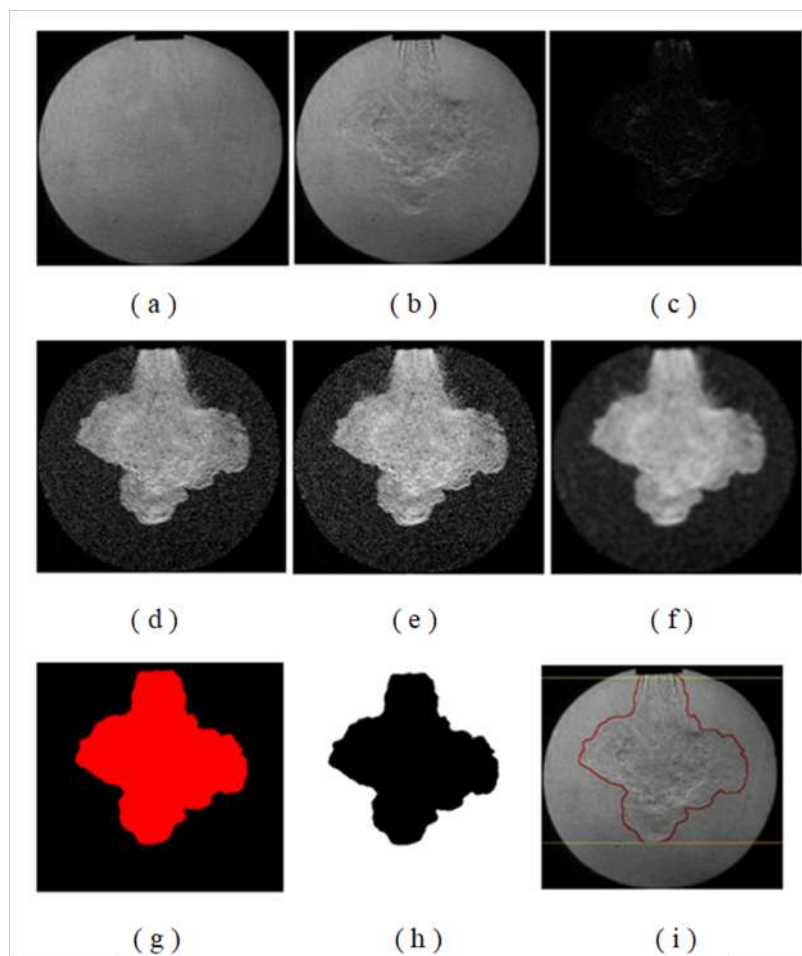


FIGURE 10.6: Image processing procedure.

The processing routine begins with the extraction of the background, through an average of images caught just before the exiting of the fuel from the nozzle (Figure 10.6-a, trace internal structure are imputable to light leakages in the nozzle). Figure 10.6-b shows the raw methane spray once injected in the chamber. To reduce undesirable noise, the subtraction of the background from the original jet image was done and the result is shown in Figure 10.6-c. From this step, some consecutive filters were implemented. A  $\gamma$  filter was applied for improving the brightness, a *contrast stretching* was employed to expand the range of brightness (Figure 10.6-e) while a blurring was then obtained using a Gaussian function (Figure 10.6-f). After binarizing the image through the *OTSU threshold*, two additional filters were applied, namely *blob filter* (Figure 10.6-g) and *fill hole filter* (Figure 10.6-h), to fill holes in the binarized image. Then, from the last image the spray outline was extracted by means of a contour recognition filter (edge detector overlaid in red on Figure 10.6-b, Figure 10.6-i). Finally, using the maximum coordinates along the y axis of the contour, the measure of the spray penetration was possible (green lines overlaid in Figure 10.6-i).

## 10.5 Numerical Methodology

### 10.5.1 Governing Equations of Compressible Flows

In order to properly describe the physics of the injection process, a new solver was developed in the OpenFoam library. Considering compressible flows in the presence of shock waves and strong discontinuities, the governing equations (mass 4.1, momentum 4.2 and total energy 4.3 conservations) are solved using the conservative variables  $\rho$ ,  $\rho\mathbf{u}$  and  $\rho e$  as in Chapter 4. The dynamic viscosity  $\mu$  is computed by Sutherland's law as a function of temperature:

$$\mu = \frac{A_s \sqrt{T}}{1 + T_s/T} \quad (10.1)$$

$A_s$  and  $T_s$  are specific constants of the single specie (Table 10.3) [398]:  
The specie diffusivity is equal to:

$$D_i = \frac{\mu_{eff}}{\rho Sc}$$

with Schmidt number  $Sc$  equal to 0.7 after Vuorinen V. et al [379].

Species	$A_s$ [ $\text{kg m}^{-1} \text{s}^{-1} \text{K}^{-0.5}$ ]	$T_s$ [K]
$N_2$	$1.4067 \cdot 10^{-6}$	111.0
$CH_4$	$1.2529 \cdot 10^{-6}$	197.8

TABLE 10.3: Sutherland's law  $A_s$  and  $T_s$  constants adopted values

### 10.5.2 Discretization and Solution

The simulation of high-speed, under-expanded jets requires numerical discretization that can capture flow discontinuities such as Mach disks, shock waves and, at the same time, avoids unwanted oscillations. Methodologies based on Riemann solvers, such as the Piecewise Parabolic Method (PPM) and Weighted Essentially Non-Oscillatory (WENO), give an efficient reproduction of compressible flow but have important drawbacks. Such approaches involve characteristic decomposition and Jacobian evaluation which make them complex and difficult to be implemented in co-located, unstructured grids that, instead, allow us to discretize complex geometries and are much more flexible than structured grids [125, 376]. Valid alternative approaches were developed; one of them uses the so-called central schemes formulations of Kurganov (KNP) and Kurganov and Tadmor (KT) [191, 192]. These methods are non-staggered second order central schemes that evaluate the fluxes on the cell faces using the values at the cell center. The cell to face flow interpolation is subdivided into an inward and outward direction with the respect to the face owner cell. A full and detailed description of KNP and KT central schemes, used in the developed solver, can be found in [125].

In order to ensure the simulation stability and to avoid solution oscillations, OpenFOAM allows the adoption of flux limiters and so VanLeer flux limiter was adopted in the performed simulations [125, 206].

Previous studies demonstrated that, in order to properly simulate under-expanded jets, higher order time discretization methods, such as Runge-Kutta 4<sup>th</sup> (RK4), are required [134, 379]. Similarly to the previously cited works, the classical RK4 explicit method was implemented in the newly developed OpenFOAM solver for integrating the solution over time. The time-stepping coefficients of the RK4 method that were chosen were [381]:

$$a_1 = a_4 = \frac{1}{6} \quad a_2 = a_3 = \frac{1}{3} \quad (10.2)$$

A complete description of the method can be found in [134, 381]. The developed solver was summarized in accordance with the flowchart of Fig. 10.7. It illustrates all of the operations performed during a generic time step and for each RK4 step: the  $\rho, \mathbf{u}, e$  field are updated, the relative fluxes recomputed and the turbulence model solved.

Finally, the temporal integration of species and turbulence transport equations was performed using a second-order backward implicit method.

### 10.5.3 Turbulence Modelling

The solution of the governing equations (4.1-4.3) is valid when the computational grid is fine enough to resolve all the flow scales [379]. This would be a Direct Numerical Simulation (DNS) of the flow which, today, is not affordable because its is too complex and time demanding. So, other modelling techniques, such as Large Eddy Simulation (LES), are preferred for under-expanded jet simulations [134, 379, 382].

Region	p (bar)	T (K)	u (m s <sup>-1</sup> )
$0 \leq l \leq 0.5$ m	1.0	348.4	0
$0.5 < l \leq 1$ m	0.1	278.7	0

TABLE 10.4: Validation case initial conditions

The concept behind the LES approach is to model the smaller scales, which are universal and not affected by the flow geometry, while explicitly solving the larger ones. This is performed by mathematically filtering the governing equations and introducing the so called Sub-Grid Stress (SGS) tensor ( $\tau_{sgs}$ ) [294].

The SGS term modelling involves an eddy viscosity approximation. A one-equation eddy viscosity model for compressible flows was adopted [147, 413]. This kind of approach, which is different from zero equations models, uses a transport equation to compute the local SGS kinetic energy  $k_{sgs}$ . Then, the sub grid scale eddy viscosity  $\nu_{sgs}$  is calculated using the  $k_{sgs}$  field and the filter dimension  $\Delta$  (usually evaluated from the grid size) according to the following relation:

$$\nu_{sgs} = C_k \Delta \sqrt{k_{sgs}} \quad (10.3)$$

where  $C_k$  is a model constant whose default value is 0.094.

Finally, using this parameter, an effective viscosity ( $\mu_{eff}$ ) is obtained and used for the solution of the governing equations (4.1-4.3) [134].

### 10.5.4 Code Validation

The developed code was initially validated using the shock tube case [346]. This is a common test case that is used in the literature to evaluate the accuracy of algorithms for compressible flow simulations and their capability for capturing shock waves and other typical features. The shock tube considered in this work was 1.0 m long, containing nitrogen and with the initial conditions listed in Table 10.4.

The domain was subdivided in two regions along the length and initialized with different pressures and temperatures. The computational domain was then discretized using a grid with 1000 elements uniformly spaced in the direction of the shocktube length; the time stepping value was  $10^{-8}$  s. The simulation results after 0.6 ms were plotted (see Figures 10.8, 10.9, 10.10 and 10.11) to show a complete agreement with the exact solution for each computed field. Moreover the code capability to capture shock-waves and the absence of solution oscillations are evident.

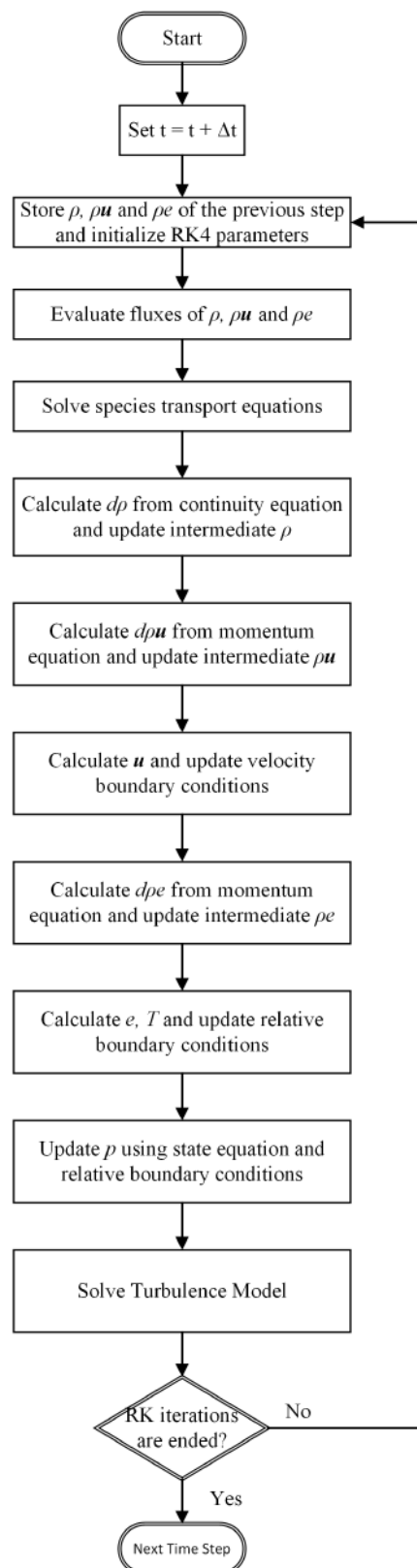


FIGURE 10.7: Flowchart representing the developed solver structure and summarize the operations performed in each calculation step.

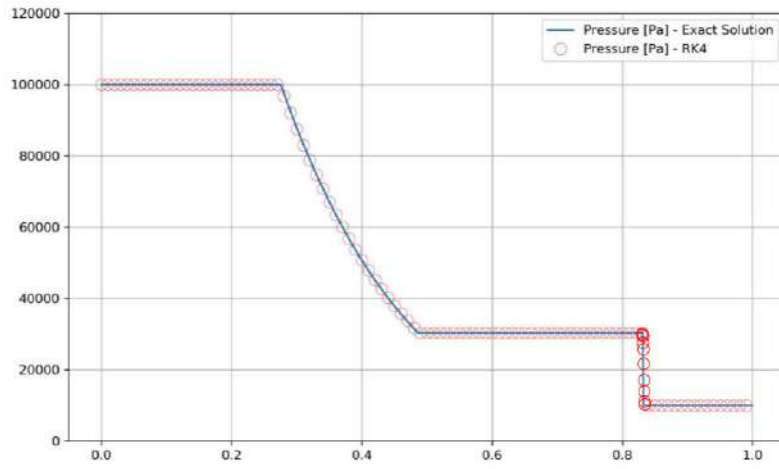


FIGURE 10.8: Shock tube validation case: comparison of exact solution with the numerical computed pressure.

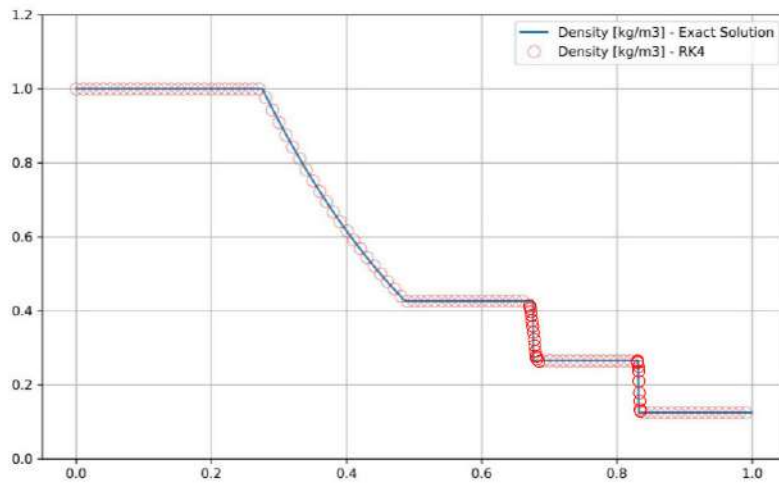


FIGURE 10.9: Shock tube validation case: comparison of exact solution with numerical computed density.

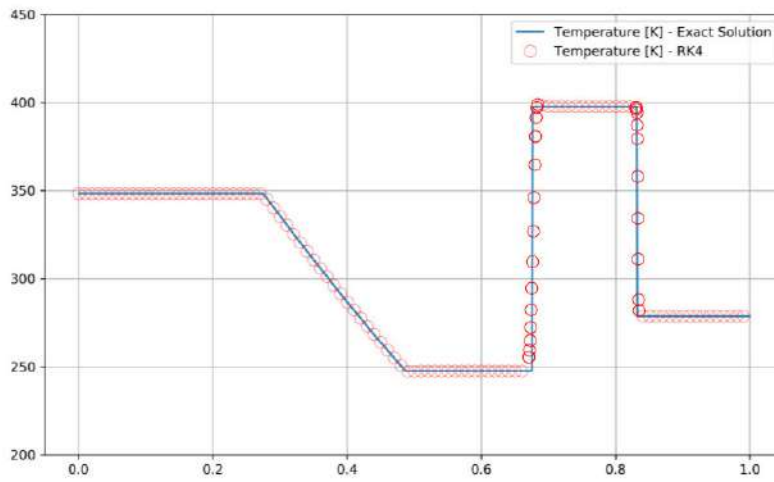


FIGURE 10.10: Shock tube validation case: comparison of exact solution with numerical computed temperature.

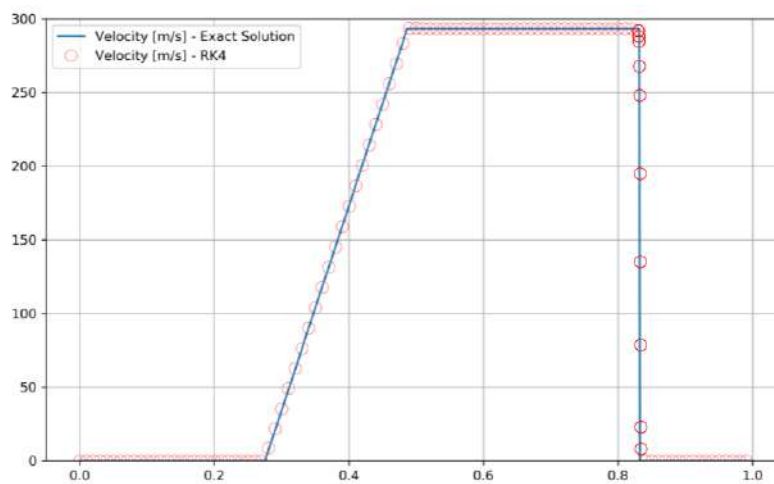


FIGURE 10.11: Shock tube validation case: comparison of exact solution with numerical computed velocity magnitude.

## 10.6 Multi-hole Injector Case Study

The computational domain is composed by the injector's internal ducts which are connected to a cylindrical tank that reproduces the CVC used in the experiments.

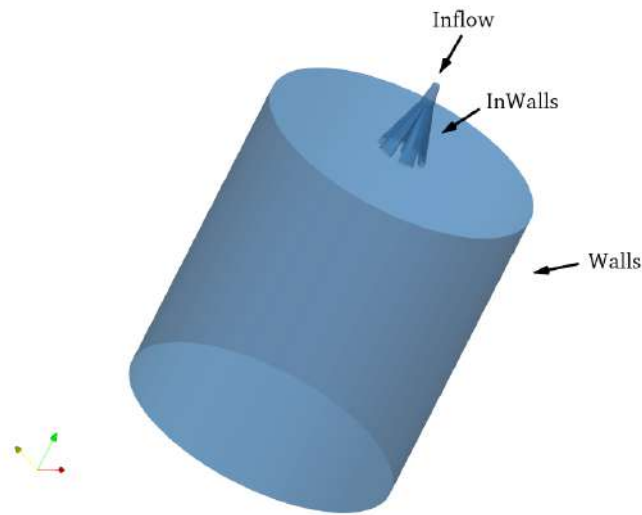


FIGURE 10.12: The boundary conditions.

Specifically boundary conditions are the following:

- Walls (magenta): walls of the injection environment. The study of the interaction of the jet with these surfaces is not a purpose of this study.
- Inlet (red): this is the section at the top of the domain where the injected gas entered the domain. The manufacturer provided the time-behaviour of the pressure at this section as represented in Figure 10.13. Consequently, using the OpenFOAM boundary conditions, a **uniform-TotalPressure** was imposed for the pressure while a **zeroGradient** was used for the velocity. The value of the total temperature is fixed at 293.15 K. The intensity of the turbulent kinetic energy was fixed at 0.08. The mass fraction of methane entering the system was fixed at unity ( $\text{CH}_4 = 1$ ) and, consequently,  $\text{N}_2 = 0$ .
- NozzleWalls (green): nozzle internal walls. A **noSlip** condition was set for velocity. Considering the results of the X-ray tomography (Figures 10.2 and 10.3) specific laws of wall were adopted for the wall. More precisely the turbulent kinetic energy and turbulent kinematic viscosity boundary conditions are **kqRWallFunction** and **nutkRoughWallFunction** respectively. The first one provided a simple wrapper around the zero-gradient condition for turbulent kinetic energy while **nutkRoughWallFunction** manipulated a wall roughness parameter to account for

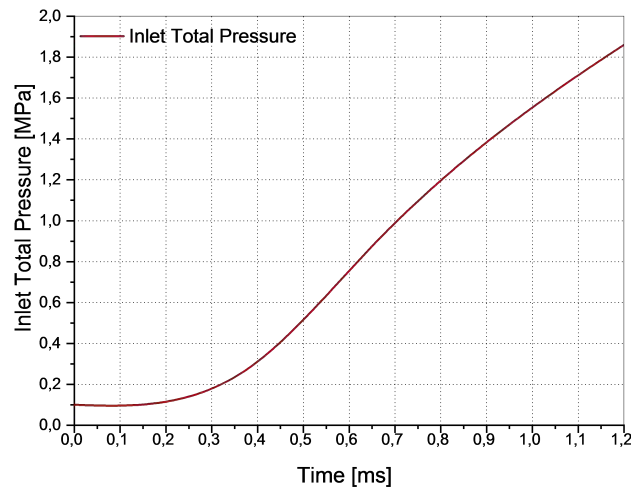


FIGURE 10.13: Total pressure boundary condition.

Ambient Pressure	1 bar
Ambient Temperature	293.15 K

TABLE 10.5: Case Study Initial Conditions

roughness effects. Full details and a complete description are available in [70].

The integration domain was initialized with the parameters reported in Table 10.5.

The geometry was discretized with two unstructured grids generated using the `snappyHexMesh` tool embedded in `OpenFOAM`. The two mesh are topologically equal and, in particular, the coarse grid has dimensions of  $100 \times 100 \times 100 \mu\text{m}$  while, for the fine grid, a refinement was adopted for the internal nozzle flow up to a grid sizing of  $50 \times 50 \times 50 \mu\text{m}$ . Following Figure 10.14 shows details of the refinement region which extends for a few diameters downstream from the nozzle.

The simulation was performed with the developed solver on the 36 cores of two Intel Xeon Gold 6140. Numerical results were then post-processed using `Paraview` software.

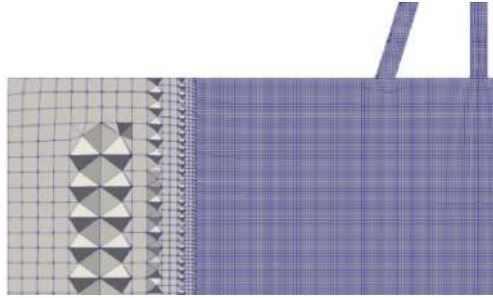


FIGURE 10.14: Particular view of the refinement region of the grid.

## 10.7 Experimental Results

The effects of injection pressure and in chamber back-pressure on evolution, morphology and tip penetration of the spray are studied.

### 10.7.1 Effect of Injection Pressure

Figure 10.15 shows the comparison between the evolutions of the spray at three different injection pressures, 1.0, 3.0, and 5.0 MPa, keeping constant pressure and temperature in the chamber ( $p_{amb}=0.5$  MPa and  $T_{amb}=293$  K, respectively). Each sequence starts at the instant  $t_{SOI}$  (time at Start Of Injection), that is the time-frame just before the gaseous jet exits from the nozzle and appears in the chamber; next images are collected at a predetermined time interval starting from  $t_{SOI}$ , as a function of the camera acquisition rate.

Figure 10.16 graphs the values of jet tip axial penetration as a function of time averaged on five consecutive injections per each test point. On the profiles, the error bars, a statistical dispersion index estimating the variability of measures carried out, are reported.

In Figure 10.17 the curves of the jet penetration speed are shown calculated as the derivative in time of the axial penetration.

Figure 10.15, 10.16 and 10.17 clearly show that:

- at very-early stage of the injection (up to about  $t_{SOI}=0.20$  ms), the effects of the injection pressure are imperceptible. In fact, the curves for the three injection pressures are superimposed. In this stage, the injector is still opening (the energizing time is the same for all injection pressures) and the pressure at the nozzle exit gradually reaches its maximum value.
- increasing time, the effect of the injection pressure becomes evident: the higher is the pressure the faster the jet penetrates. The increase of the injection pressure produces a growth of the injected fuel and of the jet momentum, being constant the injection duration. So, the higher is the injection pressure then the faster is the penetration of the front-jet as a consequence of the highest gas momentum. The tip penetrations

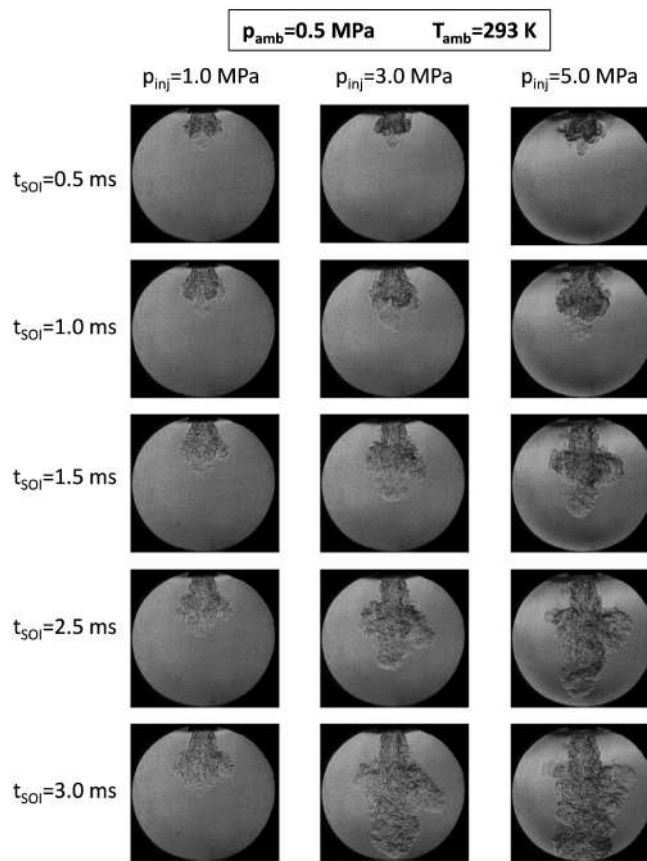


FIGURE 10.15: Evolution of the gaseous jet structure at three different injection pressures

(Figure 10.16) are upper limited around 75 mm because the tip edge reaches the bottom of the field of view. It happens at 2.33 ms and 3.27 ms for the injection pressures respectively of 5.0 and 3.0 MPa, while for 1.0 MPa injection pressure the spray does not reach the bottom of the field view.

- a two-stage development of the axial penetration curves is observed. In the early one, a linear trend with a high slope of the curves is registered. This linear trend turns toward a saturation trend at later time following a log-type bent. So, the penetration rate slows down as the jet develops further into the ambient gas.
- The two-stage behaviour can be observed for the jet penetration speed as reported in Figure 10.17. The first is characterized by a rapid decrease of the speed; then after the knee, the curves of the jet speed tend to flatten. Besides, the injection pressure is lower, later the speed curves turn into a constant trend. This suggests that the two-stage developments of the jet penetration and jet speed are strictly related to

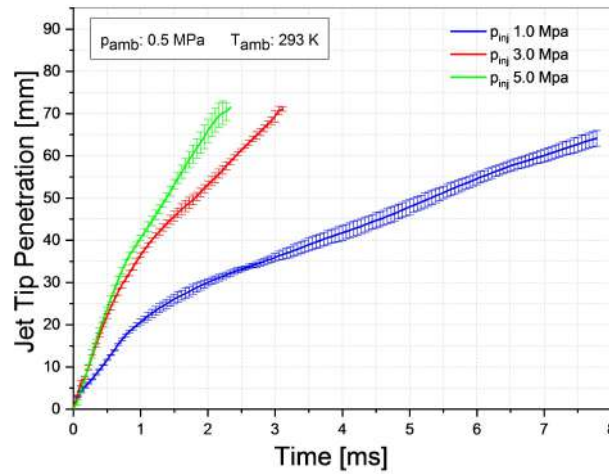


FIGURE 10.16: Axial jet tip penetration vs. time at three different injection pressures and  $p_{amb}=0.5$  MPa.

the braking effect of the gas in the chamber: lower pressures generate smaller velocities resulting in a delayed effect of the gas brake. It is worthwhile to note that a similar behaviour was previously registered by the authors for both multi-hole [12] and single-hole [420] diesel spray and for a gasoline direct injected spray [14].

## 10.7.2 Effect of back-pressure

Figure 10.18 shows the comparison between spray images, frozen at 1.0 ms after the start of injection, for four different back-pressures, 0.05, 0.1, 0.5, and 1.0 MPa, keeping constant the injection pressure and the chamber temperature ( $p_{inj}=5.0$  MPa and  $T_{amb}=293$  K, respectively).

In Figure 10.19, curves of axial jet tip penetration, with superimposed uncertainty bars, are graphed as a function of time, similarly to Figure 10.16.

Figure 10.18,10.19 clearly show that:

- During the early stages of injection, until about  $t_{SOI}=0.5$  ms, jet tip penetration curves overlap, highlighting that of the back-pressure effects are negligible.
- Later, after  $t_{SOI}=0.5$  ms, higher is the back-pressure, slower the gas penetrates inside the chamber. E.g., for a back-pressure equal to 0.05 MPa, the spray tip reaches the end of the window span around 0.94 ms from the start of injection, while reaches the end of the field of view after 3.6 ms for a back-pressure equal to 1.0 MPa.
- The jets develop over time with very different slopes, depending on the nitrogen back-pressures. For back-pressures of 0.5 and 1.0 MPa the

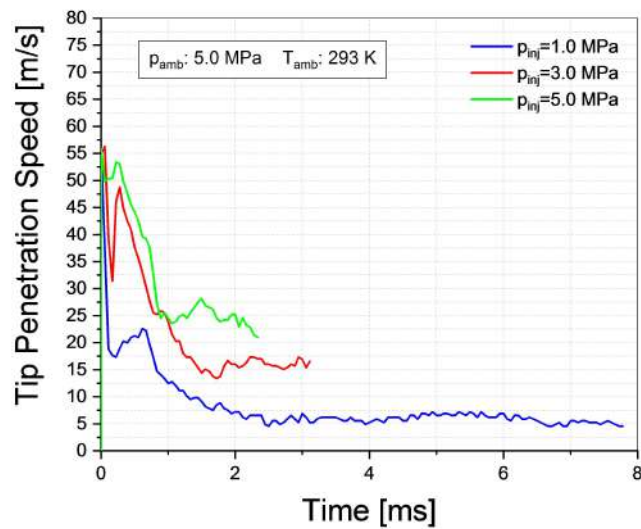


FIGURE 10.17: Jet penetration speed vs. time at three different injection pressures and  $p_{amb} = 0.5$  MPa.

penetration curves show a trend similar to that shown in Figure 10: a linear initial phase followed by a simil-logarithmic trend, highlighting the braking effect of nitrogen. For back-pressures of 0.05 0.1 MPa the braking effect of the nitrogen seems negligible, the jet penetration shows a constant and quasi-linear growth versus time.

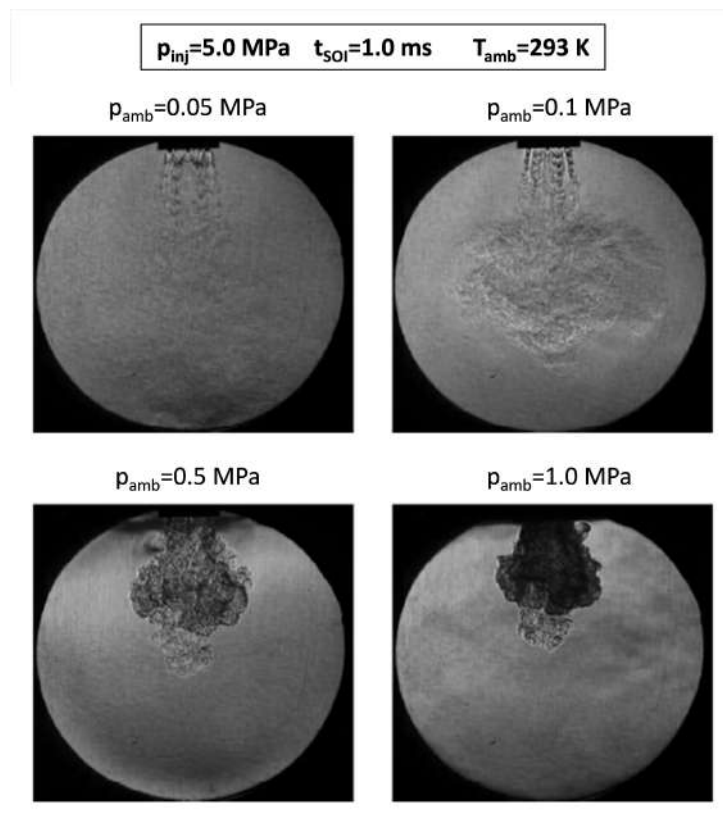


FIGURE 10.18: Effect of chamber back-pressure on spray evolution at  $t_{SOI}=1.0$  ms and  $p_{amb}=0.5$  MPa.

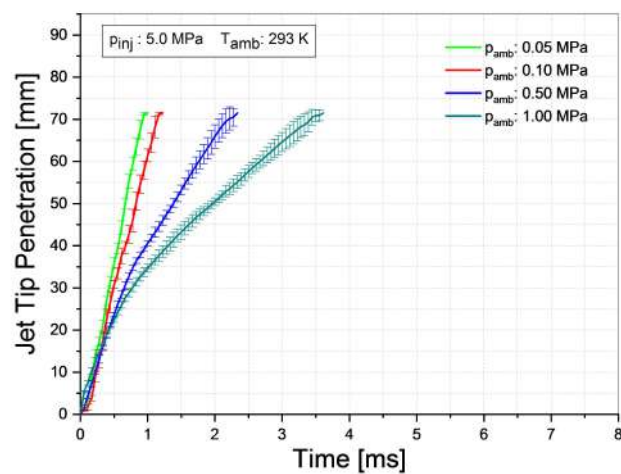


FIGURE 10.19: Axial jet penetration vs. time at four different back-pressures and  $p_{inj}=5.0$  MPa.

## 10.8 Numerical Results

The simulation allowed us to describe many aspects of the flow both in the injector's internal ducts and in the mixing region, which would otherwise be very difficult to obtain.

The first set of result regards model validation. Figure 10.20 shows a comparison of experimental and numerical axial penetration of the jet over time.

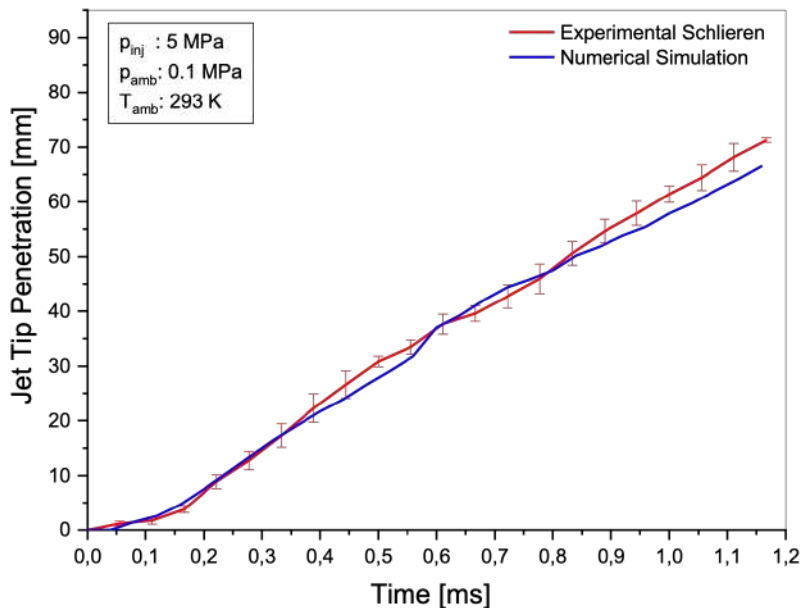


FIGURE 10.20: Experimental and numerical axial jet tip penetration vs. time

As can be observed, the agreement between the penetrations measured from the experimental images and computed from the simulations is very good and well within the combined numerical uncertainty up to 0.9 *ms* after the injection inception. In this phase, the penetration is ruled mainly by the jet momentum. On the contrary, when the spray develops in the main chamber, turbulent mixing governs the axial advancement; in this phase, the numerical observation departs from the experimental data. The observed differences suggest that a different turbulence model is required to properly capture the air-fuel entrainment.

A very complex flow field appears within the injector as shown by the temporal sequence of Figure 10.21. The Mach number contours are reported on the left hand side, together with the logarithm of density gradient on the right.

As a matter of facts, the apparatus consists of a converging-diverging portion that accelerates the flow from a subsonic, high-pressure condition at the inlet to a supersonic, low-pressure condition at the nozzle discharge, where the Mach number reaches a value of around 2.5. At this location, the duct branches off into seven smaller ducts: a central circular duct with a constant

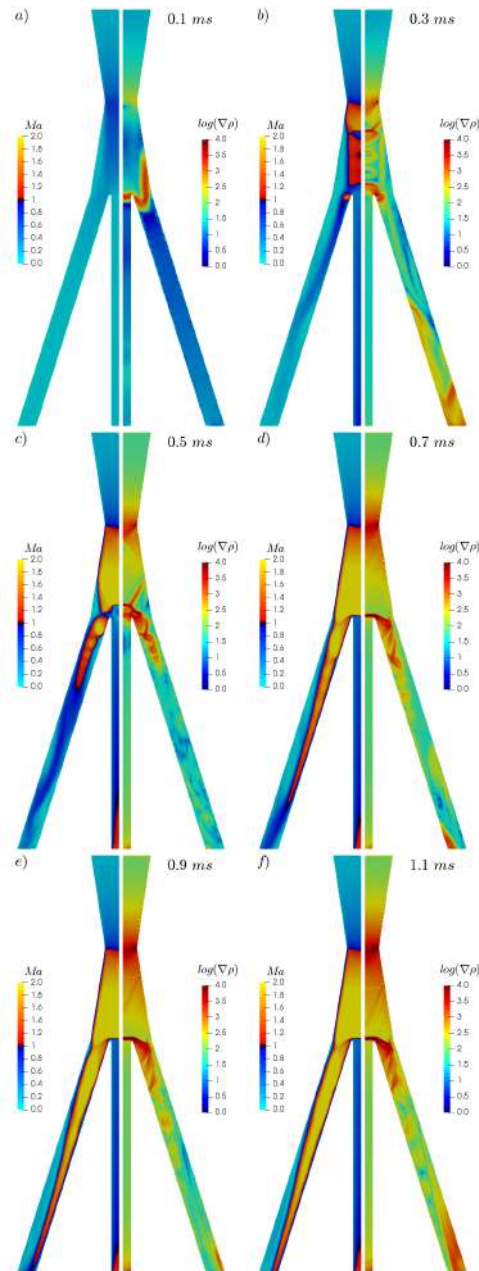


FIGURE 10.21: Temporal evolution of the spray within the injector's ducts with a multi-plot of Mach number on the left hand side and logarithm of density gradient ( $\log(\nabla\rho)$ ) on the right side of each picture.

diameter of  $0.88\text{ mm}$ , and six larger inclined ducts, whose section is a circular sector with a hydraulic diameter varying in a stream-wise direction with a value  $O(1 \sim 3)\text{ mm}$ , that drives the mixture into the main chamber.

The expected flow structure for an inviscid flow should resemble the one sketched in Figure 10.22: the flow is accelerated into the converging-diverging nozzle, attaining sonic conditions at the throat (choked flow). When the flow reaches the smaller ducts, in ideal conditions (with an absence of

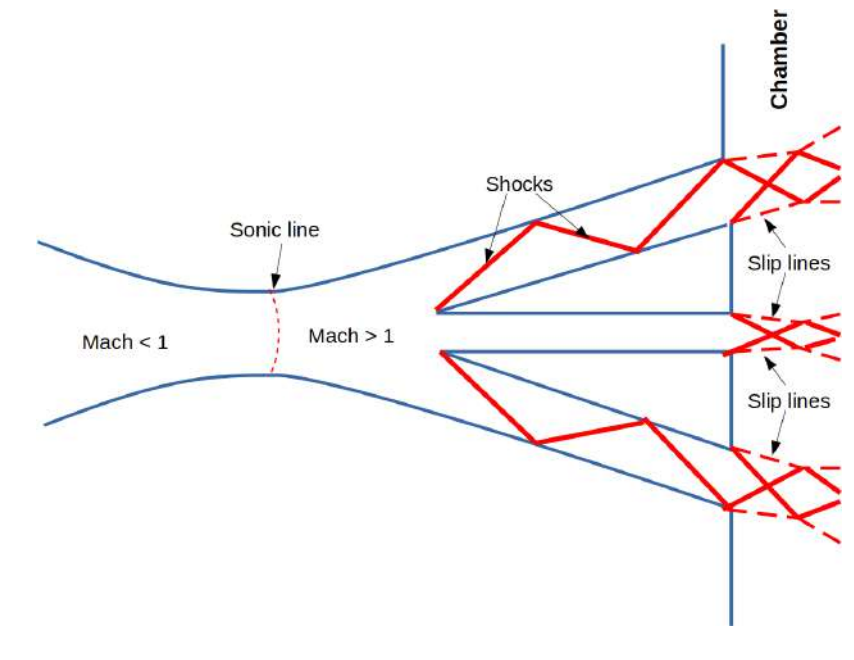


FIGURE 10.22: Flow structure - inviscid flow

viscosity), the flow would continue undisturbed in the central duct at a constant speed, pressure and temperature, the diameter would be constant and the walls adiabatic (this is not completely true for an inviscid fluid, because the flow is not exactly parallel in the central region). At the duct exit, the pressure is generally lower than in the main chamber and the flow would be re-compressed by a complex series of oblique shocks, slip surfaces and expansion fans, normally observed in an under-expanded jet. Of course, the precise structure of the jet (with diamond shocks, barrel shocks, Mach disks etc.) depends on the pressure jump at the exit. Conversely, a more complex flow structure consisting of a series of oblique shocks would appear in the side ducts; these shocks are required to divert the supersonic flow along the lateral duct and, given the Mach number of the approaching flow and the deflection angle (very small) they are expected to be attached to the corner. Therefore, the flow reduces its speeds across the oblique shocks, but remains supersonic and, like in the central duct, it reaches the exit with a pressure level which is lower than that in the main chamber. Given the flow structure described above, the discharge velocity is expected to be higher for the undisturbed flow in the central duct.

The above description is not very realistic in the present test case, because the viscous stresses play a central role in the ducts, due to the relatively low values of the Reynolds number (determined by the small hydraulic diameters). In this scenario, a better description can be gained by recalling the Fanno flow structure. In fact, by adopting the quasi-one dimensional approximation, constant cross section and steady flow (using the adiabatic walls hypothesis), it is possible to relate the local Mach number of the flow to the distance from the entrance of the duct. In particular, there are two main results that can be drawn from the theory of Fanno flows:

1. for a supersonic inflow, the Mach number in the streamwise direction can only decrease; on the contrary, for a subsonic inflow the Mach number increase; the relation between the Mach number variations and the position along the tube is given by:

$$\frac{dM^2}{M^2} = \gamma M^2 \left[ \frac{1 + \frac{\gamma-1}{2} M^2}{1 - M^2} \right] \frac{f dx}{D} \quad (10.4)$$

where  $M$  is the Mach number,  $\gamma$  the specific heat ratio,  $f$  the friction coefficient and  $D$  the diameter.

2. a critical length of the duct exists, above which a non-regular or steady solution is observed; by assuming a supersonic flow at the inlet, the critical length is given by

$$4 \frac{f L^*}{D} = \frac{1 - M_i^2}{\gamma M_i^2} + \frac{\gamma + 1}{2\gamma} \log \left[ \frac{M_i^2}{\frac{2}{\gamma + 1} \left( 1 + \frac{\gamma - 1}{2} M_i^2 \right)} \right] \quad (10.5)$$

where  $L^*$  is the critical length and  $M_i$  is the (supersonic) inflow Mach number. The ratio on the left hand side is the *Fanno parameter*.

For the range of observed Mach number at the duct inlet, in the present case, the Fanno parameter is always below 0.13. Moreover, for the adopted values of the relative roughness  $\delta/D \sim 0.06$  (for a dimensional average roughness of  $50 \mu\text{m}$ ), we obtain that the maximum  $L^*/D$  is approximately 2.3. As the length of the central duct is longer than this value, a detached and almost normal shock must appear at the entrance to slow down the inlet flow to subsonic conditions. After that, according to Fanno theory, the flow accelerates back to a sonic condition on the exit section. IN the side ducts the deceleration to subsonic conditions takes place by means of a more complex shock structure, close to a classical Mach reflection.

Once the flow enters the ducts, the friction coefficient is very similar and the exit speed is higher in the central duct, because it is shorter and with constant cross section. In fact, in addition to the viscous stress, the subsonic flow in the side ducts decelerates because of the increasing cross section.

The sketch of Figure 10.23 summarizes the flow features for the case of a viscous fluid. Of course, this description is also an approximation of the real situation because the actual flow is neither steady nor one-dimensional.

It should be noted that the jet evolution is not steady as assumed in the simplified analysis above that make use of the Fanno theory. Indeed, as shown in Figure 10.13, the inlet section pressure varies in time and, therefore, the actual flow evolution is characterized by a complex transient evolution. Nevertheless, if we consider the transient flow as a succession of quasi steady state problems, the previous description of the results based on the steady Fanno flow can be useful in understanding some relevant features.

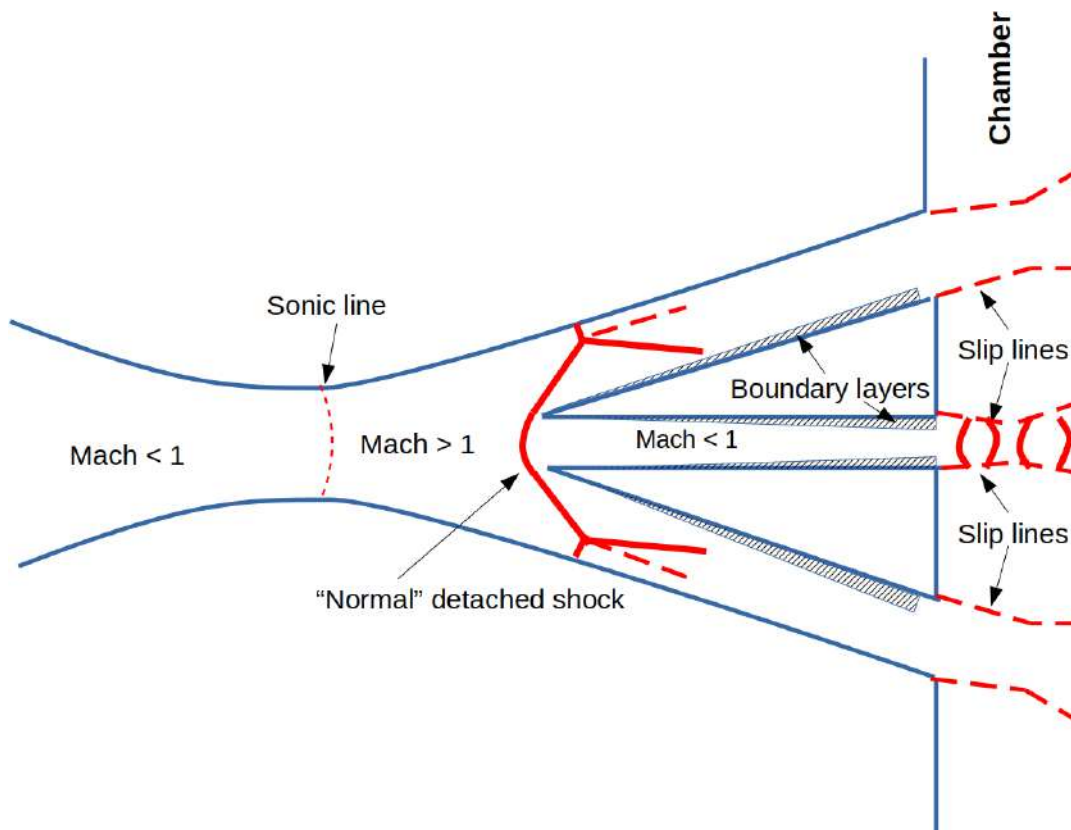


FIGURE 10.23: Flow structure - viscous flow

Once the flow reaches the main chamber, a very complex mixing region is observed, as reported in the sequence of Figure 10.24. It represents the temporal evolution of the spray in the injection environment represented by a methane concentration ( $Y_{CH_4}$ ) volume rendering. There are no simple theories capable of describing the jet development and so the flow description must rely on the simulation. Verification and validation, obtained by comparing the simulation with an analogous physical experiment, will help to quantify the reliability of the reported numerical results. After 0.3 ms, the central plume enters in the bulk introducing methane too. At 0.5 ms from the SOI (Figure 10.24-c) the lateral plumes exit creating spherical structures with higher methane concentration than the central jet. Then, the circumferential plumes develop maintaining a central core rich of methane (Figure 10.24-d, e). At 1.1 ms (Figure 10.24-f) the jet is approaching towards the bottom of the bulk, the relatively high turbulence intensity promotes the air/fuel mixing process as highlighted by tendency towards bluer tonalities.

The image-sequences of the Figure 10.25 shows the jet development at different time-steps. In order to have a clear, easy to read, representation of the results, the logarithm of the density gradient was plotted with a proper colour map. Figure 10.25-a shows the first stage of the injection when the seven plumes exit, respectively, from the six circumferential openings and from the central hole. As the injection goes on (Figure 10.25-b) the central hole's jet penetrates significantly faster than the circumferential ones which

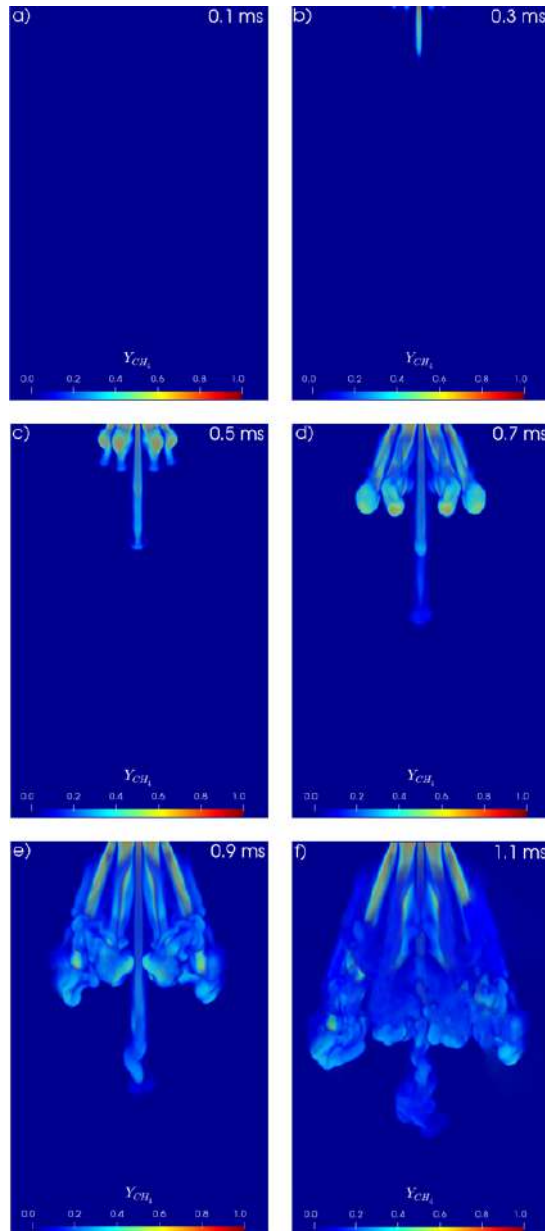


FIGURE 10.24: Temporal evolution of the spray development region represented by methane concentration ( $Y_{CH_4}$ ) volume rendering.

proceed with an evidently lower velocity. This is due to the oblique configuration of the circumferential holes that give to the jet also a radial speed component, differently from what happens in the vertical central nozzle. The injection pressure increases (Figure 10.25-c, d), as the Reynolds number, and so the first instabilities in the flow appear.

At 0.9 ms the jet is turbulent (Figure 10.25-e) and furthermore, the injection pressure is such that under-expanded structures grow in the near nozzle-field where oblique shocks are recognizable, as illustrated in the (Figure 15-f)

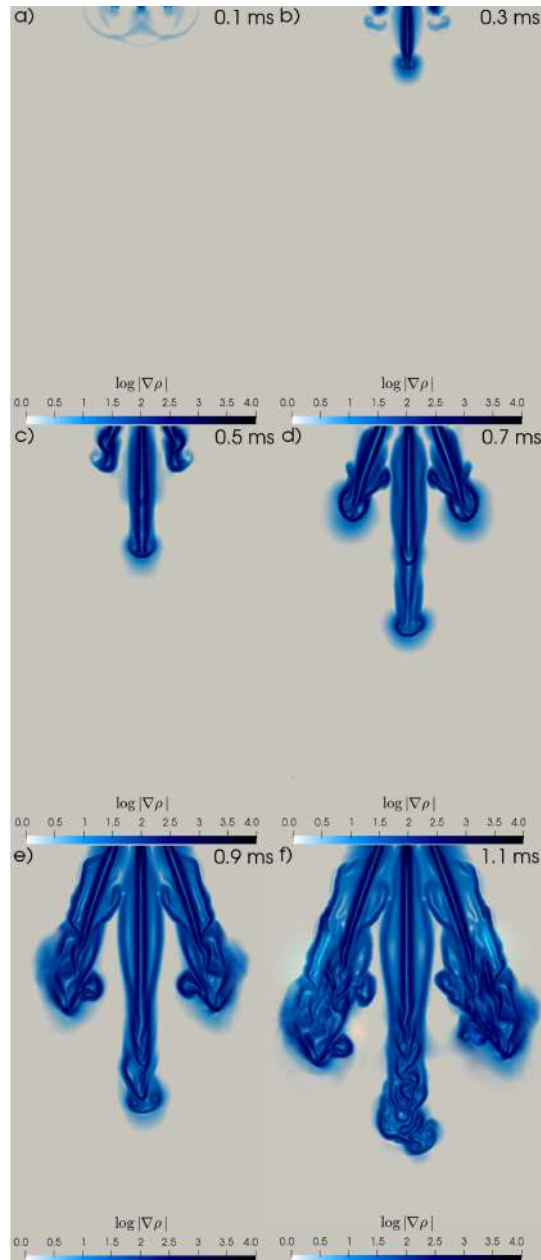


FIGURE 10.25: Temporal evolution of the spray represented with logarithm of density gradient.

and, with more details, in the Figure 10.26. The latter shows a zoomed picture of near-nozzle zone, at the end of the injection when the under-expanded structures are much more evident.

Figure 10.27 shows the Mach number as function of the vertical distance from the outflow section of the injector's central nozzle. Four time-instants were reported as parameter. Initially, at 0.5 ms, sonic conditions were already reached, but small oscillations are present. As the injection goes on, injection pressure increases and so the oscillations grow reaching, at  $t = 1.1$  ms, an amplitude of about the unity. These oscillations are linked with the

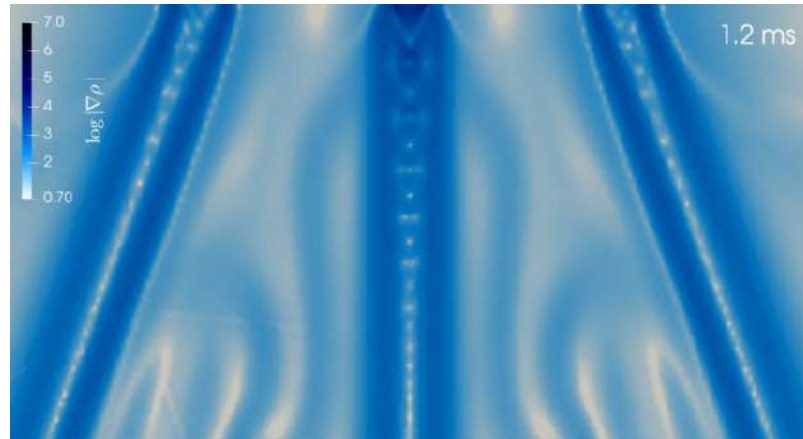


FIGURE 10.26: Zoomed view of the near-nozzle zone where, at the end of the injection; under-expanded structures compares.

presence of shock cells. Indeed, upstream each shock, the Mach number increases while, after, downstream the shock, decreases preserving the sonic conditions as we expected from the theory. Moving downwards (increasing  $z$ ), and so leaving the near nozzle zone, the shock cells disappear (Figure 10.27) and consequently the oscillations fade away.

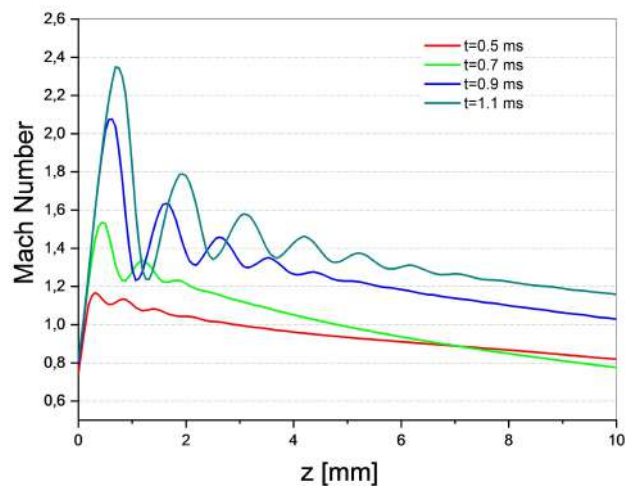


FIGURE 10.27: Mach number as function of axial distance from the central nozzle outflow section.

A quantitative estimation of the mixture quality has a relevant importance, especially with regards to the combustion process. Therefore, an already established statistical approach was applied to this case study [378, 380]. The probability density function (PDF) of mass weighted methane fraction was computed within the spray volume ( $\rho_i V_i Y_{CH_4,i}$ ) delimited using a threshold value for the mass fraction of  $Y_{CH_4,i} > 0.001$ . The probability

density function allows to obtain the distribution of instantaneous fuel concentration in each cell, thus providing numerical information about global air/gas mixture. Figure 10.28 shows the PDF computed at four different injection time intervals. After a short time, like 0.5 ms, the methane is confined in the jets cores and it is almost completely unmixed, the mixing process has not still begun, the relative red curve presents a peak around a methane mass fraction equal to the unity. This peak location gives an idea of how much methane/air was entrained [378] and, at this time step, the location corresponds to a high mass fraction value demonstrating that the entrainment is low. The injection goes on and the methane plumes grow. At 0.7 ms, the statistical distribution has a peak with a greater height. The peak height is related to the mixing between the jet and the entrained volume. A higher and narrower peak means that both the entrainment and the mixing are better [378]. Then, together with the spray volumetric growth, turbulence induced mixing effects break-up the methane rich central-core of the jet and, at 0.9 ms, the distribution has a flatter shape. The last time step is at 1.1 ms when the spray has almost reached the vessel bottom side. Mixing effects have developed and the PDF's behaviour now shows that is easier to find cells with a concentration of methane in flammable conditions. Indeed, a new peak is collocated within the two grey vertical lines. They delimit the flammable zone defined by a methane mass fraction between 0.044 and 0.15.

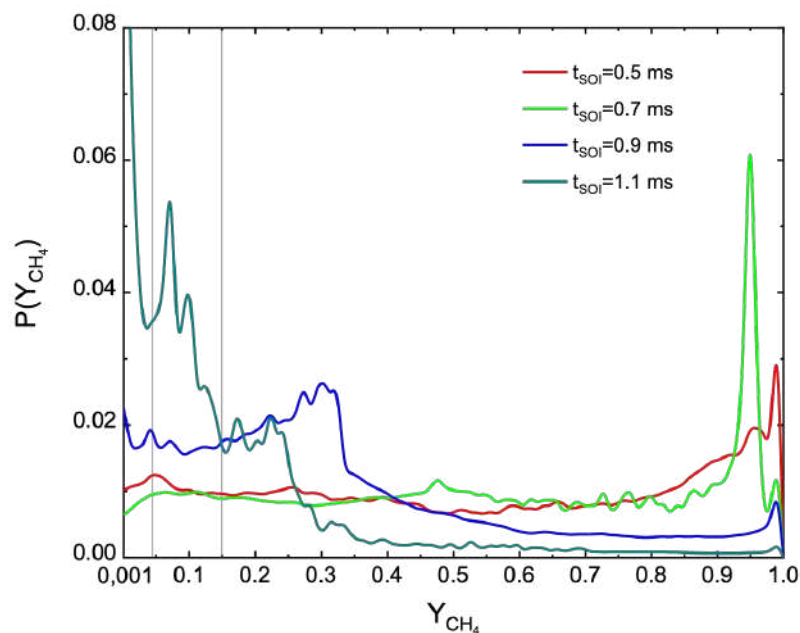


FIGURE 10.28: Probability distribution of fuel mass fraction  $Y_{CH_4,i}$  computed at four different time steps.

The integral of the PDF function between these two values represent the probability of finding methane in flammability conditions within the injection environment. Histogram of Figure 10.29 is a quick representation of such integral's results. By the end of the simulated interval about the 34% of the injected methane is in flammable condition. This value can be read as

a quantitative measurement of the injector performance in terms of mixture formation and can be exploited to make comparison with different injector configurations and operating conditions.

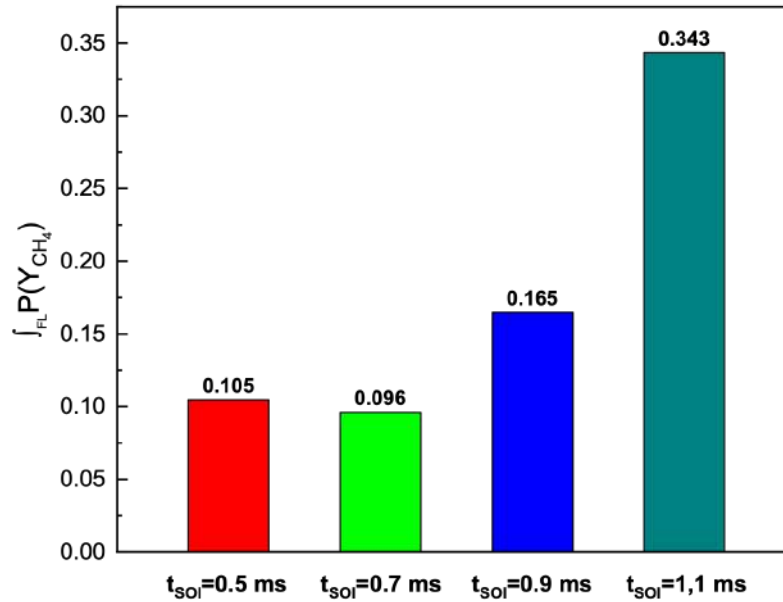


FIGURE 10.29: Probability distribution of fuel mass fraction  $Y_{CH_4,i}$  computed ad four different time steps.

## Chapter 11

# Conclusions

This chapter summarises the major findings of the studies conducted in the present thesis providing also recommendations for future work.

### 11.1 Summary

The present thesis deals about the characterization of fuel sprays in direct injection engines. Lately, this technique, broadly used in compression ignition engines, is being considered also for application in spark ignition engines because vehicles manufacturers have to meet with the latest normative about GHG and pollutant emissions.

Further than pollutant emissions reduction, other improvements are so achievable with this technology. Surely it must be mentioned engine down-sizing, thermal efficiency increasing but at the same time, some issues have to be solved. The principal one regards the short time and space available for mixture formation, indeed, placing the injector directly in the combustion chamber the spray formation process must be controlled deeply and the turbulence action exploited in order to obtain the desired mixing activity. For this reason great scientific interest is gaining around these problems aiming to find valid solutions.

The methodology broadly adopted involves performing experimental campaigns for tune and validate numerical codes for CFD simulations that allow to investigate further aspects otherwise impossible to observe and quantitatively estimate. A review of the current imaging techniques adopted for spray characterization is presented underlying also the physical principles behind such optical techniques. Then, the theoretic basics of a CFD code are detailed and the principals features of mono-phase and multi-phase simulation discussed.

The work is subdivided into two main areas of interest: liquid gasoline injection in gasoline direct injection (GDI) engines and direct injection of gaseous fuels and, in particular, methane. Following sections report the main finding of each area.

### 11.2 Liquid Fuel Injection in GDI Engines

The study of Gasoline direct-injection systems (GDI) begins from a broad literature review which highlights the importance of such technology in the

field of internal combustion engines developments. In the scenario of GDI engines research spray formation has a key-role. The attention was focussed on the Spray G injector, part of the ECN community.

Initially, a numerical reconstruction of such high-pressure spray was developed thanks to a CONVERGE CFD software. The model was validated against experimental data for standard injection conditions. Fitting between experimental and numerical is good and the computed spray shape is close to the real one. The simulation features an Eulerian-Lagrangian approach with Kelvin-Helmholtz breakup model and RANS turbulence framework. The numerical model allows obtaining further information concerning the spray behaviour and clarifying correlation with the injection parameters.

The study continues investigating injection in presence of flash boiling. Flash boiling is the sudden phase change of a fluid from liquid phase to the vapour one and it occurs operating at high temperature levels of the injected fuel and low back pressure values. It consists on the formation of vapour bubbles in the liquid fuel flow and their consequent explosion which results in sudden evaporation and catastrophic disintegration of the liquid jet, due to the occurrence of sub-saturation pressure conditions. Flash-boiling may have a significant influence in GDI engines because it can reduce the penetration length, change the spray pattern, promote the so called vapour lock within the nozzle and it involves also the spray's collapsing which is an undesired effect. If controlled, this process can be used to enhance the spray formation and the air/fuel mixing. For these reasons, a new breakup model was developed in the OpenFOAM environment **fbBreakup** and embedded in the **sprayFoam** Eulerian-Lagrangian solver. It aims to capture the droplet shattering mechanism present in the flash-boiling of fuel sprays using linear stability analysis, bubble growth and conservation laws. A radial velocity component was added to the child parcel in order to account for the spray expansion after breakup in the near-nozzle zone. Secondary breakup was then simulated using the classical Reitz-Diwakar model. This new methodology was used to simulate the ECN Spray G injector in various flash-boiling conditions. A qualitative and quantitative validation of this modelling approach was performed, relying on experimental data collected using schlieren and Mie scattering imaging techniques. The main findings are:

- The model is capable of reproducing correctly the spray liquid and vapour penetrations for different environmental conditions and injection pressures.
- Numerical uncertainty estimation, performed based on the classical procedure, ensures convergence of the solution with further grid refinement.
- The spray morphology is well reconstructed. Spray expansions, caused by flash boiling occurring in the near-nozzle zone, were reproduced thanks to the addition of the radial velocity component.
- Spray collapse, occurring only in strong flash-boiling conditions, was captured too. The reason for such spray behaviour is the formation of

an extensive low pressure zone right downstream from the injector tip in the axial direction and inside the plume rose.

- Comparison of the numerical results of  $SMD_{32}$  with experimental data acquired by [104] using the PIV technique highlights that the implemented breakup mechanism correctly estimates the diameter dimensions, but, in the meantime, great sensitivity was found with respect to the droplet's injection diameter distribution.
- The flash-boiling breakup model predicts the breakage of droplets in the near-nozzle zone where an important reduction of the parcels' diameter is present.
- The results of the evolution of the liquid film thickness within the bubble–droplet system are very similar for the different analysed conditions, while flash-boiling droplet explosion occurs faster in the presence of a lower ambient density.

Future developments of this numerical approach should consider the implementation of a specific injection model accounting for cavitation and flash boiling occurring within the injector's nozzles. This is required in order to correctly initialise the parcels' diameter.

### 11.3 Gaseous Injection Processes in Direct Injection Engines

The second area of interest regards the CNG direct injection in combustion chamber. CNG is commonly recognized as an attractive fuel for both spark-ignition (SI) and compression-ignition (CI) engines. CNG has a higher-octane number and hydrogen/carbon ratio, can be produced in renewable ways and is more widespread and cheaper than liquid fossil fuels. Lately, the interest around such gaseous fuel is growing and many design configurations have developed. In all the cases these processes involve the presence of super-sonic jets in order to inject the required mass flow. The physics of under-expanded jets as the formation of normal (Mach-discs) and oblique de-attached shock waves are discussed detailing the features. The study continues characterizing the jets issued from two different injection devices.

The first case regards a single-hole commercial injector which was experimentally and numerically investigated. The experimental study was carried out by injecting methane into a constant-volume vessel under different injection pressures and different chamber counter-pressures and temperatures. The images acquired allow to evaluate jet tip penetration, Mach disk position and spray cone-angle. Then, a CFD model of the injection process for different operating conditions was developed in order to investigate air/fuel mixing process. Such model allows a broader understanding of the jet's characteristic and, especially, provides further information not available experimentally. The simulations were performed with CONVERGE CFD software suite.

The second part of the investigations of the under-expanded jets deals with the development of a density-based OpenFOAM solver featuring Runge-kutta 4th order time discretization and central flux splitting scheme of Kurganov and Tadmor. Such numerical approach is an alternative to the classical pressure-based algorithms (used in this work for the first case study) and is regarded as being more accurate on flow field discontinues description such shock waves and Mach discs. The code was validated with a common test case and then used for simulating the injection process of an innovative high pressure, multi-hole device for direct injection of gaseous fuels. Alongside with the numerical activities the injector was studied also experimentally recording the injection process in a constant volume chamber using different injection pressures and environmental conditions. The images were recorded with the schlieren technique and a proper image post-processing performed.

The main findings of the investigations are summarized as follow:

- at sufficiently high-pressure ratios, the jet has a transient nature and involves three flow patterns: subsonic, moderately under-expanded, with its characteristic shock cells structure, and highly under-expanded with Mach disk formation and typical “barrel shock” configuration. The same flow patterns were captured by developing a LES numerical model;
- generally the jet penetration has a two-stage development: in a first phase it has a relatively high speed then, after a knee, decelerates and the curves of the jet speed tend to flatten. This is strictly related to the braking effect of the gas in the chamber.
- higher injection pressures correspond to an increase in jet tip penetration and to an increment of maximum Mach disk height;
- changing in injection pressure does not seem to affect the jet cone angle;
- higher chamber pressures correspond to a decrease of jet tip penetration and to an increase of jet cone angle;
- the variation chamber of the temperature does not seem to significantly affect axial penetration;
- the PISO algorithm is capable to reproduce under-expanded jets features however the best numerical approach involves the adoption of a density-based solution method of the governing equations;
- the flow within the ducts of an injectors is pretty complex, involves numerous discontinues in the flow field and shock-waves. Theoretically it can be described with the Fanno theory
- the spray development in the injection environment is strongly influenced by the air entrainment especially in the latest phase of the injection

- the turbulence must be selected with great attention. For future developments, an improved turbulence model will have to be used.
- the air-fuel mixing quality can be quantified through a statistical approach. A probability density function describes how the methane interacts with air and the characteristics of the mixture obtained.
- 2-D maps of methane mass fraction highlight the presence of zones composed almost uniquely by methane (potential core) surrounded at both side by nitrogen mixed layers. Downstream the potential core, methane fraction assumes lower values. It can be conclude that higher NPR imply better mixing;

These results can be exploited to deepen the knowledge of under-expanded jets evolution in engines fuelled by direct injection of the gas and, therefore, to optimize of the mixture formation process. Future studies could involves tests of the developed model against other experimental datasets.



# Bibliography

- [1] Martin Abart et al. "Basic investigations on the prediction of spray-wall and spray-fluid interaction for a GDI combustion process". In: *SETC Small Engine Technology Conference*. 2010.
- [2] R Acharya. "Interaction of waves with medium". In: *Satellite signal propagation, impairments and mitigation*. Academic Press, 2017, pp. 57–86.
- [3] Krishna S Addepalli and J M Mallikarjuna. "Effect of Engine Parameters on Mixture Stratification in a Wall-Guided GDI Engine - A Quantitative CFD Analysis". In: *SAE International Journal of Commercial Vehicles* 10.2 (2017), pp. 2017–01–0570. ISSN: 1946-3928. DOI: 10.4271/2017-01-0570. URL: <http://papers.sae.org/2017-01-0570/>.
- [4] S. Krishna Addepalli and J. M. Mallikarjuna. "Parametric analysis of a 4-stroke GDI engine using CFD". In: *Alexandria Engineering Journal* 57.1 (2018), pp. 121–130. ISSN: 11100168. DOI: 10.1016/j.aej.2016.10.007. URL: <https://doi.org/10.1016/j.aej.2016.10.007>.
- [5] S.K. Addepalli, O.P. Saw, and J.M. Mallikarjuna. "Effect of Mixture Distribution on Combustion and Emission Characteristics in a GDI Engine - A CFD Analysis". In: *SAE Technical Papers 2017-Septe* (2017). ISSN: 01487191. DOI: 10.4271/2017-24-0036.
- [6] Suresh K Aggarwal. "Modeling of a dilute vaporizing multicomponent fuel spray". In: *International journal of heat and mass transfer* 30.9 (1987), pp. 1949–1961.
- [7] Koichiro Aikawa, Takayuki Sakurai, and Jeff J. Jetter. "Development of a Predictive Model for Gasoline Vehicle Particulate Matter Emissions". In: (2010). ISSN: 1946-3952. DOI: <https://doi.org/10.4271/2010-01-2115>. URL: <https://doi.org/10.4271/2010-01-2115>.
- [8] H-E Albrecht et al. *Laser Doppler and phase Doppler measurement techniques*. Springer Science & Business Media, 2013.
- [9] P. G. Aleiferis and Z. R. Van Romunde. "An analysis of spray development with iso-octane, n-pentane, gasoline, ethanol and n-butanol from a multi-hole injector under hot fuel conditions". In: *Fuel* (2013). ISSN: 00162361. DOI: 10.1016/j.fuel.2012.07.044.
- [10] Tariq Alghamdi, Sigurdur T Thoroddsen, and JF Hernández-Sánchez. "Ultra-high speed visualization of a flash-boiling jet in a low-pressure environment". In: *International Journal of Multiphase Flow* 110 (2019), pp. 238–255.

- [11] Robert Francis Allen. "The role of surface tension in splashing". In: *Journal of colloid and interface science* 51 (1975), pp. 350–351.
- [12] L Allocca and A Montanaro. *Characterization of RME, RME Aged and Mineral Diesel Fuel Injected by a Common Rail Apparatus for EURO5 Diesel Engines*. Tech. rep. SAE Technical Paper, 2011.
- [13] L. Allocca et al. "Schlieren visualization of a GDI spray impacting on a heated wall: Non-vaporizing and vaporizing evolutions". In: *Energy* 108 (2016), pp. 93–98. ISSN: 03605442. DOI: 10.1016/j.energy.2015.09.107. URL: <http://dx.doi.org/10.1016/j.energy.2015.09.107>.
- [14] Luigi Allocca, Alessandro Montanaro, and Giovanni Meccariello. *Effects of the Ambient Conditions on the Spray Structure and Evaporation of the ECN Spray G*. Tech. rep. SAE Technical Paper, 2019.
- [15] Luigi Allocca et al. *ECN Spray G Injector: Assessment of Numerical Modeling Accuracy*. Tech. rep. SAE Technical Paper, 2018.
- [16] Di Angelo Luca Allocca Luigi De Vita Angelo. "Visualization and Characterization of CR Diesel Spray Wall-Impingement". In: *the 10th International Symposium on Flow Visualization* (2002).
- [17] John David Anderson Jr. *Fundamentals of aerodynamics*. Tata McGraw-Hill Education, 2010.
- [18] J Anez et al. "Eulerian–Lagrangian spray atomization model coupled with interface capturing method for diesel injectors". In: *International Journal of Multiphase Flow* 113 (2019), pp. 325–342.
- [19] Allen A. Aradi et al. *Direct Injection Gasoline (DIG) Injector Deposit Control with Additives*. Tech. rep. 2003. DOI: <https://doi.org/10.4271/2003-01-2024>. URL: <https://doi.org/10.4271/2003-01-2024>.
- [20] David C. Arters and Malcolm J. Macduff. *The Effect on Vehicle Performance of Injector Deposits in a Direct Injection Gasoline Engine*. Tech. rep. 2000. DOI: <https://doi.org/10.4271/2000-01-2021>. URL: <https://doi.org/10.4271/2000-01-2021>.
- [21] Abbas Zarenejad Ashkezari et al. "Investigation of Different of Spray-Wall Impingement on Performance and Emissions in DI Diesel Engines". In: *International Journal of Engineering Innovations and Research* 3.4 (2014), p. 567.
- [22] Angus Atkinson et al. "Krill (*Euphausia superba*) distribution contracts southward during rapid regional warming". In: *Nature Climate Change* 9.2 (2019), pp. 142–147.
- [23] Great Barrier Reef Marine Park Authority. *2016 coral bleaching event on the Great Barrier Reef*. Great Barrier Reef Marine Park Authority, 2017.
- [24] AVL FIRE. <https://www.avl.com/it/fire>. (accessed June 25, 2019).
- [25] Tawfik Badawy et al. "Investigation of injector coking effects on spray characteristic and engine performance in gasoline direct injection engines". In: *Applied Energy* 220. February (2018), pp. 375–394. ISSN: 03062619. DOI: 10.1016/j.apenergy.2018.03.133.

- [26] R. Bahreini et al. "Characterizing emissions and optical properties of particulate matter from PFI and GDI light-duty gasoline vehicles". In: *Journal of Aerosol Science* 90 (2015), pp. 144–153. ISSN: 18791964. DOI: 10.1016/j.jaerosci.2015.08.011. URL: <https://www.sciencedirect.com/science/article/pii/S0021850215001433>.
- [27] Chengxin Bai and A. D. Gosman. "Development of Methodology for Spray Impingement Simulation". In: *SAE Transactions* 104 (1995), pp. 550–568. ISSN: 0096736X, 25771531. URL: <http://www.jstor.org/stable/44633238>.
- [28] Chengxin Bai and AD Gosman. "Development of methodology for spray impingement simulation". In: *SAE transactions* (1995), pp. 550–568.
- [29] CX Bai, H Rusche, and AD Gosman. "Modeling of gasoline spray impingement". In: *Atomization and Sprays* 12.1-3 (2002).
- [30] Benjamin Balewski, Barbara Heine, and Cameron Tropea. "Experimental investigation of the correlation between nozzle flow and spray using laser doppler velocimeter, phase doppler system, high-speed photography, and X-ray radiography". In: *Atomization and Sprays* 20.1 (2010).
- [31] Raja Banerjee and Santhosh Kumar. "Numerical investigation of stratified air/fuel preparation in a GDI engine". In: *Applied Thermal Engineering* 104 (2016), pp. 414–428.
- [32] M. Banholzer et al. "Numerical investigation of the flow characteristics of underexpanded methane jets". In: *Physics of Fluids* 31.5 (2019), p. 056105. ISSN: 10897666. DOI: 10.1063/1.5092776. URL: <http://aip.scitation.org/doi/10.1063/1.5092776>.
- [33] Ewa A. Bardasz et al. "A Comparison of Gasoline Direct Injection and Port Fuel Injection Vehicles: Part II - Lubricant Oil Performance and Engine Wear". In: *International Fuels and Lubricants Meeting and Exposition*. SAE International, 1999. DOI: <https://doi.org/10.4271/1999-01-1499>.
- [34] Michele Bardi, Angela Di Lella, and Gilles Bruneaux. "A novel approach for quantitative measurements of preferential evaporation of fuel by means of two-tracer laser induced fluorescence". In: *Fuel* 239 (2019), pp. 521–533.
- [35] Michele Bardi, Guillaume Pilla, and Xavier Gautrot. "Experimental assessment of the sources of regulated and unregulated nanoparticles in gasoline direct-injection engines". In: *International Journal of Engine Research* 20.1 (2019), pp. 128–140. DOI: 10.1177/1468087418817448.
- [36] Eduardo J. Barrientos et al. "Particulate matter indices using fuel smoke point for vehicle emissions with gasoline, ethanol blends, and butanol blends". In: *Combustion and Flame* 167 (2016), pp. 308–319. ISSN: 15562921. DOI: 10.1016/j.combustflame.2016.01.034. URL: <https://www.sciencedirect.com/science/article/pii/S0010218016000493>.

- [37] Eduardo J. Barrientos et al. "Particulate matter indices using fuel smoke point for vehicle emissions with gasoline, ethanol blends, and butanol blends". In: *Combustion and Flame* 167 (2016), pp. 308–319. ISSN: 15562921. DOI: 10.1016/j.combustflame.2016.01.034. URL: <https://www.sciencedirect.com/science/article/pii/S0010218016000493>.
- [38] Lorenzo Bartolucci et al. *CFD and X-Ray Analysis of Gaseous Direct Injection from an Outward Opening Injector*. Tech. rep. 2016. DOI: <https://doi.org/10.4271/2016-01-0850>.
- [39] C. Baumgarten. *Mixture Formation in Internal Combustion Engines*. Heat and Mass Transfer. Springer Berlin Heidelberg, 2006. ISBN: 9783540308362. URL: <https://books.google.it/books?id=ix8WRsXA-kEC>.
- [40] C Baumgarten, J Stegemann, and G Merker. "A new model for cavitation induced primary break-up of diesel sprays". In: *Zaragoza* 9.11 (2002).
- [41] N. J. Beavis, S. S. Ibrahim, and W. Malalasekera. "Numerical Evaluation of Combustion Regimes in a GDI Engine". In: *Flow, Turbulence and Combustion* 101.4 (2018), pp. 1035–1057. ISSN: 15731987. DOI: 10.1007/s10494-018-9949-8. URL: <http://dx.doi.org/10.1007/s10494-018-9949-8>.
- [42] B Befrui et al. "LES simulation of the internal flow and near-field spray structure of an outward-opening GDI injector and comparison with imaging data". In: *SAE Technical Paper Series* 2008.724 (2008). DOI: 10.4271/2008-01-0137. URL: <http://fr.delphi.com/pdf/techpapers/2008-01-0137.pdf>{\%}5Cnpapers2://publication/uuid/0E3219AB-6F47-44BA-88EF-4405F48527B5.
- [43] Bizhan Befrui and Mario D Onofrio. "Primary Atomization of a GDI Multi-Hole Plume Using VOF-LES Method". In: *SAE Technical Paper* 2014-01-1125 (2014). DOI: 10.4271/2014-01-1125.
- [44] Bizhan Befrui et al. "GDI Multi-Hole Injector Internal Flow and Spray Analysis". In: *SAE 2011 World Congress and Exhibition*. SAE International, 2011. DOI: <https://doi.org/10.4271/2011-01-1211>. URL: <https://doi.org/10.4271/2011-01-1211>.
- [45] Bizhan Befrui et al. "Large Eddy Simulation of GDI Single-Hole Flow and Near-Field Spray". In: *SAE International Journal of Fuels and Lubricants* 5.2 (2012), pp. 2012–01–0392. ISSN: 1946-3960. DOI: 10.4271/2012-01-0392. URL: <http://papers.sae.org/2012-01-0392/>.
- [46] Bharat Bhatia and Ashoke De. *Flash Boiling in Sprays: Recent Developments and Modeling*. 2019. DOI: 10.1007/s41745-019-0104-x.
- [47] Stefan Bickert, Achim Kampker, and Dennis Greger. "Developments of CO<sub>2</sub>-emissions and costs for small electric and combustion engine vehicles in Germany". In: *Transportation Research Part D: Transport and Environment* 36 (2015), pp. 138–151.

- [48] M. Bogarra et al. "Impact of exhaust gas fuel reforming and exhaust gas recirculation on particulate matter morphology in Gasoline Direct Injection Engine". In: *Journal of Aerosol Science* 103 (2017), pp. 1–14. ISSN: 18791964. DOI: 10.1016/j.jaerosci.2016.10.001. URL: <https://www.sciencedirect.com/science/article/pii/S0021850216300659>.
- [49] Giovanni Bonandrini et al. "Numerical Study on Multiple Injection Strategies in DISI Engines for Particulate Emission Control". In: (2012). DOI: 10.4271/2012-01-0400. URL: <http://papers.sae.org/2012-01-0400/>.
- [50] Fabrizio Bonatesta et al. "Application of Computational Fluid Dynamics to Explore the Sources of Soot Formation in a Gasoline Direct Injection Engine". In: (2014). ISSN: 0148-7191. DOI: <https://doi.org/10.4271/2014-01-2569>. URL: <https://doi.org/10.4271/2014-01-2569>.
- [51] W. P. Boone et al. *Effect of MMT® Fuel Additive on Emission System Components: Detailed Parts Analysis from Clear-and MMT®-Fueled Escort Vehicles from the Alliance Study*. Tech. rep. 2005. DOI: <https://doi.org/10.4271/2005-01-1108>. URL: <https://doi.org/10.4271/2005-01-1108>.
- [52] Fabio Bozza, Vincenzo De Bellis, and Luigi Teodosio. *A Tabulated-Chemistry Approach Applied to a Quasi-Dimensional Combustion Model for a Fast and Accurate Knock Prediction in Spark-Ignition Engines*. Tech. rep. 2019. DOI: <https://doi.org/10.4271/2019-01-0471>. URL: <https://doi.org/10.4271/2019-01-0471>.
- [53] Andreas Braeuer. *In situ spectroscopic techniques at high pressure*. Elsevier, 2015.
- [54] Sebastiano Breda et al. "CFD Analysis of Combustion and Knock in an Optically Accessible GDI Engine". In: (2016). ISSN: 1946-3936. DOI: <https://doi.org/10.4271/2016-01-0601>. URL: <https://doi.org/10.4271/2016-01-0601>.
- [55] Francesco Catapano et al. *An experimental and numerical investigation of GDI spray impact over walls at different temperatures*. Tech. rep. SAE Technical Paper, 2016.
- [56] Francesco Catapano et al. *Characterization of Ethanol Blends Combustion Processes and Soot Formation in a GDI Optical Engine*. Tech. rep. 2013. DOI: <https://doi.org/10.4271/2013-01-1316>. URL: <https://doi.org/10.4271/2013-01-1316>.
- [57] Mustafa Bahattin Çelik and Bulent Ozdalyan. "Gasoline direct injection". In: *Fuel Injection*. IntechOpen, 2010.
- [58] Tak W. Chan et al. "Evaluation of a Gasoline Particulate Filter to Reduce Particle Emissions from a Gasoline Direct Injection Vehicle". In: (2012). ISSN: 1946-3952. DOI: <https://doi.org/10.4271/2012-01-1727>.

- [59] M Chase. *NIST-JANAF Thermochemical Tables, 4th Edition*. 1998. DOI: citeulike-article-id:12140840. arXiv: arXiv:1011.1669v3. URL: [http://www.aip.org/pubs/books/jpcrd{\\\_}books.html](http://www.aip.org/pubs/books/jpcrd{\_}books.html).
- [60] Ceyuan Chen et al. *LES Analysis on Cycle-to-Cycle Variation of Combustion Process in a DISI Engine*. Tech. rep. 2019. DOI: <https://doi.org/10.4271/2019-01-0006>. URL: <https://doi.org/10.4271/2019-01-0006>.
- [61] Hao Chen, Jingjing He, and Xianglin Zhong. "Engine combustion and emission fuelled with natural gas: A review". In: *Journal of the Energy Institute* 92.4 (2019), pp. 1123–1136.
- [62] Hao Chen, Peter M. Lillo, and Volker Sick. "Three-dimensional spray-flow interaction in a spark-ignition direct-injection engine". In: *International Journal of Engine Research* 17.1 (2016), pp. 129–138. ISSN: 20413149. DOI: 10.1177/1468087415608741.
- [63] Hao Chen and Volker Sick. "Three-dimensional three-component air flow visualization in a steady-state engine flow bench using a plenoptic camera". In: *SAE International Journal of Engines* 10.2017-01-0614 (2017), pp. 625–635.
- [64] Longfei Chen et al. "Characterizing particulate matter emissions from GDI and PFI vehicles under transient and cold start conditions". In: *Fuel* 189 (2017), pp. 131–140. ISSN: 00162361. DOI: 10.1016/j.fuel.2016.10.055. URL: <http://dx.doi.org/10.1016/j.fuel.2016.10.055>.
- [65] Longfei Chen et al. "Quantifying the effects of fuel compositions on GDI-derived particle emissions using the optimal mixture design of experiments". In: *Fuel* 154 (2015), pp. 252–260. ISSN: 00162361. DOI: 10.1016/j.fuel.2015.03.081. URL: <http://dx.doi.org/10.1016/j.fuel.2015.03.081>.
- [66] Longfei Chen et al. *The Influence of Ethanol Blends on Particulate Matter Emissions from Gasoline Direct Injection Engines*. Tech. rep. 2010. DOI: <https://doi.org/10.4271/2010-01-0793>. URL: <https://doi.org/10.4271/2010-01-0793>.
- [67] Marco Chiodi, Hans Jürgen Berner, and Michael Bargende. "Investigation on different injection strategies in a direct-injected turbocharged cng-engine". In: *SAE Technical Papers* (2006). ISSN: 2688-3627. DOI: 10.4271/2006-01-3000.
- [68] Iman Chitsaz et al. "Experimental and numerical investigation on the jet characteristics of spark ignition direct injection gaseous injector". In: *Applied energy* 105 (2013), pp. 8–16.
- [69] Aldo Coghe and GE Cossali. "Quantitative optical techniques for dense sprays investigation: A survey". In: *Optics and Lasers in Engineering* 50.1 (2012), pp. 46–56.

- [70] OpenFOAM Community. *OpenFOAM: User Guide v2006 The open source CFD toolbox*. 2020 (accessed July 22, 2020). URL: <https://www.openfoam.com/documentation/guides/latest/doc/index.html>.
- [71] GE Cossali, ALDO Coghe, and M Marengo. "The impact of a single drop on a wetted solid surface". In: *Experiments in fluids* 22.6 (1997), pp. 463–472.
- [72] M. Costa, U. Sorge, and L. Allocca. "CFD optimization for GDI spray model tuning and enhancement of engine performance". In: *Advances in Engineering Software* 49.1 (2012), pp. 43–53. ISSN: 09659978. DOI: 10.1016/j.advengsoft.2012.03.004. URL: <http://dx.doi.org/10.1016/j.advengsoft.2012.03.004>.
- [73] M. Costa, U. Sorge, and L. Allocca. "Numerical study of the mixture formation process in a four-stroke GDI engine for two-wheel applications". In: *Simulation Modelling Practice and Theory* 19.4 (2011), pp. 1212–1226. ISSN: 1569190X. DOI: 10.1016/j.simpat.2010.07.006. URL: <https://www.sciencedirect.com/science/article/pii/S1569190X10001590>{\#}f0015.
- [74] M. Costa et al. "Mixture preparation and combustion in a GDI engine under stoichiometric or lean charge: an experimental and numerical study on an optically accessible engine". In: *Applied Energy* 180 (2016), pp. 86–103. ISSN: 03062619. DOI: 10.1016/j.apenergy.2016.07.089. URL: <http://dx.doi.org/10.1016/j.apenergy.2016.07.089>.
- [75] M. Costa et al. "Split injection in a homogeneous stratified gasoline direct injection engine for high combustion efficiency and low pollutants emission". In: *Energy* 117 (2016), pp. 405–415. ISSN: 0360-5442. DOI: 10.1016/J.ENERGY.2016.03.065. URL: <https://www.sciencedirect.com/science/article/pii/S0360544216303097>.
- [76] M. Costa et al. "Study of mixture formation and early flame development in a research GDI (gasoline direct injection) engine through numerical simulation and UV-digital imaging". In: *Energy* 77 (2014), pp. 88–96. ISSN: 03605442. DOI: 10.1016/j.energy.2014.04.114. URL: <http://dx.doi.org/10.1016/j.energy.2014.04.114>.
- [77] Roger F. Cracknell et al. "Modelling a Gasoline Compression Ignition (GCI) Engine Concept". In: (2014). ISSN: 0148-7191. DOI: <https://doi.org/10.4271/2014-01-1305>. URL: <https://doi.org/10.4271/2014-01-1305>.
- [78] Marcia Creary. *Impacts of Climate Change on Coral Reefs and the Marine Environment*. 2020. URL: <https://www.un.org/en/chronicle/article/impacts-climate-change-coral-reefs-and-marine-environment> (visited on 11/23/2020).
- [79] Alessandro D'Adamo et al. "Development of a RANS-Based Knock Model to Infer the Knock Probability in a Research Spark-Ignition Engine". In: (2017). ISSN: 1946-3936. DOI: <https://doi.org/10.4271/2017-01-0551>. URL: <https://doi.org/10.4271/2017-01-0551>.

- [80] H Dageförde et al. "Requirements for spray and tip design of a multi-hole injector for DISI engines". In: *Proceedings of ICLASS, Tainan* (2015).
- [81] Michele D'Amico et al. "Measuring injectors fouling in internal combustion engines through imaging". In: 82 (2015), pp. 9–16. ISSN: 18766102. DOI: 10.1016/j.egypro.2015.11.873.
- [82] Andrew Davidhazy. "Introduction to shadowgraph and schlieren imaging". In: (2006).
- [83] Andrew Davidhazy. *Introduction to shadowgraph and schlieren imaging*" (2006). 2020. URL: <http://scholarworks.rit.edu/article/478> (visited on 11/23/2020).
- [84] A De Vita and L Di Angelo. "Spray Impingement Evolution of Low Pressure Gasoline Injector". In: *7th International Conference Florence ATA 2001*. 2001.
- [85] A De Vita and L Di Angelo. "Visualization and Characterization of CR Diesel Spray Wall-Impingement". In: *10th International Symposium on Flow Visualization*. 2002.
- [86] Angelo DE VITA, Luca DI ANGELO, and L Allocca. "Wall-impingement analysis of a spray from a common rail injection system for diesel engines". In: *THIESEL 2002 CONFERENCE ON THERMO-AND FLUID-DYNAMIC PROCESSES IN DIESEL ENGINES*. 2002, pp. 67–76.
- [87] Federico Demaria et al. "What is degrowth? From an activist slogan to a social movement". In: *Environmental Values* 22.2 (2013), pp. 191–215.
- [88] Jeremie Dernotte, John E. Dec, and Chunsheng Ji. "Investigation of the Sources of Combustion Noise in HCCI Engines". In: (2014). ISSN: 1946-3936. DOI: <https://doi.org/10.4271/2014-01-1272>. URL: <https://doi.org/10.4271/2014-01-1272>.
- [89] Jose M Desantes et al. "A comparison of diesel sprays CFD modeling approaches: DDM versus  $\Sigma$ -Y Eulerian atomization model". In: *Atomization and Sprays* 26.7 (2016).
- [90] Abhishek Y. Deshmukh et al. "Characterization of Hollow Cone Gas Jets in the Context of Direct Gas Injection in Internal Combustion Engines". In: (2018). ISSN: 1946-3952. DOI: <https://doi.org/10.4271/2018-01-0296>. URL: <https://doi.org/10.4271/2018-01-0296>.
- [91] Abhishek Y Deshmukh et al. "Simulation and Modeling of Direct Gas Injection through Poppet-type Outwardly-opening Injectors in Internal Combustion Engines". In: *Natural Gas Engines*. Springer, 2019, pp. 65–115.
- [92] AY Deshmukh et al. "LES of direct gas injection in internal combustion engines". In: *LES for Internal Combustion Engine Flows LES4ICE, France, Nov* (2016).
- [93] *Design and Working Principle of Simple Carburetor*. 2020. URL: <https://www.mecholic.com/2018/09/design-and-working-principle-of-carburetor.html> (visited on 11/23/2020).

- [94] Norman Dombrowski and PC Hooper. "The effect of ambient density on drop formation in sprays". In: *Chemical Engineering Science* 17.4 (1962), pp. 291–305.
- [95] Quan Dong et al. "The characteristic analysis of high-pressure gas jets for natural gas engine based on shock wave structure". In: *Energy Conversion and Management* 149 (2017), pp. 26–38.
- [96] M Drake. "Quantitative High Speed Imaging of Piston Fuel Films in Direct Injection Engines Using a Refractive-Index-Matching Technique". In: *15th Annual Conference on Liquid Atomization and Spray Systems, Madison, WI, May 2002*. 2002.
- [97] Michael C. Drake, Donald T. French, and Todd D. Fansler. "Advanced diagnostics for minimizing hydrocarbon emissions from a direct-injection gasoline engine". In: *Symposium (International) on Combustion* 26.2 (1996), pp. 2581–2587. ISSN: 00820784. DOI: 10.1016/S0082-0784(96)80091-9. URL: <https://www.sciencedirect.com/science/article/pii/S0082078496800919>.
- [98] *Driving into 2025: The Future of Electric Vehicles*. 2020. URL: <https://www.jpmorgan.com/insights/research/electric-vehicles> (visited on 11/23/2020).
- [99] Daniel Duke et al. "Recent developments in X-ray diagnostics for cavitation". In: *SAE International Journal of Fuels and Lubricants* 8.1 (2015), pp. 135–146.
- [100] Daniel J Duke et al. "Internal and near nozzle measurements of Engine Combustion Network "Spray G" gasoline direct injectors". In: *Experimental Thermal and Fluid Science* 88 (2017), pp. 608–621.
- [101] F. Duronio et al. "CFD Numerical Reconstruction of the Flash Boiling Gasoline Spray Morphology". In: *SAE Technical Papers 2020* (2020). ISSN: 01487191. DOI: 10.4271/2020-24-0010.
- [102] Francesco Duronio et al. "Gasoline direct injection engines – A review of latest technologies and trends. Part 1: Spray breakup process". In: *Fuel* 265 (2020), p. 116948. ISSN: 0016-2361. DOI: 10.1016/J.FUEL.2019.116948. URL: <https://www.sciencedirect.com/science/article/pii/S0016236119323415?dgcid=author>.
- [103] Wayne Eckerle et al. *Research Needs and Impacts in Predictive Simulation for Internal Combustion Engines (PreSICE)*. Tech. rep. USDOE Office of Science (SC)(United States), 2011.
- [104] *ECN - Engine Combustion Network*. 2020. URL: <https://ecn.sandia.gov/> (visited on 11/23/2020).
- [105] *Engine Combustion Network*. 2020. URL: <https://ecn.sandia.gov/gasoline-spray-combustion/computational-method/mesh-and-geometry/> (visited on 12/31/2020).
- [106] Iman Erfan et al. "Influence of chamber pressure on CNG jet characteristics of a multi-hole high pressure injector". In: *Fuel* 197 (2017), pp. 186–193. ISSN: 00162361. DOI: 10.1016/j.fuel.2017.02.018.

- [107] Iman Erfan et al. "Injection characteristics of gaseous jet injected by a single-hole nozzle direct injector". In: *Fuel* 160 (2015), pp. 24–34.
- [108] *European Environment Agency (EEA)*. 2020. URL: <https://www.eea.europa.eu/it> (visited on 11/23/2020).
- [109] Z Falgout and M Linne. "Cavitation inside high-pressure optically transparent fuel injector nozzles". In: vol. 656. 1. IOP Publishing. 2015, p. 012082.
- [110] L. Fan et al. "Modeling Fuel Preparation and Stratified Combustion in a Gasoline Direct Injection Engine". In: (1999). ISSN: 0148-7191. DOI: <https://doi.org/10.4271/1999-01-0175>. URL: <https://doi.org/10.4271/1999-01-0175>.
- [111] Li Fan and Rolf D. Reitz. "Development of an Ignition and Combustion Model for Spark-Ignition Engines". In: (2000). ISSN: 0148-7191. DOI: <https://doi.org/10.4271/2000-01-2809>. URL: <https://doi.org/10.4271/2000-01-2809>.
- [112] Alexandre Favre. "Turbulence: Space-time statistical properties and behavior in supersonic flows". In: *The Physics of fluids* 26.10 (1983), pp. 2851–2863.
- [113] *First WHO Global Conference on Air Pollution and Health, 30 October – 1 November 2018*. 2020. URL: <https://www.who.int/gho/phe/en/> (visited on 11/23/2020).
- [114] Stefano Fontanesi, Alessandro d'Adamo, and Christopher J Rutland. "Large-Eddy simulation analysis of spark configuration effect on cycle-to-cycle variability of combustion and knock". In: *International Journal of Engine Research* 16.3 (2015), pp. 403–418. DOI: 10.1177/1468087414566253.
- [115] Stefano Fontanesi, Stefano Paltrinieri, and Giuseppe Cantore. *LES Analysis of Cyclic Variability in a GDI Engine*. Tech. rep. 2014. DOI: <https://doi.org/10.4271/2014-01-1148>. URL: <https://doi.org/10.4271/2014-01-1148>.
- [116] Stefano Fontanesi et al. *LES Multi-cycle Analysis of a High Performance GDI Engine*. Tech. rep. 2013. DOI: <https://doi.org/10.4271/2013-01-1080>. URL: <https://doi.org/10.4271/2013-01-1080>.
- [117] Erwin Franquet et al. "Free underexpanded jets in a quiescent medium: A review". In: *Progress in Aerospace Sciences* 77 (2015), pp. 25–53.
- [118] Erwin Franquet et al. *Review on the underexpanded jets*. Sept. 2015. DOI: 10.13140/RG.2.1.2640.6883.
- [119] Michael Frenklach. "Reaction mechanism of soot formation in flames". In: *Physical chemistry chemical Physics* 4.11 (2002), pp. 2028–2037. DOI: 10.1039/B110045A.

- [120] Michael Frenklach and Hai Wang. "Detailed Mechanism and Modeling of Soot Particle Formation". In: *Soot Formation in Combustion: Mechanisms and Models*. Ed. by Henning Bockhorn. Berlin, Heidelberg: Springer Berlin Heidelberg, 1994, pp. 165–192. ISBN: 978-3-642-85167-4. DOI: 10.1007/978-3-642-85167-4\_10. URL: [https://doi.org/10.1007/978-3-642-85167-4\\_10](https://doi.org/10.1007/978-3-642-85167-4_10).
- [121] Thierry L Georjon and Rolf D Reitz. "A drop-shattering collision model for multidimensional spray computations". In: *Atomization and Sprays* 9.3 (1999).
- [122] F Giussani et al. "A 3-Phase Solver for the Simulation of Internal Nozzle Cavitating Flows in Fuel-Injectors using OpenFOAM". In: 2019, pp. 1–11.
- [123] Filippo Giussani et al. "Dynamic VOF modelling of the internal flow in GDI fuel injectors". In: *Energy Procedia* 101 (2016), pp. 574–581.
- [124] *Global greenhouse gas emissions by sector*. 2020. URL: <https://ourworldindata.org/emissions-by-sector> (visited on 11/23/2020).
- [125] Christopher J. Greenshields et al. "Implementation of semi-discrete, non-staggered central schemes in a colocated, polyhedral, finite volume framework, for high-speed viscous flows". In: *International Journal for Numerical Methods in Fluids* 63.1 (2010), pp. 1–21. ISSN: 02712091. DOI: 10.1002/flid.2069.
- [126] ESI Group et al. *OpenFOAM Documentation*. 2018.
- [127] Hengjie Guo et al. "Comparison of spray collapses at elevated ambient pressure and flash boiling conditions using multi-hole gasoline direct injector". In: *Fuel* (2017). ISSN: 00162361. DOI: 10.1016/j.fuel.2017.02.071.
- [128] Hengjie Guo et al. "Comparison of spray collapses at elevated ambient pressure and flash boiling conditions using multi-hole gasoline direct injector". In: *Fuel* 199 (2017), pp. 125–134.
- [129] Hengjie Guo et al. "Effect of flash boiling on microscopic and macroscopic spray characteristics in optical GDI engine". In: *Fuel* 190 (2017), pp. 79–89.
- [130] Hengjie Guo et al. "Radial expansion of flash boiling jet and its relationship with spray collapse in gasoline direct injection engine". In: *Applied Thermal Engineering* (2019). ISSN: 13594311. DOI: 10.1016/j.applthermaleng.2018.10.031.
- [131] AA Hairuddin, AP Wandel, and T Yusaf. "An introduction to a homogeneous charge compression ignition engine". In: *Journal of Mechanical Engineering and Sciences* 7 (2014), pp. 1042–1052. DOI: doi: 10.15282/jmes.7.2014.3.0101.

- [132] A. Hamzehloo and P. G. Aleiferis. "Gas dynamics and flow characteristics of highly turbulent under-expanded hydrogen and methane jets under various nozzle pressure ratios and ambient pressures". In: *International Journal of Hydrogen Energy* 41.15 (2016), pp. 6544–6566. ISSN: 03603199. DOI: 10.1016/j.ijhydene.2016.02.017. URL: <https://www.sciencedirect.com/science/article/pii/S0360319915316669>.
- [133] A. Hamzehloo and P.G. Aleiferis. "Numerical modelling of transient under-expanded jets under different ambient thermodynamic conditions with adaptive mesh refinement". In: *International Journal of Heat and Fluid Flow* 61 (2016), pp. 711–729. ISSN: 0142-727X. DOI: 10.1016/J.IJHEATFLUIDFLOW.2016.07.015. URL: <https://www.sciencedirect.com/science/article/pii/S0142727X16304143>.
- [134] Arash Hamzehloo and Pavlos G. Aleiferis. "LES and RANS modelling of under-expanded jets with application to gaseous fuel direct injection for advanced propulsion systems". In: *International Journal of Heat and Fluid Flow* 76 (2019), pp. 309–334. ISSN: 0142727X. DOI: 10.1016/j.ijheatfluidflow.2019.01.017. URL: <https://www.sciencedirect.com/science/article/pii/S0142727X18301668>.
- [135] Z Han, Z Xu, and N Trigui. "Spray/wall interaction models for multi-dimensional engine simulation". In: *International Journal of Engine Research* 1.1 (2000), pp. 127–146.
- [136] Jun Harada et al. "Development of direct injection gasoline engine". In: *SAE transactions* (1997), pp. 767–776.
- [137] Ballapu Harshavardhan and J. M. Mallikarjuna. "Effect of piston shape on in-cylinder flows and air-fuel interaction in a direct injection spark ignition engine - A CFD analysis". In: *Energy* 81 (2015), pp. 361–372. ISSN: 03605442. DOI: 10.1016/j.energy.2014.12.049. URL: <http://dx.doi.org/10.1016/j.energy.2014.12.049>.
- [138] Tomohiro Hayashi, Masayuki Suzuki, and Masato Ikemoto. "Effects of internal flow in a diesel nozzle on spray combustion". In: *International Journal of Engine Research* 14.6 (2013), pp. 646–654.
- [139] Xin He, Matthew A. Ratcliff, and Bradley T. Zigler. "Effects of gasoline direct injection engine operating parameters on particle number emissions". In: *Energy and Fuels* 26.4 (2012), pp. 2014–2027. ISSN: 08870624. DOI: 10.1021/ef201917p.
- [140] Sebastian Henkel et al. "Injector Fouling and Its Impact on Engine Emissions and Spray Characteristics in Gasoline Direct Injection Engines". In: *SAE International Journal of Fuels and Lubricants* 10.2 (2017), pp. 2017–01–0808. ISSN: 1946-3960. DOI: 10.4271/2017-01-0808. URL: <http://papers.sae.org/2017-01-0808/>.
- [141] W. Hergert and T. Wriedt. *The Mie Theory: Basics and Applications*. Springer Series in Optical Sciences. Springer Berlin Heidelberg, 2012. ISBN: 9783642287381. URL: <https://books.google.it/books?id=wya7BQAAQBAJ>.

- [142] Marcus Herrmann. "On simulating primary atomization using the refined level set grid method". In: *Atomization and Sprays* 21.4 (2011).
- [143] John B Heywood. *Internal combustion engine fundamentals*. McGraw-hill, 1988.
- [144] Hiro Hiroyasu and Masataka Arai. "Structures of fuel sprays in diesel engines". In: *SAE transactions* (1990), pp. 1050–1061.
- [145] Hiroyuki Hiroyasu. "Spray breakup mechanism from the hole-type nozzle and its applications". In: *Atomization and Sprays* 10.3-5 (2000).
- [146] David Holmgren. *Permaculture: Principles & pathways beyond sustainability*. Holmgren Design Services, 2002.
- [147] Shenghong Huang and Q. S. Li. "A new dynamic one-equation subgrid-scale model for large eddy simulations". In: *International Journal for Numerical Methods in Engineering* 81.7 (2010), pp. 835–865. DOI: 10.1002/nme.2715. eprint: <https://onlinelibrary.wiley.com/doi/pdf/10.1002/nme.2715>. URL: <https://onlinelibrary.wiley.com/doi/abs/10.1002/nme.2715>.
- [148] Kang Y Huh, Eunju Lee, and Jaye Koo. "Diesel spray atomization model considering nozzle exit turbulence conditions". In: *Atomization and Sprays* 8.4 (1998).
- [149] David L.S. Hung et al. *Gasoline Fuel Injector Spray Measurement and Characterization - A New SAE J2715 Recommended Practice*. 2008. DOI: <https://doi.org/10.4271/2008-01-1068>.
- [150] David L.S. Hung et al. "Gasoline Fuel Injector Spray Measurement and Characterization - A New SAE J2715 Recommended Practice". In: *SAE International Journal of Fuels and Lubricants* 1.1 (2008), pp. 534–548. DOI: <https://doi.org/10.4271/2008-01-1068>. URL: <https://doi.org/10.4271/2008-01-1068>.
- [151] David LS Hung et al. "Gasoline fuel injector spray measurement and characterization—a new SAE J2715 recommended practice". In: *SAE International Journal of Fuels and Lubricants* 1.1 (2009), pp. 534–548.
- [152] SS Hwang, Z Liu, and Rolf D Reitz. "Breakup mechanisms and drag coefficients of high-speed vaporizing liquid drops". In: *Atomization and Sprays* 6.3 (1996).
- [153] Salvatore Iaccarino et al. "Numerical Simulation and Flame Analysis of Combustion and Knock in a DISI Optically Accessible Research Engine". In: (2017). ISSN: 1946-3936. DOI: <https://doi.org/10.4271/2017-01-0555>. URL: <https://doi.org/10.4271/2017-01-0555>.
- [154] Mehmet Ilhan Ilhak et al. "Alternative Fuels for Internal Combustion Engines". In: *The Future of Internal Combustion Engines*. IntechOpen, 2019.
- [155] I. Illich. *Energy and Equity*. Ideas in progress. Harper & Row, 1974. ISBN: 9780060803278. URL: <https://books.google.it/books?id=ndG2AAAAIAAJ>.

- [156] William Imoehl et al. "A DOE Approach to Engine Deposit Testing used to Optimize the Design of a Gasoline Direct Injector Seat and Orifice". In: *SAE International Journal of Fuels and Lubricants* 5.3 (2012), pp. 1078–1095. ISSN: 1946-3960. DOI: <https://doi.org/10.4271/2012-01-1642>. URL: <https://doi.org/10.4271/2012-01-1642>.
- [157] Adrian Irimescu, Simona Merola, and Santiago Martinez. "Influence of Engine Speed and Injection Phasing on Lean Combustion for Different Dilution Rates in an Optically Accessible Wall-Guided Spark Ignition Engine". In: (2018). ISSN: 1946-3936. DOI: <https://doi.org/10.4271/2018-01-1421>. URL: <https://doi.org/10.4271/2018-01-1421>.
- [158] Lama M Itani et al. "Two-tracer LIF imaging of preferential evaporation of multi-component gasoline fuel sprays under engine conditions". In: *Proceedings of the Combustion Institute* 35.3 (2015), pp. 2915–2922.
- [159] R Jahn. "Ultrafeinstaub überwindet alle Grenzen". In: *Bilder Institut für Anatomie Universität Bern* (2006).
- [160] Hrvoje Jasak. "OpenFOAM: open source CFD in research and industry". In: *International Journal of Naval Architecture and Ocean Engineering* 1.2 (2009), pp. 89–94.
- [161] A Jeronimo and V Van Der Haegen. "Schlieren Technique–Lab Notes". In: *EUROAVIA Symposium–Mission to Mars–November–Von Karman Institute for Fluid Dynamics*. 2002.
- [162] Changzhao Jiang et al. "Effect of fuel injector deposit on spray characteristics, gaseous emissions and particulate matter in a gasoline direct injection engine". In: *Applied Energy* 203 (2017), pp. 390–402. ISSN: 03062619. DOI: 10.1016/j.apenergy.2017.06.020. URL: <http://dx.doi.org/10.1016/j.apenergy.2017.06.020>.
- [163] Changzhao Jiang et al. "Impact of gasoline direct injection fuel injector hole geometry on spray characteristics under flash boiling and ambient conditions". In: *Fuel* 241 (2019), pp. 71–82.
- [164] Qi Jiao and Rolf D. Reitz. "The Effect of Operating Parameters on Soot Emissions in GDI Engines". In: (2015). ISSN: 1946-3936. DOI: <https://doi.org/10.4271/2015-01-1071>. URL: <https://doi.org/10.4271/2015-01-1071>.
- [165] Daliang Jing et al. "Numerical Investigation on the Effect of Fuel Temperature on Spray Collapse and Mixture Formation Characteristics in GDI Engines". In: *SAE Technical Paper Series* 1 (2018), pp. 1–10. DOI: 10.4271/2018-01-0311.
- [166] Jubin Jose et al. "Effect of Fuel Injection Timing on the Mixture Preparation in a Small Gasoline Direct-Injection Engine". In: *SAE Technical Paper Series* 1 (2018). DOI: 10.4271/2018-32-0014.

- [167] Rakesh Kale and Raja Banerjee. "Experimental investigation on GDI spray behavior of isooctane and alcohols at elevated pressure and temperature conditions". In: *Fuel* 236 (2019), pp. 1–12.
- [168] Gautam Kalghatgi. "Knock onset, knock intensity, superknock and preignition in spark ignition engines". In: *International Journal of Engine Research* 19.1 (2018), pp. 7–20. DOI: 10.1177/1468087417736430. eprint: <https://doi.org/10.1177/1468087417736430>. URL: <https://doi.org/10.1177/1468087417736430>.
- [169] Gautam T Kalghatgi, Per Risberg, and Hans-Erik Ångström. *Partially pre-mixed auto-ignition of gasoline to attain low smoke and low NOx at high load in a compression ignition engine and comparison with a diesel fuel*. Tech. rep. SAE Technical paper, 2007.
- [170] Yashas Karaya, Srinivasa Krishna Addepalli, and J M Mallikarjuna. *Comparison of Conventional Intake Port and Swirl Intake Port on Mixture Formation in a GDI Engine - A CFD Analysis*. Tech. rep. 2019, pp. 1–13. DOI: 10.4271/2019-01-0010.
- [171] Yashas Karaya, Srinivasa Krishna Addepalli, and J M Mallikarjuna. "Effect of Fuel Injector Location and Nozzle-Hole Orientation on Mixture Formation in a GDI Engine: A CFD Analysis". In: (2018). ISSN: 0148-7191. DOI: <https://doi.org/10.4271/2018-01-0201>. URL: <https://doi.org/10.4271/2018-01-0201>.
- [172] Panu Karjalainen et al. "Exhaust particles of modern gasoline vehicles: A laboratory and an on-road study". In: *Atmospheric Environment* 97 (2014), pp. 262–270. ISSN: 18732844. DOI: 10.1016/j.atmosenv.2014.08.025. URL: <https://www.sciencedirect.com/science/article/pii/S1352231014006190>.
- [173] Ryuji Kawamoto et al. "Estimation of CO2 Emissions of internal combustion engine vehicle and battery electric vehicle using LCA". In: *Sustainability* 11.9 (2019), p. 2690.
- [174] Theo G Keith and James E John. *Gas Dynamics*. 2006.
- [175] Ian M Kennedy. "Models of soot formation and oxidation". In: *Progress in Energy and Combustion Science* 23.2 (1997), pp. 95–132. ISSN: 03601285. DOI: 10.1016/S0360-1285(97)00007-5. URL: <https://www.sciencedirect.com/science/article/pii/S0360128597000075>.
- [176] Imad A. Khalek, Thomas Bougher, and Jeff J. Jetter. "Particle Emissions from a 2009 Gasoline Direct Injection Engine Using Different Commercially Available Fuels". In: (2010). ISSN: 1946-3952. DOI: <https://doi.org/10.4271/2010-01-2117>. URL: <https://doi.org/10.4271/2010-01-2117>.
- [177] Muhammad Imran Khan, Tabassum Yasmin, and Abdul Shakoor. "Technical overview of compressed natural gas (CNG) as a transportation fuel". In: *Renewable and Sustainable Energy Reviews* 51 (2015), pp. 785–797.

- [178] Muhammad Mahabat Khan et al. "Experimental and numerical study of flash boiling in gasoline direct injection sprays". In: *Applied Thermal Engineering* 123 (2017), pp. 377–389.
- [179] Donghoon Kim, Stephen Sungsan Park, and Choongsik Bae. "Schlieren, Shadowgraph, Mie-scattering visualization of diesel and gasoline sprays in high pressure/high temperature chamber under GDCI engine low load condition". In: *International Journal of Automotive Technology* 19.1 (2018), pp. 1–8. ISSN: 1976-3832. DOI: 10.1007/s12239-018-0001-8. URL: <https://doi.org/10.1007/s12239-018-0001-8>.
- [180] Doohyun Kim, Angela Violi, and André Boehman. "The Effects of Injection Timing and Injected Fuel Mass on Local Charge Conditions and Emissions for Gasoline Direct Injection Engines". In: *ASME 2017 Internal Combustion Engine Division Fall Technical Conference*. American Society of Mechanical Engineers. 2017, V002T06A023–V002T06A023.
- [181] Kihyun Kim et al. "Spray and combustion characteristics of gasoline and diesel in a direct injection compression ignition engine". In: *Fuel* 109 (2013), pp. 616–626. ISSN: 0016-2361. DOI: <https://doi.org/10.1016/j.fuel.2013.02.060>. URL: <http://www.sciencedirect.com/science/article/pii/S0016236113001622>.
- [182] Taehoon Kim, Jingeun Song, and Sungwook Park. "Effects of turbulence enhancement on combustion process using a double injection strategy in direct-injection spark-ignition (DISI) gasoline engines". In: *International Journal of Heat and Fluid Flow* 56 (2015), pp. 124–136. ISSN: 0142727X. DOI: 10.1016/j.ijheatfluidflow.2015.07.013.
- [183] Taehoon Kim et al. "Numerical and experimental study on effects of fuel injection timings on combustion and emission characteristics of a direct-injection spark-ignition gasoline engine with a 50 MPa fuel injection system". In: *Applied Thermal Engineering* 144. June (2018), pp. 890–900. ISSN: 13594311. DOI: 10.1016/j.applthermaleng.2018.09.007. URL: <https://doi.org/10.1016/j.applthermaleng.2018.09.007>.
- [184] Yongha Kim et al. *Fuel Effect on Particle Emissions of a Direct Injection Engine*. Tech. rep. 2013. DOI: <https://doi.org/10.4271/2013-01-1559>. URL: <https://doi.org/10.4271/2013-01-1559>.
- [185] Janardhan Kodavasal et al. "CFD Simulation of Gasoline Compression Ignition". In: vol. Volume 2: Instrumentation, Controls, and Hybrids; Numerical Simulation; Engine Design and Mechanical Development; Keynote Papers. Internal Combustion Engine Division Fall Technical Conference. V002T06A008. Oct. 2014. DOI: 10.1115/ICEF2014-5591.
- [186] Keisuke Komada and Seoksu Moon. "Transient needle motion of an outwardly opening GDI injector and its effects on initial spray formation". In: *Fuel* 181 (2016), pp. 964–972. ISSN: 0016-2361. DOI: 10.1016/J.FUEL.2016.05.012. URL: <https://www.sciencedirect.com/science/article/pii/S0016236116303271>.

- [187] Sanghoon Kook et al. *Z-type Schlieren setup and its application to high-speed imaging of gasoline sprays*. Tech. rep. SAE Technical Paper, 2011.
- [188] B Murali Krishna and JM Mallikarjuna. "Effect of engine speed on in-cylinder tumble flows in a motored internal combustion engine—an experimental investigation using particle image velocimetry". In: *J. Appl. Fluid Mech* 4.1 (2011), pp. 1–14.
- [189] Zaira Aline Kuensch et al. *Experimental investigation on the gas jet behavior for a hollow cone piezoelectric injector*. Tech. rep. SAE Technical Paper, 2014.
- [190] Dominik Kuhnke. *Spray/wall interaction modelling by dimensionless data analysis*. Shaker, 2004.
- [191] Alexander Kurganov, Sebastian Noelle, and Guergana Petrova. "Semidiscrete Central-Upwind Schemes for Hyperbolic Conservation Laws and Hamilton–Jacobi Equations". In: *SIAM Journal on Scientific Computing* 23.3 (2001), pp. 707–740. DOI: 10.1137/S1064827500373413.
- [192] Alexander Kurganov and Eitan Tadmor. "New High-Resolution Central Schemes for Nonlinear Conservation Laws and Convection-Diffusion Equations". In: *Journal of Computational Physics* 160.1 (2000), pp. 241–282. ISSN: 00219991. DOI: 10.1006/jcph.2000.6459.
- [193] A. La Rocca et al. "Characterisation of soot in oil from a gasoline direct injection engine using Transmission Electron Microscopy". In: *Tribology International* 86 (2015), pp. 77–84. ISSN: 0301679X. DOI: 10.1016/j.triboint.2015.01.025. URL: <https://www.sciencedirect.com/science/article/pii/S0301679X15000432>.
- [194] Joshua Lacey et al. *An Optical and Numerical Characterization of Directly Injected Compressed Natural Gas Jet Development at Engine-Relevant Conditions*. Tech. rep. SAE Technical Paper, 2019.
- [195] Grazia Lamanna et al. "Towards a unified treatment of fully flashing sprays". In: *International Journal of Multiphase Flow* (2014). ISSN: 03019322. DOI: 10.1016/j.ijmultiphaseflow.2013.08.010.
- [196] Serge Latouche. "Degrowth economics". In: *Le Monde Diplomatique* 11 (2004), p. 2004.
- [197] F Leach et al. "Comparing the effect of different oxygenate components on PN emissions from GDI engines". In: (2015).
- [198] Felix C.P. Leach et al. "The effect of oxygenate fuels on PN emissions from a highly boosted GDI engine". In: *Fuel* 225 (2018), pp. 277–286. ISSN: 00162361. DOI: 10.1016/j.fuel.2018.03.148. URL: <https://www.sciencedirect.com/science/article/pii/S0016236118305568>.
- [199] Romain Lebas et al. "Numerical simulation of primary break-up and atomization: DNS and modelling study". In: *International Journal of Multiphase Flow* 35.3 (2009), pp. 247–260.
- [200] Junyong Lee, Namho Kim, and Kyoungdoug Min. "Measurement of spray characteristics using the background-oriented schlieren technique". In: *Measurement Science and Technology* 24.2 (2012), p. 025303.

- [201] Kyeong Ook Lee and Jinyu Zhu. *Evolution in Size and Morphology of Diesel Particulates Along the Exhaust System*. Tech. rep. 2004. DOI: <https://doi.org/10.4271/2004-01-1981>. URL: <https://doi.org/10.4271/2004-01-1981>.
- [202] Sanghoon Lee and Sungwook Park. "Experimental study on spray break-up and atomization processes from GDI injector using high injection pressure up to 30MPa". In: *International Journal of Heat and Fluid Flow* 45.1 (2014), pp. 14–22. ISSN: 0142727X. DOI: 10.1016/j.ijheatfluidflow.2013.11.005. URL: <http://dx.doi.org/10.1016/j.ijheatfluidflow.2013.11.005>.
- [203] Sanghoon Lee and Sungwook Park. "Spray atomization characteristics of a GDI injector equipped with a group-hole nozzle". In: *Fuel* 137 (2014), pp. 50–59. ISSN: 00162361. DOI: 10.1016/j.fuel.2014.07.063. URL: <http://dx.doi.org/10.1016/j.fuel.2014.07.063>.
- [204] Ziyong Lee et al. "Review on spray, combustion, and emission characteristics of recent developed direct-injection spark ignition (DISI) engine system with multi-hole type injector". In: *Fuel* 259 (2020), p. 116209.
- [205] Ziyong Lee et al. *Review on spray, combustion, and emission characteristics of recent developed direct-injection spark ignition (DISI) engine system with multi-hole type injector*. 2020. DOI: 10.1016/j.fuel.2019.116209. URL: <https://www.sciencedirect.com/science/article/pii/S0016236119315637>.
- [206] Bram van Leer. "Towards the ultimate conservative difference scheme. II. Monotonicity and conservation combined in a second-order scheme". In: *Journal of Computational Physics* 14.4 (1974), pp. 361–370. ISSN: 10902716. DOI: 10.1016/0021-9991(74)90019-9.
- [207] A H Lefebvre and V G McDonell. *Atomization and Sprays, Second Edition*. CRC Press, 2017. ISBN: 9781498736268. URL: <https://books.google.it/books?id=800EDgAAQBAJ>.
- [208] Yan Lei et al. "Gas jet flow characteristic of high-pressure methane pulsed injection of single-hole cylindrical nozzle". In: *Fuel* 257 (2019), p. 116081.
- [209] Fabrice Lemoine and Guillaume Castanet. "Temperature and chemical composition of droplets by optical measurement techniques: a state-of-the-art review". In: *Experiments in fluids* 54.7 (2013), p. 1572.
- [210] Zissis Samaras Leonidas Ntziachristos. *EMEP/EEA air pollutant emission inventory guidebook 2016*. 2018. URL: <https://www.eea.europa.eu/themes/air/air-pollution-sources-1/emep-eea-air-pollutant-emission-inventory-guidebook> (visited on 11/23/2020).
- [211] "LES modeling of premixed combustion using a thickened flame approach coupled with FGM tabulated chemistry". In: *Combustion and Flame* 158.9 (2011), pp. 1750–1767. ISSN: 00102180. DOI: 10.1016/j.combustflame.2011.01.005. URL: <https://www.sciencedirect.com/science/article/pii/S0010218011000204>.

- [212] Danyu Li et al. "Visualizing Near-Field Spray Characteristics With Broadband X-Rays". In: *ASME 2017 Fluids Engineering Division Summer Meeting*. American Society of Mechanical Engineers. 2017, V01BT06A005–V01BT06A005.
- [213] Tianyun Li et al. "Analysis of evaporation characteristics and heat transfer for flash-boiling sprays". In: *International Journal of Heat and Mass Transfer* 127 (2018), pp. 244–254.
- [214] Yanfei Li et al. "An exploration on collapse mechanism of multi-jet flash-boiling sprays". In: *Applied Thermal Engineering* (2018). ISSN: 13594311. DOI: 10.1016/j.applthermaleng.2018.01.102.
- [215] Yanfei Li et al. "Droplet dynamics of di spray from sub-atmospheric to elevated ambient pressure". In: *Fuel* 179 (2016), pp. 25–35. ISSN: 00162361. DOI: 10.1016/j.fuel.2016.03.047. URL: <http://dx.doi.org/10.1016/j.fuel.2016.03.047>.
- [216] Yanfei Li et al. "Morphology analysis on multi-jet flash-boiling sprays under wide ambient pressures". In: *Fuel* 211 (2018), pp. 38–47.
- [217] Yanfei Li et al. "Spray morphology transformation of propane, n-hexane and iso-octane under flash-boiling conditions". In: *Fuel* 236 (2019), pp. 677–685.
- [218] Bin Liang et al. "Comparison of PM emissions from a gasoline direct injected (GDI) vehicle and a port fuel injected (PFI) vehicle measured by electrical low pressure impactor (ELPI) with two fuels: Gasoline and M15 methanol gasoline". In: *Journal of Aerosol Science* 57 (2013), pp. 22–31. ISSN: 00218502. DOI: 10.1016/j.jaerosci.2012.11.008. URL: <http://dx.doi.org/10.1016/j.jaerosci.2012.11.008>.
- [219] Gangtao Liang and Issam Mudawar. "Review of drop impact on heated walls". In: *International Journal of Heat and Mass Transfer* 106 (2017), pp. 103–126.
- [220] Gangtao Liang and Issam Mudawar. "Review of mass and momentum interactions during drop impact on a liquid film". In: *International Journal of Heat and Mass Transfer* 101 (2016), pp. 577–599.
- [221] Mark Linne. "Imaging in the optically dense regions of a spray: A review of developing techniques". In: *Progress in Energy and Combustion Science* 39.5 (2013), pp. 403–440.
- [222] Meng-Sing Liou and Christopher J Steffen Jr. "A new flux splitting scheme". In: *Journal of Computational physics* 107.1 (1993), pp. 23–39.
- [223] Yi Liu et al. "Spray development and droplet characteristics of high temperature single-hole gasoline spray". In: *Fuel* 191 (2017), pp. 97–105. ISSN: 00162361. DOI: 10.1016/j.fuel.2016.11.068. URL: <http://dx.doi.org/10.1016/j.fuel.2016.11.068>.
- [224] Z. Liu, S. S. Hwang, and Rolf D. Reitz. "BREAKUP MECHANISMS AND DRAG COEFFICIENTS OF HIGH-SPEED VAPORIZING LIQUID DROPS". In: *Atomization and Sprays* 6.3 (1996), pp. 353–376. ISSN: 1044-5110.

- [225] Zhengbai Liu, Tomio Obokata, and Rolf D Reitz. "Modeling drop drag effects on fuel spray impingement in direct injection diesel engines". In: *SAE transactions* (1997), pp. 1377–1390.
- [226] D. D. Loureiro et al. "Primary breakup regimes for cryogenic flash atomization". In: *International Journal of Multiphase Flow* (2020). ISSN: 03019322. DOI: 10.1016/j.ijmultiphaseflow.2020.103405.
- [227] Sabino Luisi et al. *Experimental Investigation on Early and Late Intake Valve Closures for Knock Mitigation through Miller Cycle in a Downsized Turbocharged Engine*. Tech. rep. 2015. DOI: <https://doi.org/10.4271/2015-01-0760>. URL: <https://doi.org/10.4271/2015-01-0760>.
- [228] Hongliang Luo, Keiya Nishida, and Youichi Ogata. "Fuel adhesion characteristics under non-evaporation and evaporation conditions: Part 2—Effect of ambient pressure". In: *Fuel* 251 (2019), pp. 98–105.
- [229] Hongliang Luo et al. "Effect of temperature on fuel adhesion under spray-wall impingement condition". In: *Fuel* 234 (2018), pp. 56–65.
- [230] Hongliang Luo et al. "EXPERIMENTAL INVESTIGATION ON FUEL FILM FORMATION BY SPRAY IMPINGEMENT ON FLAT WALLS WITH DIFFERENT SURFACE ROUGHNESS". In: *Atomization and Sprays* 27.7 (2017).
- [231] Hongliang Luo et al. "Microscopic behavior of spray droplets under flat-wall impinging condition". In: *Fuel* 219.November 2017 (2018), pp. 467–476. ISSN: 00162361. DOI: 10.1016/j.fuel.2018.01.059. URL: <https://doi.org/10.1016/j.fuel.2018.01.059>.
- [232] Yueqi Luo et al. "Size distribution, chemical composition and oxidation reactivity of particulate matter from gasoline direct injection (GDI) engine fueled with ethanol-gasoline fuel". In: *Applied Thermal Engineering* 89 (2015), pp. 647–655. ISSN: 13594311. DOI: 10.1016/j.applthermaleng.2015.06.060. URL: <https://www.sciencedirect.com/science/article/pii/S1359431115006195>.
- [233] M. Matti Maricq, Joseph J. Szente, and Ken Jahr. "The Impact of Ethanol Fuel Blends on PM Emissions from a Light-Duty GDI Vehicle". In: *Aerosol Science and Technology* 46.5 (2012), pp. 576–583. DOI: 10.1080/02786826.2011.648780. eprint: <https://doi.org/10.1080/02786826.2011.648780>. URL: <https://doi.org/10.1080/02786826.2011.648780>.
- [234] H Marmanis and ST Thoroddsen. "Scaling of the fingering pattern of an impacting drop". In: *Physics of fluids* 8.6 (1996), pp. 1344–1346.
- [235] Amrita Mazumdar. "Principles and techniques of schlieren imaging systems". In: (2013).
- [236] R. W. McCabe et al. *Effects of MMT® Fuel Additive on Emission System Components: Comparison of Clear-and MMT®-fueled Escort Vehicles from the Alliance Study*. Tech. rep. 2004. DOI: <https://doi.org/10.4271/2004-01-1084>. URL: <https://doi.org/10.4271/2004-01-1084>.

- [237] Thibault Ménard, Sebastien Tanguy, and Alain Berlemont. “Coupling level set/VOF/ghost fluid methods: Validation and application to 3D simulation of the primary break-up of a liquid jet”. In: *International Journal of Multiphase Flow* 33.5 (2007), pp. 510–524.
- [238] *Met Office*. 2020. URL: <https://www.metoffice.gov.uk/> (visited on 11/23/2020).
- [239] CC Miesse. “Correlation of experimental data on the disintegration of liquid jets”. In: *Industrial & Engineering Chemistry* 47.9 (1955), pp. 1690–1701.
- [240] Marianna Migliaccio et al. “CFD Modeling and Validation of the ECN Spray G Experiment under a Wide Range of Operating Conditions”. In: *SAE Technical Papers*. 2019. DOI: 10.4271/2019-24-0130.
- [241] Federico Millo et al. “Numerical and experimental investigation on combustion characteristics of a spark ignition engine with an early intake valve closing load control”. In: *Fuel* 121 (2014), pp. 298–310. ISSN: 0016-2361. DOI: 10.1016/J.FUEL.2013.12.047. URL: <https://www.sciencedirect.com/science/article/pii/S0016236113011915>.
- [242] Murali-Girija Mithun, Phoevos Koukouvinis, and Manolis Gavaises. “Numerical simulation of cavitation and atomization using a fully compressible three-phase model”. In: *Physical Review Fluids* 3.6 (2018), p. 064304.
- [243] Balaji Mohan et al. “Coupled in-nozzle flow and spray simulation of Engine Combustion Network Spray-G injector”. In: *International Journal of Engine Research* (2020). ISSN: 20413149. DOI: 10.1177/1468087420960612.
- [244] Chinmoy K Mohapatra et al. “Collaborative investigation of the internal flow and near-nozzle flow of an eight-hole gasoline injector (Engine Combustion Network Spray G)”. In: *International Journal of Engine Research* 0.0 (0), p. 1468087420918449. DOI: 10.1177/1468087420918449. eprint: <https://doi.org/10.1177/1468087420918449>. URL: <https://doi.org/10.1177/1468087420918449>.
- [245] Safwan Hanis Mohd Murad et al. *Spray Behaviour and Particulate Matter Emissions with M15 Methanol/Gasoline Blends in a GDI Engine*. Tech. rep. 2016. DOI: <https://doi.org/10.4271/2016-01-0991>. URL: <https://doi.org/10.4271/2016-01-0991>.
- [246] AS Moita and ALN Moreira. “Drop impacts onto cold and heated rigid surfaces: morphological comparisons, disintegration limits and secondary atomization”. In: *International Journal of Heat and Fluid Flow* 28.4 (2007), pp. 735–752.
- [247] Joe J Monaghan. “Smoothed particle hydrodynamics”. In: *Annual review of astronomy and astrophysics* 30.1 (1992), pp. 543–574.

- [248] Alessandro Montanaro, Luigi Allocca, and Maurizio Lazzaro. "Iso-Octane Spray from a GDI Multi-Hole Injector under Non- and Flash Boiling Conditions". In: *International Powertrains, Fuels and Lubricants Meeting*. SAE International, 2017. DOI: <https://doi.org/10.4271/2017-01-2319>.
- [249] Alessandro Montanaro, Luigi Allocca, and Maurizio Lazzaro. *Iso-octane spray from a GDI multi-hole injector under non-and flash boiling conditions*. Tech. rep. SAE Technical Paper, 2017.
- [250] Alessandro Montanaro et al. "Assessment of a 3D CFD model for GDI spray impact against wall through experiments based on different optical techniques". In: *International Journal of Multiphase Flow* 84 (2016), pp. 204–216. ISSN: 03019322. DOI: [10.1016/j.ijmultiphaseflow.2016.05.007](https://doi.org/10.1016/j.ijmultiphaseflow.2016.05.007).
- [251] Alessandro Montanaro et al. *GDI Spray-Wall Interaction with Numerical Characterization: Wall Temperature Influence*. Tech. rep. SAE Technical Paper, 2015.
- [252] Alessandro Montanaro et al. *Impinging jets of fuel on a heated surface: effects of wall temperature and injection conditions*. Tech. rep. SAE Technical Paper, 2016.
- [253] Alessandro Montanaro et al. *Schlieren and mie scattering imaging system to evaluate liquid and vapor contours of a gasoline spray impacting on a heated wall*. Tech. rep. SAE Technical Paper, 2015.
- [254] S Moon et al. "Ultrafast X-ray phase-contrast imaging of high-speed fuel sprays from a two-hole diesel nozzle". In: *ILASS Americas, 22nd annual conference on liquid atomization and spray systems* (2010).
- [255] Seoksu Moon et al. "Biodiesel effects on transient needle motion and near-exit flow characteristics of a high-pressure diesel injector". In: *International Journal of Engine Research* 15.4 (2014), pp. 504–518. DOI: [10.1177/1468087413497951](https://doi.org/10.1177/1468087413497951). URL: <https://doi.org/10.1177/1468087413497951>.
- [256] Seoksu Moon et al. "Governing parameters and dynamics of turbulent spray atomization from modern GDI injectors". In: *Energy* 127 (2017), pp. 89–100. ISSN: 03605442. DOI: [10.1016/j.energy.2017.03.099](https://doi.org/10.1016/j.energy.2017.03.099). URL: <http://dx.doi.org/10.1016/j.energy.2017.03.099>.
- [257] Seoksu Moon et al. "Ultrafast X-ray study of multi-hole GDI injector sprays: Effects of nozzle hole length and number on initial spray formation". In: *Experimental Thermal and Fluid Science* 68 (2015), pp. 68–81. ISSN: 08941777. DOI: [10.1016/j.expthermflusci.2015.03.027](https://doi.org/10.1016/j.expthermflusci.2015.03.027). URL: <http://dx.doi.org/10.1016/j.expthermflusci.2015.03.027>.
- [258] A. L.N. Moreira, A. S. Moita, and M. R. Panão. "Advances and challenges in explaining fuel spray impingement: How much of single droplet impact research is useful?" In: *Progress in Energy and Combustion Science* 36.5 (2010), pp. 554–580. ISSN: 03601285. DOI: [10.1016/j.pecs.2010.01.002](https://doi.org/10.1016/j.pecs.2010.01.002).

- [259] ALN Moreira, AS Moita, and MR Panao. "Advances and challenges in explaining fuel spray impingement: How much of single droplet impact research is useful?" In: *Progress in energy and combustion science* 36.5 (2010), pp. 554–580.
- [260] Sebastian Mosbach et al. "Towards a detailed soot model for internal combustion engines". In: *Combustion and Flame* 156.6 (2009), pp. 1156–1165. ISSN: 00102180. DOI: 10.1016/j.combustflame.2009.01.003. URL: <https://www.sciencedirect.com/science/article/pii/S0010218009000054>.
- [261] Maryam Moulai et al. "Internal and Near-Nozzle Flow in a Multi-Hole Gasoline Injector Under Flashing and Non-Flashing Conditions". In: *SAE Technical Paper Series* 1 (2015). DOI: 10.4271/2015-01-0944.
- [262] CHR Mundo, M Sommerfeld, and C Tropea. "Droplet-wall collisions: experimental studies of the deformation and breakup process". In: *International journal of multiphase flow* 21.2 (1995), pp. 151–173.
- [263] CHR Mundo, Martin Sommerfeld, and Cameron Tropea. "On the modeling of liquid sprays impinging on surfaces". In: *Atomization and sprays* 8.6 (1998).
- [264] JA Nicholls. "Stream and droplet breakup by shock waves". In: *Nasa Sp-194* (1972).
- [265] W Ning et al. "Development of a next generation spray and atomization model using an Eulerian-Lagrangian methodology. 17th Int". In: *Multidimensional Engine Modeling User's Group Meeting, Detroit, MI*. 2007.
- [266] Lorenzo Nocivelli et al. "Analysis of the Spray Numerical Injection Modeling for Gasoline Applications". In: *SAE Technical Papers*. 2020. DOI: 10.4271/2020-01-0330.
- [267] Michael L Norman and Karl-Heinz A Winkler. "Supersonic jets". In: *suje* (1985).
- [268] Rosalind O'Driscoll et al. "Real world CO<sub>2</sub> and NO<sub>x</sub> emissions from 149 Euro 5 and 6 diesel, gasoline and hybrid passenger cars". In: *Science of the Total Environment* (2018). ISSN: 18791026. DOI: 10.1016/j.scitotenv.2017.11.271.
- [269] Heechang Oh and Choongsik Bae. "Effects of a split injection in a spray-guided direct-injection spark ignition engine under lean stratified operation". In: *Proceedings of the Institution of Mechanical Engineers, Part D: Journal of Automobile Engineering* 228.10 (2014), pp. 1232–1244. DOI: 10.1177/0954407013502781. eprint: <https://doi.org/10.1177/0954407013502781>. URL: <https://doi.org/10.1177/0954407013502781>.
- [270] Heechang Oh et al. "Effect of the Multiple Injection on Stratified Combustion Characteristics in a Spray-Guided DISI Engine". In: (2011). DOI: 10.4271/2011-24-0059. URL: <http://papers.sae.org/2011-24-0059/>.

- [271] Wolfgang V Ohnesorge. "Die bildung von tropfen an düssen und die auflösung flüssiger strahlen". In: *ZAMM-Journal of Applied Mathematics and Mechanics/Zeitschrift für Angewandte Mathematik und Mechanik* 16.6 (1936), pp. 355–358.
- [272] P. J. O'Rourke. "Modelling of Drop Interactions in Thick Sprays and a Comparison with Experiments". In: *I. Mech. E., C* 404.80 (1980), pp. 101–116. URL: <https://ci.nii.ac.jp/naid/10015773811/en/>.
- [273] Peter J O'Rourke and AA Amsden. "A spray/wall interaction sub-model for the KIVA-3 wall film model". In: *SAE transactions* (2000), pp. 281–298.
- [274] Peter J O'Rourke and Anthony A Amsden. *The TAB method for numerical calculation of spray droplet breakup*. Tech. rep. SAE Technical Paper, 1987.
- [275] Rajshekhar D. Oza and James F. Sinnamon. "An experimental and analytical study of flash-boiling fuel injection". In: *SAE Technical Papers*. 1983. DOI: 10.4271/830590.
- [276] Hujie Pan et al. "Experimental investigations of wall jet droplet impact on spray impingement fuel film formation". In: *Fuel* 241 (2019), pp. 33–41.
- [277] Pradipta Kumar Panigrahi and Krishnamurthy Muralidhar. *Schlieren and shadowgraph methods in heat and mass transfer*. Vol. 2. Springer, 2012.
- [278] Davide Paredi et al. "Combined Experimental and Numerical Investigation of the ECN Spray G under Different Engine-Like Conditions". In: *2018 SAE World Congress Experience, WCX 2018*. Vol. 2018. SAE International. 2018, pp. 1–15.
- [279] Davide Paredi et al. "Validation of a comprehensive computational fluid dynamics methodology to predict the direct injection process of gasoline sprays using Spray G experimental data". In: *International Journal of Engine Research* (2020). ISSN: 20413149. DOI: 10.1177/1468087419868020.
- [280] Cheolwoong Park, Sunyoun Lee, and Uihyung Yi. "Effects of engine operating conditions on particle emissions of lean-burn gasoline direct-injection engine". In: *Energy* 115 (2016), pp. 1148–1155. ISSN: 03605442. DOI: 10.1016/j.energy.2016.09.051. URL: <https://www.sciencedirect.com/science/article/pii/S0360544216312890>.
- [281] Cheolwoong Park et al. "Stratified lean combustion characteristics of a spray-guided combustion system in a gasoline direct injection engine". In: *Energy* 41.1 (2012), pp. 401–407. ISSN: 03605442. DOI: 10.1016/j.energy.2012.02.060. URL: <https://www.sciencedirect.com/science/article/pii/S0360544212001740>.
- [282] Scott E Parrish, Gaoming Zhang, and Ronald J Zink. "Liquid and vapor envelopes of sprays from a multi-hole fuel injector operating under closely-spaced double-injection conditions". In: *SAE International Journal of Engines* 5.2 (2012), pp. 400–414.

- [283] Scott E Parrish and RJ Zink. "Development and application of imaging system to evaluate liquid and vapor envelopes of multi-hole gasoline fuel injector sprays under engine-like conditions". In: *Atomization and Sprays* 22.8 (2012).
- [284] Mark A Patterson and Rolf D Reitz. "Modeling the effects of fuel spray characteristics on diesel engine combustion and emission". In: *SAE transactions* (1998), pp. 27–43.
- [285] Raul Payri et al. "Methodology for Phase Doppler Anemometry Measurements on a Multi-Hole Diesel Injector". In: *Experimental Techniques* 41.2 (2017), pp. 95–102.
- [286] Johann Peer et al. "Development of a High Turbulence, Low Particle Number, High Injection Pressure Gasoline Direct Injection Combustion System". In: *SAE International Journal of Engines* 9.4 (2016), pp. 2016–01–9046. ISSN: 1946-3944. DOI: 10.4271/2016-01-9046. URL: <http://papers.sae.org/2016-01-9046/>.
- [287] Federico Perini et al. *A Triangulated Lagrangian Ignition Kernel Model with Detailed Kinetics for Modeling Spark Ignition with the G-Equation-Part I: Geometric Aspects*. Tech. rep. 2018. DOI: <https://doi.org/10.4271/2018-01-0195>. URL: <https://doi.org/10.4271/2018-01-0195>.
- [288] *PERSONAL TRANSPORTATION FACTSHEET*. 2020. URL: <http://css.umich.edu/factsheets/personal-transportation-factsheet> (visited on 11/23/2020).
- [289] Peters, N. and Dekena, M. "Combustion Modeling with the G-Equation". In: *Oil & Gas Science and Technology - Rev. IFP* 54.2 (1999), pp. 265–270. DOI: 10.2516/ogst:1999024. URL: <https://doi.org/10.2516/ogst:1999024>.
- [290] Brian Peterson et al. "Spray-induced temperature stratification dynamics in a gasoline direct-injection engine". In: *Proceedings of the Combustion Institute* 35.3 (2015), pp. 2923–2931.
- [291] Daniele Piazzullo et al. "A 3D CFD Simulation of GDI Sprays Accounting for Heat Transfer Effects on Wallfilm Formation". In: *SAE International Journal of Engines* 10.4 (2017), pp. 2017–24–0041. ISSN: 1946-3944. DOI: 10.4271/2017-24-0041. URL: <http://papers.sae.org/2017-24-0041/>.
- [292] Walter F. Piock et al. "Fuel Pressure and Charge Motion Effects on GDI Engine Particulate Emissions". In: *SAE International Journal of Engines* 8.2 (2015), pp. 464–473. ISSN: 1946-3944. DOI: 10.4271/2015-01-0746.
- [293] Seyfi Polat et al. "A numerical study on the effects of EGR and spark timing to combustion characteristics and NO<sub>x</sub> emission of a GDI engine". In: *International Journal of Green Energy* 13.1 (2016), pp. 63–70.
- [294] Stephen B Pope. *Turbulent flows*. 2001.

- [295] Christopher Price et al. "Numerical modelling of fuel spray formation and collapse from multi-hole injectors under flash-boiling conditions". In: *Fuel* (2018). ISSN: 00162361. DOI: 10.1016/j.fuel.2018.01.088.
- [296] Philip Price et al. *Dynamic Particulate Measurements from a DISI Vehicle: A Comparison of DMS500, ELPI, CPC and PASS*. Tech. rep. 2006. DOI: <https://doi.org/10.4271/2006-01-1077>. URL: <https://doi.org/10.4271/2006-01-1077>.
- [297] J Qian and Chung King Law. "Regimes of coalescence and separation in droplet collision". In: *Journal of Fluid Mechanics* 331 (1997), pp. 59–80.
- [298] Yong Qian et al. "Review of the state-of-the-art of particulate matter emissions from modern gasoline fueled engines". In: *Applied Energy* 238. September 2018 (2019), pp. 1269–1298. ISSN: 03062619. DOI: 10.1016/j.apenergy.2019.01.179. URL: <https://doi.org/10.1016/j.apenergy.2019.01.179>.
- [299] A Abhilash Reddy and J M Mallikarjuna. "Parametric Study on a Gasoline Direct Injection Engine - A CFD Analysis". In: (2017). DOI: 10.4271/2017-26-0039. Copyright.
- [300] R. D. Reitz. "Modeling atomization processes in high-pressure vaporizing sprays". In: *Atomisation Spray Technology* 3 (1987), pp. 309–337.
- [301] R. D. Reitz and F. V. Bracco. "Mechanism of atomization of a liquid jet". In: *Physics of Fluids* 25.10 (1982), pp. 1730–1742. ISSN: 10706631. DOI: 10.1063/1.863650. URL: <https://aip.scitation.org/doi/10.1063/1.863650>.
- [302] RD REITZ. "Atomization and Other Breakup Regimes of a Liquid Jets". In: *Ph. D. Thesis, Princeton University* (1978).
- [303] Rolf D Reitz. "A photographic study of flash-boiling atomization". In: *Aerosol Science and Technology* 12.3 (1990), pp. 561–569.
- [304] Rolf D Reitz. "Computer modeling of sprays". In: *Spray Technology Short Course, Pittsburgh, PA* (1996).
- [305] Rolf D Reitz and R Diwakar. "Effect of drop breakup on fuel sprays". In: *SAE transactions* (1986), pp. 218–227.
- [306] KJ Richards, PK Senecal, and E Pomraning. "CONVERGE manual (Version 2.4)". In: *Convergent Science Inc., Madison, WI-USA* (2016).
- [307] L.F. Richardson. *Weather Prediction by Numerical Process - Scholar's Choice Edition*. Creative Media Partners, LLC, 2015. ISBN: 9781295993192. URL: <https://books.google.it/books?id=VWk6rgEACAAJ>.
- [308] Romain Rioboo, Cameron Tropea, and Marco Marengo. "Outcomes from a drop impact on solid surfaces". In: *Atomization and Sprays* 11.2 (2001).

- [309] P. J. Roache. "Quantification of uncertainty in computational fluid dynamics". In: *Annual Review of Fluid Mechanics* (1997). ISSN: 00664189. DOI: 10.1146/annurev.fluid.29.1.123.
- [310] J. Felipe Rodriguez and Wai K. Cheng. *Effect of Operation Strategy on First Cycle CO, HC, and PM/PN Emissions in a GDI Engine*. 2015. DOI: <https://doi.org/10.4271/2015-01-0887>. URL: <https://doi.org/10.4271/2015-01-0887>.
- [311] Iliia V Roisman, Kristijan Horvat, and Cam Tropea. "Spray impact: rim transverse instability initiating fingering and splash, and description of a secondary spray". In: *Physics of Fluids* 18.10 (2006), p. 102104.
- [312] Rossella Rotondi. "Modeling Mixture Formation in a Gasoline Direct Injection Engine". In: *Journal of Applied Mechanics* 73.6 (Dec. 2005), pp. 931–939. ISSN: 0021-8936. DOI: 10.1115/1.2173284. eprint: <https://asmedigitalcollection.asme.org/appliedmechanics/article-pdf/73/6/931/5474115/931\1.pdf>. URL: <https://doi.org/10.1115/1.2173284>.
- [313] MA Saad. *Compressible Fluid Dynamics*. 1993.
- [314] Victor M. Salazar and Sebastian A. Kaiser. "An optical study of mixture preparation in a hydrogen-fueled engine with direct injection using different nozzle designs". In: *SAE International Journal of Engines* 2.2 (2010), pp. 119–131. ISSN: 19463936. DOI: 10.4271/2009-01-2682.
- [315] Georges Saliba et al. "Comparison of Gasoline Direct-Injection (GDI) and Port Fuel Injection (PFI) Vehicle Emissions: Emission Certification Standards, Cold-Start, Secondary Organic Aerosol Formation Potential, and Potential Climate Impacts". In: *Environmental Science & Technology* 51.11 (2017). PMID: 28441489, pp. 6542–6552. DOI: 10.1021/acs.est.6b06509. eprint: <https://doi.org/10.1021/acs.est.6b06509>. URL: <https://doi.org/10.1021/acs.est.6b06509>.
- [316] FJ Salvador et al. "Comparison of Different Techniques for Characterizing the Diesel Injector Internal Dimensions". In: *Experimental Techniques* (2018), pp. 1–6.
- [317] V. Sankaran and S. Menon. "Subgrid combustion modeling of 3-D premixed flames in the thin-reaction-zone regime". In: *Proceedings of the Combustion Institute* 30.1 (2005), pp. 575–582. ISSN: 15407489. DOI: 10.1016/j.proci.2004.08.023. URL: <https://www.sciencedirect.com/science/article/pii/S008207840400075X>.
- [318] Durgada Sankesh, Phred Petersen, and Petros Lappas. "Flow characteristics of natural-gas from an outward-opening nozzle for direct injection engines". In: *Fuel* 218 (2018), pp. 188–202.
- [319] O. P. Saw and J. M. Mallikarjuna. "Effect of spark plug and fuel injector location on mixture stratification in a GDI engine - A CFD analysis". In: *IOP Conference Series: Materials Science and Engineering* 243.1 (2017). ISSN: 1757899X. DOI: 10.1088/1757-899X/243/1/012025.

- [320] Om Prakash Saw, Srinivasa Krishna Addepalli, and J M Mallikarjuna. "Effects of Cylinder Head Geometry on Mixture Stratification, Combustion and Emissions in a GDI Engine - A CFD Analysis". In: *SAE Technical Paper Series 1* (2019), pp. 1–13. DOI: 10.4271/2019-01-0009.
- [321] Riccardo Scarcelli et al. "Mixture formation in direct injection hydrogen engines: Cfd and optical analysis of single- and multi-hole nozzles". In: *SAE International Journal of Engines 4.2* (2011), pp. 2361–2375. ISSN: 19463936. DOI: 10.4271/2011-24-0096.
- [322] Detlev Schoeppe et al. "Requirements for future gasoline DI systems and respective platform solutions; Anforderungen an zukuenftige Otto DI-Einspritzsysteme und entsprechende Plattformloesungen". In: (2011).
- [323] Florian Schulz and Frank Beyrau. "Comparison of the Spray and the Spray/Wall Interaction of Two Gasoline Injectors". In: *International Journal of Automotive Technology 19.4* (2018), pp. 615–622.
- [324] Florian Schulz et al. "Gasoline wall films and spray/wall interaction analyzed by infrared thermography". In: *SAE International Journal of Engines 7.3* (2014), pp. 1165–1177.
- [325] A. Seaton et al. "Particulate air pollution and acute health effects". In: *The Lancet 345.8943* (1995), pp. 176–178. ISSN: 0140-6736. DOI: 10.1016/S0140-6736(95)90173-6. URL: <https://www.sciencedirect.com/science/article/pii/S0140673695901736>.
- [326] Mark Sellnau et al. "Advancement of GDCI Engine Technology for US 2025 CAFE and Tier 3 Emissions". In: *WCX World Congress Experience*. SAE International, 2018. DOI: <https://doi.org/10.4271/2018-01-0901>. URL: <https://doi.org/10.4271/2018-01-0901>.
- [327] Mark Sellnau et al. "Development of a Gasoline Direct Injection Compression Ignition (GDCI) Engine". In: *SAE International Journal of Engines 7.2* (2014), pp. 835–851. ISSN: 1946-3944. DOI: <https://doi.org/10.4271/2014-01-1300>. URL: <https://doi.org/10.4271/2014-01-1300>.
- [328] Mark Sellnau et al. "Gasoline Direct Injection Compression Ignition (GDCI) - Diesel-like Efficiency with Low CO2 Emissions". In: (2011). ISSN: 1946-3936. DOI: <https://doi.org/10.4271/2011-01-1386>. URL: <https://doi.org/10.4271/2011-01-1386>.
- [329] Mark Sellnau et al. "Gasoline Direct Injection Compression Ignition (GDCI) - Diesel-like Efficiency with Low CO2 Emissions". In: *SAE International Journal of Engines 4.1* (2011), pp. 2010–2022. ISSN: 19463936, 19463944. URL: <http://www.jstor.org/stable/26278275>.
- [330] Mark Sellnau et al. "GDCI Multi-Cylinder Engine for High Fuel Efficiency and Low Emissions". In: *SAE International Journal of Engines 8.2* (2015), pp. 775–790. ISSN: 1946-3944. DOI: <https://doi.org/10.4271/2015-01-0834>. URL: <https://doi.org/10.4271/2015-01-0834>.

- [331] Mark Sellnau et al. "Second Generation GDCI Multi-Cylinder Engine for High Fuel Efficiency and US Tier 3 Emissions". In: (2016). ISSN: 1946-3936. DOI: <https://doi.org/10.4271/2016-01-0760>. URL: <https://doi.org/10.4271/2016-01-0760>.
- [332] Mark C. Sellnau et al. "Full-Time Gasoline Direct-Injection Compression Ignition (GDCI) for High Efficiency and Low NO<sub>x</sub> and PM". In: *SAE International Journal of Engines* 5.2 (2012), pp. 300–314. ISSN: 1946-3944. DOI: <https://doi.org/10.4271/2012-01-0384>. URL: <https://doi.org/10.4271/2012-01-0384>.
- [333] Jiro Senda et al. "Modeling of diesel spray impingement on a flat wall". In: *SAE transactions* (1994), pp. 1918–1931.
- [334] PK Senecal et al. "Modeling high-speed viscous liquid sheet atomization". In: *International Journal of Multiphase Flow* 25.6-7 (1999), pp. 1073–1097.
- [335] Juhyeong Seo et al. "Experimental and Numerical Simulations of Spray Impingement and Combustion Characteristics in Gasoline Direct Injection Engines under Variable Driving Conditions". In: *Flow, Turbulence and Combustion* 96.2 (2016), pp. 391–415. ISSN: 15731987. DOI: 10.1007/s10494-015-9678-1.
- [336] HeeJe Seong, Kyeong Lee, and Seungmok Choi. *Effects of Engine Operating Parameters on Morphology of Particulates from a Gasoline Direct Injection (GDI) Engine*. Tech. rep. 2013. DOI: <https://doi.org/10.4271/2013-01-2574>. URL: <https://doi.org/10.4271/2013-01-2574>.
- [337] J Serras-Pereira et al. "Cavitation, primary break-up and flash boiling of gasoline, iso-octane and n-pentane with a real-size optical direct-injection nozzle". In: *Fuel* 89.9 (2010), pp. 2592–2607.
- [338] Gary S Settles. *Schlieren and shadowgraph techniques: visualizing phenomena in transparent media*. Springer Science & Business Media, 2001.
- [339] Lorenzo Sforza et al. "Modeling Ignition and Premixed Combustion Including Flame Stretch Effects". In: (2017). ISSN: 0148-7191. DOI: <https://doi.org/10.4271/2017-01-0553>. URL: <https://doi.org/10.4271/2017-01-0553>.
- [340] Eran Sher, Tali Bar-Kohany, and Alexander Rashkovan. "Flash-boiling atomization". In: *Progress in energy and combustion science* 34.4 (2008), pp. 417–439.
- [341] Mark A Shost et al. *GDI nozzle parameter studies using LES and spray imaging methods*. Tech. rep. SAE Technical Paper, 2014.
- [342] William A Sirignano. "Fluid dynamics of sprays—1992 Freeman scholar lecture". In: *Journal of fluids Engineering* 115.3 (1993), pp. 345–378.
- [343] Joseph Smagorinsky. "On the dynamical prediction of large-scale condensation by numerical methods". In: *Geophys. Monogr* 5 (1960), pp. 71–78.

- [344] Richard S Snedeker et al. "A study of free jet impingement. Part 1. Mean properties of free and impinging jets". In: *Journal of fluid Mechanics* 45.2 (1971), pp. 281–319.
- [345] Vlad Soare. "Phase Doppler Measurements in Diesel Dense Sprays: Optimisation of Measurements and Study of the Orifice Geometry Influence over the Spray at Microscopic Level PhD Thesis". In: *Universidad Politécnic de Valencia* (2007).
- [346] Gary A Sod. "A survey of several finite difference methods for systems of nonlinear hyperbolic conservation laws". In: *Journal of Computational Physics* 27.1 (1978), pp. 1–31. ISSN: 0021-9991. DOI: [https://doi.org/10.1016/0021-9991\(78\)90023-2](https://doi.org/10.1016/0021-9991(78)90023-2). URL: <http://www.sciencedirect.com/science/article/pii/0021999178900232>.
- [347] Haoyi Song et al. "The effects of deposits on spray behaviors of a gasoline direct injector". In: *Fuel* 180 (2016), pp. 506–513. ISSN: 00162361. DOI: 10.1016/j.fuel.2016.04.067. URL: <http://dx.doi.org/10.1016/j.fuel.2016.04.067>.
- [348] Jingeun Song et al. "Effects of the injection strategy on the mixture formation and combustion characteristics in a DISI (direct injection spark ignition) optical engine". In: *Energy* 93 (2015), pp. 1758–1768. ISSN: 03605442. DOI: 10.1016/j.energy.2015.10.058. URL: <http://dx.doi.org/10.1016/j.energy.2015.10.058>.
- [349] U. Spicher et al. *Gasoline Direct Injection (GDI) Engines - Development Potentialities*. Tech. rep. 1999. DOI: <https://doi.org/10.4271/1999-01-2938>.
- [350] Donald W Stanton and Christopher J Rutland. "Modeling fuel film formation and wall interaction in diesel engines". In: *SAE transactions* (1996), pp. 808–824.
- [351] Gunnar Stiesch. *Modeling engine spray and combustion processes*. Springer Science & Business Media, 2003.
- [352] George Stockman and Linda G. Shapiro. *Computer Vision*. 1st. Upper Saddle River, NJ, USA: Prentice Hall PTR, 2001. ISBN: 0130307963.
- [353] John Storey et al. "Characterization of Hydrocarbon Emissions from Gasoline Direct-Injection Compression Ignition Engine Operating on a Higher Reactivity Gasoline Fuel". In: *SAE International Journal of Engines* 10.4 (2017), pp. 1454–1464. ISSN: 1946-3944. DOI: <https://doi.org/10.4271/2017-01-0747>. URL: <https://doi.org/10.4271/2017-01-0747>.
- [354] CD Stow and MG Hadfield. "An experimental investigation of fluid flow resulting from the impact of a water drop with an unyielding dry surface". In: *Proceedings of the Royal Society of London. A. Mathematical and Physical Sciences* 373.1755 (1981), pp. 419–441.

- [355] Jianye Su et al. "Particle Number Emissions Reduction Using Multiple Injection Strategies in a Boosted Spark-Ignition Direct-Injection (SIDI) Gasoline Engine". In: (2014). ISSN: 1946-3936. DOI: <https://doi.org/10.4271/2014-01-2845>. URL: <https://doi.org/10.4271/2014-01-2845>.
- [356] Yu Hsuan Su and Ting Fu Kuo. "CFD-assisted analysis of the characteristics of stratified-charge combustion inside a wall-guided gasoline direct injection engine". In: *Energy* 175 (2019), pp. 151–164. ISSN: 03605442. DOI: 10.1016/j.energy.2019.03.031. URL: <https://www.sciencedirect.com/science/article/pii/S0360544219304359>.
- [357] Mark Sussman and Elbridge Gerry Puckett. "A coupled level set and volume-of-fluid method for computing 3D and axisymmetric incompressible two-phase flows". In: *Journal of computational physics* 162.2 (2000), pp. 301–337.
- [358] Peter K Sweby. "High resolution schemes using flux limiters for hyperbolic conservation laws". In: *SIAM journal on numerical analysis* 21.5 (1984), pp. 995–1011.
- [359] Zhichao Tan and Rolf D. Reitz. "Modeling Ignition and Combustion in Spark-ignition Engines Using a Level Set Method". In: (2003). ISSN: 0148-7191. DOI: <https://doi.org/10.4271/2003-01-0722>. URL: <https://doi.org/10.4271/2003-01-0722>.
- [360] Satoshi Taniguchi, Kaori Yoshida, and Yukihiro Tsukasaki. "Feasibility Study of Ethanol Applications to A Direct Injection Gasoline Engine". In: (2007), pp. 1978–1987. DOI: 10.4271/2007-01-2037. URL: <http://papers.sae.org/2007-01-2037/>.
- [361] Mingyuan Tao et al. "Numerical Modeling of Spray Formation under Flash-boiling Conditions". In: *SAE Technical Paper*. SAE International, Apr. 2020. DOI: 10.4271/2020-01-0328. URL: <https://doi.org/10.4271/2020-01-0328>.
- [362] G I TAYLOR. "The shape and acceleration of a drop in a high speed air stream". In: *The Scientific Papers of G I Taylor* 3 (1963), pp. 457–464. URL: <https://ci.nii.ac.jp/naid/10025389750/en/>.
- [363] Geoffrey Ingram Taylor. "The instability of liquid surfaces when accelerated in a direction perpendicular to their planes. I". In: *Proceedings of the Royal Society of London. Series A. Mathematical and Physical Sciences* 201.1065 (1950), pp. 192–196.
- [364] *The Chernobyl Disaster May Have Also Built a Paradise*. 2019. URL: <https://www.wired.com/story/the-chernobyl-disaster-might-have-also-built-a-paradise/> (visited on 11/23/2020).
- [365] "The engine knock analysis - An overview". In: 92 (2012), pp. 628–636. ISSN: 03062619. DOI: 10.1016/j.apenergy.2011.11.079. URL: <https://www.sciencedirect.com/science/article/pii/S0306261911007859>.

- [366] Jiangping Tian et al. "Experimental study on spray characteristics under ultra-high injection pressure for DISI engines". In: *Fuel* 186 (2016), pp. 365–374. ISSN: 00162361. DOI: 10.1016/j.fuel.2016.08.086. URL: <http://dx.doi.org/10.1016/j.fuel.2016.08.086>.
- [367] Dale R. Tree and Kenth I. Svensson. "Soot processes in compression ignition engines". In: *Progress in Energy and Combustion Science* 33.3 (2007), pp. 272–309. ISSN: 0360-1285. DOI: 10.1016/J.PECS.2006.03.002. URL: <https://www.sciencedirect.com/science/article/pii/S0360128506000608>.
- [368] Arnaud Trouvé and Thierry Poinso. "The evolution equation for the flame surface density in turbulent premixed combustion". In: *Journal of Fluid Mechanics* 278 (1994), 1–31. DOI: 10.1017/S0022112094003599.
- [369] Ching-Fen Tsai and Gene Nixon. "Transient temperature distribution of a multilayer composite wall with effects of internal thermal radiation and conduction". In: *Numerical Heat Transfer, Part A: Applications* 10.1 (1986), pp. 95–101.
- [370] Annegret Überall et al. "A literature research about particle emissions from engines with direct gasoline injection and the potential to reduce these emissions". In: *Fuel* 147.x (2015), pp. 203–207. ISSN: 00162361. DOI: 10.1016/j.fuel.2015.01.012.
- [371] Richard Van Basshuysen and Ulrich Spicher. *Gasoline engine with direct injection: processes, systems, development, potential*. Vieweg+ Teubner, 2009.
- [372] Noah Van Dam and Christopher Rutland. "Adapting diesel large-eddy simulation spray models for direct-injection spark-ignition applications". In: *International Journal of Engine Research* 17.3 (2016), pp. 291–315. ISSN: 20413149. DOI: 10.1177/1468087415572034.
- [373] Randy L Vander Wal, Gordon M Berger, and Steven D Mozes. "The combined influence of a rough surface and thin fluid film upon the splashing threshold and splash dynamics of a droplet impacting onto them". In: *Experiments in fluids* 40.1 (2006), pp. 23–32.
- [374] HK Veerstedeg and W Malalasekera. *An introduction to computational fluid dynamics*. 1995.
- [375] W. Vera-Tudela et al. "An experimental study on the effects of needle dynamics on the penetration of a high-pressure methane jet". In: *Fuel* 253 (Oct. 2019), pp. 79–89. DOI: 10.1016/j.fuel.2019.04.171.
- [376] HK Verstedeg and W Malalasekera. *An introduction to Computational Fluid Dynamics: The Finite Volume Method, 2nd edn*. 2007. ISBN: 978-0-13-127498-3.
- [377] Milan Vujanović et al. "Modelling spray and combustion processes in diesel engine by using the coupled Eulerian–Eulerian and Eulerian–Lagrangian method". In: *Energy conversion and management* 125 (2016), pp. 15–25.

- [378] V. Vuorinen et al. "Large-eddy simulation of highly underexpanded transient gas jets". In: *Physics of Fluids* 25.1 (2013), p. 016101. ISSN: 1070-6631. DOI: 10.1063/1.4772192.
- [379] V. Vuorinen et al. "Large-eddy simulation of highly underexpanded transient gas jets". In: *Physics of Fluids* 25.1 (2013), p. 016101. ISSN: 10706631. DOI: 10.1063/1.4772192. URL: <http://aip.scitation.org/doi/10.1063/1.4772192>.
- [380] V. Vuorinen et al. "Large-eddy simulation on the effect of injection pressure and density on fuel jet mixing in gas engines". In: *Fuel* 130 (2014), pp. 241–250. ISSN: 00162361. DOI: 10.1016/j.fuel.2014.04.045.
- [381] V. Vuorinen et al. "On the implementation of low-dissipative Runge-Kutta projection methods for time dependent flows using OpenFOAM®". In: *Computers and Fluids* 93 (2014), pp. 153–163. ISSN: 00457930. DOI: 10.1016/j.compfluid.2014.01.026. URL: <http://dx.doi.org/10.1016/j.compfluid.2014.01.026>.
- [382] Ville Vuorinen et al. "Large-eddy simulation of subsonic jets". In: *Journal of Physics: Conference Series* 318. SECTION 3 (2011). ISSN: 17426596. DOI: 10.1088/1742-6596/318/3/032052.
- [383] Sandip Wadekar, Michael Oevermann, and Andrei Lipatnikov. *Large Eddy Simulation of Stratified Combustion in Spray-guided Direct Injection Spark-ignition Engine*. Tech. rep. 2018. DOI: <https://doi.org/10.4271/2018-01-1420>. URL: <https://doi.org/10.4271/2018-01-1420>.
- [384] Bo Wang et al. "Investigation of deposit effect on multi-hole injector spray characteristics and air/fuel mixing process". In: *Fuel* 191 (2017), pp. 10–24. ISSN: 00162361. DOI: 10.1016/j.fuel.2016.11.055. URL: <http://dx.doi.org/10.1016/j.fuel.2016.11.055>.
- [385] Bo Wang et al. "Numerical analysis of deposit effect on nozzle flow and spray characteristics of GDI injectors". In: *Applied Energy* 204 (2017), pp. 1215–1224. ISSN: 03062619. DOI: 10.1016/j.apenergy.2017.03.094. URL: <http://dx.doi.org/10.1016/j.apenergy.2017.03.094>.
- [386] Bo Wang et al. "Numerical Investigation of the Deposit Effect on GDI Injector Nozzle Flow". In: *Energy Procedia* 105.0 (2017), pp. 1671–1676. ISSN: 18766102. DOI: 10.1016/j.egypro.2017.03.545. URL: <http://dx.doi.org/10.1016/j.egypro.2017.03.545>.
- [387] Buyu Wang et al. "Modelling soot formation from wall films in a gasoline direct injection engine using a detailed population balance model". In: *Applied Energy* (2016). ISSN: 03062619. DOI: 10.1016/j.apenergy.2015.11.011.
- [388] Buyu Wang et al. "Modelling soot formation from wall films in a gasoline direct injection engine using a detailed population balance model". In: *Applied Energy* 163 (2016), pp. 154–166. ISSN: 03062619. DOI: 10.1016/j.apenergy.2015.11.011. URL: <http://dx.doi.org/10.1016/j.apenergy.2015.11.011>.

- [389] Chongming Wang et al. "Impact of fuel and injection system on particle emissions from a GDI engine". In: *Applied Energy* 132 (2014), pp. 178–191. ISSN: 03062619. DOI: 10.1016/j.apenergy.2014.06.012. URL: <http://dx.doi.org/10.1016/j.apenergy.2014.06.012>.
- [390] Xinyan Wang and Hua Zhao. *Numerical Simulation of the Gasoline Spray with an Outward-Opening Piezoelectric Injector: A Comparative Study of Different Breakup Models*. Tech. rep. SAE Technical Paper, 2018.
- [391] Yinhui Wang et al. "The impact of fuel compositions on the particulate emissions of direct injection gasoline engine". In: *Fuel* 166 (2016), pp. 543–552. ISSN: 00162361. DOI: 10.1016/j.fuel.2015.11.019. URL: <http://dx.doi.org/10.1016/j.fuel.2015.11.019>.
- [392] Yujie Wang et al. "Ultrafast X-ray study of dense-liquid-jet flow dynamics using structure-tracking velocimetry". In: *Nature Physics* 4.4 (2008), p. 305.
- [393] C. Ward and A. Buzzi. *Dopo l'automobile. Per un nuovo modello di mobilità*. Elèuthera, 2012. ISBN: 9788896904190. URL: <https://books.google.it/books?id=8QczLgEACAAJ>.
- [394] Alan Buis NASA's Global Climate Change Website. *A Degree of Concern: Why Global Temperatures Matter*. 2020. URL: <https://climate.nasa.gov/news/2865/a-degree-of-concern-why-global-temperatures-matter/> (visited on 11/23/2020).
- [395] Chuan Fang Wei et al. "Simulation Study on Effects of Ignition Time on Particle Emission for GDI Engine". In: *Energy Research and Power Engineering 2014*. Vol. 986. Advanced Materials Research. Trans Tech Publications Ltd, Sept. 2014, pp. 870–873. DOI: 10.4028/www.scientific.net/AMR.986-987.870.
- [396] Lijiang Wei and Peng Geng. "A review on natural gas/diesel dual fuel combustion, emissions and performance". In: *Fuel Processing Technology* 142 (2016), pp. 264–278.
- [397] Yuan Wen et al. "The Impact of Injector Deposits on Spray and Particulate Emission of Advanced Gasoline Direct Injection Vehicle". In: *SAE Technical Paper* (2016). ISSN: 01487191. DOI: 10.4271/2016-01-2284.
- [398] F.M. White and S. Frank M White. *Viscous Fluid Flow*. McGraw-Hill series in mechanical engineering. McGraw-Hill, 1991. ISBN: 9780070697126. URL: <https://books.google.it/books?id=G6IeAQAAIAAJ>.
- [399] A Wierzba. "Deformation and breakup of liquid drops in a gas stream at nearly critical Weber numbers". In: *Experiments in fluids* 9.1-2 (1990), pp. 59–64.
- [400] A WIERZBA and K TAKAYAMA. "Experimental investigation of the aerodynamic breakup of liquid drops". In: *AIAA Journal* 26.11 (1988), pp. 1329–1335. ISSN: 0001-1452. DOI: 10.2514/3.10044. URL: <https://doi.org/10.2514/3.10044>.

- [401] Forman A Williams. "Spray combustion and atomization". In: *The physics of fluids* 1.6 (1958), pp. 541–545.
- [402] M Wolff et al. "High-pressure diesel spray temperature measurements using two-colour laser-induced fluorescence". In: *Measurement Science and Technology* 18.3 (2007), p. 697.
- [403] Wenzheng Xia et al. *Catalyzed Gasoline Particulate Filter (GPF) Performance: Effect of Driving Cycle, Fuel, Catalyst Coating*. Tech. rep. 2017. DOI: <https://doi.org/10.4271/2017-01-2366>.
- [404] Fangxi Xie et al. "Effects of split and single injection strategies on particle number emission and combustion of a GDI engine". In: *Proceedings of the Institution of Mechanical Engineers, Part D: Journal of Automobile Engineering* (2018). ISSN: 09544070. DOI: 10.1177/0954407018759739.
- [405] Jiaoping Xing et al. "Individual particles emitted from gasoline engines: Impact of engine types, engine loads and fuel components". In: *Journal of Cleaner Production* 149 (2017), pp. 461–471. ISSN: 09596526. DOI: 10.1016/j.jclepro.2017.02.056. URL: <https://www.sciencedirect.com/science/article/pii/S0959652617302706>.
- [406] Hongming Xu et al. "Fuel injector deposits in direct-injection spark-ignition engines". In: *Progress in Energy and Combustion Science* 50 (2015), pp. 63–80. ISSN: 03601285. DOI: 10.1016/j.pecs.2015.02.002. URL: <http://dx.doi.org/10.1016/j.pecs.2015.02.002>.
- [407] B. Yadollahi and M. Boroomand. "The effect of combustion chamber geometry on injection and mixture preparation in a CNG direct injection SI engine". In: *Fuel* 107 (2013), pp. 52–62. ISSN: 00162361. DOI: 10.1016/j.fuel.2013.01.004. URL: <http://dx.doi.org/10.1016/j.fuel.2013.01.004>.
- [408] X. Yang, J. Yang, and K. Hu. "The effect of injector position on the performance of a homogeneous direct injection gasoline engine". In: *2011 International Conference on Electric Information and Control Engineering*. 2011, pp. 6256–6259. DOI: 10.1109/ICEICE.2011.5776809.
- [409] Xiufeng Yang, Lu Dai, and Song-Chang Kong. "Simulation of liquid drop impact on dry and wet surfaces using SPH method". In: *Proceedings of the Combustion Institute* 36.2 (2017), pp. 2393–2399.
- [410] AL Yarin and DA Weiss. "Impact of drops on solid surfaces: self-similar capillary waves, and splashing as a new type of kinematic discontinuity". In: *Journal of fluid mechanics* 283 (1995), pp. 141–173.
- [411] Alexander L Yarin. "Drop impact dynamics: splashing, spreading, receding, bouncing?" In: *Annu. Rev. Fluid Mech.* 38 (2006), pp. 159–192.
- [412] Sam S Yoon and Paul E DesJardin. "Modelling spray impingement using linear stability theories for droplet shattering". In: *International Journal for Numerical Methods in Fluids* 50.4 (2006), pp. 469–489.

- [413] K YOSHIZAWA A; HORIUTI. "A statistically-derived subgrid-scale kinetic energy model for the large-eddy simulation of turbulent flows". English. In: *Journal of the Physical Society of Japan* (1985). ISSN: 0031-9015.
- [414] MR Yosri et al. "Development of a Verification Methodology for Large-Eddy Simulation of Underexpanded Natural Gas Jets". In: *Development* 10 (2018), p. 13.
- [415] Jingzhou Yu et al. "Visualization and analysis of the characteristics of transitional underexpanded jets". In: *International Journal of Heat and Fluid Flow* 44 (2013), pp. 140–154. ISSN: 0142-727X. DOI: 10.1016/J.IJHEATFLUIDFLOW.2013.05.015.
- [416] Linjun Yu et al. "Comparative Study on Gasoline HCCI and DICI Combustion in High Load Range with High Compression Ratio for Passenger Cars Application". In: *SAE International Journal of Fuels and Lubricants* 10.3 (2017). ISSN: 1946-3960. DOI: <https://doi.org/10.4271/2017-01-2257>. URL: <https://doi.org/10.4271/2017-01-2257>.
- [417] M Zampilli et al. "A Quantitative Methodology to Measure Injector Fouling Through Image Analysis". In: 101 (2016), pp. 693–700. ISSN: 18766102. DOI: 10.1016/j.egypro.2016.11.088. URL: <http://dx.doi.org/10.1016/j.egypro.2016.11.088>.
- [418] Wei Zeng et al. "Macroscopic characteristics for direct-injection multi-hole sprays using dimensionless analysis". In: *Experimental Thermal and Fluid Science* 40 (2012), pp. 81–92. ISSN: 08941777. DOI: 10.1016/j.expthermflusci.2012.02.003. URL: <http://dx.doi.org/10.1016/j.expthermflusci.2012.02.003>.
- [419] Y Zeng. "Modelling of multicomponent fuel vaporization in internal combustion engines". PhD thesis. 2000. ISBN: 0612699625.
- [420] Anqi Zhang et al. "Measurement of diesel spray formation and combustion upon different nozzle geometry using hybrid imaging technique". In: *SAE International Journal of Engines* 7.2 (2014), pp. 1034–1043.
- [421] Miaomiao Zhang et al. "Combustion, performance and particulate matter emissions analysis of operating parameters on a GDI engine by traditional experimental investigation and Taguchi method". In: *Energy Conversion and Management* 164.March (2018), pp. 344–352. ISSN: 01968904. DOI: 10.1016/j.enconman.2018.03.017. URL: <https://doi.org/10.1016/j.enconman.2018.03.017>.
- [422] Miaomiao Zhang et al. "Experimental investigation of impacts of injection timing and pressure on combustion and particulate matter emission in a spray-guided gdi engine". In: *International Journal of Automotive Technology* 19.3 (2018), pp. 393–404. DOI: <https://doi.org/10.1007/s12239-018-0038-8>.

- [423] Wenbin Zhang et al. *Effect of Fuel Detergent on Injector Deposit Formation and Engine Emissions in a Gasoline Direct Injection (GDI) Engine*. Tech. rep. 2017. DOI: <https://doi.org/10.4271/2017-01-2247>. URL: <https://doi.org/10.4271/2017-01-2247>.
- [424] F Zhao, M.-C Lai, and D.L Harrington. "Automotive spark-ignited direct-injection gasoline engines". In: *Progress in Energy and Combustion Science* 25.5 (1999), pp. 437–562. ISSN: 0360-1285. DOI: 10.1016/S0360-1285(99)00004-0. URL: <https://www.sciencedirect.com/science/article/pii/S0360128599000040>.
- [425] Lifeng Zhao et al. "The effects of EGR and ignition timing on emissions of GDI engine". In: *Science China Technological Sciences* 56.12 (2013), pp. 3144–3150. ISSN: 16747321. DOI: <https://doi.org/10.1007/s11431-013-5379-y>.
- [426] J. Zheng et al. "Simulation Guided Design for Developing Direct Injection Combustion Systems of Gasoline Engines". In: *SAE Technical Papers* 2016-Octob (2016). ISSN: 01487191. DOI: 10.4271/2016-01-2313.
- [427] Zhaolei Zheng et al. "Numerical study of the effect of piston top contour on GDI engine performance under catalyst heating mode". In: *Fuel* 157 (2015), pp. 64–72. ISSN: 0016-2361. DOI: <https://doi.org/10.1016/j.fuel.2015.04.054>. URL: <http://www.sciencedirect.com/science/article/pii/S0016236115004615>.
- [428] J. Zhou et al. "An Investigation of Abnormal Spray Behaviors of Multi-Hole GDI Injector". In: *SAE Technical Papers* (2016). ISSN: 01487191. DOI: 10.4271/2016-01-0848.
- [429] Guangfei Zhu et al. *Modeling Ignition and Combustion in Spark-Ignition Engines Based on Swept-Volume Method*. Tech. rep. 2018. DOI: <https://doi.org/10.4271/2018-01-0188>. URL: <https://doi.org/10.4271/2018-01-0188>.
- [430] Lars Zigan et al. "Effect of fuel properties on spray breakup and evaporation studied for a multihole direct injection spark ignition injector". In: *Energy & Fuels* 24.8 (2010), pp. 4341–4350.
- [431] Lars Zigan et al. "Structure of evaporating single-and multicomponent fuel sprays for 2nd generation gasoline direct injection". In: *Fuel* 90.1 (2011), pp. 348–363.
- [432] Robert D Zucker and Oscar Biblarz. *Fundamentals of gas dynamics*. John Wiley & Sons, 2002.